Virginia Commonwealth University
VCU Scholars Compass

Theses and Dissertations | Graduate School

2012

Characterization of Superhydrophobic Surfaces Fabricated Using AC-Electrospinning and Random Particle Deposition

Mohamed Samaha Jr.
Virginia Commonwealth University

Follow this and additional works at: https://scholarscompass.vcu.edu/etd

 Part of the Engineering Commons

© The Author

Downloaded from
https://scholarscompass.vcu.edu/etd/2741

This Dissertation is brought to you for free and open access by the Graduate School at VCU Scholars Compass. It has been accepted for inclusion in Theses and Dissertations by an authorized administrator of VCU Scholars Compass. For more information, please contact libcompass@vcu.edu.

School of Engineering

Virginia Commonwealth University

This is to certify that the thesis prepared by Mohamed Ahmed Ali Samaha entitled "Characterization of Superhydrophobic Surfaces Fabricated Using AC-Electrospinning and Random Particle Deposition" has been approved by his committee as satisfactory completion of the thesis requirement for the degree of Doctor of Philosophy

---

Dr. Mohamed Gad-el-Hak, Committee Chair, Mechanical & Nuclear Engineering

---

Dr. Alenka Luzar, Committee Member, Chemistry

Dr. Ümit Özgür, Committee Member, Electrical and Computer Engineering

---

Dr. Hooman V. Tafreshi, Committee Member, Mechanical & Nuclear Engineering

---

Dr. Gary C. Tepper, Committee Member and Chair of the Department of Mechanical & Nuclear Engineering

---

Dr. J. Charles Jennett, Interim Dean of the School of Engineering

---

Dr. F. Douglas Boudinot, Dean of the School of Graduate Studies

May 8, 2012

© Mohamed Ahmed Ali Samaha, 2012
All Rights Reserved

"CHARACTERIZATION OF SUPERHYDROPHOBIC SURFACES FABRICATED USING AC-ELECTROSPINNING AND RANDOM PARTICLE DEPOSITION"

A thesis submitted in partial fulfillment of the requirements for the degree of
Doctor of Philosophy
at Virginia Commonwealth University

by

MOHAMED AHMED ALI SAMAHA
M.Sc., Faculty of Engineering, Alexandria University, Egypt, 2007
B.Sc., Faculty of Engineering, Alexandria University, Egypt, 2002

Major Director:
Dr. Mohamed Gad-el-Hak
The Inez Caudwill Eminent Professor, Mechanical & Nuclear Engineering

Virginia Commonwealth University
Richmond, Virginia
May, 2012

Acknowledgment

Thanks to God (ALLAH) by whose great mercy this work has been achieved.

No words can adequately express my deepest gratitude to Professor Mohamed Gad-el-Hak for his moral help and support, continuous supervision, priceless advice, and beneficial guidance and encouragement. I will always remain grateful for all what he offered throughout this work. My respect for him will always be in my heart.

I am deeply indebted to Dr. Hooman Vahedi Tafresh for his useful guidance, valuable instructions, and unfading interest. I am grateful to him for his support and helpful discussions. I will always remember his patience and understanding.

I would like to express my sincere gratitude to Professors Gary C. Tepper and Kenneth J. Wynne for their kindly help and scientific support. I am very thankful for the opportunities that they provided me and for the use of their labs and devices.

I am also thankful to the other members of my doctoral thesis committee, Professor Alenka Luzar and Dr. Ümit Özgür, for their assistance, support, encouragement, and valuable comments. I owe special thanks to Drs. Karla M. Mossi and Dmitry Pestov for their encouragement and wonderful counseling. I am also thankful to my labmate, Dr. Ochanda, for his help. I also thank the Defense Advanced Research Projects Agency (DARPA) for funding this research, contract number W91CRB-10-1-0003, technical sponsor Captain Christopher Warren, USN. Last but not least, I thank my parents, wife, and daughters for their love, support, and encouragement throughout this work.

To my parents, wife, and daughters Mariam and Tasniem

Table of Contents

List of Figures

List of Tables

Abstract

CHARACTERIZATION OF SUPERHYDROPHOBIC SURFACES FABRICATED USING AC-ELECTROSPINNING AND RANDOM PARTICLE DEPOSITION

by Mohamed Ahmed Ali Samaha, M.Sc.

A thesis submitted in partial fulfillment of the requirements for the degree of Doctor of Philosophy at Virginia Commonwealth University

Virginia Commonwealth University, 2012

Major Director:
Dr. Mohamed Gad-el-Hak
The Inez Caudwill Eminent Professor, Mechanical & Nuclear Engineering

Surfaces with static contact angle greater than 150 degrees are typically classified as superhydrophobic. Such coatings have been inspired by the lotus leaf. As water flows over a superhydrophobic surface, "slip effect" is produced resulting in a reduction in the skin-friction drag exerted on the surface. Slip flow is caused by the entrapment of a layer of air between water and the surface. Superhydrophobicity could be utilized to design surfaces for applications such as energy conservation, noise reduction, laminar-to-turbulent-transition delay, and mixing enhancement. A popular method of manufacturing a superhydrophobic surface is microfabrication in which well-designed microgrooves and/or poles are placed on a surface in a regular configuration. This method is a costly process and cannot easily be applied to large-scale objects with arbitrary shapes. In this work, we fabricated and characterized simpler low-cost superhydrophobic coatings based on controlling the volume of entrapped air in order to enhance durability (longevity) and the properties of the coating bringing the technology closer to large-scale submerged bodies such as submarines and ships. Two

different low-cost fabricating techniques have been utilized: (i) random deposition of hydrophobic aerogel microparticles; and (ii) deposition of hydrophobic polymer micro- and nanofibers using DC-biased AC-electrospinning. The present study is aimed at providing experimental, numerical, and analytical models to characterize the superhydrophobicity and longevity of the coatings depending on the morphology of the surfaces and the concentration of the hydrophobic materials. The surface's micro/nanostructure were observed by field emission scanning electron microscopy. The degree of hydrophobicity of the coatings was estimated using drag-reduction and contact-angle measurements using a rheometer and a goniometer respectively. Furthermore, We have advanced and calibrated a novel optical technique to noninvasively measure the longevity of submerged superhydrophobic coatings subjected to different environmental conditions. We have also modeled the performance of superhydrophobic surfaces comprised of randomly distributed roughness. The numerical simulations are aimed at improving our understanding of the drag-reduction effect and the stability of the air–water interface against pressure in terms of the microstructure parameters. Moreover, we have experimentally characterized the terminal pressure (i.e. the pressure at which the air–water interface completely fails) of aerogel coatings with different morphologies.

CHAPTER 1 Introduction

1.1 Biomimetic

Several design ideas have been inspired by nature. Biological mechanisms can be studied to engineer systems for modern industrial applications. The lotus leaf possesses a peculiar water-repellent characteristic that enhances the mobility of droplets for self-cleaning purposes (Neinhuis & Barthlott, 1997). A similar effect, i.e. superhydrophobicity, enables a water strider to walk on water (Gao & Jiang, 2004). When a superhydrophobic surface is fully submersed in water, it entraps air in its pores resulting in the formation of air pockets between the solid surface and water. The entrapped air is separated from water with a thin interface anchored on the solid walls and stretched due to surface tension forces. It has been observed that a moving body of water "slips" over an air–water interface, whereas it "sticks" to a solid surface (Rothstein, 2010). Therefore, if the percentage of the surface covered by air pockets is sufficiently high, a superhydrophobic surface can cause the so called "slip effect", resulting in a reduction in the skin-friction drag exerted on the surface (Rothstein, 2010). The air–water interface area is characterized by gas fraction, the area of air–water interface divided by the total surface area. The gas fraction has an impact on the so-called slip length (Navier, 1823), which determines how much the surface can produce slipping flow and hence drag reduction. As long as the air pockets exist, the surface remains hydrophobic. In other words, the degree of hydrophobicity and the beneficial effects are diminished by the reduction of the amount of entrapped air. The longevity of a superhydrophobic surface—how long the surface can maintain the air pockets—is critical, especially in underwater applications. Superhydrophobic coatings provide a relatively simple, passive drag-reduction method, and may poten-

tially become a viable alternative to the more complex and energy consuming active or reactive flow control techniques such as wall suction/blowing (Gad-el-Hak, 2000). There are at least three challenges to overcome before field applications are feasible: (i) scaling up the application of superhydrophobic coatings to large submersibles; (ii) achieving low-cost fabrication; and (iii) preventing the entrapped air from escaping under pressure for reasonably long time, or at least periodically *rejuvenating* the surface.

1.2 Fabrication and Characterization of Superhydrophobic Surfaces

Superhydrophobic surfaces have often been produced using the same microfabrication techniques developed for the electronic industry, and in many cases consist of a regular array of microposts or microridges (Davies *et al.*, 2006; Lee *et al.*, 2008; Lee & Kim, 2009). Orientation with respect to the flow, spacing, and aspect ratio of the microstructure could be adjusted to optimize the performance of those surfaces. The orientation of microroughness, flow characteristics, and shape of air–water interface (meniscus) could all significantly affect the slip condition and hence the drag reduction. For example, Woolford *et al.* (2009) demonstrated that in a turbulent flow regime, streamwise ridges (i.e., flow direction parallel to the microridges) could lead to drag reduction, while spanwise ridges (i.e., flow direction perpendicular to the microridges) could lead to drag increase. Woolford *et al.* reason that the transverse configuration results in higher turbulence intensity, higher total and turbulence shear stress, and higher production of turbulence, and vice versa for the longitudinal configuration. Additionally, Steinberger *et al.* (2007) demonstrated that the meniscus shape influences the boundary condition, which could increase the friction. When the capillary number is significantly low (less than 10^{-4}), the capillary force dominates and the meniscus shape could be considered as a spherical cap that is stress independent. If the protrusion angle of the meniscus exceeds a specific limit, an immobile

liquid layer with significant thickness is trapped close to the solid wall, which results in increasing the drag force higher than that of a hydrophilic smooth surface.

Clearly, large-scale manufacturing of microfabricated superhydrophobic surfaces is prohibitively expensive. An alternative solution to circumvent the cost is to produce surfaces made up of random deposition of hydrophobic particles or fibers. Bhagat *et al.* (2008) developed an inexpensive method for the rapid synthesis of hydrophobic silica aerogel powder. Yang & Deng (2008) demonstrated a simple technique to produce superhydrophobic papers by using a multi-layer deposition of polymers and silica particles. Lee *et al.* (2011) fabricated a granular superhydrophobic coating by blasting the surface with sodium bicarbonate. Hwang *et al.* (2011) produced surfaces using spray-deposition to reach contact angles up to 178 degrees.

Electrospinning is another cost-effective fabrication technique that can be used to produce superhydrophobic surfaces with fibrous microstructure. This technique can be used to deposit micro- and/or nanotextured coatings by spinning hydrophobic polymers onto substrates of arbitrary geometries (Ma *et al.*, 2005; Singh *et al.*, 2005; Zhu *et al.*, 2006). Conventionally, electrospinning is performed by applying a large DC-potential between the electrospinning source (typically a hypodermic syringe) and the substrate, resulting in nonwoven fiber mats with randomly oriented fibers (Sarkar *et al.*, 2007). The random orientation of the fibers is the result of the inherent electrostatic instability of the charged jet as it travels from the spinneret to the collector. This instability can be reduced by using a DC-biased AC potential that induces short segments of alternating polarity, thereby reducing the magnitude of the destabilizing force on the fiber (Sarkar *et al.*, 2007).

The air–water interface developed due to superhydrophobicity is the surface that supports a force applied on the surface, e.g., water strider's weight. A similar force can be exerted on the air–water interface formed over a submerged superhydrophobic surface by the column of water above the surface. If the pressure is high enough, water will penetrate into the pores on the surface and replace the air, i.e.

transition from the non-wetted state (Cassie state) to the wetted state (Wenzel state). Even when the air–water interface on a superhydrophobic surface is mechanically stable, the surface is likely to lose its entrapped air content over time. This is especially the case when the surface is submerged. This effect is believed to be due to the dissolution of air in water, and is expected to accelerate when the hydrostatic pressure is increased, as the solubility of air in water increases with pressure.

1.3 Objectives

The primary objective of the present study is to fabricate, characterize, and optimize low-cost superhydrophobic coatings. Such coatings will ultimately be used on submarines, torpedoes and naval ships for the purpose of reducing skin-friction drag and flow-induced noise in both the laminar and turbulent boundary layers surrounding these vessels when cruising in seawater. We tested two different low-cost fabricating techniques. First, hydrophobic aerogel particles were deposited onto a substrate consisting of a metal coated with a thin polymer film that was used for adhesion. In this case, superhydrophobicity was achieved by a combination of hydrophobic substance (aerogel) and surface roughness (random aerogel grains). Second, hydrophobic polymer micro- and nanofibers were deposited onto solid substrates using DC-biased AC-electrospinning. This technique was selected because it can produce coatings with a high degree of fiber alignment (Sarkar *et al.*, 2007). The roughness here is generated by the fibers themselves.

The present study is aimed at providing experimental, numerical, and analytical models to characterize the superhydrophobicity and longevity of the coatings depending on the morphology of the surfaces and the concentration of the hydrophobic materials. Additionally, by using several experimental and theoretical approaches, we investigate the effects of the environmental conditions such as elevated pressures, water movements, and water salinity on the performance of the coatings.

1.4 Outline

In this thesis, seven tasks have been completed and appeared in eight journal articles and five conference papers. Each of the following chapters briefly explains a paper or more. Further details can be obtained from the journal papers, which are reprinted in the appendices.

The chapters are organized as follows. The next chapter is a literature review regarding biomimetic, fabrication and characterization of superhydrophobic surfaces. Chapter 3 explains the fabrication of superhydrophobic polystyrene fibrous coating using DC-biased AC-electrospinning. The coating's hydrophobicity was characterized based on the fibers morphology and composition. Superhydrophobic surfaces comprised of randomly deposited aerogel particles are discussed in the same chapter. Chapter 4 presents an *in situ*, noninvasive optical technique to precisely measure the effect of different environmental parameters on superhydrophobicity and longevity of the different coatings. The next chapter discusses the effects of water movement on longevity of superhydrophobic fibrous coatings in comparison with stagnant water. This simulates a moving underwater object such as a torpedo or a submarine. Chapter 6 describes the effect of elevated hydrostatic pressure on the properties of superhydrophobic coatings. This is crucial for deep underwater applications.

Effects of water salinity on the degree of hydrophobicity and longevity of the coatings were observed and discussed in Chapter 7. The next chapter presents fabrication and characterization of randomly deposited superhydrophobic aerogel coatings with different morphological characteristics. The stability the air–water interface against pressure was estimated. An image-processing technique was used to determine the gas fraction of the coatings. Chapter 9 demonstrates a model for aerogel coatings. We provided a numerical simulations to calculate drag reduction and an analytical study to predict air–water interface (meniscus) stability of superhydrophobic surfaces comprised of random roughness (e.g. aerogel coatings) and compared them to

microfabricated ordered roughness. Extensions of this study by Dr. Tafreshi's group are also explained in this chapter. Conclusions and recommendations for future work are presented in the last chapter.

CHAPTER 2 Literature Review

2.1 Characterization of Superhydrophobic Surfaces

2.1.1 Lotus Leaf

Lotus leaves, *Nelumbo nucifera*, owe their self-cleaning ability to superhydrophobicity. Neinhuis & Barthlott (1997) obtained scanning electron microscopy (SEM) images for several water-repellent plants and reported the micromorphological characteristics of 200 species. They demonstrated that the epidermal (i.e. outermost) cells of the lotus leaves form papillae, which act as microstructure roughness. The papillae are superimposed by a very dense layer of epicuticular waxes (wax crystals), also referred to as hair-like structures (Cheng *et al.*, 2006) or nanostructure roughness (Koch *et al.*, 2009). Figure 2.1 shows different degrees of magnification of lotus leaves using SEM images from zero to 10^6 times. Epicuticular waxes themselves have hydrophobic properties, which together with micro- and nanostructure roughness, result in reduced contact area between water droplets and the leaf's surface. This combination results in static contact angles exceeding 150 degrees on lotus leaves. If the surface is tilted, even with a slight angle, water droplets begin to roll off the leaves, and so collect and remove dirt from the surface demonstrating the self-cleaning effect (see Figure 2.2). Note that because of the micro- and nanostructure roughness, the contact area between dirt particles and the leaf's surface is dramatically reduced. Thus, the adhesion between the particles and the surface can be lower than that between the particles and the droplets, facilitating particle removal. Accordingly, the lotus leaf is a symbol of purity in some Asian religions (Neinhuis & Barthlott, 1997).

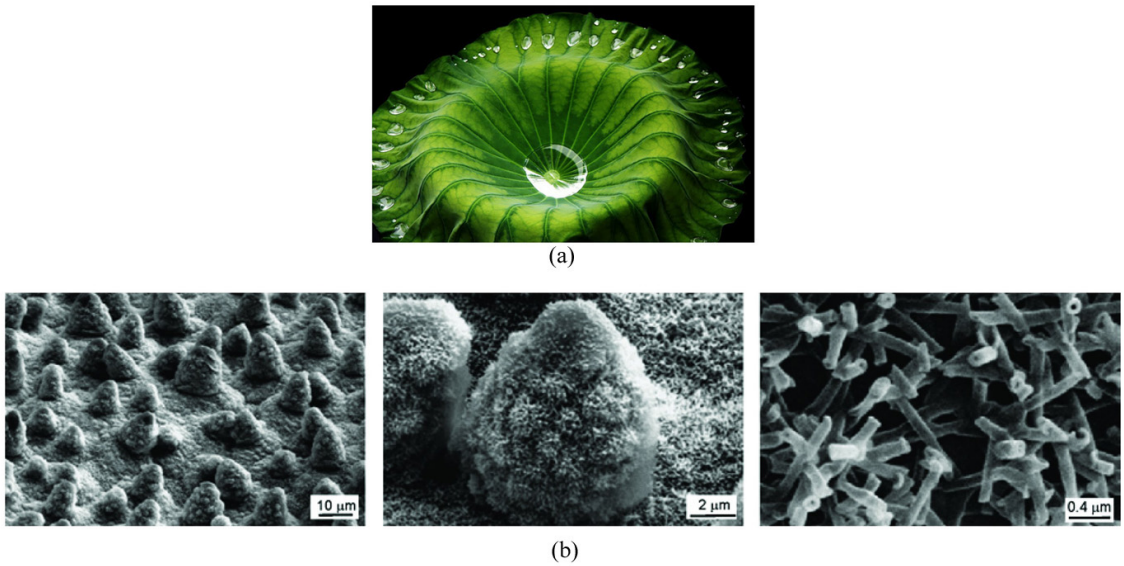

(a)

(b)

Figure 2.1: Lotus leaf: (a) Zero magnification; from website (http://www.flickr.com). (b) Three different magnification of SEM images showing morphological micro- and nanostructures; from Koch *et al.* (2009).

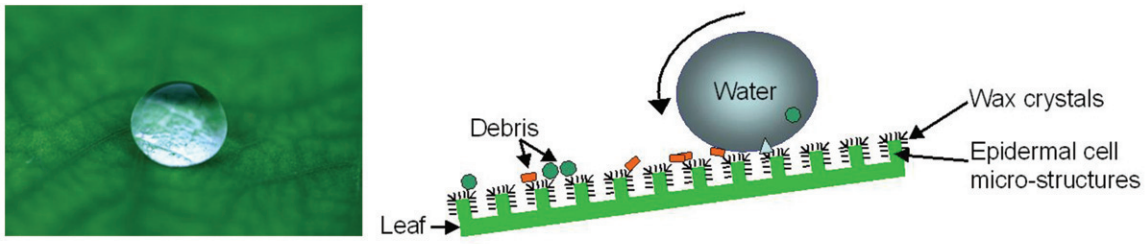

(a) (b)

Figure 2.2: (a) Water droplet beading on lotus leaf with static contact angle higher than 150 degrees; from website (http://www.hk-phy.org). (b) Schematic illustration of lotus effect; from website (http://www.thenakedscientists.com).

2.1.2 Slip Flow and Drag Reduction

When a superhydrophobic surface is submersed in water, it generates slip flow, which reduces the skin-friction drag exerted on the surface. Drag is the force produced by a fluid to resist the relative motion of a solid (Gad-el-Hak, 2000). A tremendous amount of fuel is consumed each year both by air and water vehicles and by gas and liquid transmission through pipelines in order to overcome drag (Gad-el-Hak, 2000). Drag force can be classified into two main categories, form (pressure) drag and skin-friction drag. The latter, which depends on fluid viscosity, strain rate (velocity gradient), and surface area, is the subject of this section. The multiplication of fluid viscosity and velocity gradient gives the shear stress. Figure 2.3 shows the Couette flow between two plates having a gap, h, in the normal direction, z. The upper plate is moving with velocity V_{avg} and the lower one is stationary. The lower plate can have a no-slip (sticky) or a slip boundary condition. In the case of no-slip boundary, the slope of the velocity gradient (line S1) is higher than that of slip flow (line S2), which leads to a higher shear stress.

Generally, slip is defined as a fluid dynamics condition in which there exists a relative tangential velocity between the solid surface and the fluid immediately adjacent to the surface. Slip can be encountered in several situations. For example, for gas flow, slip could occur if the mean free path of the gas (i.e. the average distance traveled by molecules between collisions) is comparable to the characteristic dimensions of the flow (Gad-el-Hak, 1999). As mentioned earlier, a superhydrophobic surface entraps air in its pore space producing two different interfaces. One is the aforementioned air–water interface on which the water slips, and the other is the solid-water interface to which the water sticks. The average slip over the entire surface is often referred to as "effective slip" (Lauga *et al.*, 2007). The air–water interface area is characterized by gas fraction, the ratio of the area of the air–water interface to the total surface area. The gas fraction is the main parameter that determines the static contact angle

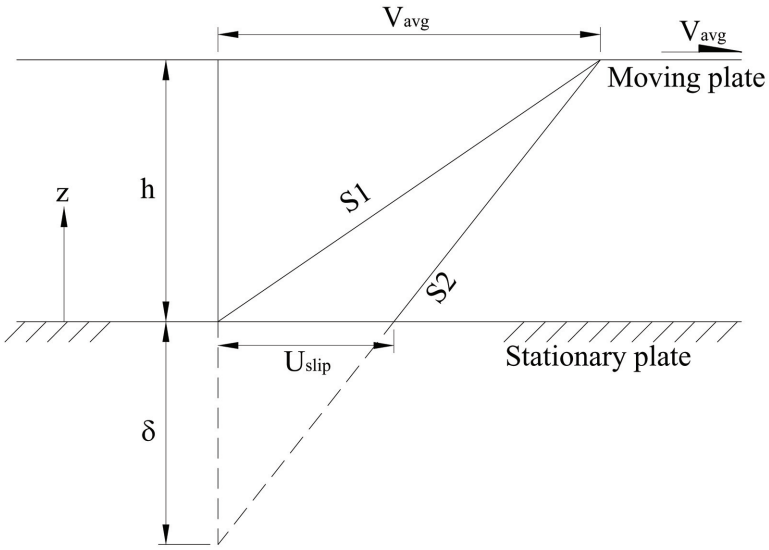

Figure 2.3: Schematic diagram of velocity profiles between fixed and moving plates in case of slip and no slip at fluid-solid interface. From Samaha *et al.* (2011*a*).

(Bico *et al.*, 1999), which characterizes the hydrophobicity of the surface. Callies *et al.* (2005) experimentally demonstrated that as gas fraction increases, static contact angle increases. Furthermore, the gas fraction has an impact on the so-called "slip length, δ" (Lee *et al.*, 2008). According to Navier's model (Navier, 1823), the magnitude of the slip velocity is proportional to the magnitude of the strain rate. The slip length is the proportionality constant as shown in Figure 2.3. Thus, the slip length can be calculated from the following equation.

$$\delta = \frac{U_{slip}}{\frac{\partial u}{\partial y}|_{wall}} \tag{2.1}$$

where U_{slip} is the area-weighted average slip velocity at the superhydrophobic wall, u is the streamwise velocity, and y is the normal direction.

Several studies have demonstrated the effect of gas fraction on the slip length (Lee *et al.*, 2008; Ybert *et al.*, 2007; Cheng *et al.*, 2009; Daniello *et al.*, 2009; Martell *et al.*, 2009). Some of these studies showed that for laminar flow, slip length increases

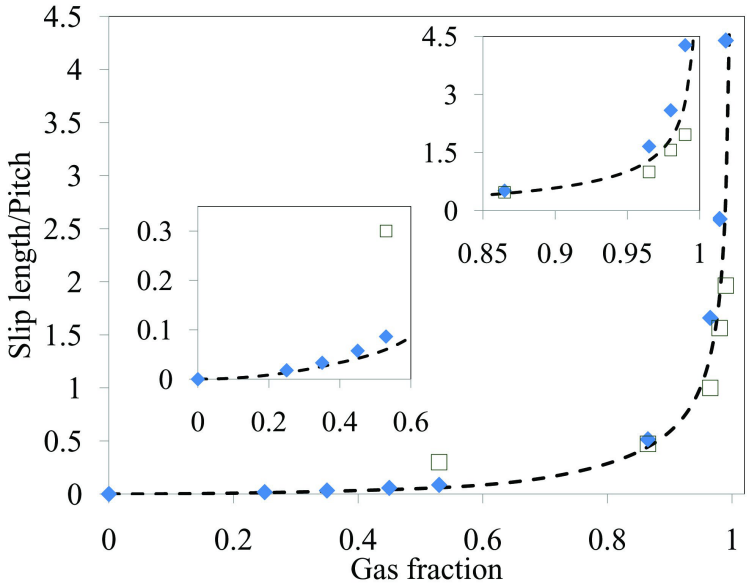

Figure 2.4: Slip length vs. gas fraction obtained for laminar flow over ordered microposts superhydrophobic surface. Experimental data of Lee *et al.* (2008) (open squares), theory of Ybert *et al.* (2007) (dashed line), and Samaha *et al.* (2011*b*) (solid diamonds).

as gas fraction increases (Figure 2.4) and hence from Equation 2.1, velocity gradient decreases (i.e. less drag). This figure shows the calculated and the measured slip lengths (normalized by the pitch; the distance between two posts) versus gas fraction for ordered microposts on a superhydrophobic surface. A closer view at gas fractions below 0.6 and above 0.85 is given in the insets for better illustration. From the figure, it is obvious that when the gas fraction, ϕ_g, is less than 0.4, the slip length is proportional to ϕ_g^2. On the other hand, if the gas fraction is higher than 0.7, the slip length is proportional to $1/\sqrt{\phi_g}$. Within the range $0.4 < \phi_g < 0.7$, interpolation is utilized. The above mathematical proportionalities are derived and validated by Ybert *et al.* (2007). The drag reduction also increases as gas fraction increases, as shown in Figure 2.5. The figure includes both experimental and numerical results for a microchannel with a microridged superhydrophobic wall.

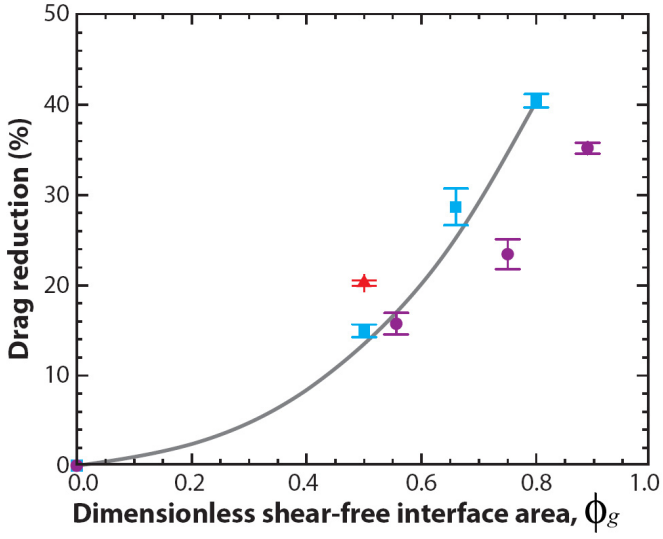

Figure 2.5: Average drag reduction as a function of dimensionless shear-free area, gas fraction. Here, 30 μm wide microridges spaced 30 μm apart (red triangles), 20 μm wide microridges spaced 20 μm apart (blue squares), and 30 μm square microposts spaced 30 μm apart (purple circles). Numerical results for 20μm wide microridges spaced 20μm apart (gray line). From Rothstein (2010).

Other studies show that for turbulent flows, increasing the shear free area (i.e. increasing the gas fraction) results in an increase in the slip velocity and drag reduction (Daniello *et al.*, 2009; Martell *et al.*, 2009). Figure 2.6 shows that skin-friction coefficient decreases by utilizing a superhydrophobic surface on one or both walls of a microchannel for a range of Reynolds numbers covering both the laminar- and turbulent-flow regimes. On the contrary, this was not observed in the work of Woolford *et al.* (2009), who demonstrated that in a turbulent flow regime, streamwise ridges (i.e. flow direction is parallel to microridges structure) can cause drag reduction, while spanwise ridges (i.e. flow direction is perpendicular to microridges structure) can increase the drag.

Obviously, the influence of the microstructural parameters of a superhydrophobic surface on its performance requires further exploration. Such surfaces could be utilized as a passive method of flow control and may potentially become a viable

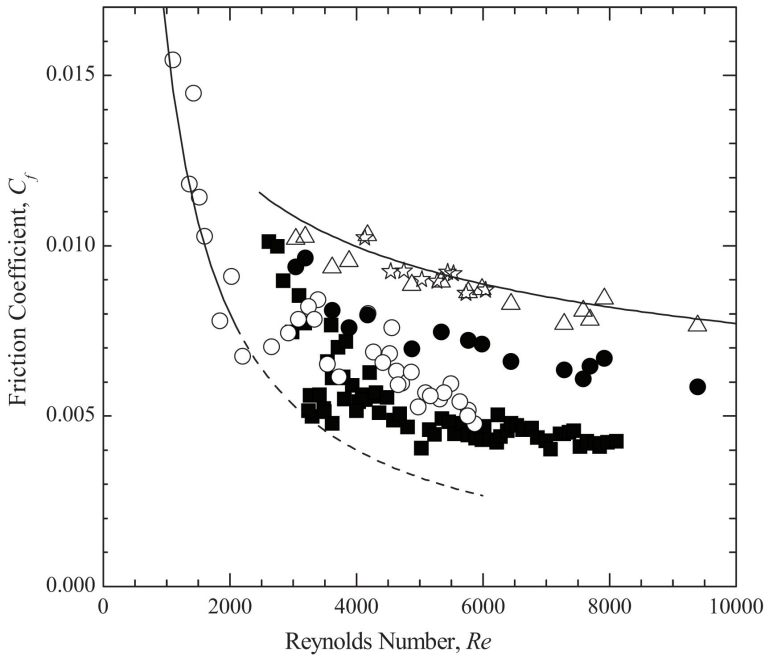

Figure 2.6: Skin-friction coefficient vs. Reynolds number. Microchannel with smooth surfaces (open triangles and open stars), with single superhydrophobic wall (solid circles), and with two superhydrophobic walls (open circles and solid squares). The theoretical predictions of the friction coefficient for a smooth channel are also shown (—). From Daniello *et al.* (2009).

alternative to the more complex and energy consuming active or reactive methods of flow control such as wall suction/blowing (Gad-el-Hak, 2000).

2.2 Microfabrication of Superhydrophobic Surfaces

2.2.1 Ordered Microstructures

Most engineered superhydrophobic surfaces are made up of microposts or microridges (Figure 2.7). The microstructure of these surfaces strongly affects gas fraction, slip length, and drag reduction, in addition to the stability of the air–water interface. For instance, in Figure 2.7a, as post diameter decreases for the same pitch (i.e. distance between two posts), gas fraction increases, which leads to an increase in the drag reduction and slip length due to the increase of the free shear area (air–water interface

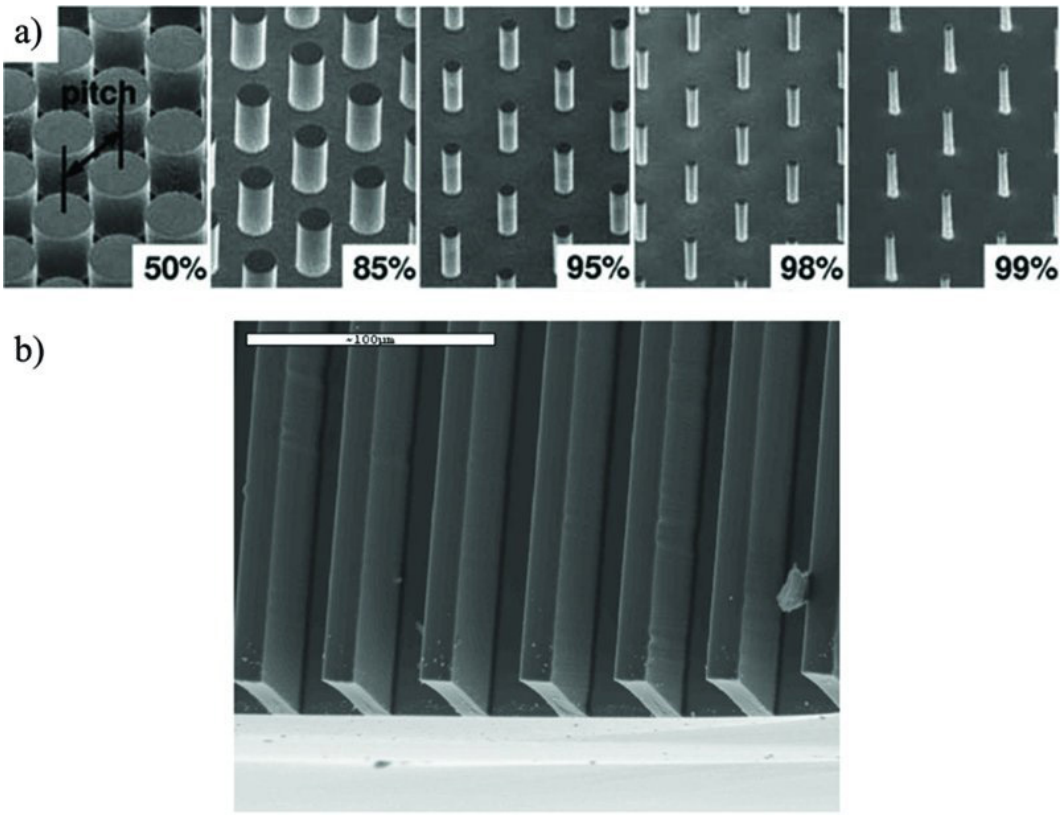

Figure 2.7: (a) Scanning electron microscopy (SEM) images of post patterns with 50 μm pitch for the displayed inset gas fractions; from Lee *et al.* (2008). (b) Image of microfabricated surface with microridges. The width of the cavities and ridges are 30 and 10 μm, respectively. The depth of the rib is 15 μm; from Maynes *et al.* (2007).

area). However, increasing the gas fraction can jeopardize the stability of the interface. A similar conclusion could be drawn for microridges.

Superhydrophobic surfaces comprised of "nanograss" and "nanobricks" are reported by Henoch *et al.* (2006) (see Figure 2.8). The surface with nanograss is reported to yield a contact angle of nearly 180°, and is composed of posts with a diameter of 400 nm and a height of 7 μm spaced 1.25 μm from one another. The surface with nanobricks is peculiar because it can better resist the elevated hydrostatic pressures due to the effect of the entrapped air in its closed cells, which can help to increase the stability of the air–water interface, as will be discussed later in this paper.

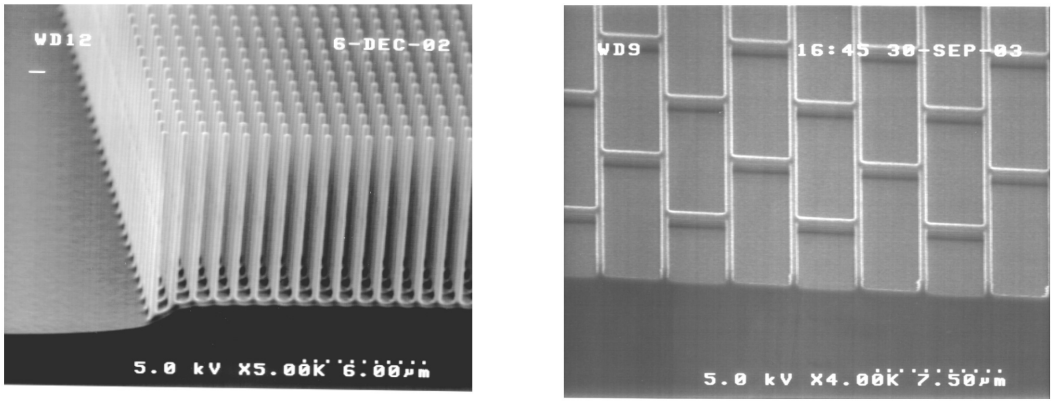

a b

Figure 2.8: (a) SEM image of silicon nanograss. (b) SEM image of silicon nanobricks. From Henoch *et al.* (2006).

The size of each cell is 4 μm $\times$ 10 μm, the height of the cell walls is about 1 μm, and the thickness of the walls is 300 nm. A surface with a texture somewhat similar to that of the nanograss structure is studied by Choi & Kim (2006). These authors present slip length of their surface in comparison to that of a smooth one. Lee & Kim (2009) demonstrated that the slip length can be maximized by superimposing a nanostructure onto a microfabricated structure, similar to the case of wax crystals on papillae of the lotus leaves as shown in Figure 2.9. These authors demonstrated that the contact angle for their surfaces can approach 180°. In addition, they showed that the slip length can be increased up to 400 μm.

2.2.2 Surfaces with Engineered Roughness

There are limitations for commercializing microfabricated surfaces such as those shown in Figures 2.7–2.9. Production cost is probably the most prohibitive issue with microfabricated surfaces. Recent studies, however, have shown that there are alternative methods for engineering superhydrophobic surfaces more cost-effectively. As discussed by Emami *et al.* (2011*a*), one can produce a superhydrophobic surface by randomly depositing hydrophobic particles (e.g. aerogel) on a substrate (see also

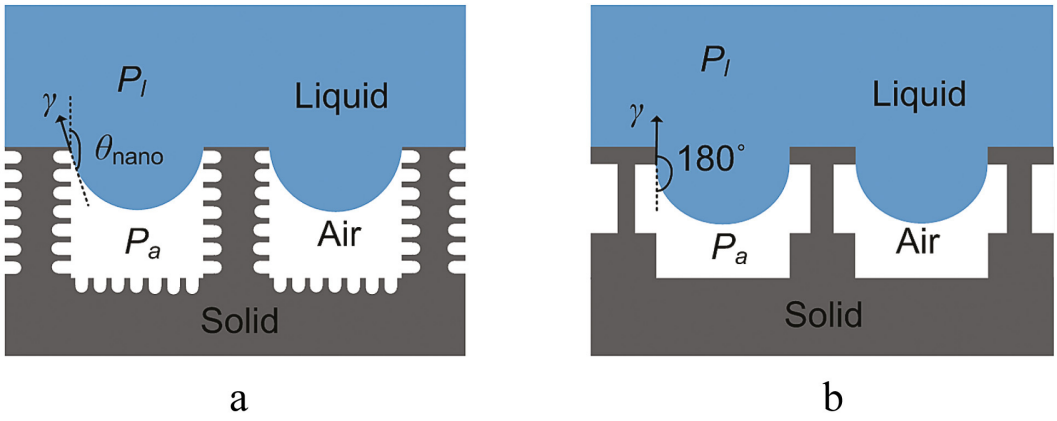

Figure 2.9: (a) Nanostructures on the sidewall. (b) Re-entrant structure. From Lee & Kim (2009).

(Yang & Deng, 2008; Bhagat *et al.*, 2008)). Figure 2.10a shows an SEM image of aerogel powders synthesized using sodium silicate and deposited on a substrate. The static contact angle is measured for a coated surface with aerogel powders to show its superhydrophobicity. Figure 2.10b shows that the contact angle for such a surface is 150°.

Electrospinning is another simple, low-cost method that can be used to deposit micro- to nanotextured coatings of a hydrophobic polymer onto substrates of arbitrary geometry (Ma *et al.*, 2005; Singh *et al.*, 2005; Zhu *et al.*, 2006). The resulting superhydrophobic surfaces can be applied in diverse applications, including self-cleaning glasses and clothes, protection against corrosion of metallic parts (in bridges, marines, under water constructions, etc.), anti-snow sticking, and reducing skin friction drag in underwater vessels such as submarines.

It is worth mentioning that the morphology of the fibers influences the hydrophobicity of the surface. For example, fiber diameter can affect the static contact angle of the coating, as shown in Figure 2.11. This figure shows that contact angle decreases with increasing fiber diameter. However, one should note that since

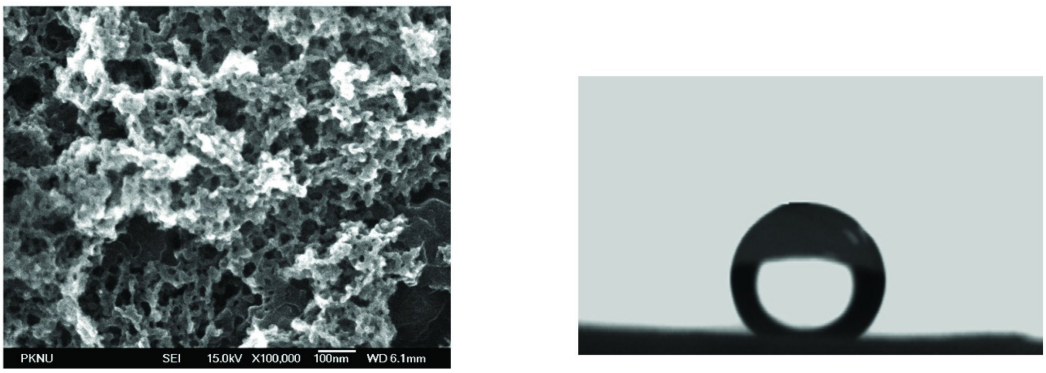

Figure 2.10: (a) SEM image of aerogel powders synthesized using sodium silicate. (b) Water droplet placed on surface of glass substrate coated with aerogel powder. The contact angle is 150°. From Bhagat *et al.* (2008).

other microstructural parameters of the surfaces reported in this figure were not kept constant while fiber diameter was varied, changes in the fiber diameter could have affected the porosity of the mat. Therefore, in the absence of more microstructural information, one should refrain from directly relating fiber diameter to contact angle. The figure shows the results for produced beaded and bead-free fibers. Beaded fibers or polymeric microdroplets could have appeared during electrospinning if the polymeric fluid did not have adequate viscoelasticity and conductivity, which leads to Rayleigh instability, i.e, domination of surface tension during the process that tends to break the liquid into droplets.

2.3 Stability of Air–Water Interface Under Elevated Pressures

2.3.1 Walking on Water

Water striders, *Gerris remigis*, possess a very rare trait that allows them to walk on water. Water striders owe this ability to the hydrophobic waxy microhairs covering their legs, microsetae, which are superimposed with nanogrooves (Gao & Jiang, 2004) as shown in Figure 2.12.

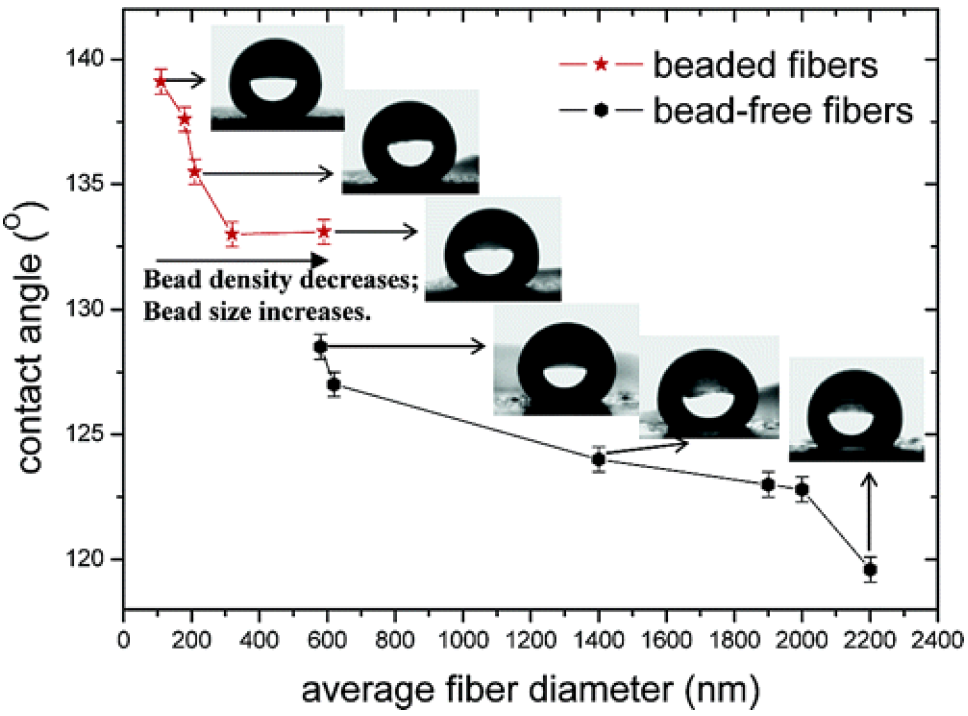

Figure 2.11: Effect of fiber's diameter on static contact angle. From Ma *et al.* (2005).

Air is entrapped between the micro- and nanostructured hairs, making their legs water repellent. Gao & Jiang (2004) used a very sensitive balance system to determine the required force for a single leg to be sunk. They demonstrate that the buoyancy force is 15 times the total body weight. Furthermore, the volume of the displaced water caused by immersing a single leg is 300 times that of the leg itself. Feng *et al.* (2007) have modeled the ultra-hydrophobicity of a water strider's leg by providing a theoretical analysis, coupled with experimental measurements, to determine how deep the leg can reach before piercing the water surface as shown in Figure 2.13. They demonstrated that the maximum depth, h_{max}, depends on the diameter, D, and the contact angle of the leg, ϕ_{leg}. Their results are shown in Figure 2.14. It can be seen that for the actual diameter range (140–180 μm) and for the measured maximum depth ($h_{max} = 4.38 \pm 0.02$ mm), the contact angle should be at least 168°, i.e. highly water repellent. Such a high contact angle allows water

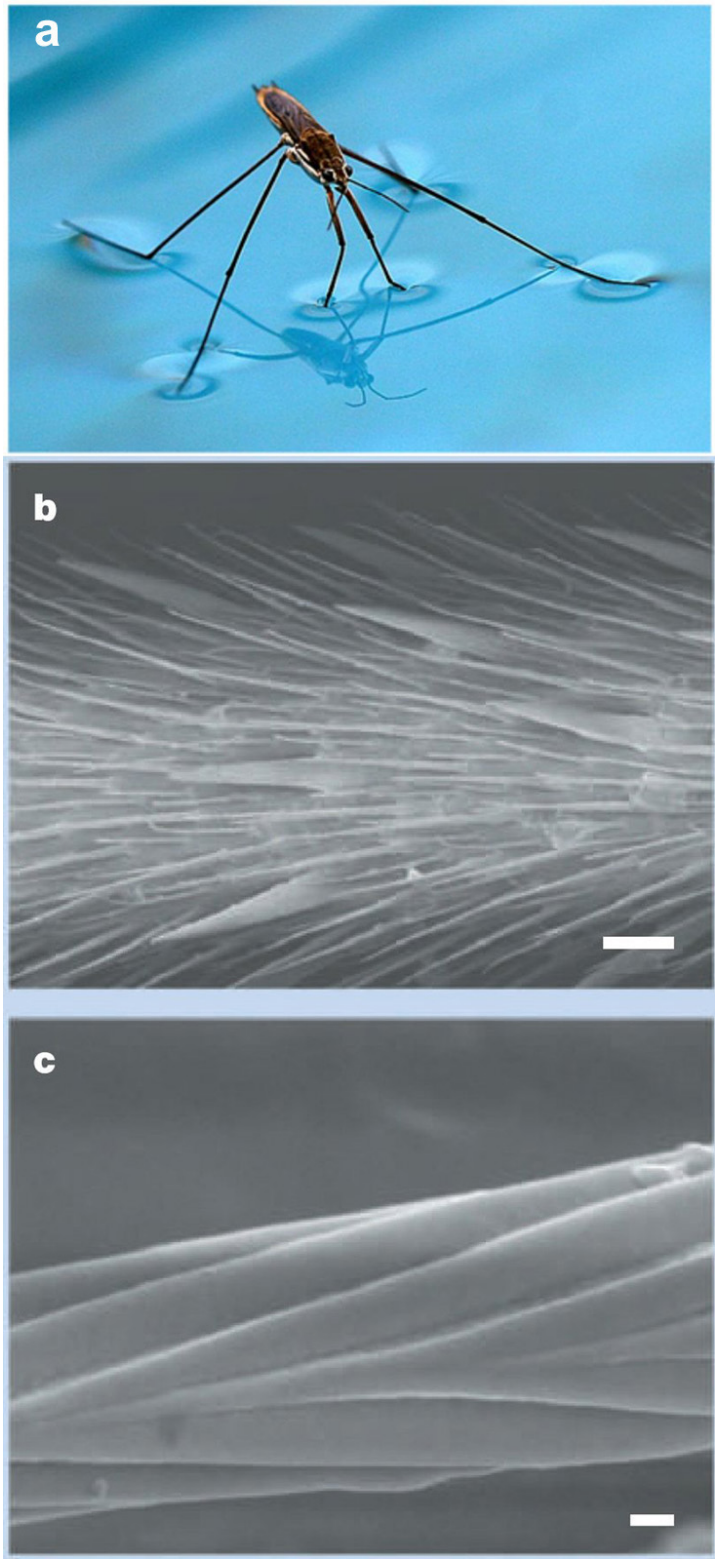

Figure 2.12: (a) Water strider stands on water; from website (http://commons.wikimedia.org). (b) SEM image of water strider's leg showing hydrophobic microsetae, scale bar 20 μm. (c) Higher magnification of single hair showing nanogrooves, scale bar 0.2 μm. Both (b) and (c) from Gao & Jiang (2004).

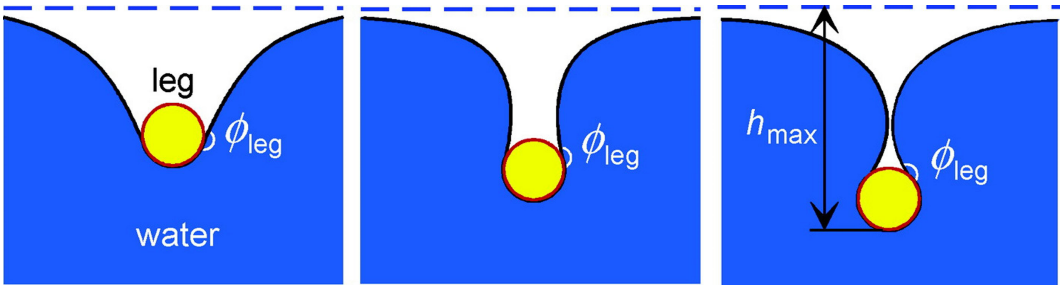

Figure 2.13: Transects of the water surface for the leg contacting the water to different depths until the maximum depth h_{max} is reached before piercing the water surface. From Feng *et al.* (2007).

striders to stand on water, even in the presence of rain or water currents.

2.3.2 Stability of Air–Water Interface under Hydrostatic Pressure

The air–water interface developed due to superhydrophobicity is the surface that supports a water strider's weight. A similar force can be exerted on the air–water interface formed over a submerged superhydrophobic surface by the column of water above the surface. If the pressure is high enough, water will penetrate into the pores on the surface and replace the air, i.e. transition from the non-wetted state (Cassie state) to the wetted state (Wenzel state). This transition is interpreted by two approaches: one based on minimizing the thermodynamic free energy (Patankar, 2004; Barbieri *et al.*, 2007), and the other using a balance of forces across the interface (Extrand, 2004, 2006; Zheng *et al.*, 2005). Lee & Kim (2009) used the latter to develop an equation to determine the maximum allowable hydrostatic pressure (critical pressure) in terms of the surface microstructure for aligned or staggered arrangement of posts as shown in the following equation.

$$P_{max}\phi_g \leq \frac{-2\gamma\sqrt{\pi(1-\phi_g)}\ \cos\theta}{L} \tag{2.2}$$

where P_{max} is the critical pressure, the pressure above which the system departs from the Cassie state, ϕ_g is the gas fraction, γ is the surface tension of the liquid (72×10^{-3}

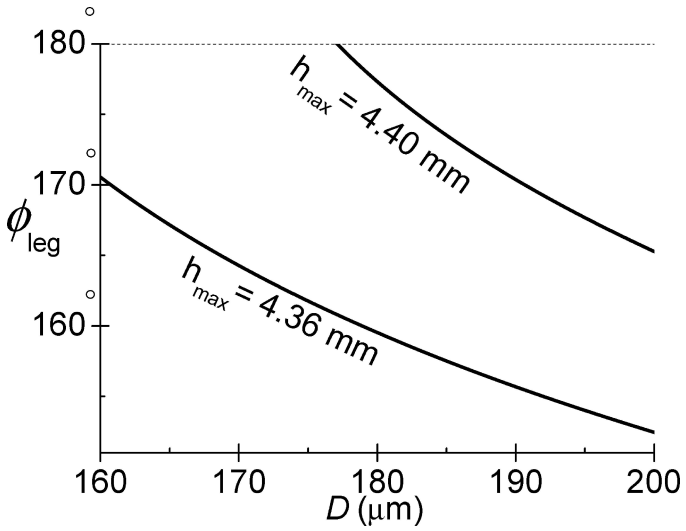

Figure 2.14: Contact angle of the leg and dimple depth. Dependence of the contact angle on the diameter of the leg in order to form the maximal dimple with depth $h_{max} = 4.38 \pm 0.02$ mm. From Feng *et al.* (2007).

N/m in case of water), θ is the contact angle, and L is the pitch (distance between two posts). In a related experimental study, Sheng & Zhang (2011) demonstrated the effects of elevated pressures on the superhydrophobicity of lotus leaves by measuring the contact angle of a droplet on a leaf before and after the experiment. According to Lafuma & Quéré (2003), superhydrophobicity could be explained using the models independently developed by Wenzel (1936) and Cassie & Baxter (1944). The former is more applicable to slightly hydrophobic materials (contact angles just above 90 degrees for a smooth surface). Both models have a linear relation between the apparent contact angle on a rough surface and the corresponding contact angle on a smooth surface. The Wenzel and Cassie models intersect at a contact angle that Lafuma and Quéré called 'critical angle' below which the metastability of the Cassie state may be observed. Therefore, in order to avoid the metastability, the material of the surface should have a smooth-surface contact angle greater than that above critical angle.

2.4 Longevity Characterization of Superhydrophobic Coatings

The longevity of a submerged superhydrophobic surface depends primarily on the amount of time that air remains trapped within the surface microstructure. In other words, the degree of hydrophobicity and hence the beneficial effects are diminished by the reduction of the amount of air. Recently, several approaches have been developed to estimate the longevity of superhydrophobic surface, i.e., the time until transition from dewetted (Cassie) to wetted (Wenzel) state. Bobji *et al.* (2009) used an optical technique to measure how long the surface could maintain its hydrophobicity under different hydrostatic pressures. This was accomplished by counting the number of shiny spots per unit area on the surface—an indication of the existence of an air–water interface. Similar studies were performed using a laser beam to investigate the effect of the surface structure on the longevity (Sakai *et al.*, 2009). Poetes *et al.* (2010) used a similar technique for the same test but for different superhydrophobic coatings additionally, they mathematically interpreted the decay of longevity with pressure. Using optical measurements, Lei *et al.* (2010) demonstrated that the wetting transition due to pressure could be either reversible (switching from nonwetted to wetted or vice versa) or irreversible (permanent wetting) depending on the value of the applied pressure. Rathgen & Mugele (2010) developed an optical method to determine the contact angle and microscopic shape of the air–warter interface under different hydrostatic pressure.

Keeping and/or restoring the air layer between the surface and water were undertaken by some studies. For example, Stephani & Goldstein (2010) utilized the electrolysis process to continuously generate air bubbles between a solid surface and water that leads to producing drag reduction even if the surface is not hydrophobic. Moreover, Lee & Kim (2011) used a similar process to *rejuvenate* the dead coatings, i.e., gas restoration for the wetted coatings to be converted back to be nonwetted. This process was carried out for microfabricated surfaces. More details about the

literature can be found in Rothstein (2010) and Samaha *et al.* (2012*c*). The latter is reprinted in Appendix I.

CHAPTER 3 Fabrication

3.1 Electrospinning

Electrospinning of superhydrophobic polymers is a simple, low-cost method that can be used to deposit micro- to nanofibrous coatings onto substrates of arbitrary geometry. The resulting superhydrophobic surfaces could be applied in various ways, including self-cleaning, protection from corrosion, and reducing skin-friction drag in underwater vessels such as submarines. Conventionally, electrospinning is performed by applying a large DC-potential between the electrospinning source (typically a hypodermic syringe) and the substrate, resulting in a randomly oriented nonwoven fiber mats. The random orientation of the fibers is the result of the inherent electrostatic instability of the charged jet as it travels from the spinneret to the collection substrate. This instability can be overcome by applying a DC-biased AC-potential that induces short segments of alternating polarity, thereby reducing the magnitude of the destabilizing force on the fiber (Sarkar *et al.*, 2007). In addition, the presence of both positive and negative charges on the surface of the rotating collector minimizes the local electric field perturbations caused by residual charge accumulation on the fibers as shown in Figure 3.1. We used this technique to fabricate superhydrophobic coatings and perform characteristic and morphologic studies on them. Hydrophobic polymer, polystyrene (PS; Mn = 170,000), was purchased from Sigma-Aldrich Chemicals (St. Louis, Missouri). N,N-Dimethylformamide (DMF) and high-performance chromatography-grade toluene were also obtained from Sigma-Aldrich and were used without further purification. Polymer fibers were fabricated using the DC-biased AC-electrospinning technique. Fibers were electrospun from solutions with 15, 18, 20, 25 and 30% weight (wt) PS. The static contact angles, a measure of surface hydrophobicity, were measured using a contact-angle ramé-hart goniometer and droplets of

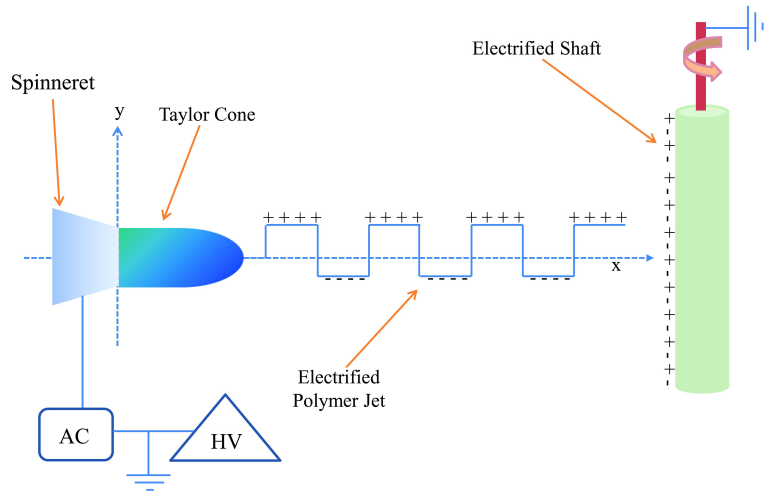

Figure 3.1: An illustration of an electrified polymer jet during a DC-biased AC-electrospinning.

deionized water on the specimen. Contact-angle measurements were performed on coatings consisting of porous and non-porous fibers, and the fiber porosity had no observable effect on superhydrophobicity, indicating that the air gaps between the fibers and not the internal fiber porosity are responsible for the observed superhydrophobicity. We further show that hydrophobicity can be controlled by varying the percent weight of the polymer and by adding some additives in the electrospun solution. a sample of results are shown in Table 3.1. The morphology of the fiber and its surface structure were observed by field emission scanning electron microscopy, FESEM, made by Hitachi, Japan (Model S-70). A sample of the produced fibers is shown in Figure 3.2, which demonstrates SEM images of micro/nanofibers produced from an 18 wt % PS solution. We further show that hydrophobicity can be controlled by varying the percent weight of the polymer and by adding some additives in the electrospun solution. Finally, rheological experiments in parallel-plate geometry were performed on a rheometer made by Anton Paar Corporation (model Physica MCR 301) and it shows a drag reduction. More details of the above have appeared in Ochanda *et al.*

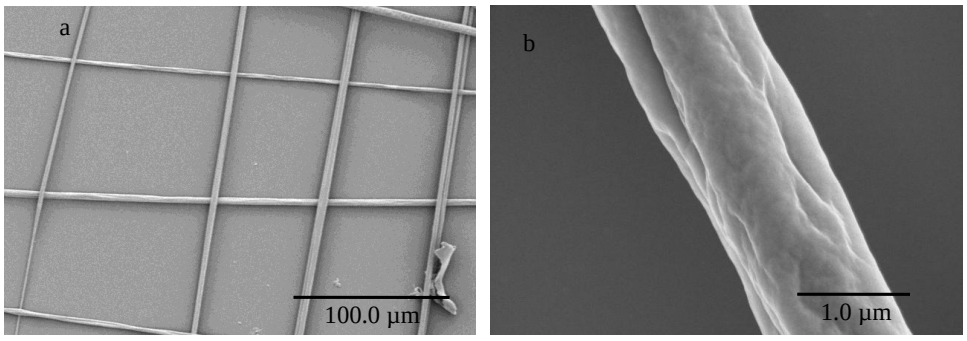

Figure 3.2: SEM image of 18 wt % polystyrene fibers with 1 wt % fluoro-elastomer and 2% glass beads showing (a) grid-like structure and (b) high magnification of single fiber.

(2012*a*), reprinted in Appendix II.

Table 3.1: Effect of additives on the hydrophobicity of polystyrene fibers at different percent weight polystyrene.

Case	% wt PS	% wt Glass Beads	% wt Zonyl TBC	Contact Angle (deg.)
1	15	—	—	136
2	18	—	—	140
2	18	2.0	—	145
2	18	2.0	1.0	157
3	25	—	—	153
3	25	0.5	—	160
3	25	1.0	—	160
4	30	—	—	167
4	30	1.0	—	156

The present study demonstrates that a mono-layer of the produced fibers has a high degree of fiber alignment as shown in Figure 3.2 a. However, alignment is lost as more layers are added (Figure 3.3). We reason that this effect is caused by the decreased conductivity as more layers of the non-conductive polymer are added. We solved this problem by adding a 1 wt % highly conductive material to the solution such as Tetrabutylammonium chloride or Graphene, which results in several layers

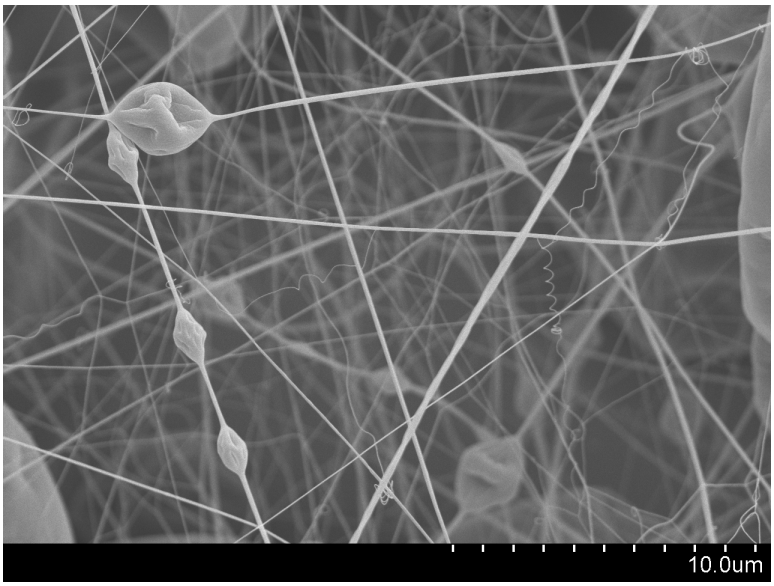

Figure 3.3: SEM image of 18 wt % polystyrene fibers showing several layers of random fibers.

of fibers with high degree of alignment without affecting the superhydrophobicity as shown in Figure 3.4.

3.2 Random Particles Deposition

Herein, we used another technique to produce superhydrophobic coatings, which are closer to natural surfaces found, for example, lotus leaves. Hydrophobic aerogel beads made of amorphous silicon dioxide (aerogel) having almost 99.8% porosity were acquired from United Nuclear Scientific (Laingsburg, Michigan). The beads were ground and filtered through four stages of sieves purchased from McMaster.CARR (Chicago, Illinois) with mesh sizes of 43, 104, 150, and 210 μm. Starting with the smallest mesh size, the aerogel particles were sieved to separate the finest particles. The remaining particles in the first sieve were then filtered in the next one, and the procedure was repeated until four categories of aerogel particles were obtained. From each category, aerogel particles were deposited onto a metallic substrate coated with a thin polymer

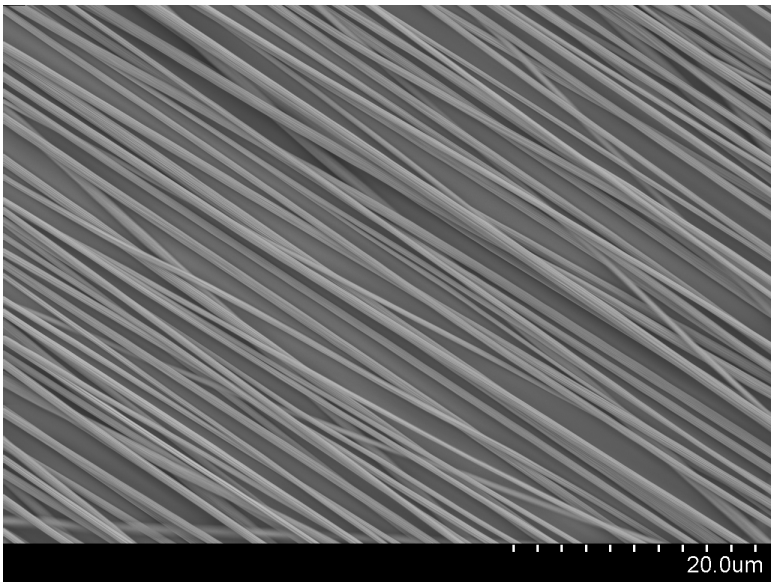

Figure 3.4: SEM image of 18 wt % polystyrene fibers with 1 wt % Graphene showing high degree of alignment.

film for adhesion. The surface morphology was studied using a field-emission scanning electron microscope (FESEM) (S-70, Hitachi, Japan). Figure 3.5 shows SEM images of the four aerogel coatings with different particle-size ranges. The inset in the figure shows a water droplet on each coating with a static contact angle of 155° or higher, and an average contact-angle hysteresis of about 3°, demonstrating each coating's superhydrophobicity. As can be seen in parts b, c and d of the same figure, few particles exist with sizes smaller than the prescribed range determined from the mesh size of a particular sieve. We reason that the electrostatic charge of the particles is responsible for attracting few particles to each other, and therefore giving the particle conglomerate a larger virtual size. The deposited particles provide the surface roughness and porosity necessary to entrap air when the surface is submerged in water. As water flows over the coating, the interface between the entrapped air and the water has very low skin friction, resulting in slip flow and drag reduction. Characterization of such surfaces will come later in Chapter 8.

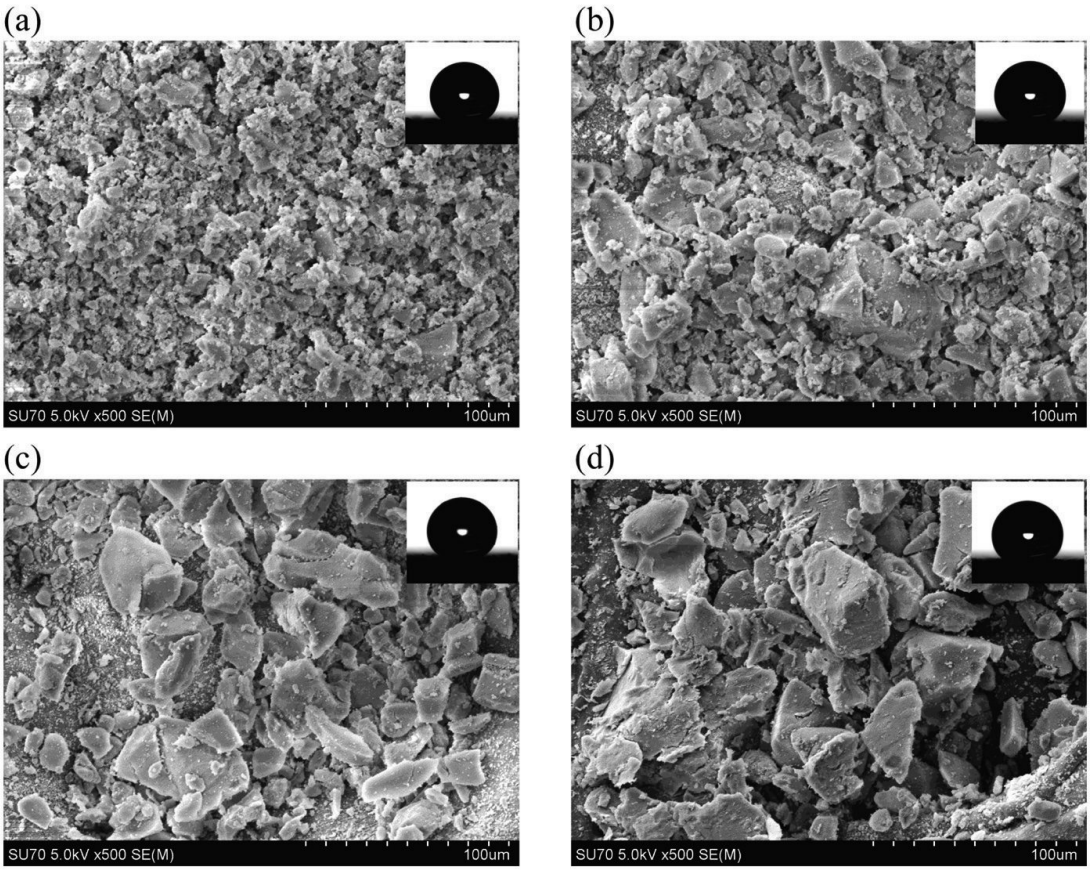

Figure 3.5: SEM images of superhydrophobic aerogel coatings with different particle-size ranges. (a) 0–43 μm; (b) 43–104 μm; (c) 104–150 μm; (d) 150–210 μm. Upper right inset in each figure shows a water droplet on top of the particular coating.

CHAPTER 4 Characterization of Superhydrophobic Coatings

4.1 Optical Method

Superhydrophobic coating can entrap air resulting in a surface with both air–water and solid–water interfaces. The presence of the air–water interface is responsible for the measurable decrease in shear stress and retaining the superhydrophobicity in addition to producing shiny spots that can be optically measured. The objective of this task is to advance and calibrate a novel optical technique to non-invasively measure the longevity of submerged superhydrophobic coatings—how long the surface can entrap air underwater—subjected to different environmental conditions. We used an optical spectroscopy system made by Photon Technology International, Inc. (model QuantaMaster^{TM} 30) to quantify the intensity of reflected light in the visible range scattered from a superhydrophobic surface completely submerged in a controlled water vessel (Figure 4.1). The time-dependent light reflection intensity could be measured at a single wavelength or integrated over a range of wavelengths. It is desirable to measure in situ the degree of hydrophobicity of coatings fabricated with different techniques and subjected to different environments. Those environments are not possible to reproduce during traditional contact-angle or rheometer measurements, and include a broad range of water pressures (i.e. depths), constant or time-dependent pressures, water with different degrees of salinity or dissolved air, still or moving water, etc. The optical spectroscopy system used herein was previously utilized for different purposes and applications that prove the precision of this device, which motivates us to use it as a new method to measure surface's hydrophobicity. Figure 4.2 is a plot of the normalized average reflected light intensity (defined as the integration of the intensity over all wavelengths divided by the wavelength range).

a)

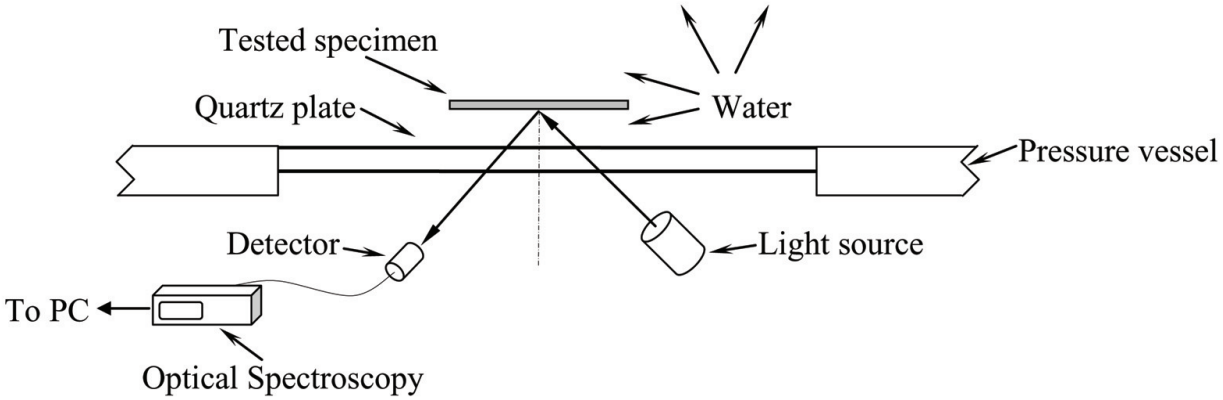

b)

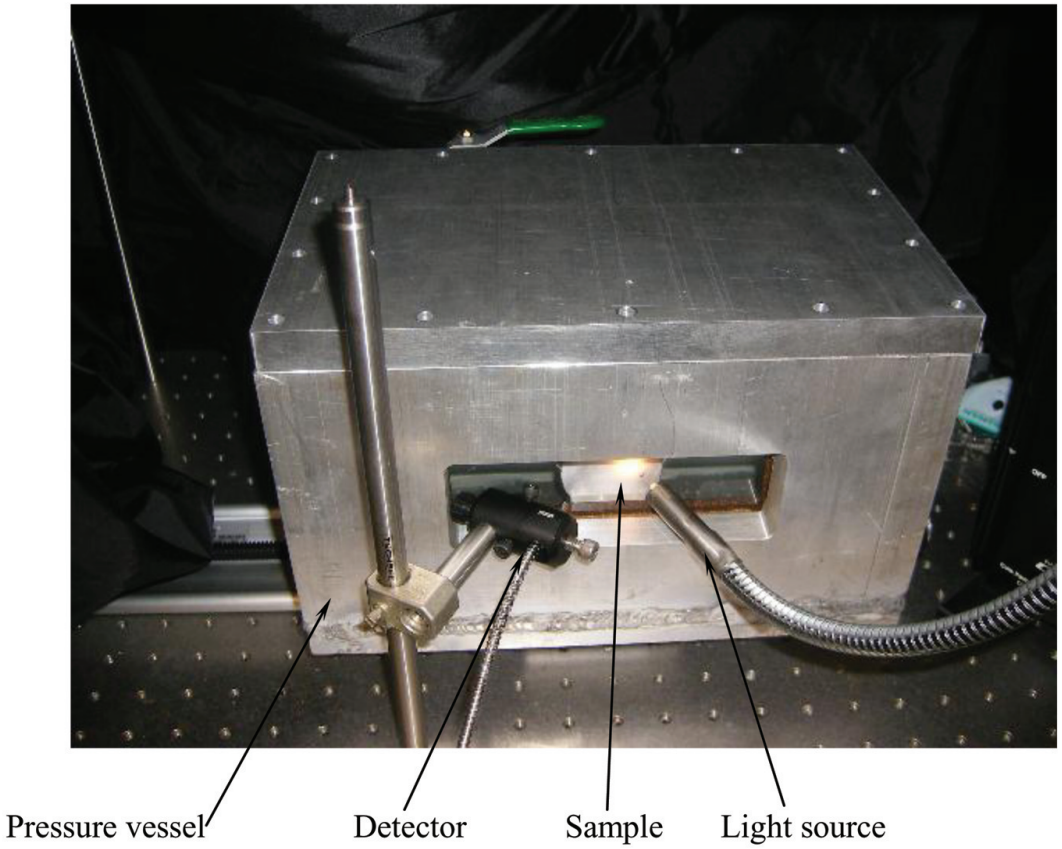

Figure 4.1: (a) Schematic of the optical spectroscopy system. (b) Photograph of the pressure vessel.

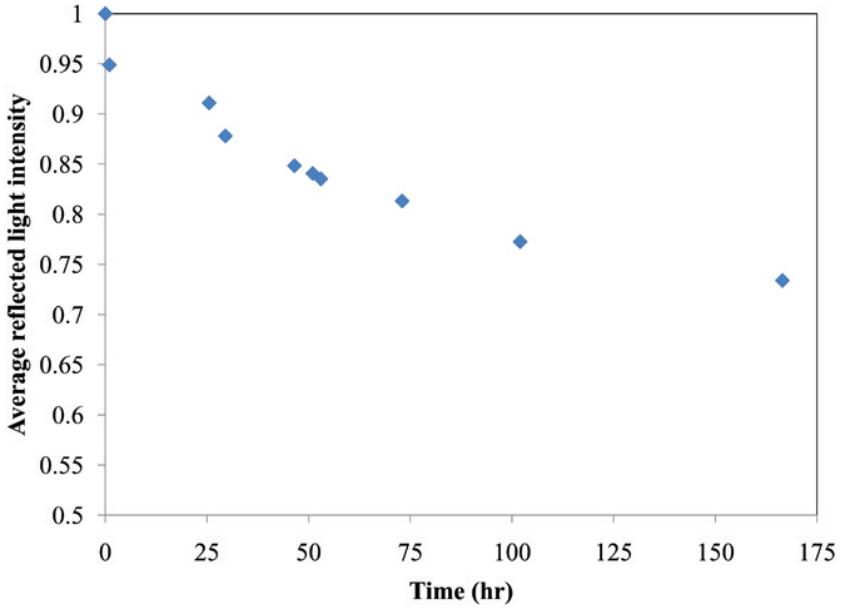

Figure 4.2: Average reflected light intensity reduction with time for a spun fibers sample.

All of the light scattering measurements were performed under atmospheric pressure. From the figure, it can be seen that the average reflected light intensity decreased by about 27% in 166.5 hours of water submersion that indicates the loss of trapped air and a corresponding reduction in superhydrophobicity.

4.2 Rheological and Contact-Angle Measurements

In order to validate the novel optical technique developed herein, the results were compared with drag reduction data using a rheometer made by Anton Paar Corporation (model Physica MCR 301) and static contact angles and contact-angle hysteresis using a ramé-hart goniometer (model number 100-25-A). The measurements indicate that the results of the light-scattering surface characterization technique correlate strongly with both contact-angle and drag-reduction measurements. The contact-angle hysteresis measurements further validate the light-scattering method. In situ

characterization of submerged hydrophobic surfaces using optical light scattering represents a new and useful tool for real-time estimation of hydrophobicity and drag reduction. More details about the setup and mathematical calculations have appeared in Samaha *et al.* (2011*a*), reprinted in Appendix III.

CHAPTER 5 Influence of Flow on Longevity

In this chapter, we study the effect of water movement on the degree of hydrophobicity and longevity of superhydrophobic polystyrene spun-fiber coatings as a step toward understanding the influence of environmental factors on the performance of superhydrophobic surfaces. No experimental study has yet been devoted to examine the impact of water flow on longevity. The time-dependent hydrophobicity of the submerged coating in the pressure vessel was determined while exposing the coating to a rudimentary wall-jet flow. Rheological studies were performed to determine the effect of the flow on drag reduction. The flow is supplied using a submersible pump to produce a three-dimensional wall jet over the coating. The piping system includes a stepper delivery valve to precisely control the flow. The tubes are flexible transparent smooth hoses (10 mm diameter). The tested coating sample and the water-flow system are installed immersed under water inside the pressure vessel (Samaha *et al.*, 2011*a*). The jet-Reynolds number ($\mathrm{Re} = U_0 d/\nu$) is used to characterize the delivered flow, where U_0 is the average water-jet velocity at nozzle exit that can be controlled using the flow control valve, d is the nozzle exit diameter (8.5 mm), and ν is the kinematic viscosity of water.

5.1 Longevity Test

Figure 5.1 shows the period that the samples take for wetting transition (longevity) against jet-Reynolds number (Re). The figure demonstrates that as Re increases, longevity deteriorates. We reason that as water flows (even if with a relatively small Reynolds number), the flowrate strongly enhances the dissolution of the entrapped air in water where the mass-transfer free-convection regime turns into a forced convection one. For further investigation, we repeated the previous measurements for identical

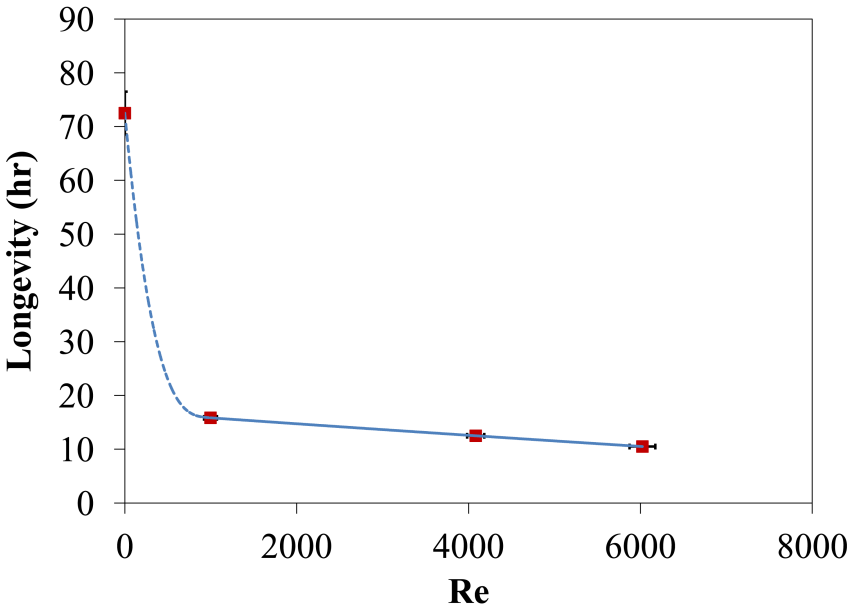

Figure 5.1: Effect of water movement on longevity of superhydrophobic fibrous coating. Solid and broken lines are best fit of experimental data in forced, free and mixed convection regimes.

samples with light spots located at different distances, x, from the nozzle exit but the nozzle-exit Reynolds number is kept constant (Re = 6023). Figure 5.2 demonstrates the measured longevity at different distances, x. It is obvious that the longevity increases with increasing x. This is because of the reduction of the flow velocity in the flow direction (wall-jet flow characteristics) that reduces the rate of air dissolution in water.

5.2 Analytical Considerations

We have analytically calculated the convection coefficient for the still-water case (free convection) , which is used with the experimental data to to obtain the coefficients for the water-movement cases. Figure 5.3 shows the dimensionless convection coefficient (Sherwood number) corresponding to the data shown in Figure 5.1, and demonstrates the expected increase of the convection coefficient (h_m) with increasing

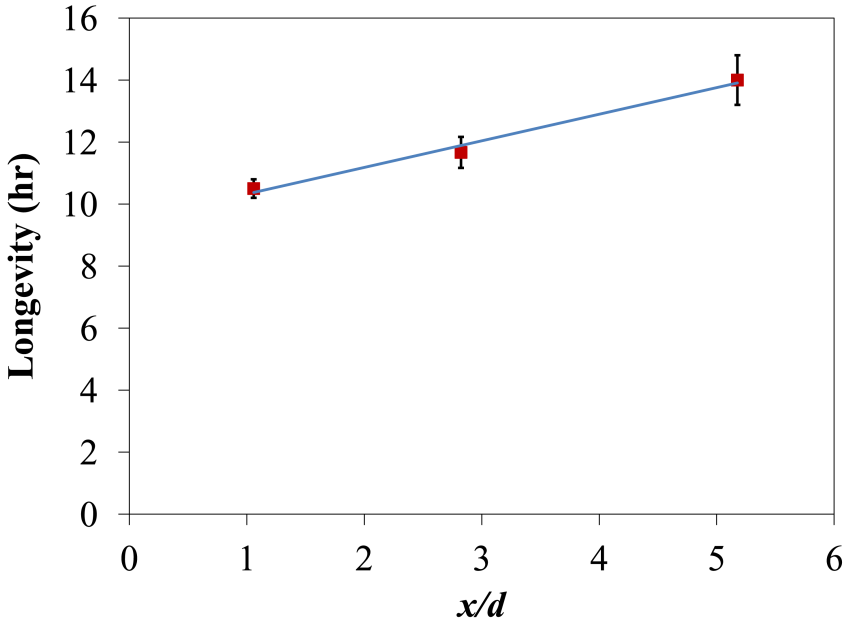

Figure 5.2: Longevity of the coating at several locations, x. Jet-Reynolds number is kept constant for all cases, Re = 6023. Solid line is best fit of experimental data.

Reynolds number. The figure also demonstrates that h_m of the water-movement cases are much larger than that of the still-water one even for relatively low Reynolds number. Again, the flow enhances the dissolution of the entrapped air in water, which leads to much higher convection coefficient. Similar conclusion could be drawn when changing the position x along the wall jet, as shown in Figure 5.4. The velocity decay in the flow direction results in decreasing the convection coefficient. Additionally, Figure 5.4 demonstrates that the convection coefficient decreases linearly within the specified range of distance x, which agrees well with prior studies (Mabuchi & Kumada, 1972; Kanna & Das, 2005) The light-scattering data were compared to drag-reduction measurements for further verification, and good correlation was observed between the two techniques. The results show that the water movement over superhydrophobic surfaces significantly affects their hydrophobicity, which opens a pathway for developing a better surface that could be used for underwater applica-

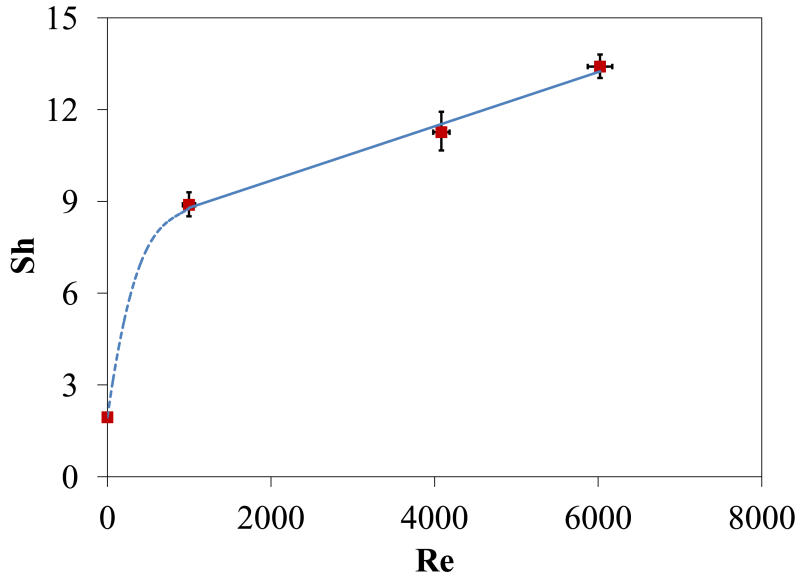

Figure 5.3: Dimensionless mass-transfer convection coefficient against jet-Reynolds number. Solid and broken lines are best fit of experimental data in forced, free and mixed convection regimes.

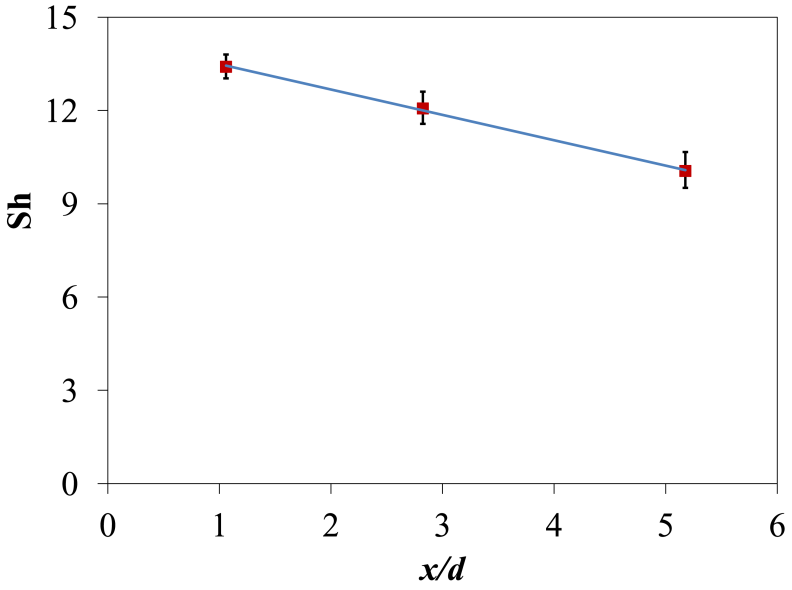

Figure 5.4: Dimensionless mass-transfer convection coefficient against location x. Jet-Reynolds number is kept constant for all cases, Re = 6023. Solid line is best fit of experimental data.

tions and could survive longer under different flow conditions additionally, looking for an applicable air-restoration method to enable the coating to recover its hydrophobicity. More details about the flow effects have appeared in Samaha *et al.* (2012*b*), reprinted in Appendix IV.

CHAPTER 6 Sustainability of Superhydrophobicity Under Pressure

In this chapter, we study the effect of elevated pressures on the degree of hydrophobicity and longevity of superhydrophobic polystyrene spun-fiber coatings as a step toward understanding the influence of environmental factors on the performance of superhydrophobic surfaces. Prior studies have demonstrated that superhydrophobicity of surfaces is influenced by hydrostatic pressure. Longevity of a superhydrophobic surface depends on how long it can entrap air, which is significantly affected by pressure. The time-dependent hydrophobicity of the submerged coating in a pressure vessel was measured under different pressures. Rheological studies were performed to determine the effect of the pressure on drag reduction and slip length.

6.1 Longevity Test Under Pressure

We previously demonstrated the use of light scattering as an indirect means of characterizing the amount of air trapped within submerged superhydrophobic coatings against time (Samaha *et al.*, 2011*a*). In our technique, the reflected light spectrum could be measured as a function of the pressure and time. The spectrum is then integrated to obtain a wavelength-averaged reflection intensity. All measurements are carried out by projecting the light on a small portion of the sample with a diameter of 3 mm. The light intensity decreases with time for all samples, which indicates the loss of trapped air and a corresponding reduction in the degree of superhydrophobicity. This effect is believed to be due to the dissolution of air in water (Bobji *et al.*, 2009; Sakai *et al.*, 2009; Poetes *et al.*, 2010). Figure 6.1 shows the period that the samples take for wetting transition (longevity) against the elevated pressure. Each displayed point is an average of three different measurements. The figure demonstrates that as

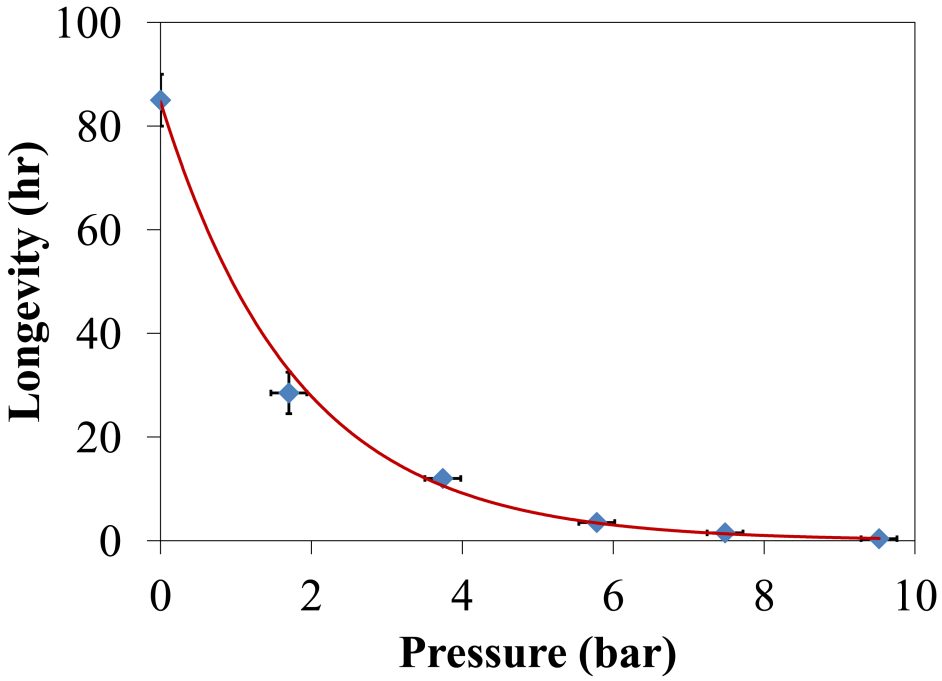

Figure 6.1: Effect of elevated pressure on longevity of superhydrophobic fibrous coating. Solid line is exponential fit of experimental data.

pressure increases, longevity exponentially deteriorates and this is in good agreement with previous studies (Poetes *et al.*, 2010). The figure also indicates that the terminal pressure (Samaha *et al.*, 2012*a*) for this particular coating—the pressure beyond which the surface undergoes a global transition from the Cassie state to the Wenzel state—can go up to 9.5 bars, which is about hundred times that indicated by previous studies (Poetes *et al.*, 2010). We reason that the scale of microroughness (the distances between the fibers) is about five microns at some locations and approaches nanoscale at others while that of the previous studies (Poetes *et al.*, 2010) is of order a hundred microns. The significantly low microroughness scale of our fibrous coating increases the sustainability of the air–water interface against pressure, indicating that such coatings could potentially be used for deep underwater applications.

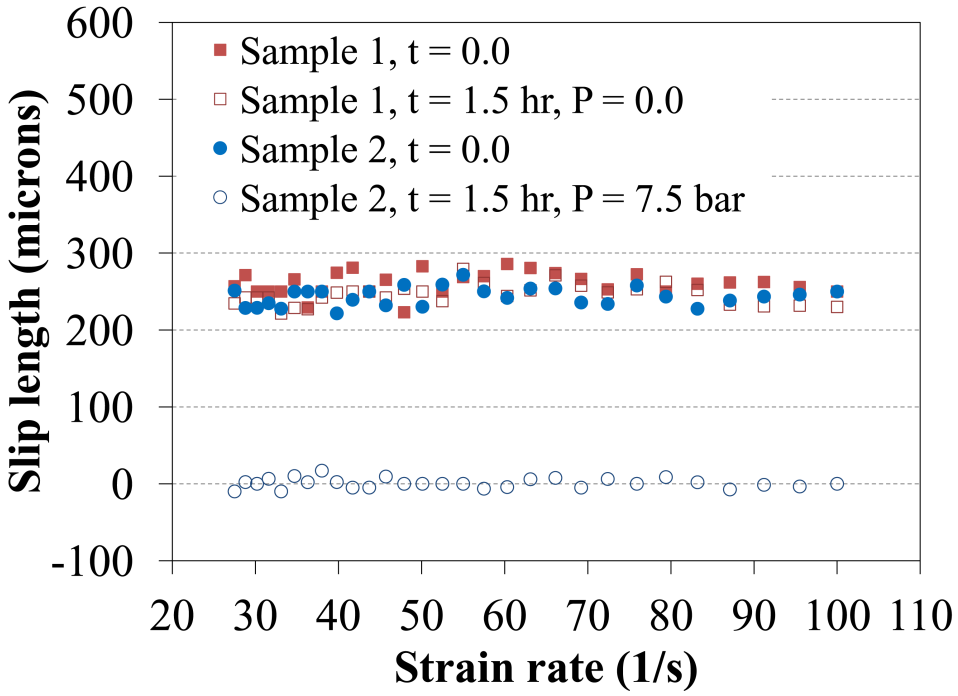

Figure 6.2: Slip length for two identical samples subjected to two different elevated pressures during longevity test.

6.2 Rheological test

To further investigate the superhydrophobicity of the coatings after exposure to different elevated pressures, we measured the slip length as a quantity to characterize the slip produced by such a coating. The slip length has been determined before and after exposing two identical samples to a pressurized longevity test for about 1.5 hour. The first sample was immersed in water at atmospheric pressure while the second one was subjected to 7.5 bars. As can be seen in Figure 6.2, before the two samples were subjected to the longevity test, the slip length of them is approximately the same, which verifies that the samples are identical. After the test is finished, the first sample loses only about 5% on average of its original slip but that of the second one was completely diminished. This validates the results shown in Figure 6.1. We

also measured the drag-reduction percentage for the above mentioned two samples. The first sample loses only about 4% on average of its original drag-reduction but the second one completely loses its superhydrophobicity. This agrees well with the optical measurements and confirms that the elevated pressure over superhydrophobic coatings accelerates their wetting transition. More details about the pressure effects have appeared in Samaha *et al.* (2012*d*), reprinted in Appendix V.

CHAPTER 7 Salinity Effects on Hydrophobicity and Longevity

Previous studies on submerged superhydrophobic surfaces focused on performance variables such as drag reduction and longevity. However, in order to use such surfaces for practical applications, environmental factors such as water salinity must be investigated and understood. In this work, experiments were carried out to investigate the impact of salt (sodium chloride, NaCl) concentrations in aqueous solutions on the hydrophobicity and longevity of polystyrene fibrous coatings. Rheological studies using salt water as a test fluid were performed to determine the effect of salt concentration on drag reduction. Contact-angle measurements were used to validate the results from the rheometer. In situ noninvasive optical reflection was used to measure the longevity of the coating—time-dependent loss of entrapped air within the coating—as a function of salinity. The superhydrophobic coating used herein consisted of polystyrene (PS) fibers that were deposited using DC-biased AC-electrospinning. Electrospinning is scalable and far less expensive than conventional methods (e.g. microfabrication), bringing the technology closer to large-scale submerged bodies such as submarines and ships.

7.1 Effect of Salinity on Hydrophobicity

Sodium chloride solutions of concentration ranging from 3.5 to 31 weight percent in D.I. water were prepared to investigate their effect on the hydrophobicity of the PS fiber coatings. A drag reduction of more than 20 % was observed at all NaCl concentrations. Figure 7.1 is a plot of the drag reduction averaged over the full range of strain rate versus the NaCl concentration and shows a modest decrease in drag reduction with increasing salinity. There is a bulk electrostatic modulation of molecular

interactions that originates from the polarization and reorientation of water molecules in the bulk phase. Both electrostatics and solvent-induced forces are modified by the presence of salts (Song *et al.*, 1991), which leads to an increase in the attractive force between the fluid and the surface, i.e., reduces hydrophobicity. Meanwhile, NaCl is adsorbed on PS fibers, which can be treated as an interaction of forces including Van der Waals attractive and electrostatic forces with the former favoring adsorption of Na^+ and Cl^- ions on PS surface. In general, the hydrophobicity of a surface and, hence, its hydrophobic force is controlled by changes in surface composition. We reason that the decrease in hydrophobic force in the presence of electrolytes (anion and cation) is due to the adsorption of the ions on the surface (Angarska *et al.*, 2004; Christenson *et al.*, 1989). This is supported by Gouy–Chapman theory, which predicts that added salt systematically promotes solute adsorption because salt can decrease the free energy of forming a charged monolayer with increasing ionic strength (Persson *et al.*, 2003). Contact-angle measurements of droplets with different NaCl concentrations were performed to verify the effect of salinity on hydrophobicity of the fibrous coatings used in the rheometer test and a good agreement has been observed.

7.2 Longevity Studies: Salt Effects

We have also investigated the effect of water salinity on longevity of surface. We have used our previously mentioned optical technique (Samaha *et al.*, 2011*a*) as an indirect, time-dependent measurement of the amount of air trapped within a submerged superhydrophobic fiber surface. The reflected light spectrum was obtained as a function of time and was integrated to obtain wavelength-averaged reflection intensity. Figure 7.2 shows the normalized average reflected light intensity versus time for two typical samples of the superhydrophobic fibrous coating. One of them was immersed in D.I. water. The other one was immersed in 3.5 % wt NaCl solution (typical salinity of ocean water). It can be seen from the figure that the immersed sample in D.I. water becomes completely hydrophilic after 136 hours whereas the sample submerged in salt

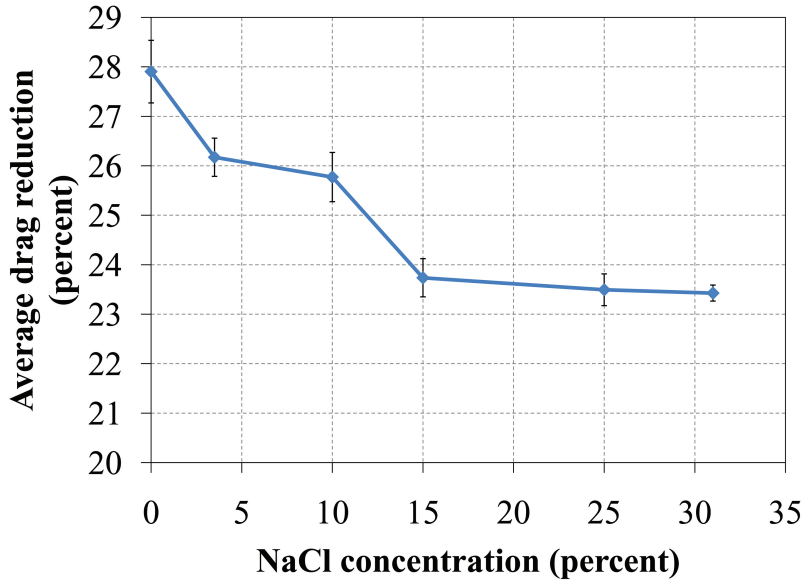

Figure 7.1: Effect of salt concentration on average drag reduction of PS fibrous coating.

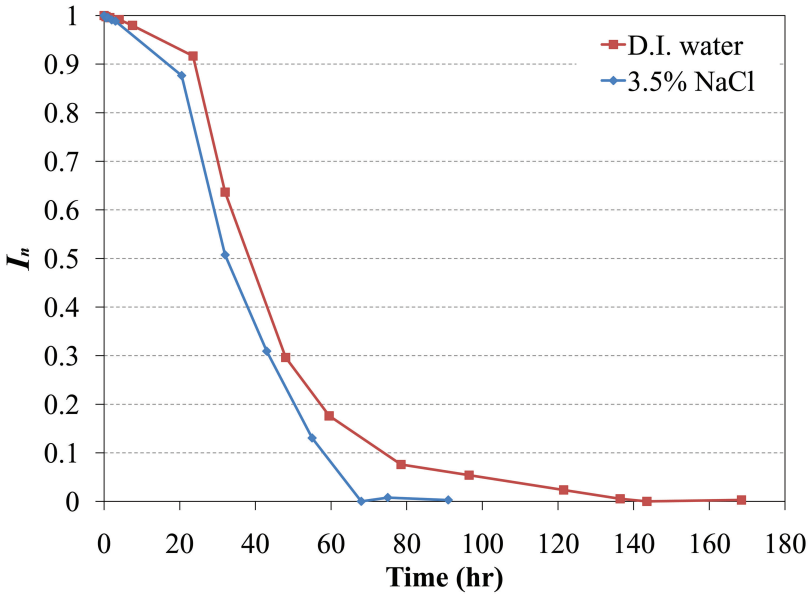

Figure 7.2: Effect of salinity on longevity of PS fibrous coating.

water takes only 68 hours to become hydrophilic. Therefore, this observation indicates that the onset of wetting or transition from the Cassie state to the Wenzel state starts earlier for samples in salt solution than those in D.I. water. More details about salinity effects have appeared in Ochanda *et al.* (2012*b*), reprinted in Appendix VI.

CHAPTER 8 Experiments on Superhydrophobic Surfaces Comprised of Random Roughness

In this chapter, we used a different technique other than electrospinning to produce superhydrophobic coatings. The one used in this work is closer to natural surfaces found, for example, on lotus leaves. Herein, hydrophobic aerogel particles with different average diameters are randomly deposited onto metallic substrates with a thin adhesive coating to achieve a combination of hydrophobicity and surface roughness. The resulting surfaces show different degrees of superhydrophobicity and are used to study the effects of elevated pressure on the drag reduction and the degree of hydrophobicity (survivability) of such surfaces when used for underwater applications. Several previous studies presented numerical and/or analytical models to evaluate the influence of pressure on the superhydrophobicity. Experimental studies, however, are lacking. In this work, we measure the impact of pressure on the stability of the meniscus (air–water interface). The experiments utilize the three previously mentioned instruments: (i) the developed optical technique to characterize the time-dependent hydrophobicity in conjunction with a pressure vessel in which the submerged coating is exposed to elevated pressures; (ii) the parallel-plate rheometer where the coating's slip length and drag reduction are measured; and (iii) the goniometer to measure the static contact angle as well as contact-angle hysteresis. We investigate the effects of the coating's morphological parameters, such as particle size and porosity, on both the wetting-transition pressure resistance and the drag-reduction advantage. We developed and validated an image-thresholding technique to estimate the gas area fraction of the coating.

8.1 Fabrication

As discussed in Chapter 3, hydrophobic aerogel beads made of amorphous silicon dioxide having almost 99.8% porosity were acquired from United Nuclear Scientific (Laingsburg, Michigan). The beads were ground and filtered through four stages of sieves purchased from McMaster.CARR (Chicago, Illinois) with mesh sizes of 43, 104, 150, and 210 μm. Starting with the smallest mesh size, the aerogel particles were sieved to separate the finest particles. The remaining particles in the first sieve were then filtered in the next one, and the procedure was repeated until four categories of aerogel particles were obtained. From each category, aerogel particles were deposited onto a metallic substrate coated with a thin polymer film for adhesion. The surface morphology was studied using a field-emission scanning electron microscope (FESEM) (S-70, Hitachi, Japan). Figure 8.1 shows SEM images of the four aerogel coatings with different particle-size ranges. The inset in the figure shows a water droplet on each coating with a static contact angle of 155° or higher, and an average contact-angle hysteresis of about 3°, demonstrating each coating's superhydrophobicity.

8.2 Gas Area Fraction

Figure 8.2 shows the thresholded images of those shown in Figure 8.1. The white regions represents the upper areas of the particles that could be in contact with water when the surface is submerged. This could be estimated by calculating the total area covered with white pixels. Meanwhile, the black regions represent the voided locations in which air is entrapped. The ratio of the black area to the total one represents the gas area fraction (GAF). The segmentation process is performed using Ostu's algorithm (Otsu, 1979) in which the gray levels of the original image are split into two classes at the optimum thresholding value at which the intra-class variance of both classes is minimal. The image-processing technique was validated by testing a grid-mesh sample with known gas area fraction and a good agreement was observed.

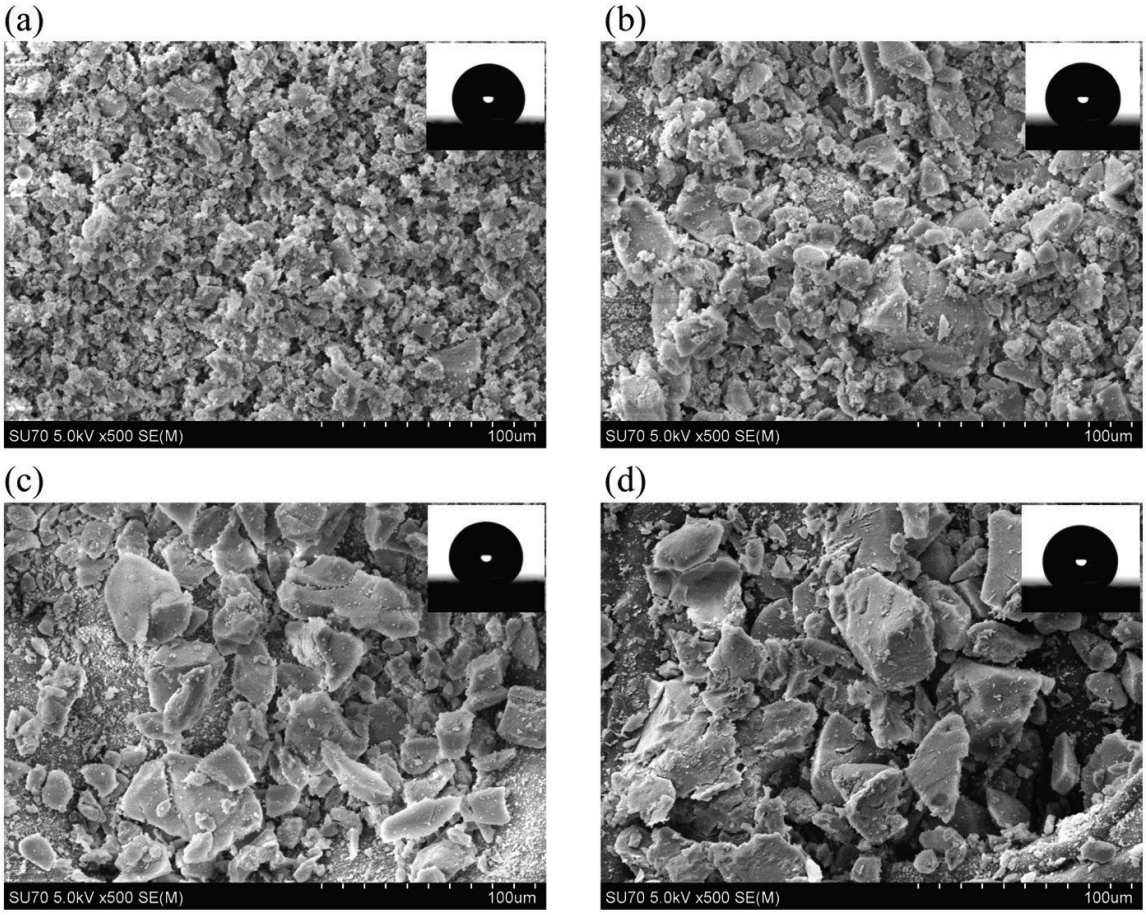

Figure 8.1: SEM images of superhydrophobic aerogel coatings with different particle-size ranges. (a) 0–43 μm; (b) 43–104 μm; (c) 104–150 μm; (d) 150–210 μm. Upper right inset in each figure shows a water droplet on top of the particular coating.

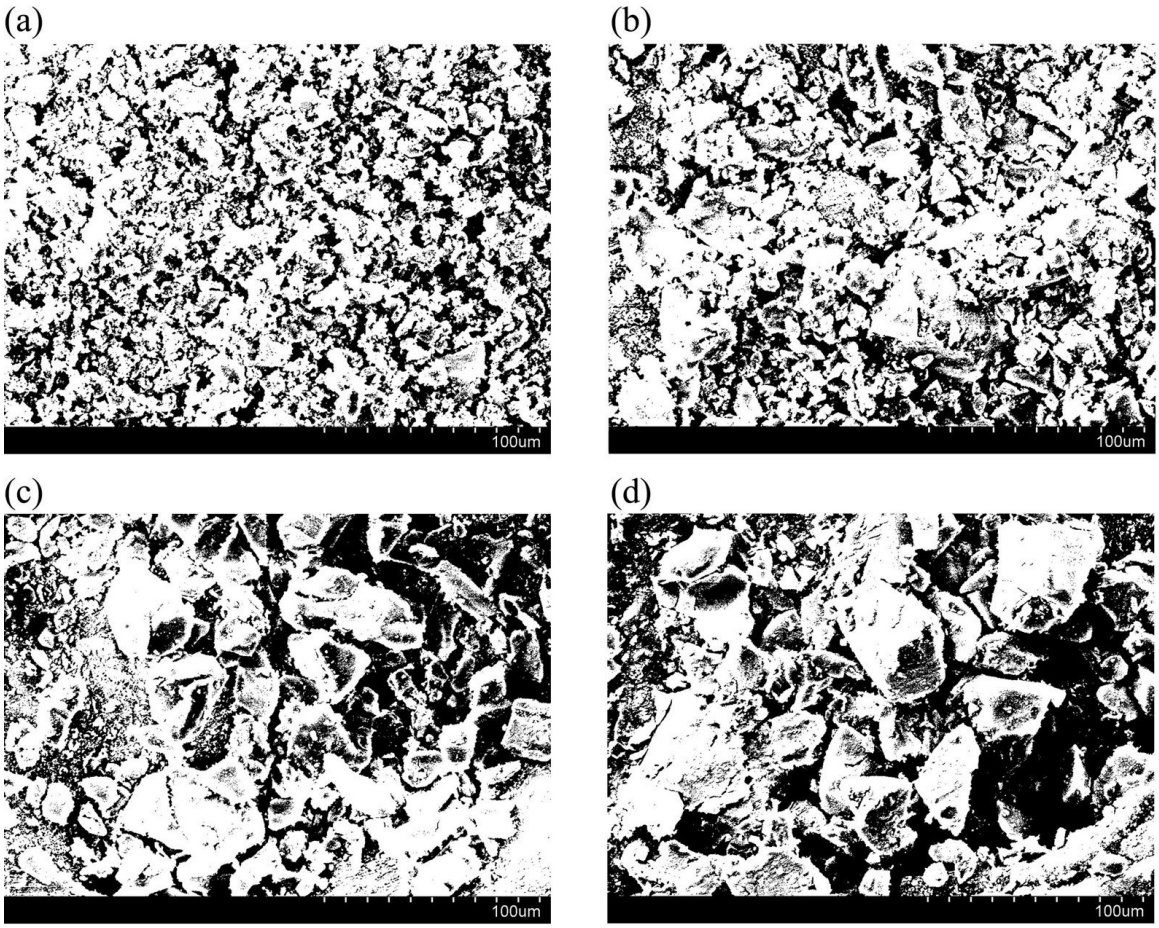

Figure 8.2: Thresholded SEM images of superhydrophobic aerogel coatings with different particle-size ranges. (a) 0–43 μm; (b) 43–104 μm; (c) 104–150 μm; (d) 150–210 μm.

8.3 Terminal Pressure Test

Figure 8.3 shows the normalized average reflected light intensity, I_n, versus ambient pressure for the four aerogel samples with different average gas area fractions. The figure demonstrates that the light intensity decreases with increasing pressure for all coatings, indicating the loss of trapped air due to the breakup of the air–water inter-

face. As mentioned earlier, this effect could be interpreted in terms of the balance between the liquid pressure from one side and the capillary forces and the air pressure inside entrapped the pores from the other side (Patankar, 2004; Barbieri *et al.*, 2007; Extrand, 2004, 2006; Zheng *et al.*, 2005; Samaha *et al.*, 2011*b*; Emami *et al.*, 2011*a*,*b*). If the hydrostatic pressure overcomes the other two forces, the meniscus fails leading to the surface transitioning from the Cassie state to the Wenzel state. From the figure, it is obvious that the reduction in the light intensity with increasing pressure did not occur abruptly. This is due the heterogeneity of the coatings. Therefore, the failure happens locally wherever the local gas area fraction across the sample is larger than the critical value corresponding to the given hydrostatic pressure. As the light-beam covers the whole sample, the measurements are the integration of all wetted and non-wetted spots across the area of investigation. Thus, the pressure at which the entire surface is transitioned to the Wenzel state is henceforth referred to as the terminal pressure. The terminal pressure is to be contrasted to the critical pressure at which transition to wetted state only commences. Figure 8.4 shows that the terminal pressure is reduced as the gas area fraction is increased, as expected (Patankar, 2004; Barbieri *et al.*, 2007; Extrand, 2004, 2006; Zheng *et al.*, 2005; Samaha *et al.*, 2011*b*; Emami *et al.*, 2011*a*,*b*). Furthermore, the figure demonstrates a higher terminal pressure for the sample with 0.27 average gas fraction because this sample was made of the finest aerogel particles. The light-scattering data were compared to contact-angle, drag reduction, and slip-length measurements for mutual verification, and good agreements were observed among all measurements. The measurements reported here show that terminal pressures as high as about 600 kPa (equivalent to an underwater depth of about 60 m) can be achieved with coatings made up aerogel particles. The present study opens a pathway for cost-effective fabricating superhydrophobic coatings for underwater applications. Experiments on aerogel coating have appeared in Samaha *et al.* (2012*a*), reprinted in Appendix VII.

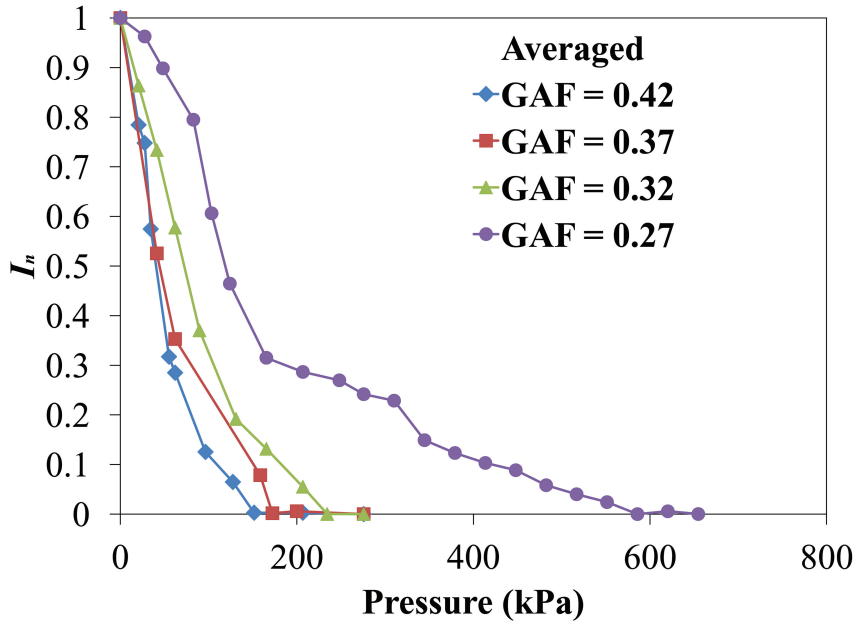

Figure 8.3: Effect of pressure on reflected light intensity from immersed coating samples.

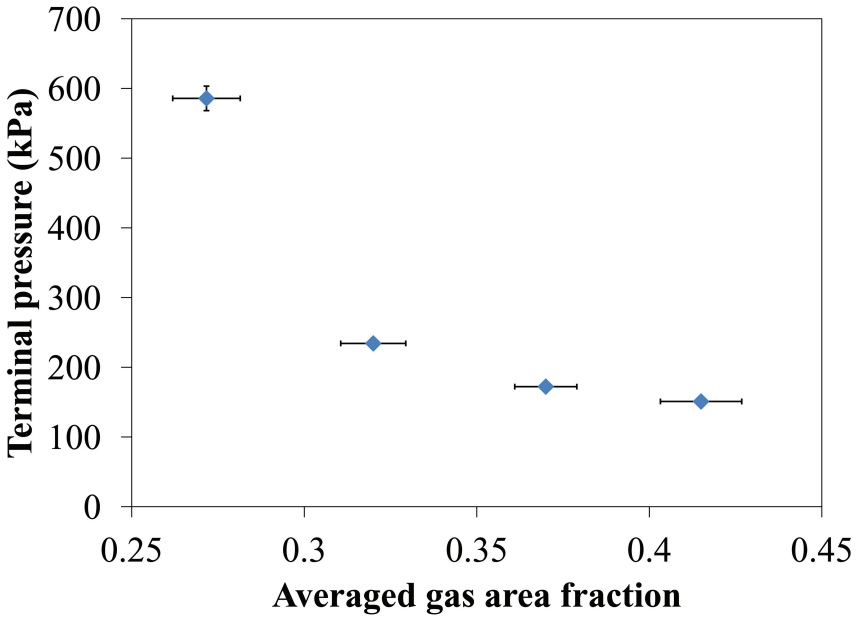

Figure 8.4: Effect of gas area fraction on terminal pressure.

CHAPTER 9 Numerical Studies on Superhydrophobic Surfaces Comprised of Random Roughness

The objective of this task is to simulate via computational fluid dynamics the performance of superhydrophobic surfaces having idealized random roughness or hydrophobic sites (posts or particles) that resembles natural superhydrophobic surfaces such as lotus leaf, or those produced via random deposition of hydrophobic particles, and compare such surfaces to those manufactured via microfabrication. The comparison is based on the effect of the gas fraction (ratio of shear-free area to total area), which generally reduces the skin friction and increases the slip length. Random deposition of hydrophobic particles method is far less expensive than microfabrication, making the technology more practical for large submerged bodies such as submarines and ships. Fluid flow simulation is carried out for steady, incompressible, laminar flow of water in a microchannel having a superhydrophobic bottom surface. The continuity and the momentum equations are numerically integrated using the CFD code from Fluent Inc. For comparison and validation, we have also simulated the flow over superhydrophobic surfaces made up of aligned or staggered microposts for channel flows as well as streamwise or spanwise ridges configurations for pipe flows. The present results are compared with theoretical and experimental studies reported in the literature and good agreement has been observed.

9.1 Skin Friction

Our numerical results indicate that the gas fraction has an important impact on the characteristics of a superhydrophobic surface, as it affects the slip length and therefore the pressure drop and the skin-friction coefficient. In the canonical case of fully-developed laminar flow between two parallel, smooth plates, the friction coeffi-

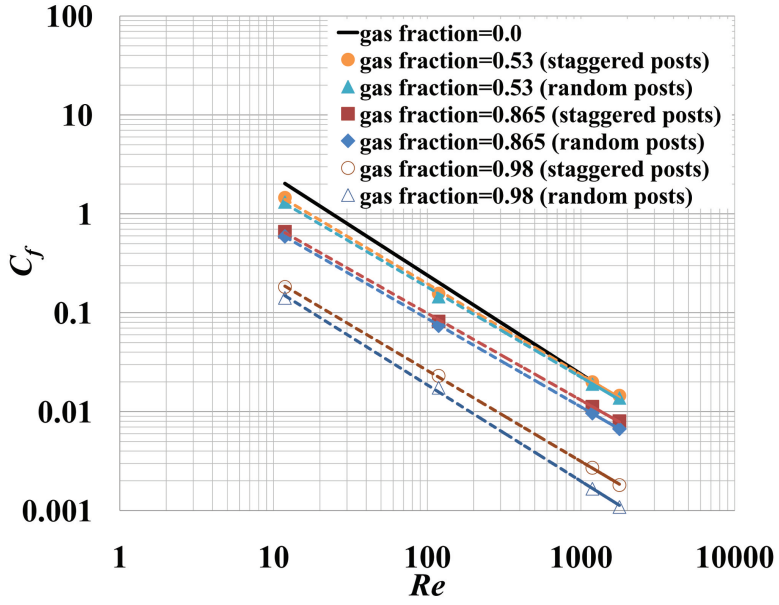

Figure 9.1: Skin-friction coefficient versus Reynolds number (Moody diagram) for different gas fractions.

cient is a function of the Reynolds number ($C_f = 24/Re$), where $C_f = 2\tau_{wall}/\rho U^2$, τ_{wall} is area-weighted average shear stress, and U is average bulk fluid velocity. The numerical results indicate that for superhydrophobic surfaces, similar functionality exists between the friction coefficient and Reynolds number, but with different constants depending on the gas fraction. As can be seen from Figures 9.1, the friction coefficient decreases with increasing the gas fraction for surfaces with staggered posts and randomly distributed posts. In addition, the difference between the skin-friction coefficient of the random posts and that of the staggered posts increases by increasing the gas fraction.

9.2 Meniscus Stability

We present an analytical study for the condition at which the air–water interface (meniscus) may transition from the non-wetted state (Cassie state) to the wetted state (Wenzel state). This is important in practical applications for submersed bod-

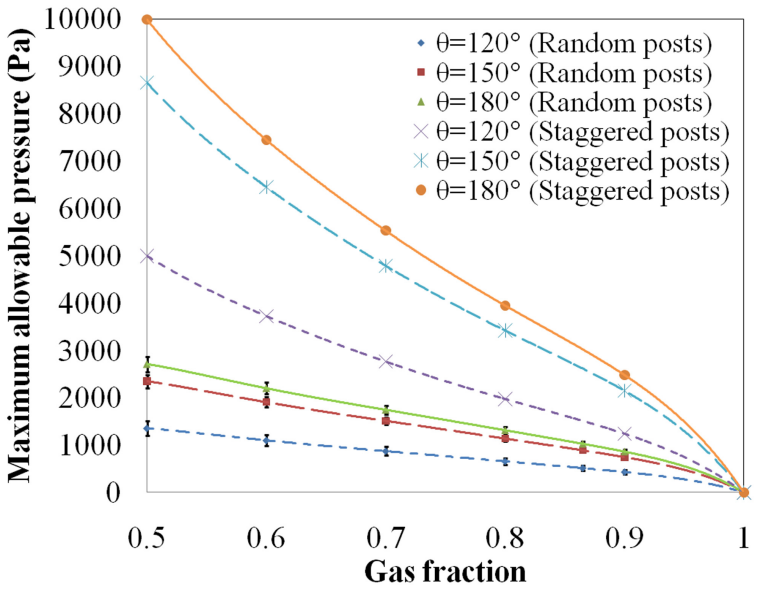

Figure 9.2: Maximum allowable pressure as a function of gas fraction and contact angle for both random and staggered posts.

ies because once the thin gas layer is replaced by liquid, none of the beneficial effects remain. The results of both random and staggered posts are shown in Figure 9.2 for comparison. It is obvious that the maximum allowable pressure is reduced dramatically in case of random posts indicating that superhydrophobic surfaces with random roughness distributions are much more susceptible to failure under hydrostatic pressure. In summary, the numerical simulations indicate that the random distribution of surface roughness has more favorable effect on drag reduction than aligned or staggered one has, as long as the gas fraction is kept the same. This effect peaks at about 30% as the gas fraction increases to 0.98. The stability of the meniscus, however, is strongly influenced by the average spacing between the roughness peaks, which needs to be carefully examined before a surface can be recommended for fabrication. More details of the above have appeared in Samaha *et al.* (2011*b*), reprinted in Appendix VIII.

9.3 Additional Studies

Extensions of the above study were performed by our colleagues in Dr. Tafreshi's group. For example, Emami *et al.* (2011*a*) conducted a similar study in 3-D space. In particular, they simulated the stability of air–water interface formed on granular superhydrophobic coatings comprised of randomly distributed spherical aerogel particles in comparison to the ordered distributed ones. These authors also conducted a series of 3-D full-morphology (FM) numerical simulations and analytical expressions to predict the critical pressure (pressure beyond which the surface departs from the Cassie state) against solid volume fraction of their granular porous coatings, as shown in Figure 9.3. This figure shows that the air–water interface can sustain more pressure as the solid volume fraction increases. Moreover, the surface with random particles is more susceptible to failure under hydrostatic pressure, as expected.

Emami *et al.* (2011*b*) developed a mathematical framework to calculate the exact shape of the air–water interface, and so predict the stability of the air–water interface on superhydrophobic surfaces made up of randomly distributed posts of different diameters, heights, and materials. This was accomplished by using the Young–Laplace equation to derive a second-order partial differential equation that was solved numerically via finite element method. Figure 9.4 shows an example of an air–water interface formed over a superhydrophobic surface comprised of randomly distributed posts with diameters ranging between 8 to 12 μm, and heights ranging between 50 to 51 μm, leading to a gas fraction of 65%. The deflection of the interface under a hydrostatic pressure of 3400 Pa can be seen. The posts are assumed to be made of a material with a contact angle of 120°. The authors extended this work to predict the meniscus shape and stability of the air–water interface for surfaces comprised of pores with arbitrary shapes and depths (Emami *et al.*, 2012*b*) and those comprised of fibers (Emami *et al.*, 2012*a*) as shown in Figures 9.5 and 9.6.

To study the stability of air–water interface formed over superhydrophobic

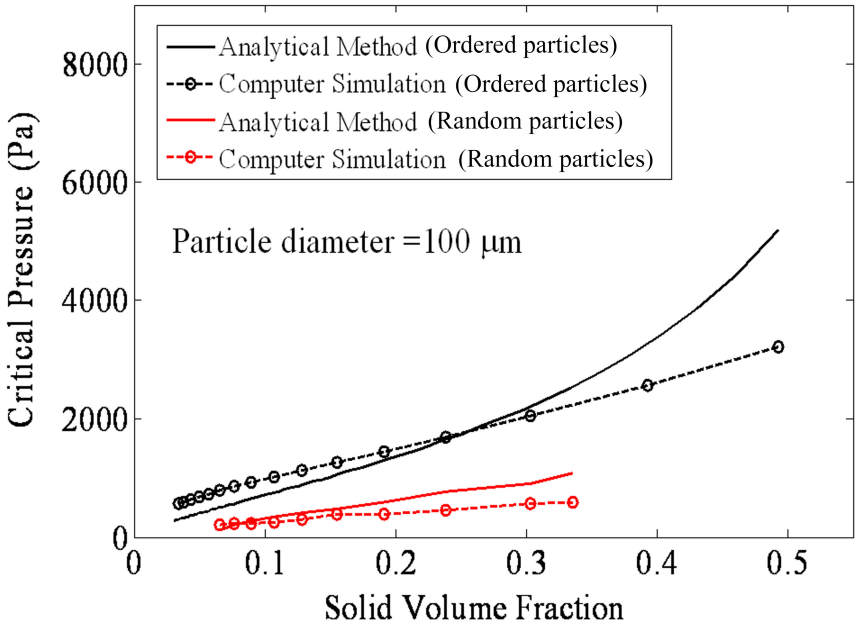

Figure 9.3: Numerically and analytically calculated critical pressure against solid volume of fraction for ordered aerogel particles and random ones. Figure adapted from Emami *et al.* (2011*a*).

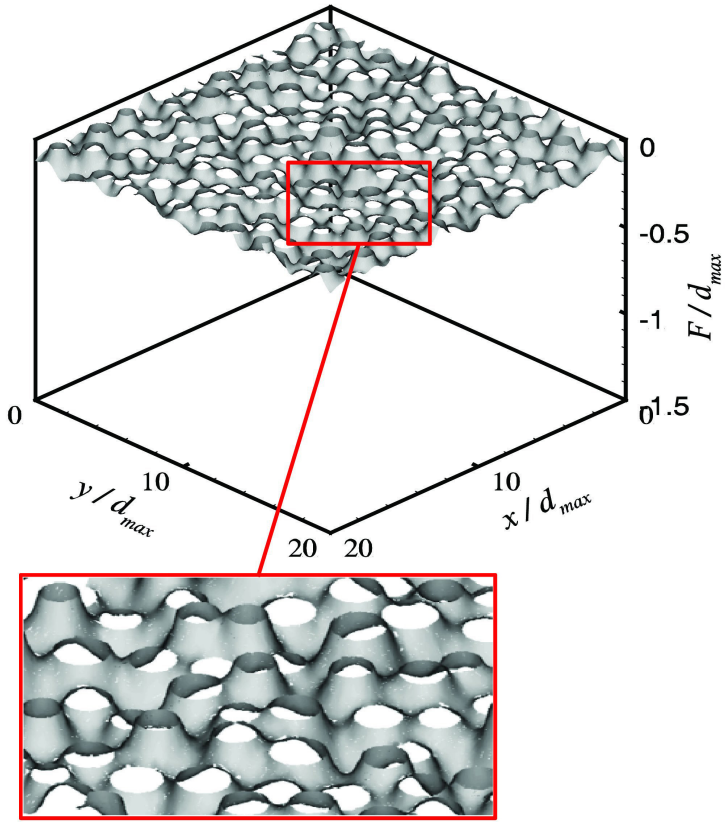

Figure 9.4: Calculated meniscus surfaces for superhydrophobic surface with randomly distributed posts of random diameters and heights at P=3400 Pa. Here, d_{max} refers to maximum post's diameter. Variables x, y, and F are Cartesian coordinates. Figure adapted from Emami *et al.* (2011*b*).

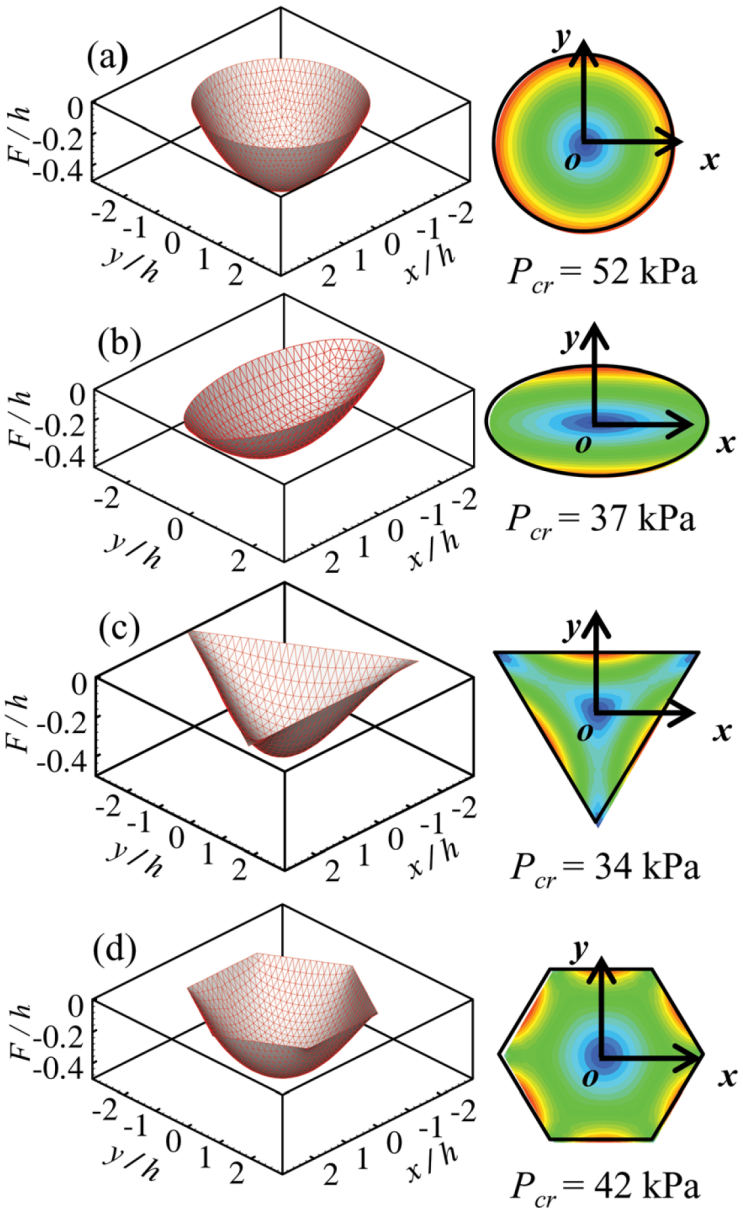

Figure 9.5: Calculated air–water interface at the critical hydrostatic pressures, over pores with (a) circular; (b) elliptical; (c) triangular; and (d) hexagonal cross-sections. Contour plots show the interface gradient value. Here, h refers to the thickness of the flat surface. Contour values correspond to 0–0.6. Reprented from Emami *et al.* (2012*b*).

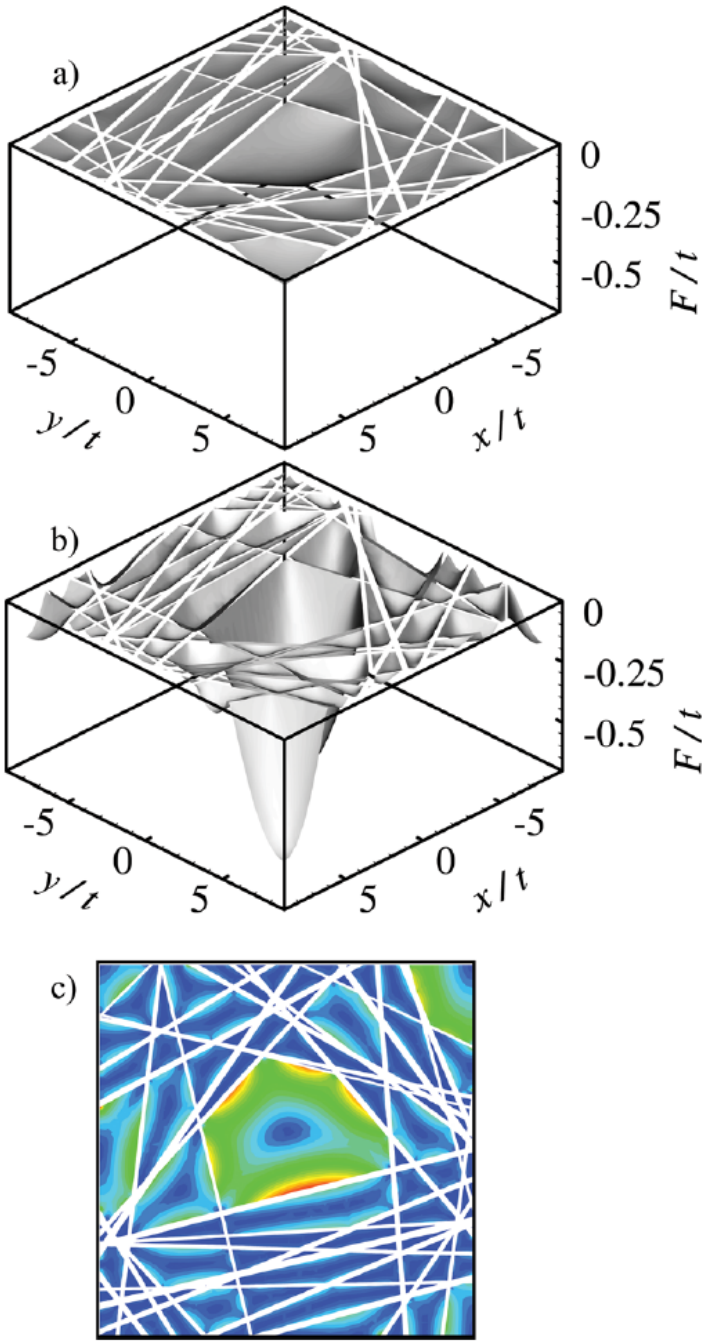

Figure 9.6: Calculated meniscus surfaces for a fibrous superhydrophobic surface (a) at P=5 kPa; and (b) at the critical pressure P=46 kPa; (c) calculated gradient contours at the critical pressure P=46 kPa. Blue to red represents 0 to 0.6 in the contours. Reprented from Emami *et al.* (2012*a*).

coatings composed of randomly oriented nanofibers, Bucher *et al.* (2012) conducted a series of FM simulations in 3-D virtual domains resembling the internal microstructure of electrospun fiber mats. Figure 9.7 shows an example of the FM simulations for two different hydrostatic pressures conducted by Bucher et al. The solid volume fraction and fiber diameter are 10% and 500 nm, respectively. It can be seen that, by increasing the pressure, the water (red color) fills a greater fraction of the pore space. Figure 9.8 shows the critical pressure as a function of the coating's morphology for bimodal (composed of two different fiber diameters) fibrous media with random fiber orientations in terms of solid volume fraction and fine fiber diameter, d_f. It can be seen that critical pressure increases with increasing solid volume fraction or fine fiber diameter, when other microstructural parameters are held constant.

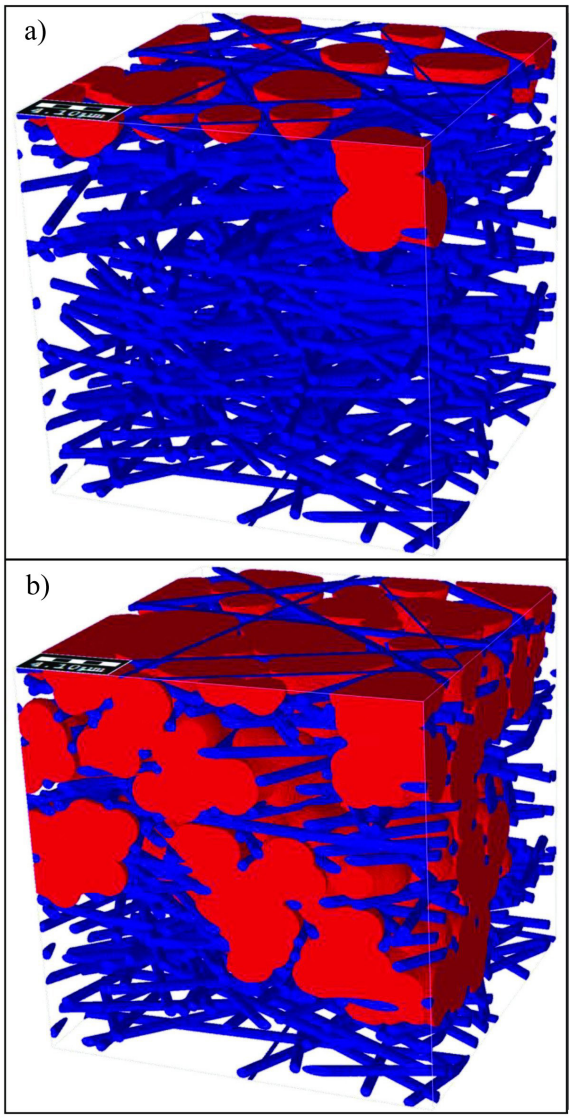

Figure 9.7: A visualization of two stages of water intrusion into a unimodal fibrous structure with random in-plane fiber orientation, using the full morphology method. Corresponding pressures are: (a) 58.983 kPa; (b) 77.333 kPa. The non-wetting fluid (water) represented in the red region is made up of spheres fitted into the domain. Figure adapted from Bucher *et al.* (2012).

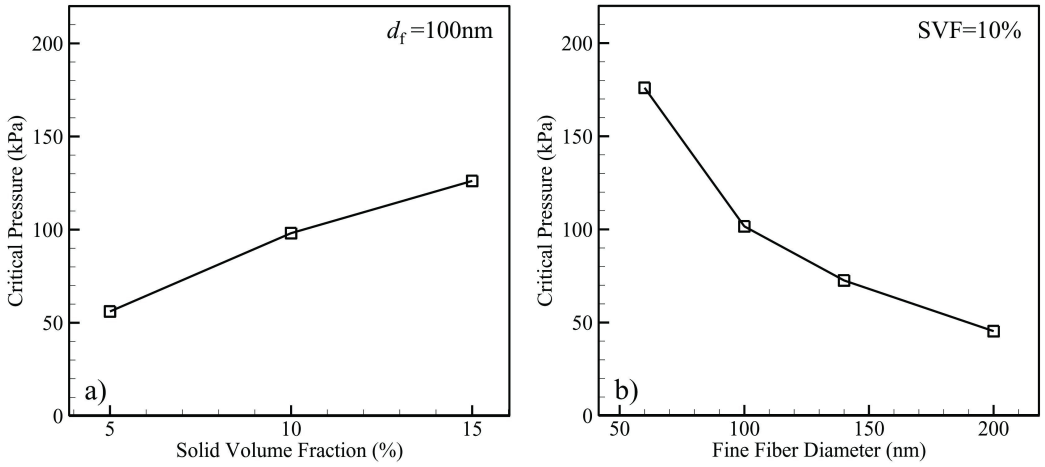

Figure 9.8: Critical pressure predictions for layered, randomly oriented media compared against variations in one of four microstructural parameters: (a) solid volume fraction; (b) fiber diameter. For both (a) and (b), coarse-to-fine fiber diameter ratio (R_{cf}) = 5 and coarse number fraction (n_c) = 0.1. Figure adapted from Bucher *et al.* (2012).

CHAPTER 10 Conclusions and Future Outlook

10.1 Conclusions

Superhydrophobic coatings have been experimentally, numerically and analytically studied in order to examine their ability to reduce drag, hydrophobicity, and survivability and longevity under different environmental conditions. We have presented two kinds of superhydrophobic coatings that are produced using relatively simple low-cost fabricating techniques. The first one is produced by deposition of hydrophobic polymer micro- and nanofibers using DC-biased AC-electrospinning. The second one is generated by random deposition of hydrophobic aerogel microparticles. The results show that both coatings can produce about 20% drag reduction. The longevity of those coatings can reach more than a week under some conditions. Additionally, they could sustain pressure head of about 100 meter of water. All of these show that such coatings could be a good candidate for deep underwater applications as a relatively simple passive (non-energy consuming) drag-reduction flow-control method. The effects of several environmental conditions on the performance of the fibrous coatings have been studied. First of all, the water movement over superhydrophobic surfaces significantly affects their hydrophobicity and longevity. With increasing flow velocity over the coatings, the longevity dramatically decreases. We reason that increasing the flowrate increases the mass-transfer convection coefficient, which leads to enhancing the dissolution of entrapped air in water and thus accelerating the transition to the wetted state. Secondly, increasing the hydrostatic pressure over such surfaces results in exponential decay of their longevity. Third, salinity of the water can decrease both hydrophobicity and longevity of the surfaces.

On the other hand, we have measured the terminal pressure of submerged superhydrophobic coatings made up of randomly deposited polydisperse aerogel par-

ticles. Four surfaces with different aerogel-particle mean sizes were tested. To estimate the coating's gas area fraction, an image-thresholding technique was applied to several SEM images of the four coatings. The measurements show the increase of terminal pressure with decreasing gas area fraction over man-made granular superhydrophobic coatings because the samples with lower gas fraction are made of finer aerogel particles that can sustain higher pressures without transition to wetted state (by keeping the entrapped air layer). Moreover, we have numerically studied superhydrophobic surfaces comprised of random roughness (like the aerogel ones). Our results indicate that the skin-friction coefficient (i.e., pressure drop) decreases by increasing the surface gas fraction (i.e., shear-free area). Comparing surfaces having random hydrophobic roughness (particles) with those having staggered microposts, we showed that the former causes less friction drag, especially at high gas fractions. The difference in the average skin-friction coefficients between these two configurations is increased by increasing the gas fraction. Our interface stability analysis using the Voronoi algorithm, however, has revealed that superhydrophobic surfaces made by randomly depositing microparticles or microposts are more susceptible to elevated hydrostatic pressures. It was shown that at a given maximum allowable pressure, surfaces with random post distribution produce less drag reduction than those made up of staggered post.

The present study shows that the environmental parameters significantly affects the hydrophobicity and longevity of superhydrophobic surfaces that opens a pathway for developing a better surface that could be used for underwater applications and could survive longer under different conditions additionally, looking for an applicable air-restoration method to enable the coating to recover its hydrophobicity.

10.2 Future Outlook

Superhydrophoboc surfaces were demonstrated by several experimental, numerical, and analytical studies to reduce drag for both laminar and turbulent flows. This

reinforces the optimistic view that these surfaces could be used for drag reduction purposes, especially in marine environments. For example, it is well known that submarines consume a large amount of fuel to overcome the skin-friction drag produced on their bodies. Intensive flow-control studies have been performed to develop different active, reactive, and passive methods to reduce this drag force. Superhydrophobic coatings are aimed to be utilized as a passive method and may potentially become a viable alternative to the more complex and energy consuming active or reactive flow control techniques such as wall suction/blowing. We propose some useful tasks that could contribute to the development of superhydrophobic coatings.

10.2.1 Fiber's Morphology and Coating's Thickness

Herein, we suggest optimizing and controlling the morphology of the coating's fibers in order to get the coating that has the best hydrophobicity and longevity. We have succeeded to get both random and aligned fibers as discussed in chapter three. Therefore, we propose studying the effects of environments on the performance of both coatings. Additionally, we could control the fiber's diameter to optimize the solid volume fraction of the coating, which has an impact on hydrophobicity and longevity. This can be achieved by changing the electrospinning conditions.

The coating's thickness is one of the most important issues that are needed to investigate their impact on superhydrophobicity of the surface. We need to determine the best coating thickness that can optimize the drag reduction and longevity characterizations. It is known that the solid volume of fraction of the coatings—fibers volume divided by total volume—has an impact on drag reduction and critical pressure at which the air–water interface (meniscus) fails (Emami *et al.*, 2011*a*). Definitely, the solid volume of fraction is affected by the coating thickness. We have succeeded to exact measure the coating thickness using thickness gauge (J-40-T) made by Electromatic Equipment Co., Inc., which has precision as low as 10 μm and therefore, we can get an experimental correlation for hydrophobicity and longevity against coating's

thickness.

10.2.2 Air/Oxygen Absorption in Water

The effect of air/Oxygen concentration on longevity is an important environmental parameter that it could be accomplished. We propose to assess the longevity and hydrophobicity of the coating when it is subjected to air dissolved in water in comparison with D.I. water because this simulates practical water body like oceans. We have got dissolved oxygen meter made by EXTECH Instruments (model number 407510) to measure the concentration of oxygen in water. The rate of dissolution of the trapped air between the surface and water could be affected by the presence of air in water, which leads to influence the degree of hydrophobicity of the surface.

10.2.3 Grand-Scale Model

We propose constructing a 'grand-scale' model. Based on a specific set of goals, such model may be used to design and optimize a superhydrophobic coating. Increasing the critical pressure, drag reduction, and longevity of a coating are the three targets to be accomplished. These could be carried out by controlling the coating's parameters. However, the environmental conditions have also an impact on the aforementioned targets. The grand model should include all the parameters and conditions to study their effects simultaneously. Figure 10.1 is a flow chart that indicates that the three targets are influenced by the coating's parameters and variation of environmental conditions.

In our laboratory, we fabricate two types of superhydrophobic coatings: spun fiber and aerogel particles. Polystyrene weight percentage, fiber's diameter, and fiber's alignment are the parameters that could be controlled for the spun fiber coating. For the aerogel one, particle's diameter could also be controlled. Solid volume of fraction and coating's thickness could be optimized for both coatings. Environmental conditions such as water movement, salt concentration, and air/oxygen absorption could

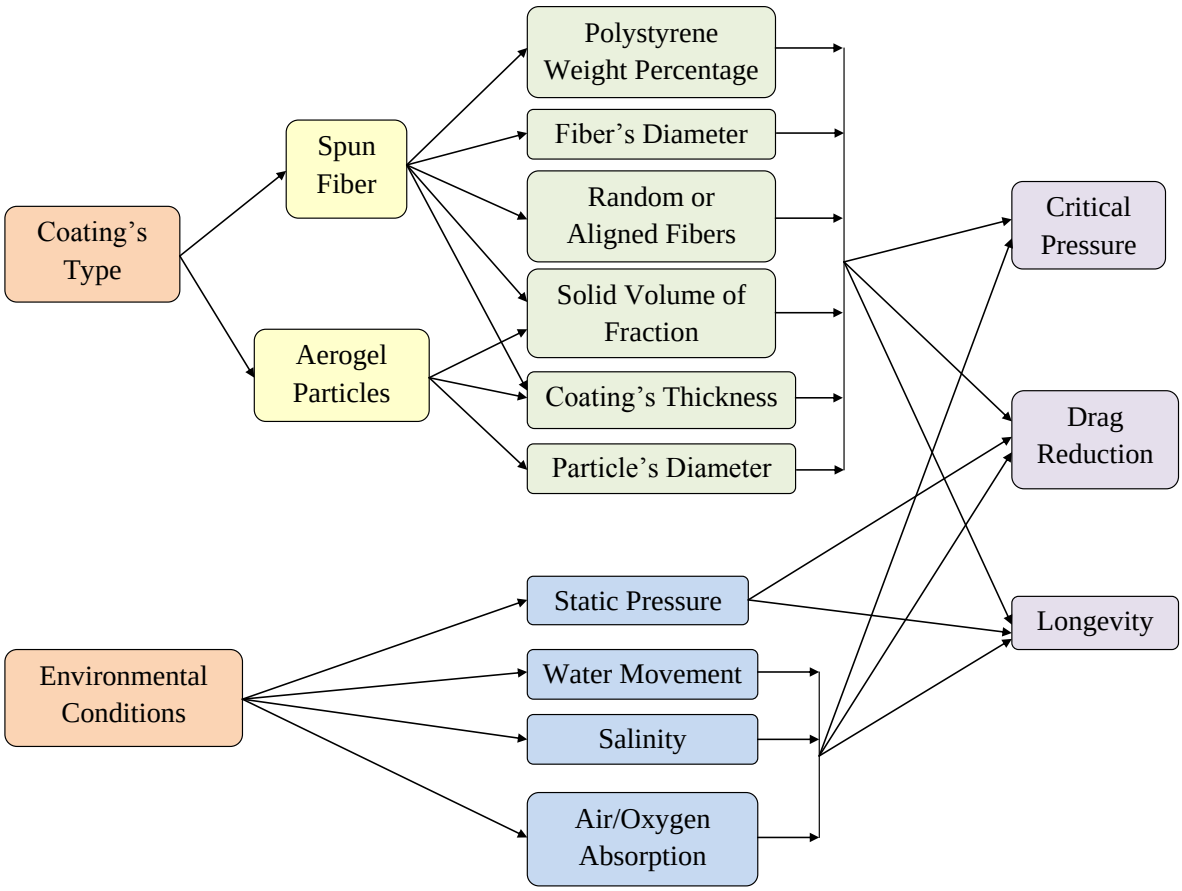

Figure 10.1: Engineering targets and corresponding parameters in grand-scale model.

also affect the three targets. In addition, the static pressure could significantly affect the longevity and drag reduction. We anticipate that one or more of those parameters and conditions may lead to contradictory benefits. For example, by increasing the fiber's diameter, drag reduction may increase but the longevity may decrease. Thus, the grand-scale model should optimize that parameter in order to yield the 'best' coating characteristics. We suggest to put the entire numerical and experimental results available into a unified framework. For example, by using both the experimental data discussed in chapters 5 and 6 and the numerical results discussed in subsection 9.3, we may be able to establish several empirical correlations that can relate both longevity and critical pressure (targets) to both flow conditions and applied pressure (environments). This would allow optimization of the coating's beneficial properties.

10.2.4 Additional Topics

There are significant issues that need to be resolved in order for the manufacturing of such coatings to be feasible. First of all, the microstructure of the coating should be strong enough to sustain the developed shear stress without erosion especially for turbulent flow. Secondly, the coating should keep its hydrophobicity for an acceptable time frame (reasonable longevity). Moreover, if the coating becomes hydrophilic, an infield method should be developed to *rejuvenate* the surface to return it to its hydrophobic state. Third, the coating should be durable enough to sustain environmental conditions such as water salinity, depth, circulation, and biofouling. Finally, the fabrication processes should be extended from lab scale to large industrial scale applications. All of these issues require further research and development before superhydrophobic coatings could be utilized under realistic circumstances. A review about the current status development of superhydrophobic surfaces has appeared in Samaha *et al.* (2012*c*), reprinted in Appendix I.

Bibliography

Angarska, J. K., Dimitrova, B. S., Danov, K. D., Kralchevsky, P. A., Ananthapadmanabhan, K. P. & Lips, A. 2004 Detection of the hydrophobic surface force in foam films by measurements of the critical thickness of the film rupture. *Langmuir* **20**, 1799–1806.

Barbieri, L., Wagner, E. & Hoffmann, P. 2007 Water wetting transition parameters of perfluorinated substrates with periodically distributed flat-top microscale obstacles. *Langmuir* **23**, 1723–1734.

Bhagat, S. D., Kim, Y-H., Suh, K-H., Ahn, Y-S., Yeo, J-G. & Han, J-H. 2008 Super hydrophobic silica aerogel powders with simultaneous surface modification, solvent exchange and sodium ion removal from hydrogels. *Microporous Mesoporous Mater.* **112**, 504–509.

Bico, J., Marzolin, C. & Quéré, D. 1999 Pearl drops. *Europhys. Lett.* **47**, 220–226.

Bobji, M., Kumar, S. V., Asthana, A. & Govardhan, R. N. 2009 Underwater sustainability of the "cassie" state of wetting. *Langmuir* **25**, 12120–12126.

Bucher, T. M., Emami, B., Tafreshi, H. V., Gad-el-Hak, M. & Tepper, G. C. 2012 Modeling resistance of nanofibrous superhydrophobic coatings to hydrostatic pressures: the role of microstructure. *Phys. Fluids* **24**, 022109.

Callies, M., Chen, Y., Marty, F., Pépin, A. & Quéré, D. 2005 Microfabricated textured surfaces for super-hydrophobicity investigations. *Microelectron. Eng.* **78–79**, 100–105.

Cassie, A. B. D. & Baxter, S. 1944 Wettability of porous surfaces. *Trans. Faraday Soc.* **40**, 546–551.

Cheng, Y. P., Teo, C. J. & Khoo, B. C. 2009 Microchannel flow with superhydrophobic surfaces: Effects of reynolds number and pattern width to channel height ratio. *Phys. Fluids* **21**, 122004.

Cheng, Y. T., Rodak, D. E. & Hayden, C.A. 2006 Effects of micro- and nanostructures on the self-cleaning behaviour of lotus leaves. *Nanotechnology* **17**, 1359–1362.

Choi, C-H. & Kim, C-J. 2006 Large slip of aqueous liquid flow over a nanoengineered superhydrophobic surface. *Phys. Rev. Lett.* **96**, 066001.

Christenson, H. K., Claesson, P. M., Berg, J. & Herder, P. C. 1989 Forces between fluorocarbon surfactant monolayers - salt effects on the hydrophobic interaction. *J. Phys. Chem.* **93**, 1472–1478.

Daniello, R., Waterhouse, N. E. & Rothstein, J. P. 2009 Turbulent drag reduction using superhydrophobic surfaces. *Phys. Fluids* **21**, 085103.

Davies, J., Maynes, D., Webb, B. W. & Woolford, B. 2006 Laminar flow in a microchannel with superhydrophobic walls exhibiting transverse ribs. *Phys. Fluids* **18**, 087110.

Emami, B., Bucher, T. M., Tafreshi, H. V., Pestov, D., Gad-el-Hak, M. & Tepper, G. C. 2011*a* Simulation of meniscus stability in superhydrophobic granular surfaces under hydrostatic pressures. *Colloids Surf. A* **385**, 95–103.

Emami, B., Tafreshi, H. V., Gad-el-Hak, M. & Tepper, G. C. 2011*b* Predicting shape and stability of air–water interface on superhydrophobic surfaces with randomly distributed, dissimilar posts. *Appl. Phys. Lett.* **98**, 203106.

Emami, B., Tafreshi, H. V., Gad-el-Hak, M. & Tepper, G. C. 2012*a* Effect of fiber orientation on shape and stability of airwater interface on submerged superhydrophobic electrospun thin coatings. *J. Appl. Phys.* **111**, 064325.

Emami, B., Tafreshi, H. V., Gad-el-Hak, M. & Tepper, G. C. 2012*b* Predicting shape and stability of air–water interface on superhydrophobic surfaces comprised of pores with arbitrary shapes and depths. *Appl. Phys. Lett.* **100**, 013104.

Extrand, C. W. 2004 Criteria for ultralyophobic surfaces. *Langmuir* **20**, 5013–5018.

Extrand, C. W. 2006 Designing for optimum liquid repellency. *Langmuir* **22**, 1711–1714.

Feng, X-Q., Gao, X., Wu, Z., Jiang, L. & Zheng, Q-S. 2007 Superior water repellency of water strider legs with hierarchical structures: experiments and analysis. *Langmuir* **23**, 4892–4896.

Gad-el-Hak, M. 1999 The fluid mechanics of microdevices—the freeman scholar lecture. *J. Fluids Eng.* **121**, 5–33.

Gad-el-Hak, M. 2000 *Flow Control: Passive, Active, and Reactive Flow Management*. Cambridge University Press, London, United Kingdom.

Gao, X. & Jiang, L. 2004 Water-repellent legs of water striders. *Nature* **432**, 36.

Henoch, C., Krupenkin, T. N., Kolodner, P., Taylor, J. A., Hodes, M. S., Lyons, A. M., Peguero, C. & Breuer, K. 2006 Turbulent drag reduction using superhydrophobic surfaces. In *3rd AIAA Flow Control Conference, San Francisco, California*, p. 3192.

Hwang, H. S., Kim, N. H., Lee, S. G., Lee, D. Y., Cho, K. & Park, I. 2011 Facile fabrication of transparent superhydrophobic surfaces by spray deposition. *ACS Appl. Mater. Interfaces* **3**, 2179–2183.

Kanna, P. R. & Das, M. K. 2005 Conjugate forced convection heat transfer from a flat plate by laminar plane wall jet flow. *Int. J. Heat Mass Transfer* **48**, 2896–2910.

Koch, K., Bhushan, B., Jung, Y. C. & Barthlott, W. 2009 Fabrication of artificial lotus leaves and significance of hierarchical structure for superhydrophobicity and low adhesion. *Soft matter* **5**, 1386–1393.

Lafuma, A. & Quéré, D. 2003 Superhydrophobic states. *Nat. Mater.* **2**, 457–460.

Lauga, E., Brenner, M. P. & Stone, H. A. 2007 *Microfluidics: the no-slip boundary condition, in: C. Tropea, A. Yarin, J. Foss (Eds.), Handbook of Experimental Fluid Dynamics*. Springer, New York.

Lee, C., Choi, C-H. & Kim, C-J. 2008 Structured surfaces for giant liquid slip. *Phys. Rev. Lett.* **101**, 064501.

Lee, C. & Kim, C-J. 2009 Maximizing the giant slip on superhydrophobic microstructures by nanostructuring their sidewalls. *Langmuir* **25**, 12812–12818.

Lee, C. & Kim, C-J. 2011 Underwater restoration and retention of gases on superhydrophobic surfaces for drag reduction. *Phys. Rev. Lett.* **106**, 014502.

Lee, S., Kim, D. & Hwang, W. 2011 Artificial lotus leaf structure made by blasting with sodium bicarbonate. *Curr. Appl Phys.* **11**, 800–804.

Lei, L., Li, H., Shi, J. & Chen, Y. 2010 Metastable underwater superhydrophobicity. *Langmuir* **26**, 3666–3669.

Ma, M., Mao, Y., Gupta, M., Gleason, K. K. & Rutledge, G. C. 2005 Superhydrophobic fabrics produced by electrospinning and chemical vapor deposition. *Macromolecules* **38**, 9742–9748.

Mabuchi, I. & Kumada, M. 1972 Studies on heat transfer to turbulent jets with adjacent boundaries: 1st report, flow development and mass transfer in plane turbulent wall jet. *B. JSME* **15**, 1236–1245.

Martell, M., Perot, J. B. & Rothstein, J. P. 2009 Direct numerical simulations of turbulent flows over superhydrophobic surfaces. *J. Fluid Mech.* **620**, 31–41.

Maynes, D., Jeffs, K., Woolford, B. & Webb, B. W. 2007 Laminar flow in a microchannel with hydrophobic surface patterned microribs oriented parallel to the flow direction. *Phys. Fluids* **19**, 093603.

Navier, C. L. M. H. 1823 Memoire sur les lois du mouvement des fluides. *Mem. Acad. R. Sci. Inst. France* **6**, 389–440.

Neinhuis, C. & Barthlott, W. 1997 Characterization and distribution of water-repellent, self-cleaning plant surfaces. *Ann. Bot.* **79**, 667–677.

Ochanda, F. O., Samaha, M. A., Tafreshi, H. V., Tepper, G. C. & Gad-el-Hak, M. 2012*a* Fabrication of superhydrophobic fiber coatings by dc-biased ac-electrospinning. *J. Appl. Polym. Sci.* **123**, 1112–1119.

Ochanda, F. O., Samaha, M. A., Tafreshi, H. V., Tepper, G. C. & Gad-el-Hak, M. 2012*b* Salinity effects on the degree of hydrophobicity and longevity for superhydrophobic fibrous coatings. *J. Appl. Polym. Sci.* **124**, 5021–5026.

Otsu, N. 1979 A threshold selection method from gray-level histograms. *IEEE Trans. Syst. Man Cybern* **9**, 62–66.

Patankar, N. A. 2004 Transition between superhydrophobic states on rough surfaces. *Langmuir* **20**, 7097–7102.

Persson, C. M., Jonsson, A. P., Bergström, M. & Eriksson, J. C. 2003 Testing the gouy–chapman theory by means of surface tension measurements for sds–nacl–h_2o mixtures. *J. Colloid Interface Sci.* **267**, 151–154.

Poetes, R., Holtzmann, K., Franze, K. & Steiner, U. 2010 Metastable underwater superhydrophobicity. *Phys. Rev. Lett.* **105**, 166104.

Rathgen, H. & Mugele, F. 2010 Microscopic shape and contact angle measurement at a superhydrophobic surface. *Faraday Discuss.* **146**, 49–56.

Rothstein, J. P. 2010 Slip on superhydrophobic surfaces. *Annu. Rev. Fluid Mech.* **42**, 89–109.

Sakai, M., Yanagisawa, T., Nakajima, A., Kameshima, Y. & Okada, K. 2009 Effect of surface structure on the sustainability of an air layer on superhydrophobic coatings in a water–ethanol mixture. *Langmuir* **25**, 13–16.

Samaha, M. A., Ochanda, F. O., Tafreshi, H. V., Tepper, G. C. & Gad-el-Hak, M. 2011*a* *In Situ*, non-invasive characterization of superhydrophobic coatings. *Rev. Sci. Instrum.* **82**, 045109.

Samaha, M. A., Tafreshi, H. V. & Gad-el-Hak, M. 2011*b* Modeling drag reduction and meniscus stability of superhydrophobic surfaces comprised of random roughness. *Phys. Fluids* **23**, 012001.

Samaha, M. A., Tafreshi, H. V. & Gad-el-Hak, M. 2012*a* Effects of hydrostatic pressure on the drag reduction of submerged aerogel-particle coatings. *Colloids Surf. A* **399**, 62–70.

Samaha, M. A., Tafreshi, H. V. & Gad-el-Hak, M. 2012*b* Influence of flow on longevity of superhydrophobic coatings. *Langmuir* **under review**.

Samaha, M. A., Tafreshi, H. V. & Gad-el-Hak, M. 2012*c* Superhydrophobic surfaces: from the lotus leaf to the submarine. *C. R. Mec.* **340**, 18–34.

Samaha, M. A., Tafreshi, H. V. & Gad-el-Hak, M. 2012*d* Sustainability of superhydrophobicity under pressure. *Phys. Fluids* **under review**.

Sarkar, S., Deevi, S. & Tepper, G. 2007 Biased ac electrospinning of aligned polymer nanofibers. *Macromol. Rapid Commun.* **28**, 1034–1039.

Sheng, X. & Zhang, J. 2011 Air layer on superhydrophobic surface underwater. *Colloids Surf., A* **377**, 374–378.

Singh, A., Steely, L. & Allcock, H. R. 2005 Poly[bis(2,2,2-trifluoroethoxy)phosphazene] superhydrophobic nanofibers. *Langmuir* **21**, 11604–11607.

Song, J. D., Ryoo, R. & Jhon, M. S. 1991 Anion binding properties of poly(vinylpyrrolidone) in aqueous solution studied by halide nmr spectroscopy. *Macromolecules* **24**, 1727–1730.

Steinberger, A., Conttin-Bizonne, C., Kleimann, P. & Charlaix, E. 2007 High friction on a bubble mattress. *Nat. Mater.* **6**, 665–668.

Stephani, K. A. & Goldstein, D. B. 2010 An examination of trapped bubbles for viscous drag reduction on submerged surfaces. *J. Fluid. Eng.—T. ASME* **132**, 041303.

Wenzel, R. N. 1936 Resistance of solid surfaces to wetting by water. *Ind. Eng. Chem.* **28**, 988–994.

Woolford, B., Prince, J., Maynes, D. & Webb, B. W. 2009 Particle image velocimetry characterization of turbulent channel flow with rib patterned superhydrophobic walls. *Phys. Fluids* **21**, 085106.

Yang, H. & Deng, Y. 2008 Preparation and physical properties of superhydrophobic papers. *J. Colloid Interface Sci.* **325**, 588–593.

Ybert, C., Barentin, C., Cécile, C-B., Joseph, P. & Bocquet, L. 2007 Achieving large slip with superhydrophobic surfaces: Scaling laws for generic geometries. *Phys. Fluids* **19**, 123601.

Zheng, Q. S., Yu, Y. & Zhao, Z. H. 2005 Effects of hydraulic pressure on the stability and transition of wetting modes of superhydrophobic surfaces. *Langmuir* **21**, 12207–12212.

Zhu, M., Zuo, W., Yu, H., Yang, W. & Chen, Y. 2006 Superhydrophobic surface directly created by electrospinning based on hydrophilic material. *J. Mater. Sci.* **41**, 3793–3797.

APPENDIX I: Superhydrophobic surfaces: From the lotus leaf to the submarine

Following is a reprint of the paper "Superhydrophobic surfaces: From the lotus leaf to the submarine," by Samaha, M.A., Tafreshi, H.V., and Gad-el-Hak, M., *Comptes Rendus de l'Académie des Sciences: Mécanique*, vol. 340, pp. 18–34, 2012.

C. R. Mecanique 340 (2012) 18–34

Contents lists available at SciVerse ScienceDirect

Comptes Rendus Mecanique

www.sciencedirect.com

Biomimetic flow control

Superhydrophobic surfaces: From the lotus leaf to the submarine

Mohamed A. Samaha, Hooman Vahedi Tafreshi, Mohamed Gad-el-Hak *

Department of Mechanical & Nuclear Engineering, Virginia Commonwealth University, Richmond, VA 23284-3015, USA

ARTICLE INFO

Article history:
Available online 30 December 2011

Keywords:
Biomimetic
Superhydrophobic
Slip flow
Drag reduction
Lotus effect
Microfabrication
Electrospinning

ABSTRACT

In this review we discuss the current state of the art in evaluating the fabrication and performance of biomimetic superhydrophobic materials and their applications in engineering sciences. Superhydrophobicity, often referred to as the *lotus effect*, could be utilized to design surfaces with minimal skin-friction drag for applications such as self-cleaning and energy conservation. We start by discussing the concept of the *lotus effect* and continue to present a review of the recent advances in manufacturing superhydrophobic surfaces with ordered and disordered microstructures. We then present a discussion on the resistance of the air–water interface to elevated pressures—the phenomenon that enables a water strider to walk on water. We conclude the article by presenting a brief overview of the latest advancements in studying the longevity of submerged superhydrophobic surfaces for underwater applications.

© 2011 Académie des sciences. Published by Elsevier Masson SAS. All rights reserved.

1. Introduction

Several design ideas have been inspired by nature. Biological mechanisms can be studied to engineer systems for modern industrial applications. The lotus leaf possesses a peculiar water-repellent characteristic that enhances the mobility of droplets for self-cleaning purposes [1]. A similar effect, i.e. superhydrophobicity, enables a water strider to walk on water [2]. When a superhydrophobic surface is fully submersed in water, it entraps air in its pores resulting in the formation of air pockets between the solid surface and water. The entrapped air is separated from water with a thin interface anchored on the solid walls and stretched due to surface tension forces. It has been observed that a moving body of water "slips" over an air–water interface, whereas it "sticks" to a solid surface [3]. Therefore, if the percentage of the surface covered by air pockets is sufficiently high, a superhydrophobic surface can cause the so-called "slip effect", resulting in a reduction in the skin-friction drag exerted on the surface [3]. As long as the air pockets exist, the surface remains hydrophobic. In other words, the degree of hydrophobicity and the beneficial effects are diminished by the reduction of the amount of entrapped air. The longevity of a superhydrophobic surface—how long the surface can maintain the air pockets—is critical, especially in underwater applications.

Engineered superhydrophobic surfaces are often comprised of microridges or microposts arranged in an ordered configuration on a solid flat surface. These surfaces have been extensively studied and developed to produce slip effect [4]. Large-scale manufacturing of such surfaces, however, is prohibitively expensive. On the contrary, surfaces manufactured by random deposition of hydrophobic particles [5–7] or fibers [8–11] could offer more cost-effective alternatives for production of large superhydrophobic surfaces, as will be discussed later in this article.

In the next section, we discuss the lotus leaf effect and the underlying fluid mechanics of slip effect. In Section 3, we review the different manufacturing techniques used for fabrication of superhydrophobic surfaces. In Section 4, we discuss

* Corresponding author.
E-mail addresses: samahama@vcu.edu (M.A. Samaha), htafreshi@vcu.edu (H.V. Tafreshi), gadelhak@vcu.edu (M. Gad-el-Hak).
URLs: http://www.people.vcu.edu/~htafreshi/ (H.V. Tafreshi), http://www.people.vcu.edu/~gadelhak/ (M. Gad-el-Hak).

1631-0721/$ – see front matter © 2011 Académie des sciences. Published by Elsevier Masson SAS. All rights reserved.
doi:10.1016/j.crme.2011.11.002

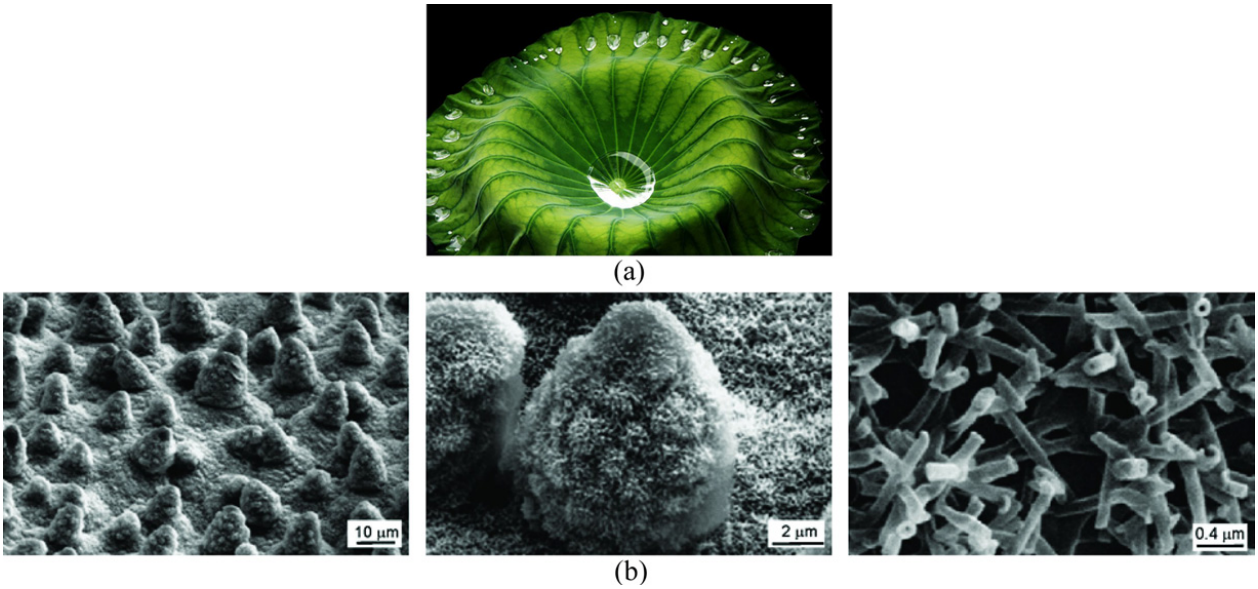

Fig. 1. Lotus leaf: (a) Magnification of one. From website [14]; (b) Three different magnification of SEM images showing morphological micro- and nanostructures. From Koch et al. [13].

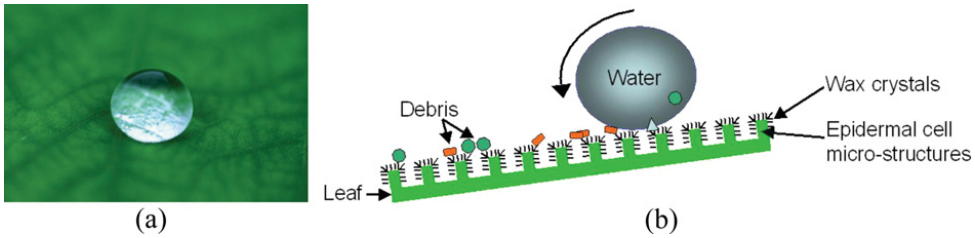

Fig. 2. (a) Water droplet beading on lotus leaf with static contact angle higher than 150 degrees. From website [15]; (b) Schematic illustration of lotus effect. From website [16].

the stability of the air–water interface under elevated pressures, the key concept that allows water to support the weight of a water strider. In Section 5, we present a discussion on the latest advances in measuring the longevity of submerged superhydrophobic surfaces. In the "Future outlook" section, we give suggestions and recommendations to improve and enhance the current fabricated surfaces. This will be followed by our conclusions, given in Section 7.

2. Characterization of superhydrophobic surfaces: the lotus effect

2.1. Lotus leaf

Lotus leaves, *Nelumbo nucifera*, owe their self-cleaning ability to superhydrophobicity. Neinhuis and Barthlott [1] obtained scanning electron microscopy (SEM) images for several water-repellent plants and reported the micromorphological characteristics of 200 species. They demonstrated that the epidermal (i.e. outermost) cells of the lotus leaves form papillae, which act as microstructure roughness. The papillae are superimposed by a very dense layer of epicuticular waxes (wax crystals), also referred to as hair-like structures [12] or nanostructure roughness [13]. Fig. 1 shows different degrees of magnification of lotus leaves using SEM images from one to 10^6 times. Epicuticular waxes themselves have hydrophobic properties, which together with micro- and nanostructure roughness, result in reduced contact area between water droplets and the leaf's surface. This combination results in static contact angles exceeding 150 degrees on lotus leaves. If the surface is tilted, even with a slight angle, water droplets begin to roll off the leaves, and so collect and remove dirt from the surface demonstrating the self-cleaning effect (see Fig. 2). Note that because of the micro- and nanostructure roughness, the contact area between dirt particles and the leaf's surface is dramatically reduced. Thus, the adhesion between the particles and the surface can be lower than that between the particles and the droplets, facilitating particle removal. Accordingly, the lotus leaf is a symbol of purity in some Asian religions [1].

To demonstrate the importance of nanoscale wax crystals on the lotus effect, Cheng et al. [12] altered the surface structure of a lotus leaf without affecting the chemical composition. They heated the leaf to 150 °C (thermal annealing) to melt the waxy crystals, leaving the microstructures intact, and found a decrease in the static contact angle of the treated leaf. Neinhuis and Barthlott [1] reported that the lotus effect tends to keep the leaves dry, which helps to protect the plant against pathogens such as fungi by denying these parasitic organisms the moisture that they require to germinate. Moreover,

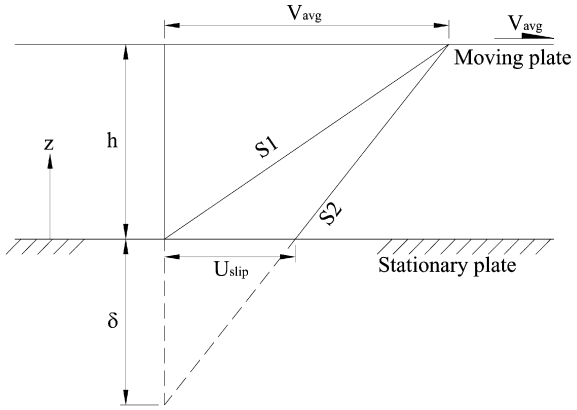

Fig. 3. Schematic diagram of velocity profiles between fixed and moving plates in case of slip and no slip at fluid–solid interface. From Samaha et al. [18].

since CO_2 diffuses 10^4 times faster in air than in water, the water-repellent leaves allow CO_2 to be more easily absorbed, ensuring an adequate supply of CO_2 for photosynthesis, even in habitats with high air humidity [1].

2.2. Slip flow and drag reduction

When a superhydrophobic surface is submersed in water, it generates slip flow, which reduces the skin-friction drag exerted on the surface. Drag is the force produced by a fluid to resist the relative motion of a solid [17]. A tremendous amount of fuel is consumed each year both by air and water vehicles and by gas and liquid transmission through pipelines in order to overcome drag [17]. Drag force can be classified into two main categories, form (pressure) drag and skin-friction drag. The latter, which depends on fluid viscosity, strain rate (velocity gradient), and surface area, is the subject of this section. The multiplication of fluid viscosity and velocity gradient gives the shear stress. Fig. 3 shows the Couette flow between two plates having a gap, h, in the normal direction, z. The upper plate is moving with velocity V_{avg} and the lower one is stationary. The lower plate can have a no-slip (sticky) or a slip boundary condition. In the case of no-slip boundary, the slope of the velocity gradient (line S1) is higher than that of slip flow (line S2), which leads to a higher shear stress.

Generally, slip is defined as a fluid dynamics condition in which there exists a relative tangential velocity between the solid surface and the fluid immediately adjacent to the surface. Slip can be encountered in several situations. For example, for gas flow, slip could occur if the mean free path of the gas (i.e. the average distance traveled by molecules between collisions) is comparable to the characteristic dimensions of the flow [19]. As mentioned earlier, a superhydrophobic surface entraps air in its pore space producing two different interfaces. One is the aforementioned air–water interface on which the water slips, and the other is the solid–water interface to which the water sticks. The average slip over the entire surface is often referred to as "effective slip" [20]. The air–water interface area is characterized by the gas fraction, the ratio of the area of the air–water interface to the total surface area. The gas fraction is the main parameter that determines the static contact angle [21], which characterizes the hydrophobicity of the surface. Callies et al. [22] experimentally demonstrated that as gas fraction increases, static contact angle increases. Furthermore, the gas fraction has an impact on the so-called "slip length, δ" [23]. According to Navier's model [24], the magnitude of the slip velocity is proportional to the magnitude of the strain rate. The slip length is the proportionality constant as shown in Fig. 3. Thus, the slip length can be calculated from the following equation:

$$\delta = \frac{U_{slip}}{\frac{\partial u}{\partial y}\big|_{wall}} \tag{1}$$

where U_{slip} is the area-weighted average slip velocity at the superhydrophobic wall, u is the streamwise velocity, and y is the normal direction.

Several studies have demonstrated the effect of the gas fraction on the slip length [23,25–36]. Some of these studies showed that for laminar flow, slip length increases as gas fraction increases (Fig. 4) and hence from Eq. (1), velocity gradient decreases (i.e. less drag). This figure shows the calculated and the measured slip lengths (normalized by the pitch; the distance between two posts) versus gas fraction for ordered microposts on a superhydrophobic surface. A closer view at gas fractions below 0.6 and above 0.85 is given in the insets for better illustration. From the figure, it is obvious that when the gas fraction, ϕ_g, is less than 0.4, the slip length is proportional to ϕ_g^2. On the other hand, if the gas fraction is higher than 0.7, the slip length is proportional to $1/\sqrt{\phi_g}$. Within the range $0.4 < \phi_g < 0.7$, interpolation is utilized. The above mathematical proportionalities are derived and validated by Ybert et al. [30]. The drag reduction also increases as gas fraction increases, as shown in Fig. 5. The figure includes both experimental and numerical results for a microchannel with a microridged superhydrophobic wall.

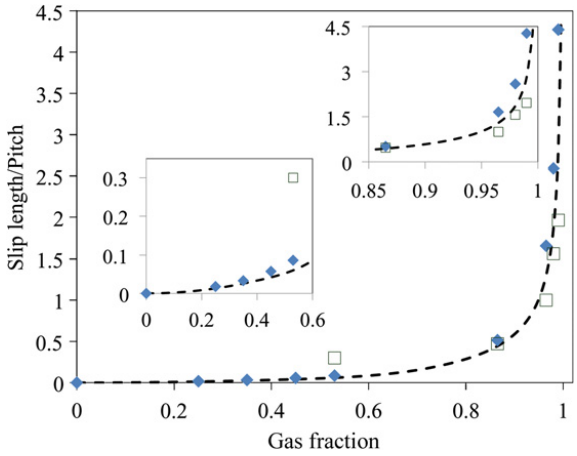

Fig. 4. Slip length vs. gas fraction obtained for laminar flow over ordered microposts superhydrophobic surface. Experimental data of Lee et al. [23] (open squares), theory of Ybert et al. [30] (dashed line), and Samaha et al. [36] (solid diamonds).

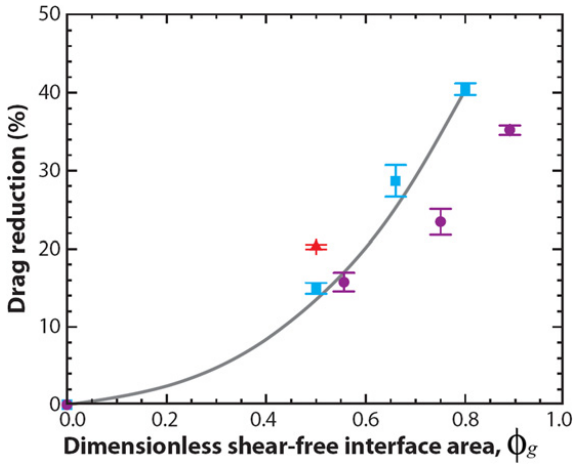

Fig. 5. Average drag reduction as a function of dimensionless shear-free area, gas fraction. 30 μm wide microridges spaced 30 μm apart (triangles), 20 μm wide microridges spaced 20 μm apart (squares), and 30 μm square microposts spaced 30 μm apart (circles). Numerical results for 20 μm wide microridges spaced 20 μm apart (gray line). From Rothstein [3].

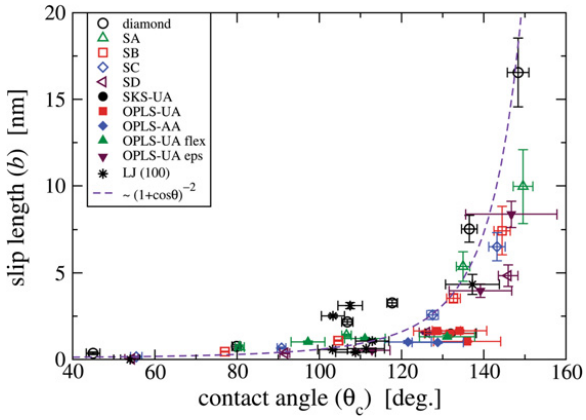

Fig. 6. Slip length of water as a function of contact angle on various smooth surfaces. The results are obtained by Huang et al. [37] using molecular dynamics simulations.

The slip boundary condition has been studied theoretically using molecular dynamics (MD) simulations [37–39]. These simulations convincingly demonstrated that the greater the hydrophobicity of the surface, the larger the slip length will be. Fig. 6 shows computed slip length using MD simulations versus contact angle θ_c for different surfaces [37,38]. The numerical results are curve-fitted using the relation $b \propto (1 + \cos\theta_c)^{-2}$, where b is the slip length. Static contact angles clearly are a measure of the degree of hydrophobicity of a solid surface.

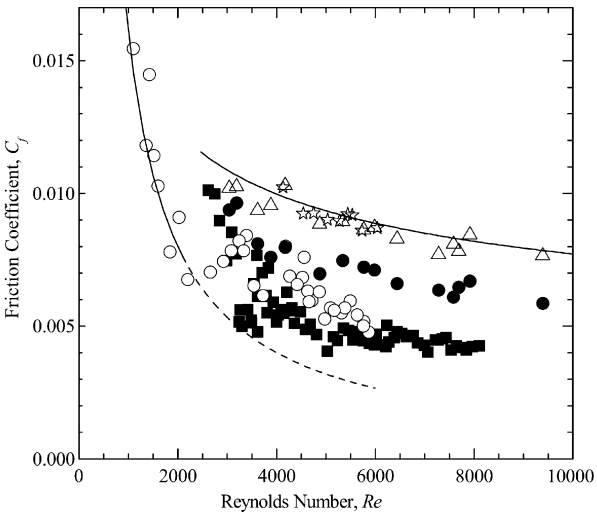

Fig. 7. Skin-friction coefficient vs. Reynolds number. Microchannel with smooth surfaces (open triangles and open stars), with single superhydrophobic wall (solid circles), and with two superhydrophobic walls (open circles and solid squares). The theoretical predictions of the friction coefficient for a smooth channel are also shown (—). From Daniello et al. [32].

Other studies show that for turbulent flows, increasing the shear-free area (i.e. increasing the gas fraction) results in an increase in the slip velocity and drag reduction [32,33]. Fig. 7 shows that skin-friction coefficient decreases by utilizing a superhydrophobic surface on one or both walls of a microchannel for a range of Reynolds numbers covering both the laminar- and turbulent-flow regimes. On the contrary, this was not observed in the work of Woolford et al. [35], who demonstrated that in a turbulent-flow regime, streamwise ridges (i.e. flow direction is parallel to microridges structure) can cause drag reduction, while spanwise ridges (i.e. flow direction is perpendicular to microridges structure) can increase the drag.

Obviously, the influence of the microstructural parameters of a superhydrophobic surface on its performance requires further exploration. Such surfaces could be utilized as a passive method of flow control and may potentially become a viable alternative to the more complex and energy consuming active or reactive methods of flow control such as wall suction/blowing [17].

3. Microfabrication of superhydrophobic surfaces

3.1. Ordered microstructures

Most engineered superhydrophobic surfaces are made up of microposts or microridges (Fig. 8). The microstructure of these surfaces strongly affects the gas fraction, slip length, and drag reduction, in addition to the stability of the air–water interface. For instance, in Fig. 8(a), as post diameter decreases for the same pitch (i.e. distance between two posts), the gas fraction increases, which leads to an increase in the drag reduction and slip length due to the increase of the free shear area (air–water interface area). However, increasing the gas fraction can jeopardize the stability of the interface. Criteria describing the stability based on roughness design were given by Bico et al. [40]. A similar conclusion could be drawn for microridges.

Superhydrophobic surfaces comprised of “nanograss” and “nanobricks” are reported by Henoch et al. [41] (see Fig. 9). The surface with nanograss is reported to yield a contact angle of nearly 180°, and is composed of posts with a diameter of 400 nm and a height of 7 μm spaced 1.25 μm from one another. The surface with nanobricks is peculiar because it can better resist the elevated hydrostatic pressures due to the effect of the entrapped air in its closed cells, which can help to increase the stability of the air–water interface, as will be discussed later in this paper. The size of each cell is 4 μm $\times$ 10 μm, the height of the cell walls is about 1 μm, and the thickness of the walls is 300 nm. A surface with a texture somewhat similar to that of the nanograss structure is studied by Choi and Kim [42]. These authors present slip length of their surface in comparison to that of a smooth one. Lee and Kim [4] demonstrated that the slip length can be maximized by superimposing a nanostructure onto a microfabricated structure, similar to the case of wax crystals on papillae of the lotus leaves as shown in Fig. 10. These authors demonstrated that the contact angle for their surfaces can approach 180°. In addition, they showed that the slip length can be increased up to 400 μm.

3.2. Surfaces with engineered roughness

There are limitations for commercializing microfabricated surfaces such as those shown in Figs. 8–10. Production cost is probably the most prohibitive issue with microfabricated surfaces. Recent studies, however, have shown that there are alternative methods for engineering superhydrophobic surfaces more cost-effectively. As discussed by Emami et al. [5], one

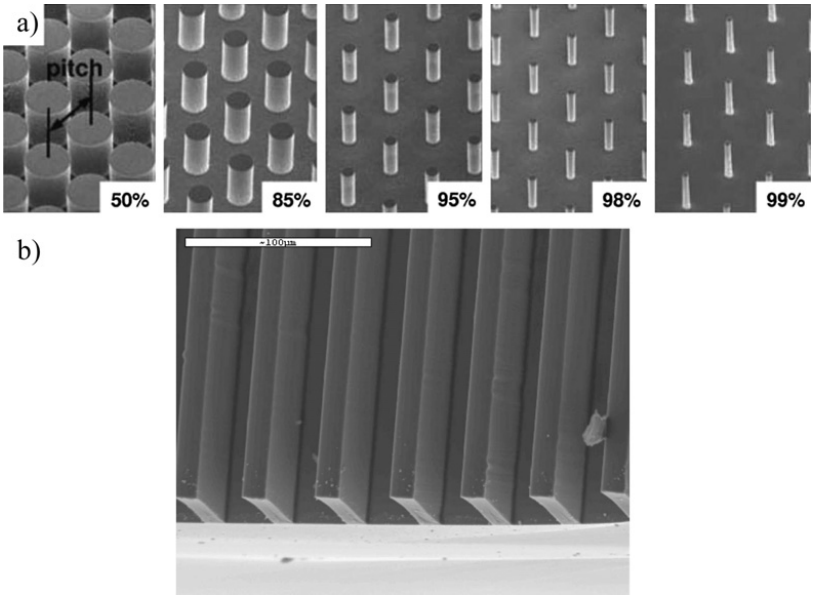

Fig. 8. (a) Scanning electron microscopy (SEM) images of post patterns with 50 μm pitch for the displayed inset gas fractions. From Lee et al. [23]; (b) Image of microfabricated surface with microridges. The width of the cavities and ridges are 30 and 10 μm, respectively. The depth of the rib is 15 μm. From Maynes et al. [29].

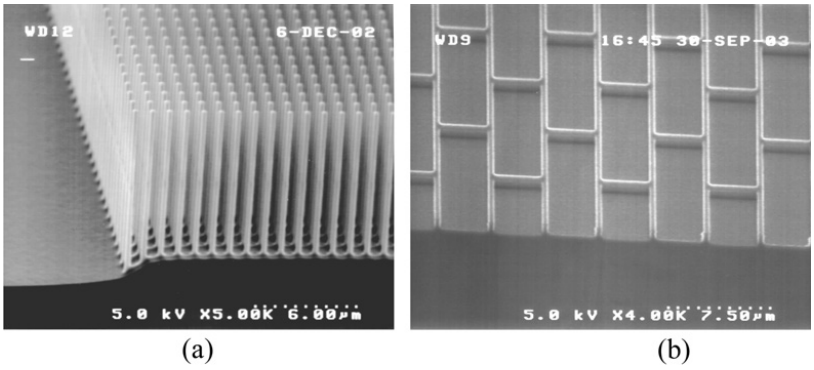

Fig. 9. (a) SEM image of silicon nanograss; (b) SEM image of silicon nanobricks. From Henoch et al. [41].

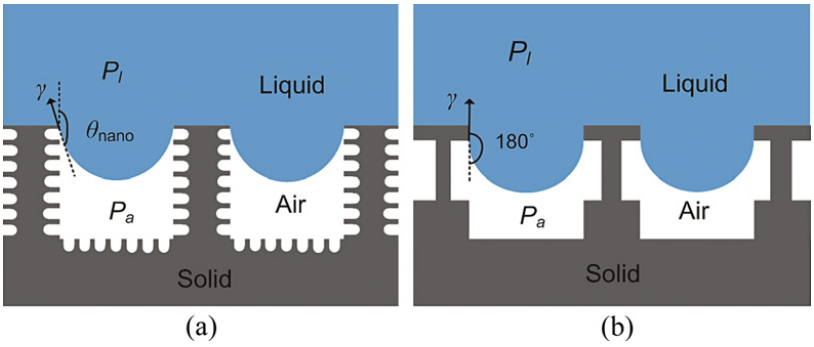

Fig. 10. (a) Nanostructures on the sidewall; (b) Re-entrant structure. From Lee and Kim [4].

can produce a superhydrophobic surface by randomly depositing hydrophobic particles (e.g. aerogel) on a substrate (see also [6,7]). Fig. 11(a) shows an SEM image of aerogel powders synthesized using sodium silicate and deposited on a substrate. The static contact angle is measured for a coated surface with aerogel powders to show its superhydrophobicity. Fig. 11(b) shows that the contact angle for such a surface is 150°.

Samaha et al. [36] simulated the performance of superhydrophobic surfaces having idealized random roughness (posts or particles) and compare their results with those of surfaces manufactured via microfabrication. Their numerical simulations indicated that the gas fraction has a significant impact on the characteristics of a superhydrophobic surface, as it affects the slip length and therefore the skin-friction coefficient. As can be seen in Fig. 12, the friction coefficient decreases with

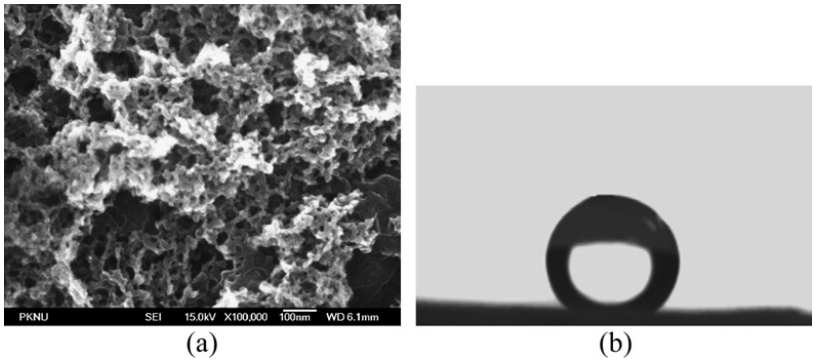

Fig. 11. (a) SEM image of aerogel powders synthesized using sodium silicate; (b) Water droplet placed on surface of glass substrate coated with aerogel powder. The contact angle is 150°. From Bhagat et al. [7].

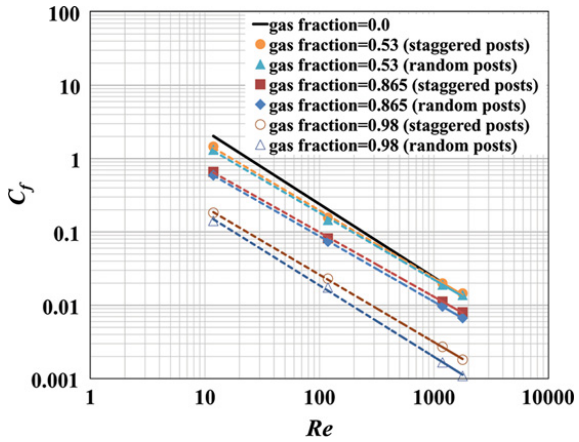

Fig. 12. Skin-friction coefficient versus Reynolds number (Moody diagram) for different gas fractions. From Samaha et al. [36].

increasing gas fraction for surfaces with staggered posts and randomly distributed posts. In addition, the difference between the skin-friction coefficient of the random posts and that of the staggered posts increases by increasing the gas fraction. Thus, the surface with randomly distributed posts possesses better drag reduction than in the case of staggered, distributed posts.

Electrospinning is another cost-effective fabrication technique that can be used to produce superhydrophobic surfaces with fibrous microstructure. This technique can be used to deposit micro- and/or nanotextured coatings by spinning hydrophobic polymers onto substrates of arbitrary geometries [8–11]. Conventionally, electrospinning is performed by applying a large DC-potential between the electrospinning source (typically a hypodermic syringe) and the substrate, resulting in nonwoven fiber mats with randomly oriented fibers [43]. The random orientation of the fibers is the result of the inherent electrostatic instability of the charged jet as it travels from the spinneret to the collector. This instability can be reduced by using a DC-biased AC potential that induces short segments of alternating polarity, thereby reducing the magnitude of the destabilizing force on the fiber (see Fig. 14(a)) [43].

Fig. 14 shows SEM images of fiber mats produced via DC-electrospinning and DC-biased AC-electrospinning. As shown in Fig. 14, DC-biased AC-electrospinning provides a better control over the microstructure of deposited fibrous mats. The insert in Fig. 14(b) shows a water droplet on the coating with a static contact angle of 157 degrees, proving superhydrophobicity even in the case of random fiber deposit [11]. This is because, similar to the case of microfabricated surfaces, such superhydrophobic fibrous coatings can provide the porosity that is necessary to entrap air when the surface is immersed in water. As expected, when water flows over such a surface, a reduction in the skin friction is observed [18].

Samaha et al. [18] measured drag reduction and slip length for such a coating. They used a rheometer made by the Anton Paar Corporation (model Physica MCR 301) equipped with two parallel rotating discs separated by a small fluid-filled gap. One disc is stationary and attached to a water cooling system for temperature control. The second disc rotates at a prescribed speed and is connected to an air bearing to minimize friction. Compressed air at about 6 atm supports the bearing. The rotating disc is connected to a torque–speed measuring system used to calculate the shear stress developed by the fluid, and the measured rotational speed is used to calculate the strain rate. Equations governing this motion are derived to calculate both drag reduction and slip length from the measured stress–strain rate relation. As will be displayed later in this paper, the results of generated drag reduction by the spun-fiber coating are shown in Fig. 28, which confirm the superhydrophobicity of this cost-effective fabricated coating. In addition, the slip length results attained using this fabrication approach are comparable to those obtained using ordered micro/nanostructure surfaces [4].

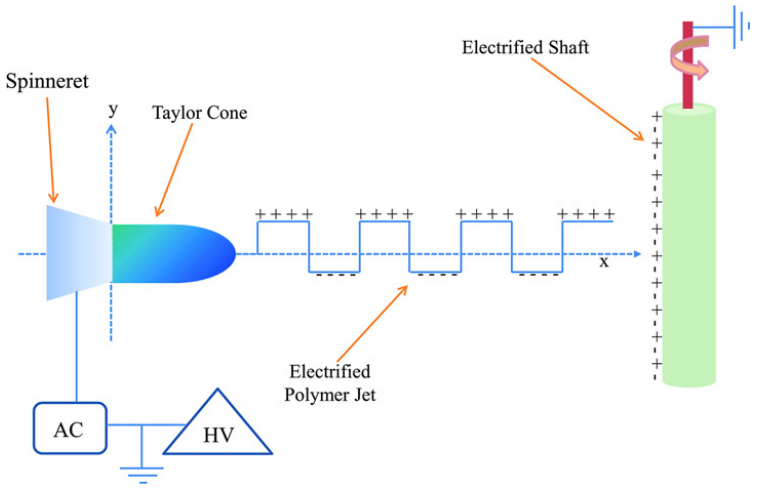

Fig. 13. Schematic illustration of electrified polymer jet during DC-biased AC-electrospinning. From Ochanda et al. [11].

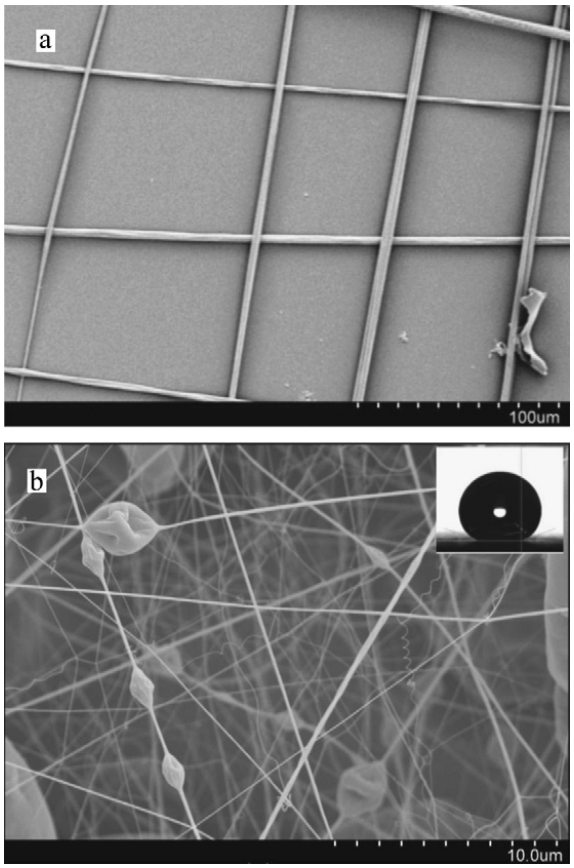

Fig. 14. SEM images of 18% weight polystyrene fibers with 1% weight fluoro-elastomer. (a) Grid-like structure of a mono-layer; (b) Several layers of fibers show random orientation. Upper right insert in (b) shows a water droplet on top of this particular coating. The figure adapted from Samaha et al. [18].

It is worth mentioning that the morphology of the fibers influences the hydrophobicity of the surface. For example, fiber diameter can affect the static contact angle of the coating, as shown in Fig. 15. This figure shows that contact angle decreases with increasing fiber diameter. However, one should note that since other microstructural parameters of the surfaces reported in this figure were not kept constant while fiber diameter was varied, changes in the fiber diameter could have affected the porosity of the mat. Therefore, in the absence of more microstructural information, one should refrain from directly relating fiber diameter to contact angle. The figure shows the results for produced beaded and bead-free fibers. Beaded fibers or polymeric microdroplets could have appeared during electrospinning if the polymeric fluid did not have adequate viscoelasticity and conductivity, which leads to the Rayleigh instability, i.e., domination of surface tension during the process that tends to break the liquid into droplets.

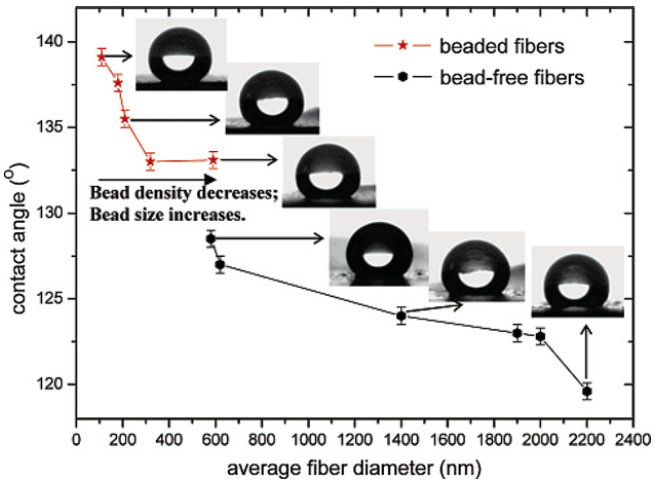

Fig. 15. Effect of fiber's diameter on static contact angle. From Ma et al. [8].

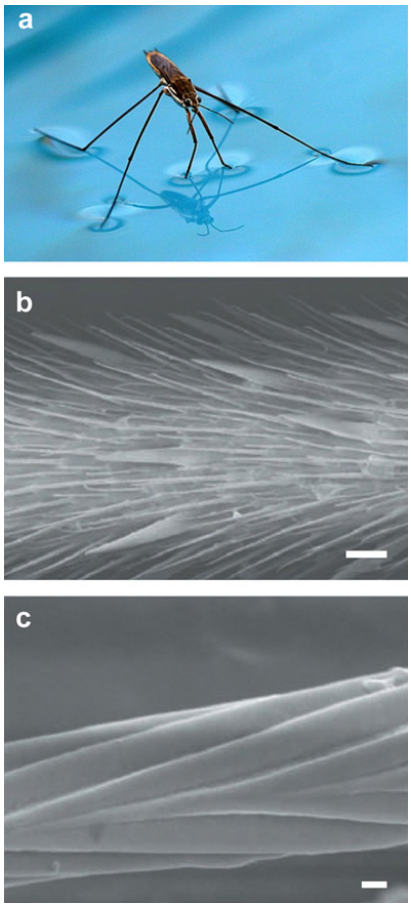

Fig. 16. (a) Water strider stands on water. From website [44]; (b) SEM image of water strider's leg showing hydrophobic microsetae, scale bar 20 μm; (c) Higher magnification of single hair showing nanogrooves, scale bar 0.2 μm. (b) and (c) from Gao and Jiang [2].

4. Stability of air–water interface under elevated pressures: water striders

4.1. Walking on water

Water striders, *Gerris remigis*, possess a very rare trait that allows them to walk on water. Water striders owe this ability to the hydrophobic waxy microhairs covering their legs, microsetae, which are superimposed with nanogrooves [2] as shown in Fig. 16.

Air is entrapped between the micro- and nanostructured hairs, making their legs water repellent. Gao and Jiang [2] used a very sensitive balance system to determine the required force for a single leg to be sunk. They demonstrate that the

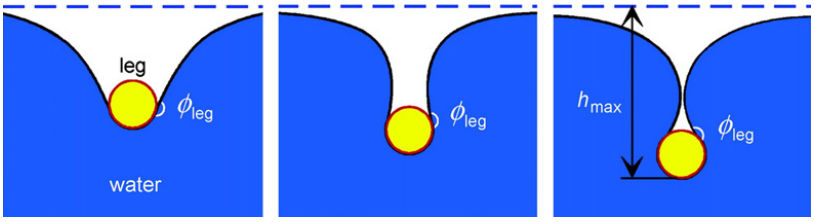

Fig. 17. Transects of the water surface for the leg contacting the water to different depths until the maximum depth h_{max} is reached before piercing the water surface. From Feng et al. [45].

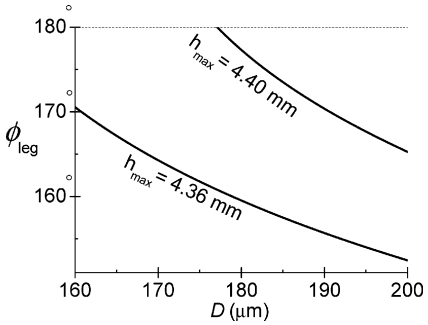

Fig. 18. Contact angle of the leg and dimple depth. Dependence of the contact angle on the diameter of the leg in order to form the maximal dimple with depth $h_{max} = 4.38 \pm 0.02$ mm. From Feng et al. [45].

buoyancy force is 15 times the total body weight. Furthermore, the volume of the displaced water caused by immersing a single leg is 300 times that of the leg itself. Feng et al. [45] have modeled the ultra-hydrophobicity of a water strider's leg by providing a theoretical analysis, coupled with experimental measurements, to determine how deep the leg can reach before piercing the water surface as shown in Fig. 17. They demonstrated that the maximum depth, h_{max}, depends on the diameter, D, and the contact angle of the leg, ϕ_{leg}. Their results are shown in Fig. 18. It can be seen that for the actual diameter range (140–180 μm) and for the measured maximum depth ($h_{max} = 4.38 \pm 0.02$ mm), the contact angle should be at least 168°, i.e. highly water-repellent. Such a high contact angle allows water striders to stand on water, even in the presence of rain or water currents.

Water striders have the ability to flit about quickly, where the propulsive forces on the insect are generated by a combination of form drag and curvature forces [46]. According to Hu et al. [47], water striders use their superhydrophobic legs to create hemispherical vortices, which transfer the momentum beneath the water surface that develops enough hydrodynamic force to propel the insect, similar to using oars to move a boat. Several water-walking machines are inspired by water striders and other insects [48]. The devices are designed and constructed to precisely mimic the natural locomotion mechanisms of the insects.

Water striders are natural predators of spiders and other insects that fall onto the water surface. They use their front legs to sense ripples developed by a falling prey [49] and grab onto it. The superhydrophobicity of a water strider's legs is its survival mechanism, allowing it to float, run on water, and sense prey for feeding. It is worth mentioning that other species such as spiders and several other insects are covered with hydrophobic hairs similar to those of water strider, but for a different purpose. The entrapped air (plastron) is utilized by spiders and similar species for underwater breathing. The mechanics of plastron respiration are demonstrated by Flynn and Bush [50].

4.2. Stability of air–water interface under hydrostatic pressure

The air–water interface developed due to superhydrophobicity is the surface that supports a water strider's weight. A similar force can be exerted on the air–water interface formed over a submerged superhydrophobic surface by the column of water above the surface. If the pressure is high enough, water will penetrate into the pores on the surface and replace the air, i.e. transition from the non-wetted state (Cassie state) to the wetted state (Wenzel state). This transition is interpreted by two approaches: one based on minimizing the thermodynamic free energy [51,52], and the other using a balance of forces across the interface [53–55]. Lee and Kim [4] used the latter to develop an equation to determine the maximum allowable hydrostatic pressure (critical pressure) in terms of the surface microstructure for aligned or staggered arrangement of posts as shown in the following equation:

$$P_{max}\phi_g \leqslant \frac{-2\gamma\sqrt{\pi(1-\phi_g)}\cos\theta}{L} \tag{2}$$

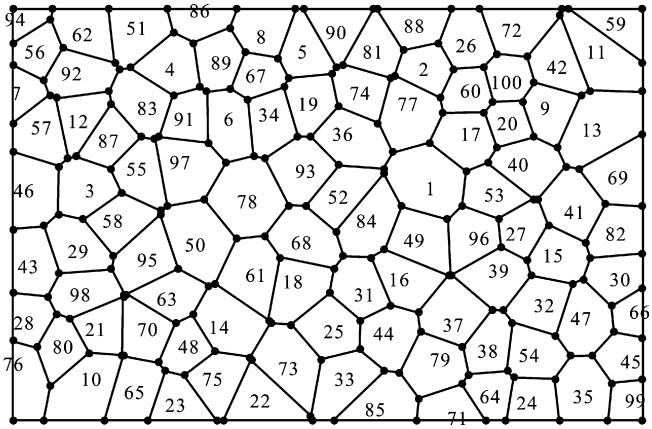

Fig. 19. Voronoi diagram obtained for randomly distributed posts. The numbers shown in this figure refer to the posts and their locations. From Samaha et al. [36].

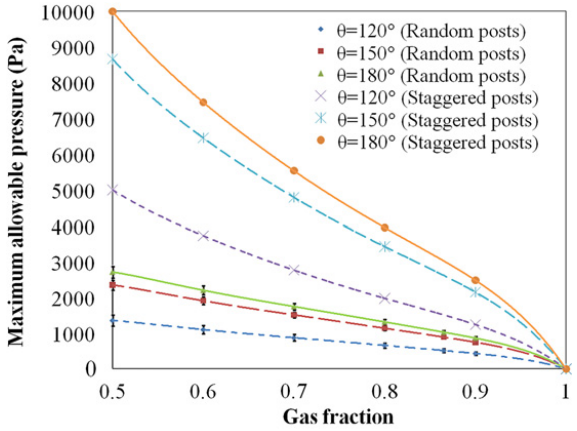

Fig. 20. Maximum allowable pressure as a function of gas fraction and contact angle for both random and staggered posts. From Samaha et al. [36].

where P_{max} is the critical pressure, the pressure above which the system departs from the Cassie state, ϕ_g is the gas fraction, γ is the surface tension of the liquid (72×10^{-3} N/m in case of water), θ is the contact angle, and L is the pitch (distance between two posts).

Samaha et al. [36] utilized a Voronoi diagram [56] to determine the local gas fraction and the maximum pitch for superhydrophobic surfaces made up of randomly distributed posts. This information is used in Eq. (2) to determine the maximum allowable hydrostatic pressure, which corresponds to the post that has the maximum local gas fraction. In a Voronoi diagram, the superhydrophobic surface is divided into cells, as shown in Fig. 19. Each post has a single surrounding Voronoi cell consisting of all points on the surface that are closer to that post than to any other post. The sides of a Voronoi cell are the locations of the points on the surface that are equidistant from the two nearest posts. The Voronoi nodes are the points equidistant from three (or more) posts. Note that a Voronoi diagram provides a *rational* tool to compute the *local* gas fraction and maximum pitch when dealing with random posts.

The maximum allowable pressures for surfaces comprised of random and staggered posts are compared with each other in Fig. 20. It can be seen that the maximum allowable pressure decreases dramatically when the posts are arranged randomly. The results of this figure indicate that superhydrophobic surfaces with random roughness are more susceptible to failure under hydrostatic pressures. Therefore, although random posts can result in a better drag reduction (see Fig. 12), they are more likely to fail under elevated pressures.

Emami et al. [5] conducted a similar study in 3-D space. In particular, they simulated the stability of air–water interface formed on granular superhydrophobic coatings comprised of randomly distributed spherical aerogel particles in comparison to the ordered distributed ones. These authors also conducted a series of 3-D full-morphology (FM) numerical simulations and analytical expressions to predict the critical pressure (pressure beyond which the surface departs from the Cassie state) against solid volume fraction of their granular porous coatings, as shown in Fig. 21. This figure shows that the air–water interface can sustain more pressure as the solid volume fraction increases. Moreover, the surface with random particles is more susceptible to failure under hydrostatic pressure, as expected.

Emami et al. [57] developed a mathematical framework to calculate the exact shape of the air–water interface, and so predict the stability of the air–water interface on superhydrophobic surfaces made up of randomly distributed posts of different diameters, heights, and materials. This was accomplished by using the Young–Laplace equation to derive a second-

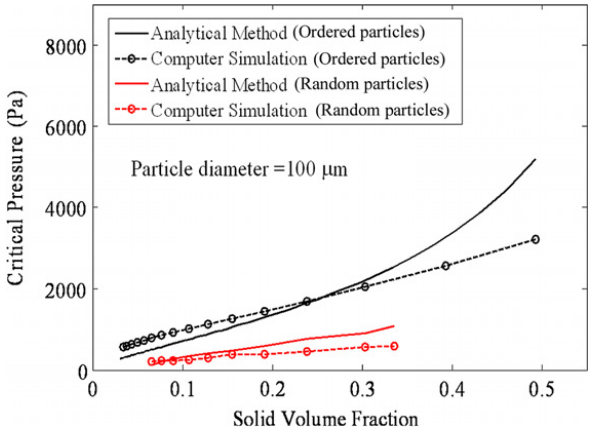

Fig. 21. Numerically and analytically calculated critical pressure against solid volume of fraction for ordered aerogel particles and random ones. Figure adapted from Emami et al. [5].

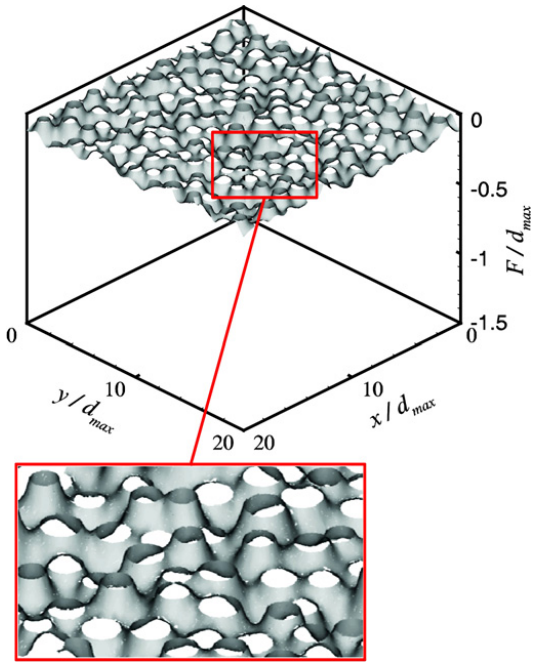

Fig. 22. Calculated meniscus surfaces for superhydrophobic surface with randomly distributed posts of random diameters and heights at $P = 3400$ Pa. d_{max} refers to maximum post's diameter. x, y, and F are Cartesian coordinates. Figure adapted from Emami et al. [57].

order partial differential equation that was solved numerically via finite element method. Fig. 22 shows an example of an air–water interface formed over a superhydrophobic surface comprised of randomly distributed posts with diameters ranging between 8 to 12 μm, and heights ranging between 50 to 51 μm, leading to a gas fraction of 65%. The deflection of the interface under a hydrostatic pressure of 3400 Pa can be seen. The posts are assumed to be made of a material with a contact angle of 120°.

To study the stability of the air–water interface formed over superhydrophobic coatings composed of randomly oriented nanofibers, Bucher et al. [58] conducted a series of FM simulations in 3-D virtual domains resembling the internal microstructure of electrospun fiber mats.

Fig. 23 shows an example of the FM simulations for two different hydrostatic pressures conducted by Bucher et al. The solid volume fraction and fiber diameter are 10% and 500 nm, respectively. It can be seen that, by increasing the pressure, the water (red color) fills a greater fraction of the pore space. Fig. 24 shows the critical pressure as a function of the coating's morphology for bimodal (composed of two different fiber diameters) fibrous media with random fiber orientations in terms of solid volume fraction and fine fiber diameter, d_f. It can be seen that critical pressure increases with increasing solid volume fraction or fine fiber diameter, when other microstructural parameters are held constant.

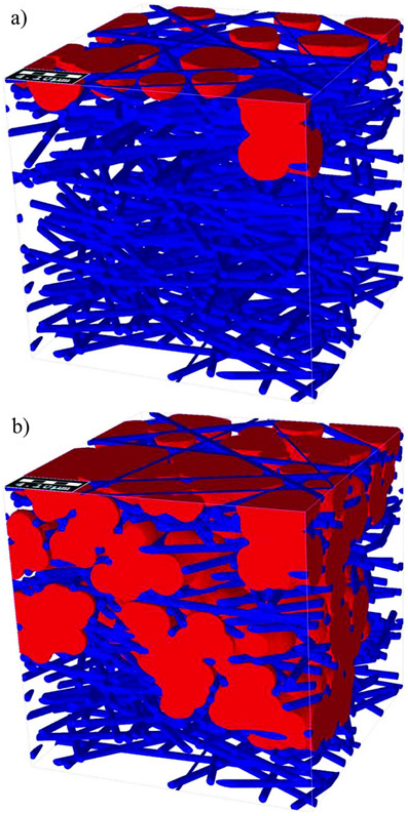

Fig. 23. A visualization of two stages of water intrusion into a unimodal fibrous structure with random in-plane fiber orientation, using the full-morphology method. Corresponding pressures are: (a) 58.983 kPa; (b) 77.333 kPa. The non-wetting fluid (water) represented in the red region is made up of spheres fitted into the domain. Figure adapted from Bucher et al. [58].

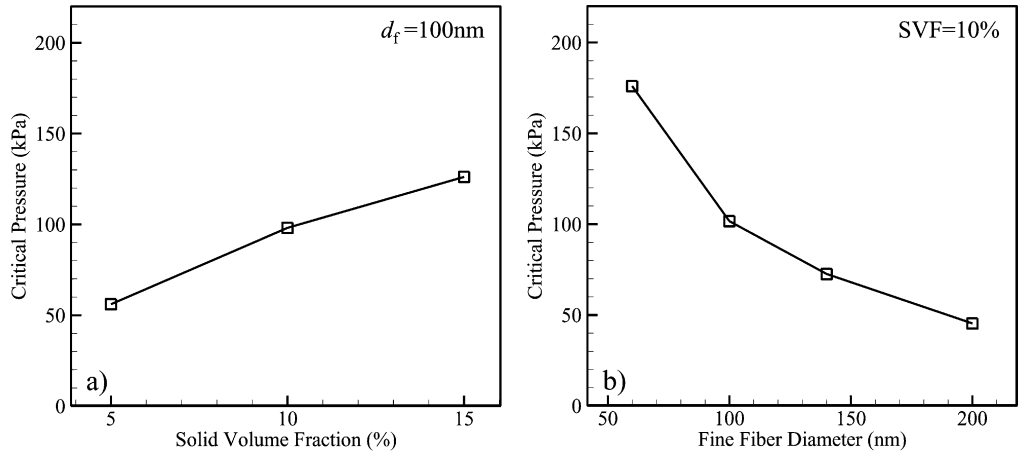

Fig. 24. Critical pressure predictions for layered, randomly oriented media compared against variations in one of four microstructural parameters: (a) solid volume fraction; (b) fiber diameter. For both (a) and (b), coarse-to-fine fiber diameter ratio (R_{cf}) = 5 and coarse number fraction (n_c) = 0.1. Figure adapted from Bucher et al. [58].

5. Longevity characterization of superhydrophobic coatings

Even when the air–water interface on a superhydrophobic surface is mechanically stable, the surface is likely to lose its entrapped air content over time. This is especially the case when the surface is submerged. This effect is believed to be due to the dissolution of air in water, and is expected to accelerate when the hydrostatic pressure is increased, as the solubility of air in water increases with pressure.

Bobji et al. [59] used an optical technique to measure how long superhydrophobic surfaces can entrap air underwater (surface longevity) by measuring the number of shiny spots that indicate an interface between air and water. Similar studies were performed using a laser beam to investigate the effect of the surface structure on the longevity [60]. Moreover, Poetes et al. [61] used a similar technique for the same test, but for different superhydrophobic coatings. Samaha et al. [18]

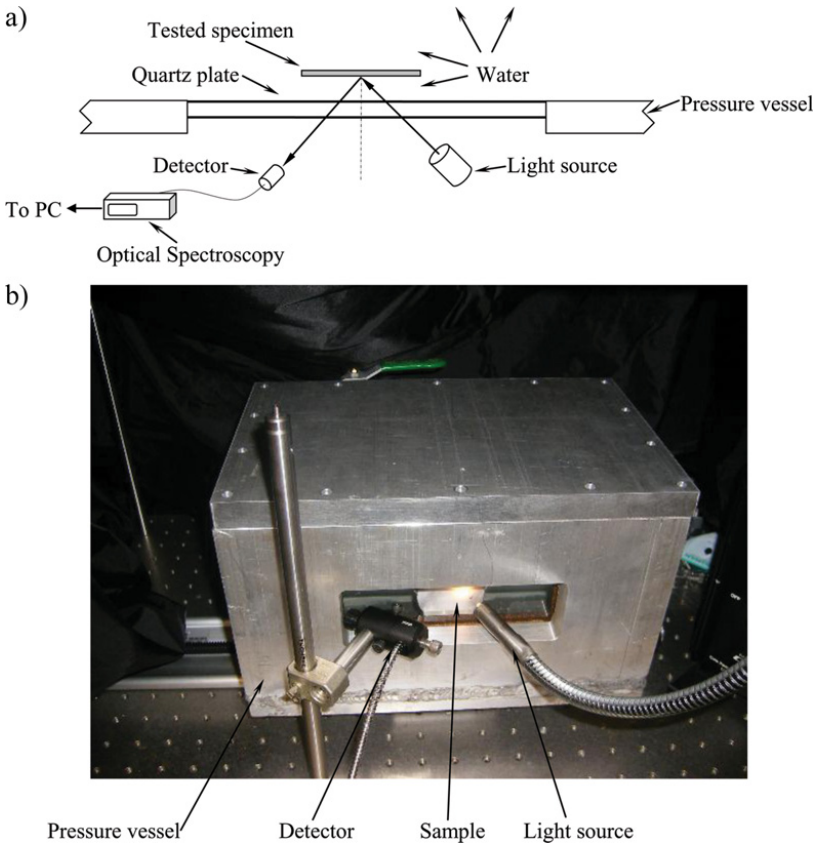

Fig. 25. (a) Schematic of the optical spectroscopy system. (b) Photograph of the pressure vessel. From Samaha et al. [18].

developed an optical technique to measure the longevity of submerged superhydrophobic coatings subjected to different environmental conditions. They used an optical spectroscopy system to quantify the intensity of reflected light in the visible range scattered from the surface (Fig. 25). The time-dependent light reflection intensity was measured at both a single wavelength and integrated over a range of wavelengths. Note that it is important to be able to measure the hydrophobicity of a surface *in situ* because the traditional contact angle or rheometer measurements may not necessarily represent the environment in which a surface may operate in practice. This includes, but is not limited to a broad range of time-dependent hydrostatic pressures (i.e. depths), and different degrees of salinity and/or air saturation. It is also of particular importance to be able to test a surface hydrophobicity over time under moving or still water. The optical spectroscopy system proposed by Samaha et al. can be utilized as a noninvasive method to measure surface hydrophobicity under the above conditions.

Fig. 26 shows the normalized reflected light intensity as a function of time and wavelength for an electrospun fibrous coating (discussed in Section 3.2) submerged in water for 166.5 h. The light intensity decreases with time at all wavelengths, which indicates a reduction in the volume of the entrapped air over time, and so the superhydrophobicity of the surface. Fig. 27 shows the normalized average reflected light intensity (the integral of the light intensity over all wavelengths divided by the wavelength range). The results shown in this figure were obtained under atmospheric pressure. It can be seen from Fig. 27 that the average reflected light intensity decreased by about 27% after 166.5 h of continuous submersion in water.

For validation, Samaha et al. [18] compared the results obtained from the optical system with drag-reduction data using the rheometer discussed in Section 3.2. Fig. 28 shows the measured drag reduction versus strain rate for the fibrous coating before and after immersing the coated sample in water. The results indicate that the coating is still capable of reducing the drag after 166.5 hours of immersion in water under atmospheric pressure. The average drag reduction was decreased by about 31% with respect to that of the fresh specimen, which is close to that reduction in light intensity using the optical system.

For further validation static contact angles and contact-angle hysteresis are measured for the same sample using a ramé-hart goniometer (model number 100-25-A). The measurements indicate that the results of the light-scattering surface characterization technique correlate strongly with both contact-angle and drag-reduction measurements. The contact-angle hysteresis measurements further validate the light-scattering method. Low-contact-angle hysteresis was observed for the fresh superhydrophobic sample. However, more noticeable hysteresis was seen for aged specimens. These results are consistent with the observations of other researchers [21,62–64]. *In situ* characterization of submerged hydrophobic surfaces using optical light scattering represents a new and useful tool for real-time estimation of hydrophobicity and drag reduction.

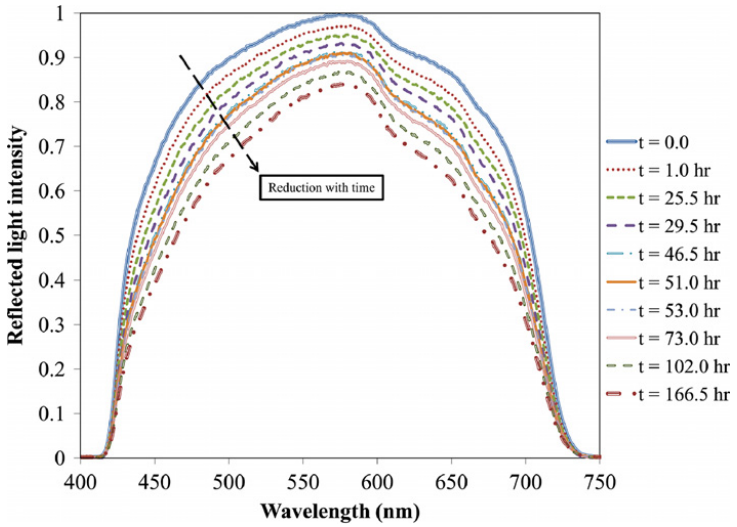

Fig. 26. Reduction in reflected light intensity with time for a spun-fiber sample. Measurements are taken for the entire visible-light spectrum. From Samaha et al. [18].

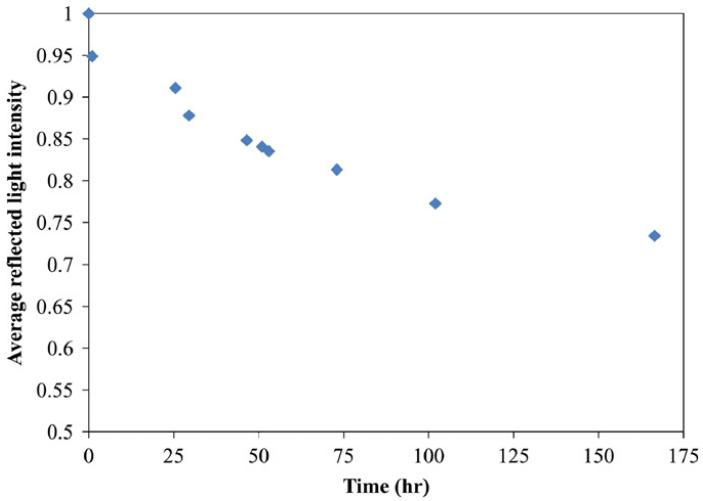

Fig. 27. Average reflected light intensity reduction with time for a spun-fiber sample. From Samaha et al. [18].

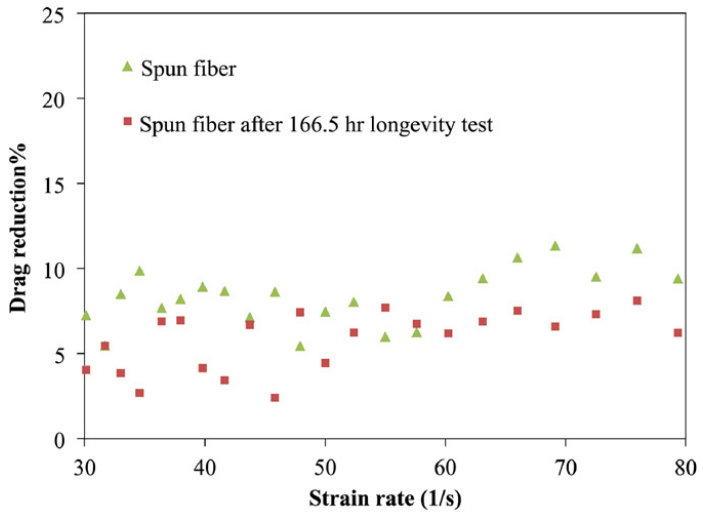

Fig. 28. Drag reduction versus strain rate. From Samaha et al. [18].

6. Future outlook

Superhydrophobic surfaces were demonstrated by several experimental, numerical, and analytical studies to reduce drag for both laminar and turbulent flows. This reinforces the optimistic view that these surfaces could be used for drag-reduction purposes, especially in marine environments. For example, it is well known that submarines consume a large amount of fuel to overcome the skin-friction drag produced on their bodies. Intensive flow-control studies have been performed to develop different active, reactive, and passive methods to reduce this drag force. Superhydrophobic coatings are aimed to be utilized as a passive method and may potentially become a viable alternative to the more complex and energy consuming active or reactive flow-control techniques such as wall suction/blowing. However, there are still significant issues that need to be resolved in order for the manufacturing of such coatings to be feasible. First of all, the microstructure of the coating should be strong enough to sustain the developed shear stress without erosion especially for turbulent flow. Secondly, the coating should keep its hydrophobicity for an acceptable time frame (reasonable longevity). Moreover, if the coating becomes hydrophilic, an infield method should be developed to rejuvenate the surface to return it to its hydrophobic state. Third, the coating should be durable enough to sustain environmental conditions such as water salinity, depth, circulation, and biofouling. Finally, the fabrication processes should be extended from lab scale to large industrial scale applications. All of these issues require further research and development before superhydrophobic coatings could be utilized under realistic circumstances.

7. Conclusions

Currently, the lotus effect is employed to produce water-repellent paint and fabrics for self-cleaning or waterproofing applications. However, it also could be utilized for mobile submerged surfaces to generate drag reduction and slip flow, which takes place at the interface between the entrapped air and water. The performance of the surface is characterized by slip length, which is strongly affected by gas fraction, both for both laminar and turbulent flow.

For submerged superhydrophobic surfaces, this interface is stable against the transition from non-wetted (Cassie) state to wetted (Wenzel) state due to pressure. Several theoretical analyses and numerical simulations have been performed to estimate the critical pressure for different microstructures. The longevity of these surfaces can be measured via drag-reduction data using a rheometer or contact-angle measurements. Noninvasive optical measuring system can measure the real-time effects of such environments.

Microfabrication could be utilized to produce superhydrophobic surfaces with different properties. However, it cannot be applied to large-scale bodies with arbitrary shape. Simpler lower-cost fabrication techniques are being developed to meet those requirements. Experimental measurements and numerical simulations have been performed to characterize the hydrophobicity and longevity of these surfaces in comparison with those produced via ordered-microstructure processes. Both techniques are under research and development to produce the optimum surface that can produce high drag reduction and possesses reasonable longevity. Such coatings will ultimately be used on submarines, torpedoes, and naval ships for the purpose of reducing skin-friction drag in both the laminar and turbulent boundary layers surrounding these vessels when cruising in seawater.

Acknowledgements

This research is sponsored by the Defense Advanced Research Projects Agency (DARPA), contract number W91CRB-10-1-0003, technical sponsor Captain Christopher Warren, USN. The content of this paper does not necessarily reflect the position or the policy of the Government, and no official endorsement should be inferred.

References

[1] C. Neinhuis, W. Barthlott, Characterization and distribution of water-repellent, self-cleaning plant surfaces, Ann. Bot. 79 (1997) 667–677.
[2] X. Gao, L. Jiang, Water-repellent legs of water striders, Nature 432 (2004) 36.
[3] J.P. Rothstein, Slip on superhydrophobic surfaces, Annu. Rev. Fluid Mech. 42 (2010) 89–109.
[4] C. Lee, C.-J. Kim, Maximizing the giant slip on superhydrophobic microstructures by nanostructuring their sidewalls, Langmuir 25 (2009) 12812–12818.
[5] B. Emami, T.M. Bucher, H.V. Tafreshi, D. Pestov, M. Gad-el-Hak, G.C. Tepper, Simulation of meniscus stability in superhydrophobic granular surfaces under hydrostatic pressures, Colloids Surf. A 385 (2011) 95–103.
[6] H. Yang, Y. Deng, Preparation and physical properties of superhydrophobic papers, J. Colloid Interface Sci. 325 (2008) 588–593.
[7] S.D. Bhagat, Y.-H. Kim, K.-H. Suh, Y.-S. Ahn, J.-G. Yeo, J.-H. Han, Super hydrophobic silica aerogel powders with simultaneous surface modification, solvent exchange and sodium ion removal from hydrogels, Microporous Mesoporous Mater. 112 (2008) 504–509.
[8] M. Ma, Y. Mao, M. Gupta, K.K. Gleason, G.C. Rutledge, Superhydrophobic fabrics produced by electrospinning and chemical vapor deposition, Macromolecules 38 (2005) 9742–9748.
[9] A. Singh, L. Steely, H.R. Allcock, Poly[bis(2,2,2-trifluoroethoxy)phosphazene] superhydrophobic nanofibers, Langmuir 21 (2005) 11604–11607.
[10] M. Zhu, W. Zuo, H. Yu, W. Yang, Y. Chen, Superhydrophobic surface directly created by electrospinning based on hydrophilic material, J. Mater. Sci. 41 (2006) 3793–3797.
[11] F.O. Ochanda, M.A. Samaha, H.V. Tafreshi, G.C. Tepper, M. Gad-el-Hak, Fabrication of superhydrophobic fiber coatings by DC-biased AC-electrospinning, J. Appl. Polym. Sci. 123 (2012) 1112–1119.
[12] Y.T. Cheng, D.E. Rodak, C.A. Hayden, Effects of micro- and nano-structures on the self-cleaning behavior of lotus leaves, Nanotechnology 17 (2006) 1359–1362.

[13] K. Koch, B. Bhushan, Y.C. Jung, W. Barthlott, Fabrication of artificial Lotus leaves and significance of hierarchical structure for superhydrophobicity and low adhesion, Soft Matter 5 (2009) 1386–1393.
[14] http://www.flickr.com/photos/rachelyin/3203932476/.
[15] http://www.hk-phy.org/atomic_world/lotus/lotus01_e.html.
[16] http://www.thenakedscientists.com/HTML/articles/article/biomimeticsborrowingfrombiology/.
[17] M. Gad-el-Hak, Flow Control: Passive, Active, and Reactive Flow Management, Cambridge University Press, London, United Kingdom, 2000.
[18] M.A. Samaha, F.O. Ochanda, H.V. Tafreshi, G.C. Tepper, M. Gad-el-Hak, *In situ*, non-invasive characterization of superhydrophobic coatings, Rev. Sci. Instrum. 82 (2011) 045109.
[19] M. Gad-el-Hak, The fluid mechanics of microdevices – The Freeman scholar lecture, J. Fluids Eng. 121 (1999) 5–33.
[20] E. Lauga, M.P. Brenner, H.A. Stone, Microfluidics: the no-slip boundary condition, in: C. Tropea, A. Yarin, J. Foss (Eds.), Handbook of Experimental Fluid Dynamics, Springer, New York, 2007.
[21] J. Bico, C. Marzolin, D. Quéré, Pearl drops, Europhys. Lett. 47 (1999) 220–226.
[22] M. Callies, Y. Chen, F. Marty, A. Pépin, D. Quéré, Microfabricated textured surfaces for super-hydrophobicity investigations, Microelectron. Eng. 78–79 (2005) 100–105.
[23] C. Lee, C.-H. Choi, C.-J. Kim, Structured surfaces for giant liquid slip, Phys. Rev. Lett. 101 (2008) 064501.
[24] C.L.M.H. Navier, Memoire sur les lois du mouvement des fluides, Mem. Acad. R. Sci. Inst. France 6 (1823) 389–440.
[25] E. Lauga, H.A. Stone, Effective slip in pressure-driven Stokes flow, J. Fluid Mech. 489 (2003) 55–77.
[26] J. Ou, J.B. Perot, J.P. Rothstein, Laminar drag reduction in microchannels using ultrahydrophobic surfaces, Phys. Fluids 16 (2004) 4635–4643.
[27] J. Ou, J.P. Rothstein, Direct velocity measurements of the flow past drag-reducing ultrahydrophobic surfaces, Phys. Fluids 17 (2005) 103606.
[28] J. Davies, D. Maynes, B.W. Webb, B. Woolford, Laminar flow in a microchannel with superhydrophobic walls exhibiting transverse ribs, Phys. Fluids 18 (2006) 087110.
[29] D. Maynes, K. Jeffs, B. Woolford, B.W. Webb, Laminar flow in a microchannel with hydrophobic surface patterned microribs oriented parallel to the flow direction, Phys. Fluids 19 (2007) 093603.
[30] C. Ybert, C. Barentin, C.-B. Cécile, P. Joseph, L. Bocquet, Achieving large slip with superhydrophobic surfaces: Scaling laws for generic geometries, Phys. Fluids 19 (2007) 123601.
[31] Y.P. Cheng, C.J. Teo, B.C. Khoo, Microchannel flow with superhydrophobic surfaces: Effects of Reynolds number and pattern width to channel height ratio, Phys. Fluids 21 (2009) 122004.
[32] R. Daniello, N.E. Waterhouse, J.P. Rothstein, Turbulent drag reduction using superhydrophobic surfaces, Phys. Fluids 21 (2009) 085103.
[33] M. Martell, J.B. Perot, J.P. Rothstein, Direct numerical simulations of turbulent flows over superhydrophobic surfaces, J. Fluid Mech. 620 (2009) 31–41.
[34] A.M.J. Davis, E. Lauga, The friction of a mesh-like super-hydrophobic surface, Phys. Fluids 21 (2009) 113101.
[35] B. Woolford, J. Prince, D. Maynes, B.W. Webb, Particle image velocimetry characterization of turbulent channel flow with rib patterned superhydrophobic walls, Phys. Fluids 21 (2009) 085106.
[36] M.A. Samaha, H.V. Tafreshi, M. Gad-el-Hak, Modeling drag reduction and meniscus stability of superhydrophobic surfaces comprised of random roughness, Phys. Fluids 23 (2011) 012001.
[37] D. Huang, C. Sendner, D. Horinek, R. Netz, L. Bocquet, Water slippage versus contact angle: a quasiuniversal relationship, Phys. Rev. Lett. 101 (2008) 226101.
[38] C. Sendner, D. Horinek, L. Bocquet, R. Netz, Interfacial water at hydrophobic and hydrophilic surfaces: slip, viscosity, and diffusion, Langmuir 25 (2009) 10768–10781.
[39] L. Bocquet, E. Charlaix, Nanofluidics, from bulk to interfaces, Chem. Soc. Rev. 39 (2010) 1073–1095.
[40] J. Bico, U. Thiele, D. Quéré, Wetting of textured surfaces, Colloids Surf. A 206 (2002) 41–46.
[41] C. Henoch, T.N. Krupenkin, P. Kolodner, J.A. Taylor, M.S. Hodes, A.M. Lyons, C. Peguero, K. Breuer, Turbulent drag reduction using superhydrophobic surfaces, in: 3rd AIAA Flow Control Conference, San Francisco, California, 2006, p. 3192.
[42] C.-H. Choi, C.-J. Kim, Large slip of aqueous liquid flow over a nanoengineered superhydrophobic surface, Phys. Rev. Lett. 96 (2006) 066001.
[43] S. Sarkar, S. Deevi, G. Tepper, Biased AC electrospinning of aligned polymer nanofibers, Macromol. Rapid Commun. 28 (2007) 1034–1039.
[44] http://commons.wikimedia.org/wiki/File:Water-strider-1.jpg.
[45] X.-Q. Feng, X. Gao, Z. Wu, L. Jiang, Q.-S. Zheng, Superior water repellency of water strider legs with hierarchical structures: experiments and analysis, Langmuir 23 (2007) 4892–4896.
[46] J.W.M. Bush, D.L. Hu, Walking on water: biolocomotion at the interface, Annu. Rev. Fluid Mech. 38 (2006) 339–369.
[47] D.L. Hu, B. Chan, J.W.M. Bush, The hydrodynamics of water strider locomotion, Nature 424 (2003) 663–666.
[48] D.L. Hu, M. Prakash, B. Chan, J.W.M. Bush, Water-walking devices, Exp. Fluids 43 (2007) 769–778.
[49] G.M. Stonedahl, J.D. Lattin, The Gerridae or water striders of Oregon and Washington (Hemiptera:Heteroptera), Technical Bulletin 144, Oregon State University, 1982, pp. 1–36.
[50] M.R. Flynn, J.W.M. Bush, Underwater breathing: the mechanics of plastron respiration, J. Fluid Mech. 608 (2008) 275–296.
[51] N.A. Patankar, Transition between superhydrophobic states on rough surfaces, Langmuir 20 (2004) 7097–7102.
[52] L. Barbieri, E. Wagner, P. Hoffmann, Water wetting transition parameters of perfluorinated substrates with periodically distributed flat-top microscale obstacles, Langmuir 23 (2007) 1723–1734.
[53] C.W. Extrand, Criteria for ultralyophobic surfaces, Langmuir 20 (2004) 5013–5018.
[54] C.W. Extrand, Designing for optimum liquid repellency, Langmuir 22 (2006) 1711–1714.
[55] Q.S. Zheng, Y. Yu, Z.H. Zhao, Effects of hydraulic pressure on the stability and transition of wetting modes of superhydrophobic surfaces, Langmuir 21 (2005) 12207–12212.
[56] A. Okabe, B. Boots, K. Sugihara, S.N. Chiu, D.G. Kendall, Spatial Tessellations: Concepts and Applications of Voronoi Diagrams, second edition, John Wiley & Sons Ltd., Chichester, UK, 2000.
[57] B. Emami, H.V. Tafreshi, M. Gad-el-Hak, G.C. Tepper, Predicting shape and stability of air–water interface on superhydrophobic surfaces with randomly distributed, dissimilar posts, Appl. Phys. Lett. 98 (2011) 203106.
[58] T.M. Bucher, B. Emami, H.V. Tafreshi, M. Gad-el-Hak, G.C. Tepper, Modeling resistance of nanofibrous superhydrophobic coatings to hydrostatic pressures: the role of microstructure, Phys. Fluids, submitted for publication.
[59] M. Bobji, S.V. Kumar, A. Asthana, R.N. Govardhan, Underwater sustainability of the “Cassie” state of wetting, Langmuir 25 (2009) 12120–12126.
[60] M. Sakai, T. Yanagisawa, A. Nakajima, Y. Kameshima, K. Okada, Effect of surface structure on the sustainability of an air layer on superhydrophobic coatings in a water–ethanol mixture, Langmuir 25 (2009) 13–16.
[61] R. Poetes, K. Holtzmann, K. Franze, U. Steiner, Metastable underwater superhydrophobicity, Phys. Rev. Lett. 105 (2010) 166104.
[62] D. Quéré, A. Lafuma, J. Bico, Slippy and sticky microtextured solids, Nanotechnology 14 (2003) 1109–1112.
[63] A. Lafuma, D. Quéré, Superhydrophobic states, Nat. Mater. 2 (2003) 457–460.
[64] D. Quéré, Wetting and roughness, Annu. Rev. Mater. Res. 38 (2008) 71–99.

APPENDIX II: Superhydrophobic Coatings Fabrication by Electrospinning

Following is a reprint of the paper "Fabrication of Superhydrophobic Fiber Coatings by DC-Biased AC-Electrospinning," by Ochanda, F.O., Samaha, M.A., Tafreshi, H.V., Tepper, G.C., and Gad-el-Hak, M., *Journal of Applied Polymer Science*, vol. 123, pp. 1112–1119, 2012.

Fabrication of Superhydrophobic Fiber Coatings by DC-Biased AC-Electrospinning

Fredrick O. Ochanda, Mohamed A. Samaha, Hooman Vahedi Tafreshi, Gary C. Tepper, Mohamed Gad-el-Hak

Department of Mechanical & Nuclear Engineering, Virginia Commonwealth University, Richmond, Virginia 23284-3015

Received 4 February 2011; accepted 25 March 2011
DOI 10.1002/app.34583
Published online 9 August 2011 in Wiley Online Library (wileyonlinelibrary.com).

ABSTRACT: Mesh-like fiber mats of polystyrene (PS) were deposited using DC-biased AC-electrospinning. Superhydrophobic surfaces with water contact angles greater than 150° and gas fraction values of up to 97% were obtained. Rheological study was conducted on these fiber surfaces and showed a decrease in shear stress when compared with a noncoated surface (no slip), making them excellent candidates for applications requiring the reduction of skin-friction drag in submerged surfaces. We have also shown that addition of a second, low-surface energy polymer to a solution of PS can be used to control the fiber internal porosity depending on the concentration of the second polymer. Contact-angle measurements on mats consisting of porous and nonporous fibers have been used to evaluate the role of the larger spaces between the fibers and the pores on individual fibers on superhydrophobicity. © 2011 Wiley Periodicals, Inc. J Appl Polym Sci 123: 1112–1119, 2012

Key words: superhydrophobic surfaces; electrospinning; DC-biased AC-electrospinning; superhydrophobic fibrous coatings; fabrication and characterization of superhydrophobic surfaces

INTRODUCTION

Superhydrophobicity is achieved by combining nano- or microscale roughness with a low-surface free energy material. As water flows over such a surface, a "slip effect" is generated, resulting in a reduction in the skin-friction drag exerted on the surface.[1] Several methods have been used to fabricate superhydrophobic surfaces, including sol–gel processing[2] and solution casting,[3] chemical vapor deposition,[4] laser/plasma/chemical etching,[5] lithography,[6] electrical/chemical reaction and deposition,[7] layer-by-layer and self-assembly,[8] and electrospinning. Except for the last, all of these methods are complicated and require special equipment, high temperature or vacuum conditions, or low-surface energy material modification involving multiple steps, which makes it difficult for practical applications in large-scale coatings.

Electrospinning is a simple, low-cost method that can be used to deposit micro- to nanotextured coatings of a hydrophobic polymer onto substrates of arbitrary geometry. The resulting superhydrophobic surfaces can be applied in diverse applications, including self-cleaning glasses and clothes, protection against corrosion of metallic parts (in bridges, marines, under water constructions, etc.), antisnow sticking, and reducing skin-friction drag in underwater vessels such as submarines. Superhydrophobic coatings can be utilized as a passive method of flow control and may potentially become a viable alternative to the more complex and energy consuming active or reactive flow control techniques such as wall suction/blowing.[9] Conventionally, electrospinning is performed by applying a large DC-potential between the electrospinning source (typically a hypodermic syringe) and the substrate, resulting in a randomly oriented nonwoven fiber mats. The random orientation of the fibers is the result of the inherent electrostatic instability of the charged jet as it travels from the spinneret to the collection substrate. This instability can be overcome by applying a DC-biased AC-potential that induces short segments of alternating polarity, thereby reducing the magnitude of the destabilizing force on the fiber.[10] In addition, the presence of both positive and negative charges on the surface of the rotating collector minimizes the local electric field perturbations caused by residual charge accumulation on the fibers.

Different groups have fabricated superhydrophobic surfaces using electrospinning and other wet chemical approaches.[11–13] Sun and coworkers[14] demonstrated the preparation of superhydrophobic, anisotropically aligned carbon nanotube films by chemical vapor deposition on silicon substrates with quadrate micropillar arrays prepared by photo-lithography. Grid-like "nanograss" and "nanobrick"

Correspondence to: M. Gad-el-Hak (gadelhak@vcu.edu).

© 2011 Wiley Periodicals, Inc.

TABLE I
DC-Biased AC-Electrospinning Conditions

AC voltage	DC voltage	Average voltage	Frequency	% duty	Pump rate	Nozzle–Shaft distance
11 kV_{p-p}	4.8 kV	4.8 kV	500 Hz	50	0.9 mL/h	5–7 cm

superhydrophobic surfaces fabricated lithographically at Bell Laboratories have also been reported.[15] However, these surfaces made from silicon posts had to be coated with a hydrophobic material to impart superhydrophobic characteristics. Their skin-friction tests showed drag reduction due to air trapped between the posts and grids. Wang et al.[16] also fabricated a superhydrophobic copper mesh by knitting copper wire, followed by the deposition of copper clusters and long-chain fatty acids.

Although superhydrophobic surfaces consisting of mats of randomly oriented, nonwoven electrospun fibers have been reported, at this time, the effect of fiber orientation on surface hydrophobicity has not previously been investigated. Recently, Tepper and coworkers[10] showed that DC-biased AC-electrospining can be used to prepare aligned 1-D polymer nanofibers, but no superhydrophobic studies were performed on these polymer fibers. Within this article, we describe a method for fabricating orthogonal, superhydrophobic fiber coatings using a single step approach. To the best of our knowledge, this is the first example in which mesh-like (grid-like) superhydrophobic fiber surfaces have been fabricated using electrospinning. Contact-angle measurements were performed on coatings consisting of porous and nonporous fibers, and the fiber porosity had no observable effect on superhydrophobicity, indicating that the air gaps between the fibers and not the internal fiber porosity are responsible for the observed superhydrophobicity. We further show that hydrophobicity can be controlled by varying the percent weight of the polymer in the electrospun solution.

EXPERIMENTAL APPROACH

Hydrophobic polymer, polystyrene (PS; Mn = 170,000), was purchased from Sigma-Aldrich Chemicals (St. Louis, Missouri) and used as received. *N*,*N*-Dimethylformamide (DMF) and toluene at high performance liquid chromatography grade were also obtained from Sigma-Aldrich and were used without further purification. Polymer fibers were fabricated using the DC-biased AC-electrospinning technique. The fibers were electrospun from solutions with 15, 18, 20, 25, and 30 wt % PS. The polymer was first dissolved in a solvent mixture of DMF and toluene with a 1 : 1 weight ratio. In addition, other additives such as glass beads and fluoro-elastomer (Zonyl TBC) were added to the electrospinning solutions to determine their effect on hydrophobicity. Electrospinning was conducted at 22°C with a relative humidity of 45% and a solution feed rate of 0.9 mL/h, controlled using a syringe pump. The fibers were collected by a rotating shaft at a distance of 5–7 cm from the spinneret. Directional fiber bundles were obtained from a rotational shaft collector at a tangential velocity from 23 to 30 m/s. A function generator was used to generate the AC signal in the form of a square wave at selected frequency, amplitude, and duty cycle. A high voltage amplifier with ± 10 kV_{ac}, and frequency range of DC to 30 kHz was employed to amplify the output of the function generator by biasing the AC voltage to an optimum DC value. The fibers were collected on the substrate for a specified amount of time and then rotated about 90° for the same specified amount of time to generate a grid-like geometry. The experimental conditions for the electrospinning process are summarized in Table I.

The static contact angles, a measure of surface hydrophobicity, were measured using a contact-angle ramé-hart goniometer and droplets of deionized water on the specimen. Droplets of about 3 μL in volume (diameter of about 1.8 mm) were gently deposited on the substrate using a microsyringe. All measurements were made at five different points for each sample at 20 ± 1°C. An image of the droplet was taken by an F1 Series Digital Camera and transferred to a PC for contact-angle determination. The morphology of the fiber and its surface structure were observed by field emission scanning electron microscopy (FESEM; *S*-70, Hitachi, Japan). Because of the nonconductivity of our samples and to minimize the charging effects, the samples were sputter-coated with gold–palladium at a set point of 35 mA for 60 s. The gold–palladium coating's thickness under those conditions was 50 nm. The acceleration voltage and working distance for each image were 5 kV and 10 mm, respectively. Finally, rheological experiments in parallel-plate geometry were performed on an MCR 300 (Paar Physica).

RESULTS AND DISCUSSION

Effect of surface morphology on superhydrophobic coatings

Using a DC-biased AC-potential to charge the solution performs two functions. The electrospinning jet from the DC-biased AC-potential consists of short segments of alternating polarity which significantly

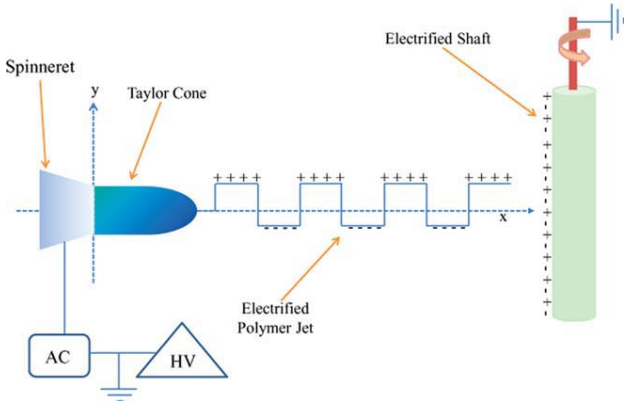

Figure 1 An illustration of an electrified polymer jet during a DC-biased AC-electrospinning. [Color figure can be viewed in the online issue, which is available at wileyonlinelibrary.com.]

reduces the inherent instability of the electrospinning jet as shown in Figure 1. This allows the fibers to be wound onto the rotating collector with greater ease and alignment. The presence of both positive and negative charges on the surface of the rotating collector minimizes the local electric fields associated with surface charge accumulation. The deposited mat of hydrophobic polymer fibers provides the surface roughness and porosity necessary to entrap air when the surface is immersed in water. As water flows over this surface, the interface between the entrapped air and the water has very low skin friction, resulting in slip flow and drag reduction. The grid-like arrangement of fibers prevents liquid from wetting into the space (pitch) between fiber posts, similar to microposts made by a microfabrication method. This requires that the fiber post spacing be close enough (typically micrometers) to counteract gravitational and other pressures that might cause wetting into the space between the posts. However, if superhydrophobicity is to be achieved, the fraction of the water droplet surface that contacts the low-surface energy posts should be much less than the fractional area of the water droplet contacting the air. The grid-like geometry of fibers has the advantage of careful control of the pitch, but with additional microscale surface roughness on the posts in a single step that further increases the hydrophobicity. Compared with a random fiber geometry, a grid-like fiber geometry results in well-controlled, high void volume, and high porosity. Furthermore, the roughness details and the void volume can be controlled at a dimension much smaller than the droplet size. Examining the dimension of the pitch (25–80 μm), the typical droplet size reported here (1.8 mm) is more than an order of magnitude larger.

The effect of percent weight of PS on the hydrophobicity of electrospun fiber coatings was investigated. Figure 2 is a plot of the contact angle versus the percent weight of the polymer. The contact angle increases monotonically with polymer weight percent and becomes superhydrophobic at 25 wt %. This is consistent with the observed morphological evolution as a function of polymer concentration. At low percentage weight, electrospinning generates predominantly droplets (particles) with very few fibers. With an increase in polymer concentration, more fibers are generated with a few cases of beads-on-string morphology. At an optimum concentration, the ratio of fibers to beads should give the highest superhydrophobicity. Images of water droplets on fiber surfaces at different percentage polymer weight are shown in Figure 3.

The addition of glass particles of size 5 μm has resulted in an increase in contact angle on the 18 wt %

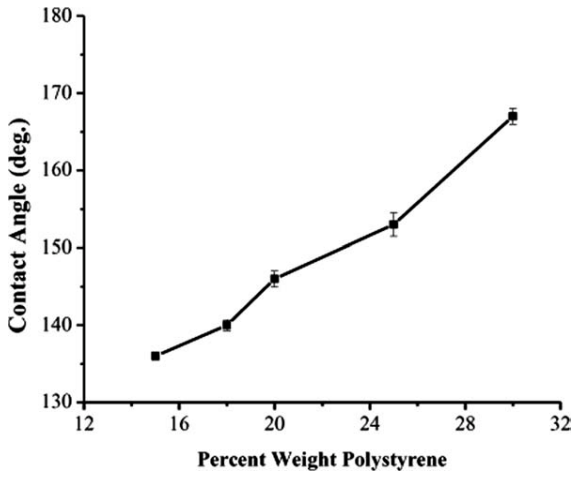

Figure 2 Water contact angles of electrospun fibers as a function of percent weight polystyrene.

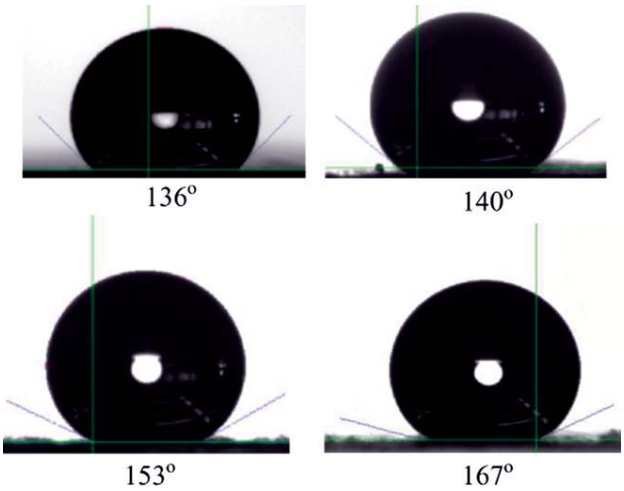

Figure 3 Contact angles of fibers as a function of percent weight of polystyrene. From left to right, top to bottom: 15 wt %, 18 wt %, 25 wt %, and 30 wt %. [Color figure can be viewed in the online issue, which is available at wileyonlinelibrary.com.]

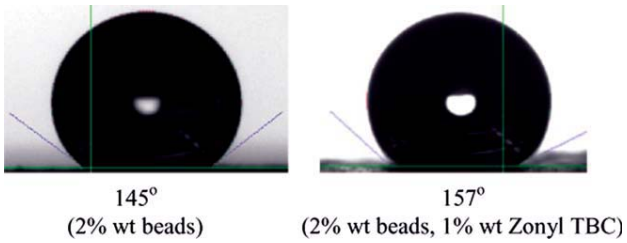

Figure 4 A water droplet on 18 wt % polystyrene fibers coating. [Color figure can be viewed in the online issue, which is available at wileyonlinelibrary.com.]

PS fiber coating from 140° to 145°. When 1 wt % fluoro-elastomer (Zonyl TBC) was added to the 18 wt % PS solution with glass particles, a large increase in contact angle was observed (157°) as shown in Figure 4. This could be ascribed to a decrease in surface energy as a result of the fluoro-elastomer (Zonyl TBC), which also increased the solution concentration of the PS blend. The addition of glass particles to 25 wt % solution also resulted in an increase in the contact angle from 153° to 160° (see Fig. 5). However, there was a slight decrease in contact angle when glass particles were added to 30 wt % PS coating from 167° to 156° (see Fig. 6). Further decrease in contact angle occurred with the addition of epoxyhexylisobutyl POSS (polyhedral oligomeric silsesquioxane) with a water contact angle of 150°. The decrease in contact angle when POSS is added to PS can be attributed to the epoxy functionality of the POSS that might have altered the surface energy of the PS coating. The effect of different additives on the hydrophobicity of electrospun PS fibers is summarized in Table II.

To measure the intrinsic hydrophobicity of PS, the polymer was dissolved in a DMF/toluene mixed solvent (1 : 1) at a concentration of 15 wt %. A PS thin film was fabricated by spin-casting on a microscope glass. The water contact angle of the spin cast PS film was determined to be 96.9 ± 1.1° and an optical image of the droplet is shown in Figure 7. Based on this we conclude that PS is chemically hydrophobic (water contact angle was higher than 90°) but is not superhydrophobic without surface roughness. The superhydrophobic coatings shown in Figure 9 are a

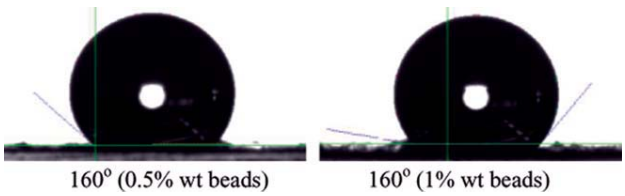

Figure 5 A water droplet on 25 wt % polystyrene fibers coating. [Color figure can be viewed in the online issue, which is available at wileyonlinelibrary.com.]

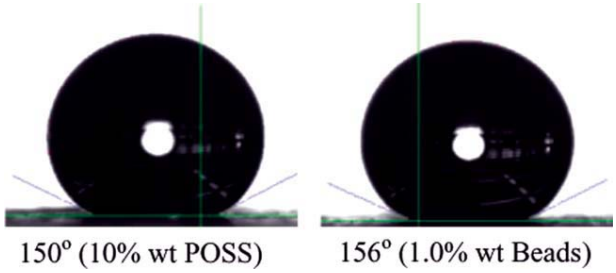

Figure 6 A water droplet on 30 wt % polystyrene fibers coating. [Color figure can be viewed in the online issue, which is available at wileyonlinelibrary.com.]

result of the web-like structure with empty spaces between the fibers.

To fully understand the hydrophobicity of the PS electrospun fiber surface, theoretical considerations are necessary. The contact angle on a composite surface (θ_r) can be expressed by Cassie and Baxter equation.[17–19]

$$\cos\theta_r = f_1 \cos\theta - f_2$$

In this equation, f_1 and f_2 represent the fractions of solid surface and air in a composite surface, respectively (i.e., $f_1 + f_2 = 1$), whereas θ is the equilibrium contact angle on a flat, solid surface. This equation can be used to show that an increase in air fraction, f_2, results in an increase in contact of the PS fiber surface. We measured the water contact angle on different PS fiber surfaces. The average contact angle on the different porous PS fiber surfaces has been summarized in the Table II. These values, together with the contact angle of a smooth PS film, made by spin coating a PS solution, have been used to estimate f_2. The f_2 value for different PS fiber surfaces (i.e., different percent weight PS) is shown in Table III. It should be noted from the Table that the film of air occupies about 68–97% of the contact area (solid–

TABLE II
Effect of Additives on the Hydrophobicity of Polystyrene Fibers at Different Percent Weight Polystyrene

Case	wt % PS	wt % glass beads	wt % zonyl TBC	wt % POSS	Contact angle (deg.)
1	15	—	—	—	136
2	18	—	—	—	140
2	18	2.0	—	—	145
2	18	2.0	1.0	—	157
3	25	—	—	—	153
3	25	0.5	—	—	160
3	25	1.0	—	—	160
3	25	—	—	10	152
4	30	—	—	—	167
4	30	1.0	—	—	156
4	30	—	—	10	150

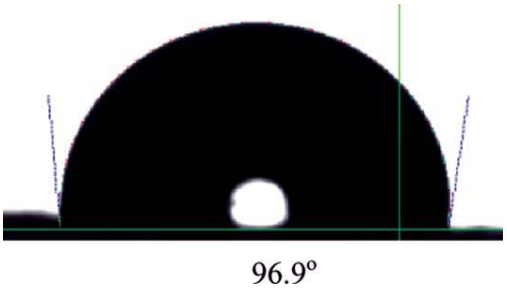

Figure 7 Contact angle of spin cast 15 wt % PS thin film. [Color figure can be viewed in the online issue, which is available at wileyonlinelibrary.com.]

liquid interface) when the fiber surface is in contact with the water droplet. This is responsible for the superhydrophobicity of the surface.

Electrospun fiber morphology

PS mats were produced by electrospinning from solutions with concentrations ranging from 18 to 30 wt % PS as shown in Figures 8–11. The electrospun fibers obtained from a solution containing PS and Toluene/DMF (1 : 1, w/w) were orthogonally oriented and each fiber had an average diameter of 2.5 ± 1.2 μm ($N = 60$), a flat surface with irregular pores of diameter 500 ± 100 nm ($N = 60$) and regular pores of diameter 150 ± 50 nm, as reported by Rabolt and coworkers.[20,21] This porous morphology results from the different evaporation fronts of the mixed solvents and the phase separation of the polymer in the mixed solvents, during electrospinning.

The surface morphology of the electrospun PS fibers shows continuous and oriented electrospun fibers with uniform cylindrical pores and large-scale grooves along the individual fibers. These figures also show that the surface of the PS electrospun fibers is rough enough that air can be present in between individual fiber layers. The coatings shown here can be regarded as a composite surface consisting of fibers and air. Both of the nonwoven electrospun membranes had a rougher surface morphology than the spin cast films. As a result, they were found to have a much higher water contact angle. It is revealed that micro- and nanoscale hierarchical structures on the PS fiber mesh play an important role in obtaining the unique superhydrophobic property. This electrospinning approach has the benefit of introducing different pore structures and hence achieving hierarchical surfaces in a single step.

The addition of a second polymer to a solution of PS has been shown to change the porosity of the resulting fibers, as illustrated by Figure 8, where pores and groves along the single fiber have been eliminated. This feature has no effect on the superhydrophobicity of this sample, which proves that the large porous network resulting from the air caught in the spaces between fibers is responsible for superhydrophobicity, and that pores on individual fibers play a minimal role. This phenomenon has been verified further by making an 18% PS with 0.5% of fluoro-elastomer composite and observing the trend from the scanning electron microscopy

TABLE III
Estimate of Air Fraction on Composite Surface in Contact with Droplet from Cassie–Baxter Equation

Case	Percent weight PS	Contact angle (deg.)	Air fraction
1	15	136	68.0
2	18	140	73.4
2	18 (+2% glass beads)	145	79.5
2	18 (+2% glass beads + 1% fluoro-elastomer)	157	91.0
3	25	153	87.5
3	25 (+10% POSS)	152	86.7
3	25 (+1% glass beads)	160	93.0
4	30	167	97.0
4	30 (+1% glass beads)	160	93.0
4	30 (+10% POSS)	150	85.0

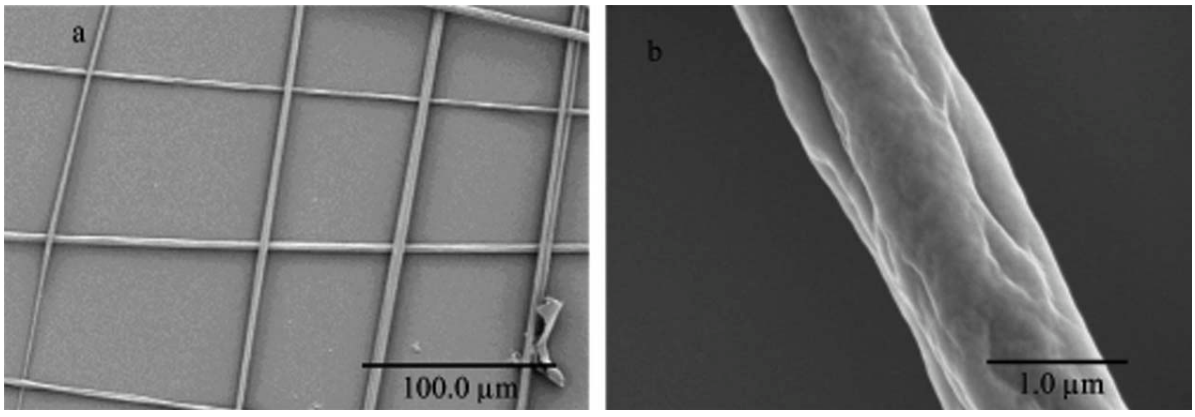

Figure 8 SEM image of 18 wt % polystyrene fibers with 1 wt % fluoro-elastomer and 2% glass beads showing (a) grid-like structure and (b) high magnification of single fiber.

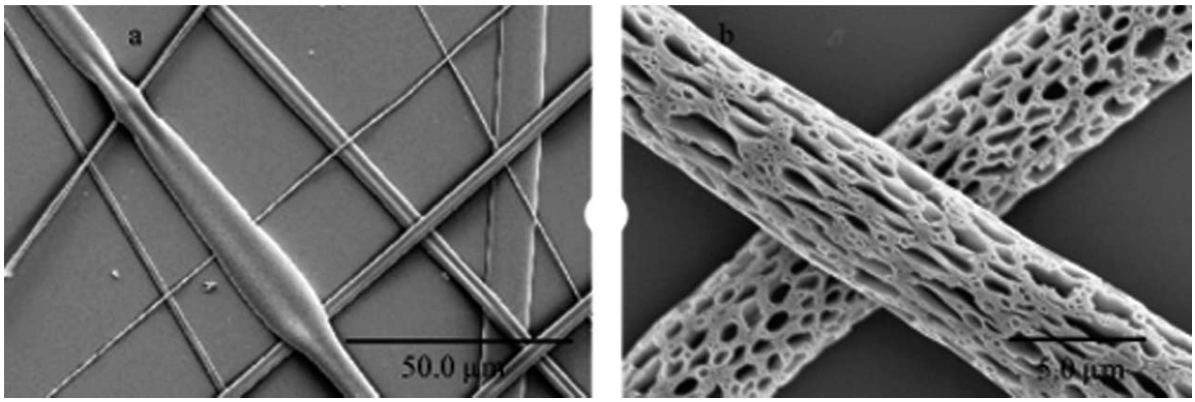

Figure 9 SEM image of 20 wt % polystyrene fibers showing (a) grid-like structure and (b) high magnification of single fiber exhibiting porous network.

(SEM) image shown in Figure 12. From the image, the pores are incompletely filled when compared with the case of 18% PS with 1.0% fluoro-elastomer. This observation shows that morphology and surface features of the electrospun fibers can be controlled by the addition of a small percent weight of a second polymer. Therefore, we conclude that a minimum concentration of fluoro-elastomer is required to completely eliminate the fiber pores. This ability to control the morphology of fiber coatings using DC-biased AC-electrospinning makes this fabrication approach very attractive for preparing surfaces for different applications.

Rheology of mesh-like superhydrophobic fiber coatings

A rheometer made by Anton Paar Corp. (model number MCR 300), equipped with two parallel rotating discs separated by a small fluid-filled gap, was used to measure the stress–strain rate relation. One disc is stationary and attached to a water cooling system for temperature control. The second disc rotates at a prescribed speed and is connected to an air bearing to minimize friction. Compressed air at about 6 atm supports the bearing. The rotating disc is connected to a torque-speed measuring system used to calculate the shear stress developed by the fluid, and the measured rotational speed is used to calculate the strain rate. The stress–strain rate relation was measured for both superhydrophobic samples as well as smooth control surfaces. The test samples were attached to the stationary disc and had the same diameter as the rotating disc. Figure 13 shows the measured stress–strain curve for a noncoated disc (no slip), a superhydrophobic surface produced by the DC-biased AC-electrospinning technique.

The results show that the electrospun superhydrophobic PS fiber coating has lower shear stress than a noncoated disc (no slip). This result is consistent with the high contact-angle measurements, which indicate that the fluid in contact with the surface is also in contact with the trapped air, enabling the water layer to roll or slip. This phenomenon of low viscous friction on the superhydrophobic fiber

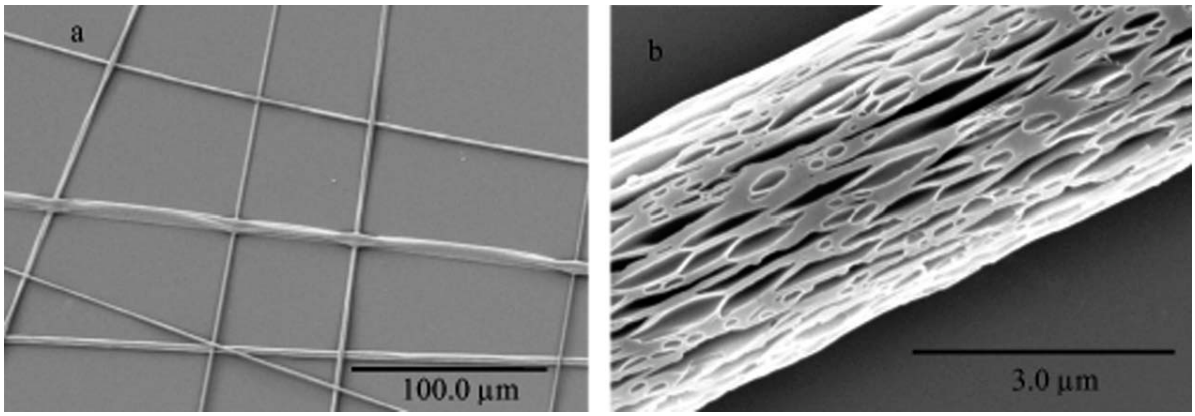

Figure 10 SEM image of 25 wt % polystyrene fibers showing (a) grid-like structure and (b) high magnification of single fiber exhibiting porous network.

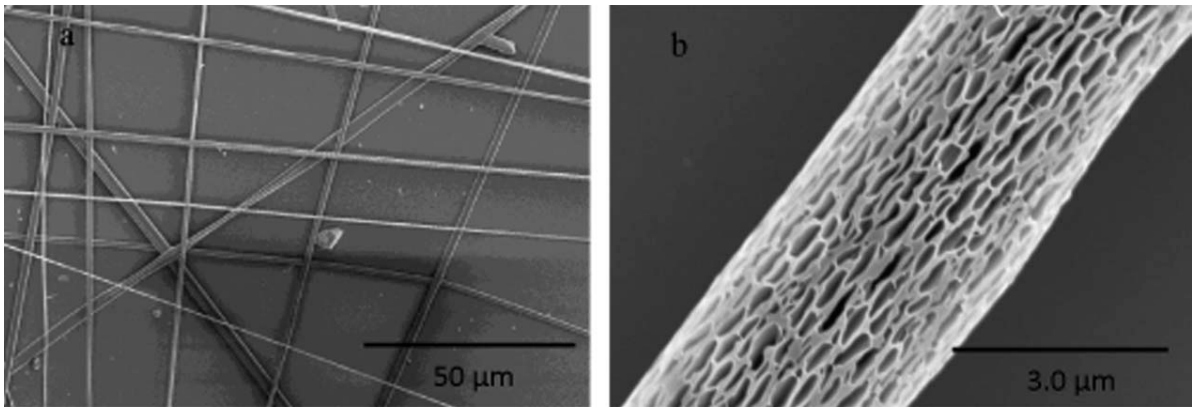

Figure 11 SEM image of 30 wt % polystyrene fibers showing (a) grid-like structure and (b) high magnification of single fiber exhibiting porous network.

surfaces is expected to open new opportunities for drag reduction in underwater bodies, especially submarines. A more detailed rheological study of the superhydrophobic electrospun fibers is under way.

CONCLUSIONS

Mesh-like PS fibers were synthesized by a simple DC-biased AC-electrospinning process and deposited onto metal substrates. The synthesized fibers were found to be superhydrophobic, with water contact angles up to 167°. These fiber coatings are far less expensive to fabricate when compared with those made with micro- or nanofabrication techniques. These results confirm that the physical surface structure is an important element affecting the surface hydrophobicity, in addition to the intrinsic hydrophobicity of materials such as PS. Rheological study conducted on these grid-like fiber surfaces showed a decrease in shear stress when compared with a noncoated surface (no slip). These surfaces are expected to have potential applications in submarine and ship coatings for the purpose of reducing of skin-friction drag and flow-induced noise. We have also shown that the addition of a second, low-surface energy polymer to a solution of PS can be used to control the internal porosity of the fibers, depending on the concentration of the second polymer. Contact-angle measurements indicated no effect on the superhydrophobicity on addition of second polymer, an indication that the large porous network due to spaces between the fibers is primarily responsible for superhydrophobicity and that pores on individual fibers play a minimal role.

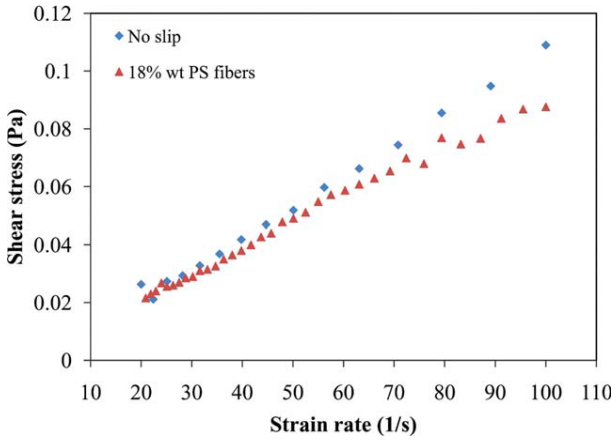

Figure 13 Plot of stress–strain curve of 18 wt % polystyrene fiber surface containing 1 wt % fluoro-elastomer. The figure shows lower shear stress when compared with no-slip surface. [Color figure can be viewed in the online issue, which is available at wileyonlinelibrary.com.]

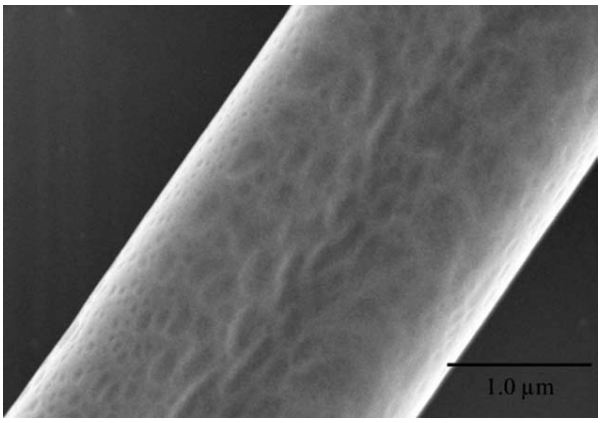

Figure 12 SEM image of 18 wt % polystyrene with 0.5 wt % fluoro-elastomer showing partially filled pores along the fiber.

This research is sponsored by the Defense Advanced Research Projects Agency (DARPA), contract number W91CRB10^{-1}-0003, technical sponsor Captain Christopher Warren, USN. The content of this article does not necessarily reflect the position or the policy of the Government, and no official endorsement should be inferred.

References

1. Rothstein, J. P. Annu Rev Fluid Mech 2010, 42, 89.
2. Shirtcliffe, N. J.; Hale, G.; Newton, H. I.; Perry, C. C. Langmuir 2003, 19, 5626.
3. Erbil, H. Y.; Demirel, A. L.; Avci, Y.; Mert, O. Science 2003, 299, 1377.
4. Love, J. C.; Gates, B. D.; Wolfe, D. B.; Paul, K. E.; Whitesides, G. M. Nano Lett 2002, 2, 891.
5. Fresnais, J.; Chapel, J. P.; Poncin-Epaillard, F. Surf Coat Technol 2006, 200, 5296.
6. Pozzato, A.; Zilio, S. D.; Fois, G.; Vendramin, D.; Mistura, G.; Belotti, M.; Chen, Y.; Natali, M. Microelectron Eng 2006, 83, 884.
7. Shi, F.; Wang, Z. Q.; Zhang, X. Adv Mater 2005, 17, 1005.
8. Zhao, N.; Shi, F.; Wang, Z. Q.; Zhang, X. Langmuir 2005, 21, 4713.
9. Gad-el-Hak, M. Flow Control: Passive, Active, and Reactive Flow Management; Cambridge University Press: London, United Kingdom, 2000.
10. Sarkar, S.; Deevi, S.; Tepper, G. Macromol Rapid Commun 2007, 28, 1034.
11. Jiang, L.; Zhao, Y.; Zhai, J. Angew Chem Int Ed Engl Suppl. 2004, 43, 4338.
12. Ma, M.; Mao, Y.; Gupta, M.; Gleason, K. K.; Rutledge, G. C. Macromolecules 2005, 38, 9742.
13. Acatay, K.; Simsek, E.; Ow-Yang, C.; Menceloglu, Y. Z. Angew Chem Int Ed 2004, 43, 5210.
14. Jin, M.; Feng, X.; Feng, L.; Sun, T.; Zhai, J.; Li, T.; Jiang, L. Adv Mater 1997 2005, 17.
15. Krupenkin, T. N.; Taylor, J. A.; Schneider, T. M.; Yang, S. Langmuir 2004, 20, 3824.
16. Wang, S.; Song, Y.; Jiang, L. Nanotechnology 2007, 18, 015103.
17. Cassie, A. B. D.; Baxter, S. Trans Faraday Soc 1944, 40, 546.
18. Hoefnagels, H. F.; Wu, D.; de With, G.; Ming, W. Langmuir 2007, 23, 13158.
19. Chao-Hua, X.; Shun-Tian, J.; Jing, Z.; Li-Qiang, T.; Hong-Zheng, C.; Mang, W. Sci Technol Adv Mater 2008, 9, 035008.
20. Megelski, S.; Stephens, J. S.; Chase, D. B.; Rabolt, J. F. Macromolecules 2002, 35, 8456.
21. Casper, C. L.; Stephens, J. S.; Tassi, N. G.; Chase, D. B.; Rabolt, J. F. Macromolecules 2004, 37, 573.

APPENDIX III: Characterization of Superhydrophobic Coatings

Following is a reprint of the paper "*In Situ*, non-invasive characterization of superhydrophobic coatings," by Samaha, M.A., Ochanda, F.O., Tafreshi, H.V., Tepper, G.C., and Gad-el-Hak, M., *Review of Scientific Instruments*, vol. 82, pp. 045109.1–045109.7, 2011.

In situ, noninvasive characterization of superhydrophobic coatings

Mohamed A. Samaha, Fredrick O. Ochanda, Hooman Vahedi Tafreshi, Gary C. Tepper, and Mohamed Gad-el-Hak[a)]

Department of Mechanical and Nuclear Engineering, Virginia Commonwealth University, Richmond, Virginia 23284-3015, USA

(Received 25 January 2011; accepted 22 March 2011; published online 21 April 2011)

Light scattering was used to measure the time-dependent loss of air entrapped within a submerged microporous hydrophobic surface subjected to different environmental conditions. The loss of trapped air resulted in a measurable decrease in surface reflectivity and the kinetics of the process was determined in real time and compared to surface properties, such as porosity and morphology. The light-scattering results were compared with measurements of skin-friction drag, static contact angle, and contact-angle hysteresis. The *in situ*, noninvasive optical technique was shown to correlate well with the more conventional methods for quantifying surface hydrophobicity, such as flow slip and contact angle. © *2011 American Institute of Physics*. [doi:10.1063/1.3579498]

I. INTRODUCTION

Superhydrophobicity is a surface property resulting from a combination of material hydrophobicity and micro- or nanoscale surface roughness. The phenomenon is primarily characterized by water droplets beading on the solid surface with contact angles exceeding 150°. As water flows over such surface, "slip effect" is produced resulting in a reduction in the skin-friction drag exerted on the surface.[1] Superhydrophobic coatings can be utilized as a passive method of flow control and may potentially become a viable alternative to the more complex and energy consuming active or reactive flow control techniques, such as wall suction/blowing.[2] Most engineered superhydrophobic surfaces are made up of microposts or microridges manufactured via microfabrication techniques. As reviewed by Samaha *et al.*,[3] such surfaces have been extensively studied in the last few years experimentally, analytically, and numerically.[4–10]

A submerged superhydrophobic surface can entrap air between the microposts or microridges resulting in a surface with both air–water and solid–water interfaces. The presence of the air–water interface is responsible for the measurable decrease in shear stress. Cheng *et al.*[11] calculated the influence of the total shear-free area or the air–water interface area (at which slip effect takes place) as well as its dependency on slip length. The stability of the air–water interface (meniscus), i.e., the sustainability of the interface for conversion from nonwetted (Cassie) to wetted (Wenzel) state, against pressure for the staggered microposts was reviewed by Lee *et al.*[12] Samaha *et al.*[3] performed similar studies to numerically calculate both drag reduction and slip length and mathematically estimate the stability limit of the air–water interface for superhydrophobic surfaces with random roughness, e.g., surfaces made via random particle deposition.[13,14] As long as the air is entrapped, the surface remains hydrophobic. In other words, the degree of hydrophobicity and hence the beneficial effects are diminished by the reduction of the amount of air. The longevity of a superhydrophobic surface was studied by Bobji *et al.*[15] They used an optical technique to measure how long the surface can entrap air underwater by measuring the number of shiny spots, each is an indication of an interface between air and water. Similar studies were performed using a laser beam to investigate the effect of the surface structure on longevity.[16]

The objective of the present study is to advance and calibrate a novel optical technique to noninvasively measure the longevity of submerged superhydrophobic coatings subjected to different environmental conditions. We used an optical spectroscopy system to quantify the intensity of reflected light in the visible range scattered from a superhydrophobic surface completely submerged in a controlled water vessel. The time-dependent light-reflection intensity could be measured at a single wavelength or integrated over a range of wavelengths. It is desirable to measure *in situ* the degree of hydrophobicity of coatings fabricated with different techniques and subjected to different environments. Those environments are not possible to reproduce during traditional contact-angle or rheometer measurements and include a broad range of water pressures (i.e., depths), constant or time-dependent pressures, water with different degrees of salinity or dissolved air, still or moving water, etc. However, the novel optical technique developed herein needs to be calibrated against traditional methods for measuring hydrophobicity.

The optical spectroscopy system used herein was previously utilized for different purposes and applications. In geochemistry, e.g., it was used to screen soil and sediment to study the distribution of heavy metals along soil profile.[17] In biology, it was used to detect and classify bacterial pathogens.[18] In chemistry, it was used to study the excitation and reaction of chemical solutions.[19] All of these examples and others prove the precision of this device, which motivated us to use it to measure the time-dependent surface's hydrophobicity.

In order to validate this novel technique, the results were compared with drag-reduction data using a rheometer, as well as static contact angle and contact-angle hysteresis using a

a)Author to whom correspondence should be addressed. Electronic mail: gadelhak@vcu.edu.

 © 2011 American Institute of Physics

Downloaded 27 Apr 2011 to 128.172.52.138. Redistribution subject to AIP license or copyright; see http://rsi.aip.org/about/rights_and_permissions

goniometer. We fabricated the superhydrophobic surfaces using two different low-cost techniques. First, hydrophobic aerogel particles were deposited onto a substrate consisting of a metal coated with a thin polymer film that was used for adhesion. In this case, superhydrophobicity was achieved by a combination of hydrophobic substance (aerogel) and surface roughness (random aerogel grains). The second technique is electrospinning and is explained in Sec. II. Although the present study focuses on coatings fabricated using electrospinning, it is clear that the advanced optical technique can be used with any coating fabrication method including, of course, microfabrication.

II. FABRICATION

Hydrophobic polymer micro- and nanofibers were deposited onto aluminum substrates using the dc-biased ac-electrospinning technique invented at VCU.[20] This fabrication method was selected because it can produce coatings with a high degree of fiber alignment, but it is clear that the characterization method advanced in this paper should work regardless of the technique used to fabricate a superhydrophobic coating. Polystyrene (PS; Mw = 190 000) was dissolved in a toluene/dimethyl-*n*,*n*-formamide (DMF) mixed solvent at weight percentages of 15, 18, 25, and 30, and stirred for about 2 h. Figure 1 shows SEM images of micro/nanofibers produced from an 18% solution. As shown in Fig. 1(a), a monolayer of these fibers has a high degree of fiber alignment. However, alignment is lost as more layers are added [Fig. 1(c)]. We hypothesize that this effect is caused by the decreased conductivity as more layers of the nonconductive polymer are added.

The inset in Fig. 1(c) shows a water droplet on the coating with a static contact angle of 157°, proving superhydrophobicity even in the case of random fiber deposit. A high magnification image of a single fiber from the monolayer is shown in Fig. 1(b). The diameter of the fiber is about 1 μm. The deposited mat of hydrophobic polymer fibers provides the surface roughness and porosity necessary to entrap air when surface is immersed in water. As water flows over this surface, the interface between the entrapped air and the water has very low skin friction resulting in slip flow and drag reduction.

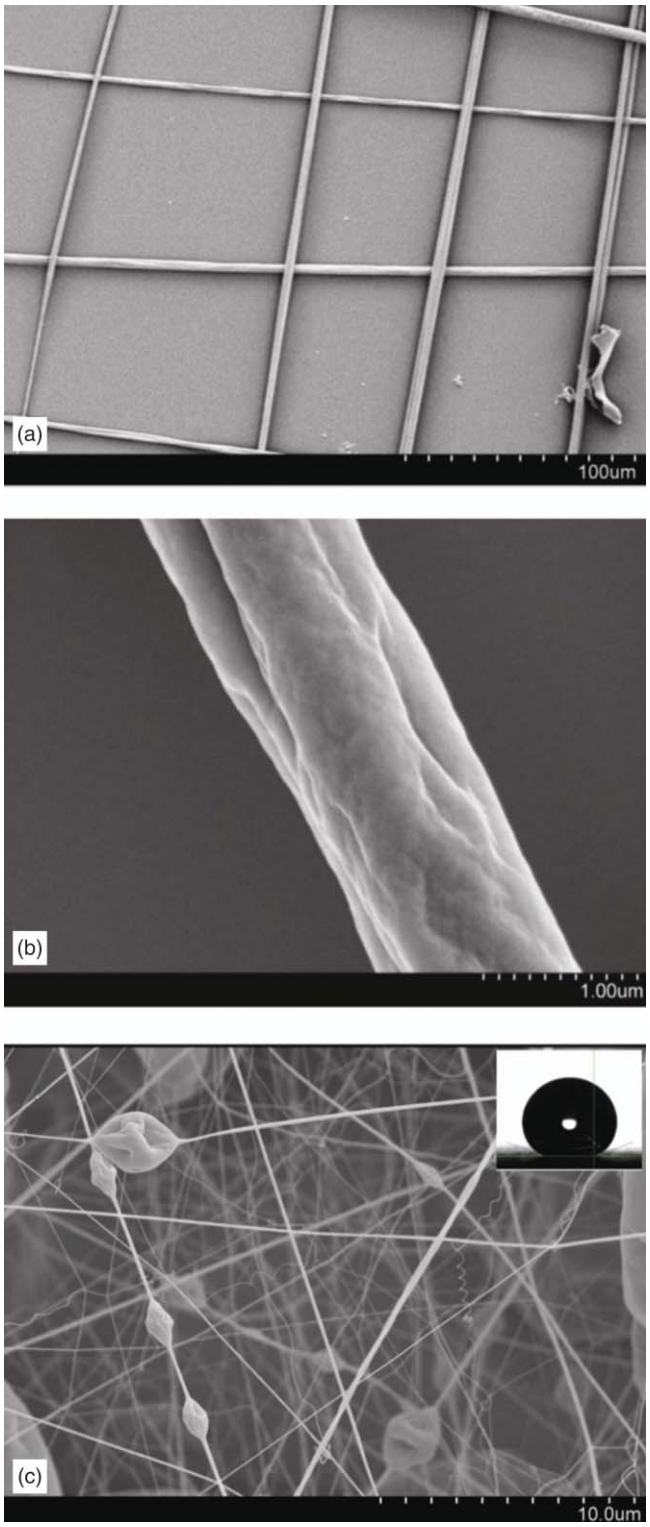

FIG. 1. SEM image of 18% weight polystyrene fibers with 10% weight fluoroelastomer. (a) Gridlike structure of a monolayer; (b) highly magnified image of a single fiber; and (c) several layers of fibers show random orientation. Upper right inset in (c) shows a water droplet on top of this particular coating.

III. EXPERIMENTAL APPROACH

A. Longevity test

The kinetics of air loss from submerged superhydrophobic coatings was measured using an optical spectroscopy system made by Photon Technology International, Inc. (model QuantaMaster™ 30). The intensity of a broad-spectrum white light reflected from the submerged surface was measured as a function of time and wavelength using the setup schematically depicted in Fig. 2(a), and a photograph of the pressure vessel is shown in Fig. 2(b). As the reflectivity coefficient is greater for the air–water interface than for the solid–water interface, the intensity of the reflected light decreases as the amount of trapped air decreases. The loss of trapped air will cause a transition from nonwetted (Cassie) state to wetted (Wenzel) state. The reflected white light is applied to a Czerny–Turner monochromator, schematically depicted in Fig. 3. In the common Czerny–Turner design,[21–23] the white light source (A) is directed to an entrance slit (B). The slit is located at the effective focus of a collimating curved mirror (C). Therefore, the

Downloaded 27 Apr 2011 to 128.172.52.138. Redistribution subject to AIP license or copyright; see http://rsi.aip.org/about/rights_and_permissions

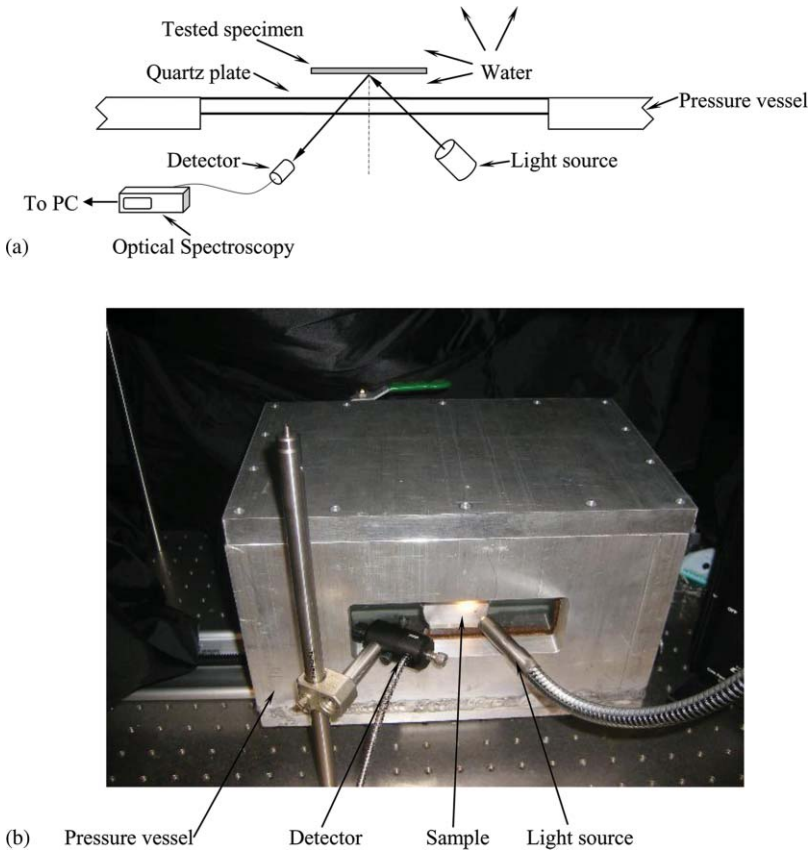

FIG. 2. (Color online) (a) Schematic of the optical spectroscopy system. (b) Photograph of the pressure vessel.

light rays are reflected in parallel streams that are diffracted from the grating (D) and then are directed to a collimating mirror (E) that refocuses the dispersed light to an exit slit (F). The intensity of light for each wavelength is then measured with time.

B. Drag measurements using Anton Paar rheometer

In order to validate the longevity measurements using the optical spectroscopy system, the results were compared with drag-reduction data using a rheometer as well as measurements of both static contact angle and hysteresis using a goniometer. We start by describing the drag measurements in this subsection.

A rheometer made by Anton Paar Corporation (model Physica MCR 301), equipped with two parallel rotating discs separated by a small fluid-filled gap as schematically shown in Fig. 4, was used to measure the stress–strain rate relation. One disc is stationary and attached to a water cooling system for temperature control. The second disc rotates at a prescribed speed and is connected to an air bearing to minimize friction. Compressed air at about 6 atm supports the bearing. The rotating disc is connected to a torque–speed measuring system used to calculate the shear stress developed by the fluid, and the measured rotational speed is used to calculate the strain rate. The stress–strain rate relation was measured for both superhydrophobic samples as well as smooth control surfaces. The test samples were attached to the stationary disc and had the same diameter as the rotating disc. The equation governing this motion is an exact solution of the Navier–Stokes equation and can be readily reduced to

$$V_\theta = \frac{\omega r}{h} z, \tag{1}$$

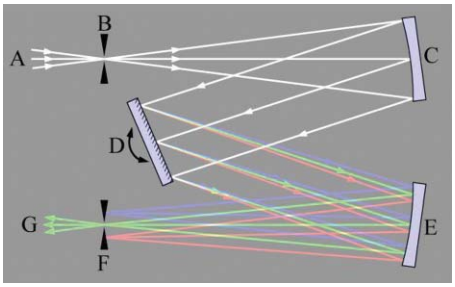

FIG. 3. (Color online) Czerny–Turner monochromator (Ref. 24).

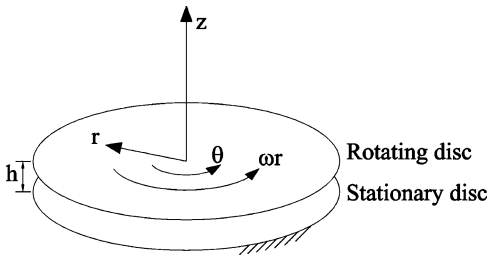

FIG. 4. Schematic diagram showing the rheometer's discs. Cylindrical coordinates are indicated.

Downloaded 27 Apr 2011 to 128.172.52.138. Redistribution subject to AIP license or copyright; see http://rsi.aip.org/about/rights_and_permissions

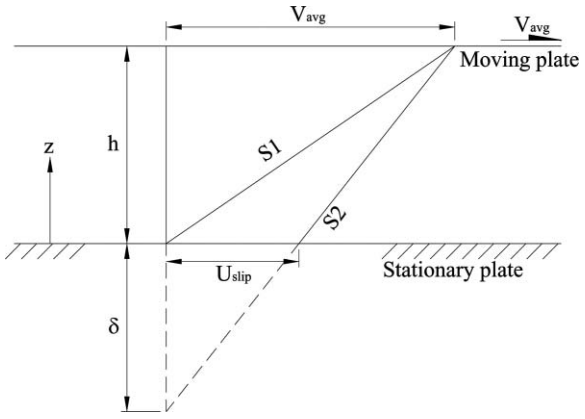

FIG. 5. Tangential velocity profiles for both slip and no-slip flow between the rheometer's discs.

where V_θ is the local linear velocity in the rotational direction θ (see Fig. 4), ω is the angular velocity of the rotating disc, r and z are, respectively, the radial and axial coordinates, and h is the gap between the two discs.

As shown in Fig. 5, the tangential velocity V_θ increases linearly with the normal distance from the stationary disc, z, for both no-slip (line S1) and slip-flow (line S2) boundary conditions at the stationary disc. Here, V_{avg} is the average tangential velocity of the rotating disc, U_{slip} is the slip velocity at the stationary disc in case of considering slip flow, and δ is the slip length. According to Navier's model,[25] the magnitude of the slip velocity is proportional to the magnitude of the strain rate, and the slip length is the proportionality constant. Thus, the slip length δ is defined by the following equation:

$$\delta = \frac{U_{\text{slip}}}{\left.\frac{\partial V_\theta}{\partial z}\right|_{\text{wall}}}, \tag{2}$$

where $(\frac{\partial V_\theta}{\partial z}|_{\text{wall}})$ is the slope of the velocity profile at the stationary disc.

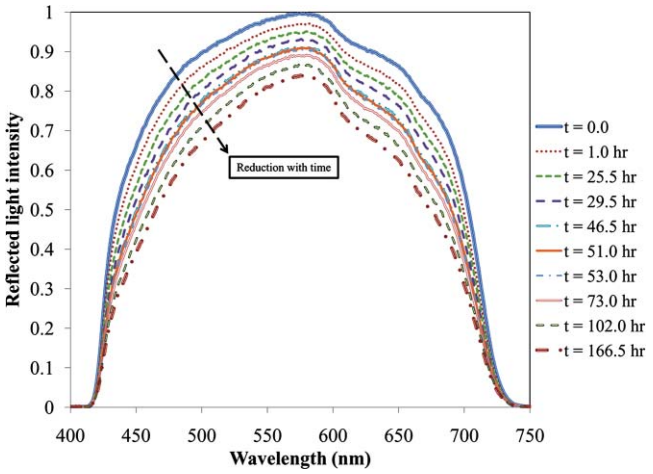

FIG. 6. (Color online) Reduction in reflected light intensity with time for a spun-fiber sample. Measurements are taken for the entire visible-light spectrum.

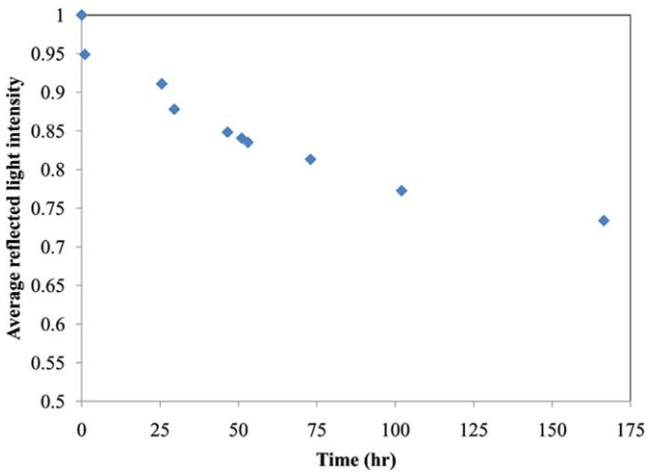

FIG. 7. (Color online) Average reflected-light intensity reduction with time for a spun-fiber sample.

From the geometry of Fig. 5, the slip length δ can be calculated from the following equation:

$$\delta = \frac{\left.\frac{\partial V_\theta}{\partial z}\right|_{\text{wall, S1}}}{\left.\frac{\partial V_\theta}{\partial z}\right|_{\text{wall, S2}}} \times h - h, \tag{3}$$

where $(\frac{\partial V_\theta}{\partial z}|_{\text{wall, S1}})$ and $(\frac{\partial V_\theta}{\partial z}|_{\text{wall, S2}})$ are, respectively, the slopes of lines S1 and S2, which can be readily calculated by dividing the measured shear stress τ_{wall} by water viscosity. Furthermore, the slip velocity U_{slip} can be calculated from

$$U_{\text{slip}} = \delta \times \left.\frac{\partial V_\theta}{\partial z}\right|_{\text{wall, S2}}. \tag{4}$$

Finally, the skin friction coefficient C_f can be calculated from

$$C_f = \frac{2\tau_{\text{wall}}}{\rho(\omega R)^2}, \tag{5}$$

where ρ is the water density, and R is the disc radius. Combining these equations, one can calculate the percentage drag

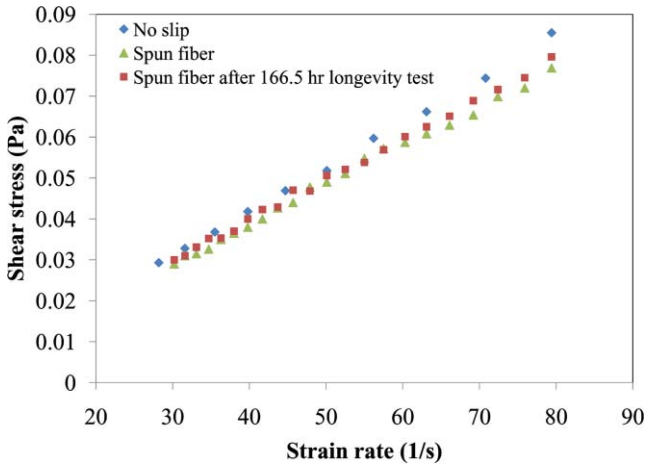

FIG. 8. (Color online) Stress–strain rate curve.

Downloaded 27 Apr 2011 to 128.172.52.138. Redistribution subject to AIP license or copyright; see http://rsi.aip.org/about/rights_and_permissions

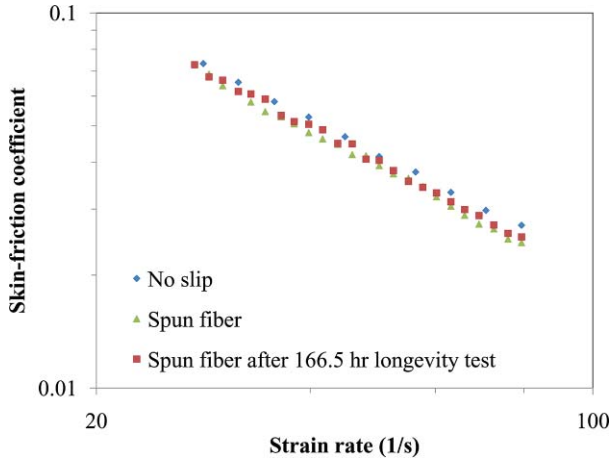

FIG. 9. (Color online) Skin-friction coefficient vs strain rate.

reduction, $DR\%$ as

$$DR\% = \frac{(C_f)_{\text{No Slip}} - (C_f)_{\text{Slip}}}{(C_f)_{\text{No Slip}}} \times 100. \quad (6)$$

C. Contact-angle measurements using ramé-hart goniometer

In this subsection, the goniometer measurements used to validate the optical spectroscopy system are briefly described. Static contact angles exceeding 150° and small contact-angle hysteresis[26] are strong indicators of surface hydrophobicity, and those were measured using a contact-angle ramé-hart goniometer (model number 100-25-A). Droplets of deionized water of about 3 μl in volume (diameter of about 1.5 mm) were gently deposited on the coated surface using a microsyringe. All measurements were made at six different surface locations on each sample at a temperature of 20 ± 1°C. An image of the droplet was taken by an F1 Series digital camera and transferred to a personal computer for contact-angle determination.

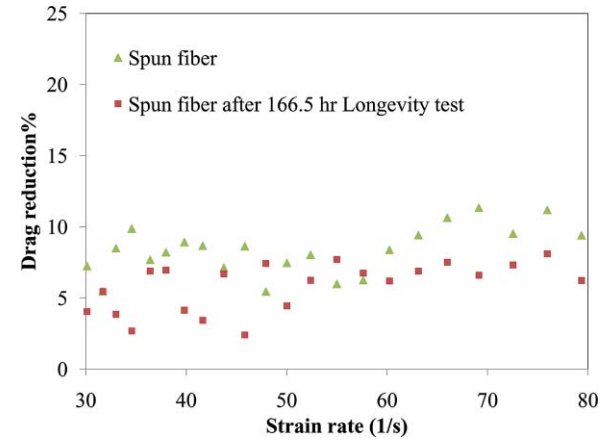

FIG. 10. (Color online) Drag reduction vs strain rate.

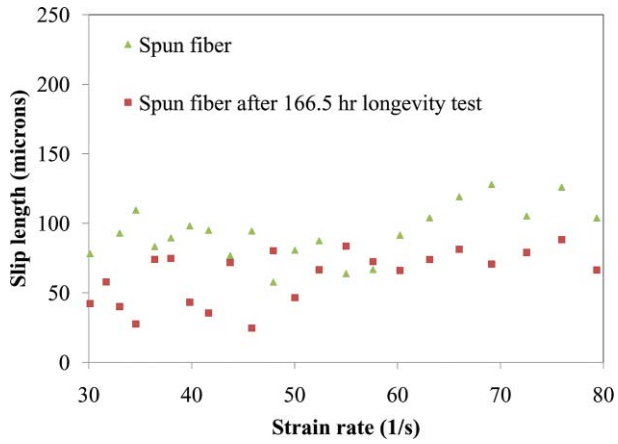

FIG. 11. (Color online) Slip length vs strain rate.

IV. RESULTS AND DISCUSSION

Figure 6 shows the normalized reflected-light intensity as a function of time and wavelength for an electrospun-fiber sample submerged in water for 166.5 h. The light intensity decreases with time at all wavelengths which indicates the loss of trapped air and a corresponding reduction in the degree of superhydrophobicity. Note that after 166.5 h, the specimen is still generating drag reduction (see Fig. 10).

Figure 7 is a plot of the normalized average reflected-light intensity (defined as the integration of the intensity over all wavelengths divided by the wavelength range). All of the light-scattering measurements were performed under atmospheric pressure, although the pressure vessel is designed to test different environments including much higher pressures. It can be seen from Fig. 7 that the average reflected-light intensity decreased by about 27% after 166.5 h of continuous submersion in water.

Figure 8 shows the measured stress–strain rate curve for a smooth disc (no slip) and a superhydrophobic surface consisting of polymer fibers both before and after 166.5 h of water immersion. By applying Eq. (5), the measured data are used to determine the skin-friction coefficient as shown in Fig. 9. This figure shows, as expected, that the skin friction is maximum for no-slip condition and minimum for fresh spun-fiber

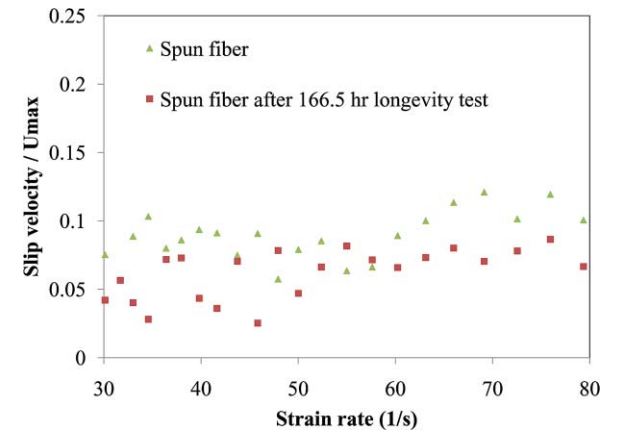

FIG. 12. (Color online) Slip velocity vs strain rate.

Downloaded 27 Apr 2011 to 128.172.52.138. Redistribution subject to AIP license or copyright; see http://rsi.aip.org/about/rights_and_permissions

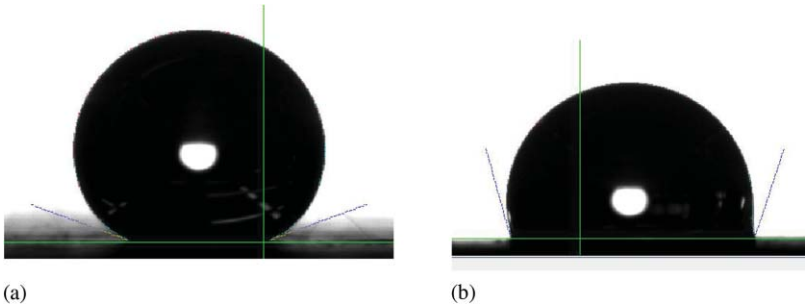

FIG. 13. (Color online) Contact-angle measurements for spun-fiber specimen. (a) Before longevity test, 157°. (b) After 166.5 h longevity test, 108°.

sample. Figure 10 shows the drag reduction and Fig. 11 shows the slip length versus strain rate for the same two hydrophobic surfaces. The drag reduction and slip length indicate the degree and efficiency of the coating's superhydrophobicity. Figure 12 shows slip velocity, which determines how the hydrophobic surface can generate slipping flow. The slip velocity is normalized with the maximum linear velocity of the rotating disc. Figures 10–12 show the same trend; an inverse proportionality to the shear stress, which is decreased due to the presence of the superhydrophobic surface (lower flow resistance).

It is worth noting that the results attained using the low-cost fabrication approach used herein are comparable to those obtained using micro- and nanofabricated surfaces.[27] The experiments also indicate that spun fiber is still capable of reducing the drag after 166.5 h immersion in water under atmospheric pressure (longevity test). The average drag reduction decreased by about 31% with respect to that of the fresh specimen, and the change in drag reduction is comparable to the measured decrease in reflected-light intensity (27%).

Another way to characterize surface hydrophobicity is to measure the static contact angle. Figure 13 shows contact-angle measurements of the same spun-fiber specimen used in both rheometer and longevity tests. The measurement indicates that the angle is about 157° for the fresh sample [Fig. 13(a)]. After 166.5 h immersion in water under atmospheric pressure, the contact angle becomes about 108° [Fig. 13(b)]. Thus, the contact angle decreases by about 31%, which is comparable to the 27% decrease in reflected-light intensity, and nearly identical to the change in drag reduction.

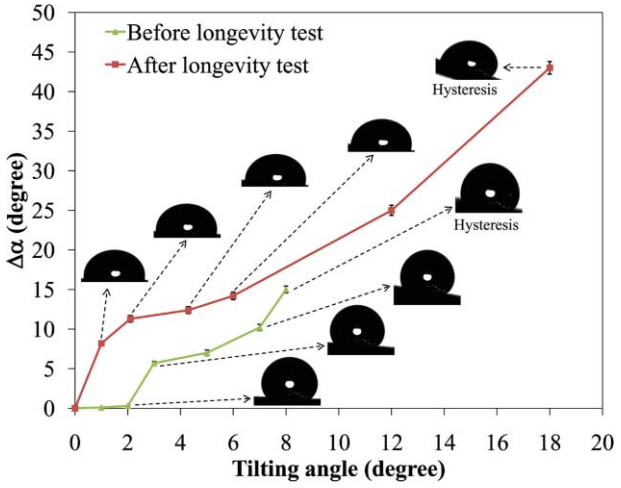

FIG. 14. (Color online) Contact-angle hysteresis measurements using surface-tilting method.

It is well known[28–32] that as the surface on which a water drop is placed is tilted, the downhill contact angle increases while the uphill contact angle decreases. As the tilt increases, those two angles continue to increase and decrease, respectively, until the drop starts to move. Advancing and receding contact angles are defined as the downhill and uphill contact angles just before the drop starts to move. Hysteresis represents the difference between the advanced and receding angles (at incipient motion). Small hysteresis indicates higher degree of superhydrophobicity.

Figure 14 is a plot of the difference between the downhill and the uphill contact angles, $\Delta\alpha$, versus the tilting angle for two typical samples of the spun-fiber specimen, one for a fresh sample and the second at the conclusion of the longevity test. The figure shows that $\Delta\alpha$ for the fresh sample is always lower than that of the sample immersed for 166.5 h. Furthermore, the figure also indicates that the contact-angle hysteresis before the longevity test is 15° and that after the longevity test is 43°. This once again confirms that the fresh sample is more hydrophobic and keeps a larger amount of entrapped air.

Therefore, the results of the light-scattering surface characterization technique correlate strongly with both contact-angle and drag-reduction measurements. The contact-angle hysteresis measurements further validate the light-scattering method. *In situ* characterization of submerged hydrophobic surfaces using light scattering represents a new and useful tool for real-time estimation of hydrophobicity and drag reduction.

V. CONCLUSIONS

We used an *in situ*, noninvasive light-scattering technique to measure the air loss in submerged hydrophobic and superhydrophobic surfaces. The light-scattering results were compared to contact-angle and drag-reduction measurements, and a strong correlation between the three characterization methods was observed. The results show that the ratio of the relative reflected-light intensity for the submerged sample after 166.5 h to that of the fresh sample approaches the corresponding drag-reduction and contact-angle ratios. Those results are additionally verified by the measurements of contact-angle hysteresis.

Downloaded 27 Apr 2011 to 128.172.52.138. Redistribution subject to AIP license or copyright; see http://rsi.aip.org/about/rights_and_permissions

The developed light-scattering methodology could be used to characterize superhydrophobic surfaces fabricated with any viable methodology, and subjected to different environments, which may include a broad range of water pressures (i.e., depths), constant or time-dependent pressures, water with different degrees of salinity or dissolved air, and still or moving water.

ACKNOWLEDGMENTS

This research is sponsored by the Defense Advanced Research Projects Agency (DARPA), Contract No. W91CRB-10-1-0003, technical sponsor Captain Christopher Warren, USN. The content of this paper does not necessarily reflect the position or the policy of the Government, and no official endorsement should be inferred.

[1]J. P. Rothstein, Annu. Rev. Fluid Mech. **42**, 89 (2010).
[2]M. Gad-el-Hak, *Flow Control: Passive, Active, and Reactive Flow Management* (Cambridge University Press, Cambridge, London, 2000).
[3]M. A. Samaha, H. V. Tafreshi, and M. Gad-el-Hak, Phys. Fluids **23**, 012001 (2011).
[4]J. Ou, J. B. Perot, and J. P. Rothstein, Phys. Fluids **16**, 4635 (2004).
[5]J. Ou and J. P. Rothstein, Phys. Fluids **17**, 103606 (2005).
[6]P. Joseph, C. Cottin-Bizonne, J.-M. Benoit, C. Ybert, C. Journet, P. Tabeling, and L. Bocquet, Phys. Rev. Lett. **97**, 156104 (2006).
[7]R. Truesdell, A. Mammoli, P. Vorobieff, P. van Swol, and C. J. Brinker, Phys. Rev. Lett. **97**, 044504 (2006).
[8]M. Martell, J. B. Perot, and J. P. Rothstein, J. Fluid Mech. **620**, 31 (2009).
[9]C. J. Teo and B. C. Khoo, Microfluid. Nanofluid. **7**, 353 (2009).
[10]R. Daniello, N. E. Waterhouse, and J. P. Rothstein, Phys. Fluids **21**, 085103 (2009).
[11]Y. P. Cheng, C. J. Teo, and B. C. Khoo, Phys. Fluids **21**, 122004 (2009).
[12]C. Lee, C.-H. Choi, and C.-J. Kim, Phys. Rev. Lett. **101**, 064501 (2008).
[13]H. Yang and Y. Deng, J. Colloid Interface Sci. **325**, 588 (2008).
[14]S. D. Bhagat, Y.-H. Kim, K.-H. Suh, Y.-S. Ahn, J.-G. Yeo, and J.-H. Han, Microporous Mesoporous Mater. **112**, 504 (2008).
[15]M. Bobji, S. V. Kumar, A. Asthana, and R. N. Govardhan, Langmuir **25**, 12120 (2009).
[16]M. Sakai, T. Yanagisawa, A. Nakajima, Y. Kameshima, and K. Okada, Langmuir **25**, 13 (2009).
[17]O. Gonzalez-Fernandez and I. Queralt, Appl. Spectrosc. **64**, 1045 (2010).
[18]M. Sohn, D. S. Himmelsbach, F. E. Barton, and P. J. Fedorka-Cray, Appl. Spectrosc. **63**, 1251 (2009).
[19]V. I. Tomin and R. Jaworski, Opt. Spectrosc. **109**, 618 (2010).
[20]S. Sarkar, S. Deevi, and G. Tepper, Macromol. Rapid Commun. **28**, 1034 (2007).
[21]H. Hess, M. Antia, and V. Vogel, Rev. Sci. Instrum. **75**, 266 (2004).
[22]G. Wünsch, A. Wennemer, and J. W. McLaren, Spectrochim. Acta B **46**, 1517 (1991).
[23]M. Czerny and A. F. Turner, Z. Phys. A: Hadrons Nucl. **61**, 792 (1930).
[24]See http://en.wikipedia.org/wiki/Monochromator.
[25]C. L. M. H. Navier, Mem. Acad. R. Sci. Inst. Fr. **6**, 389 (1823).
[26]Hysteresis is defined as the difference between advanced and receding angles for a moving contact line or for a drop on the verge of moving on a tilted surface.
[27]C. Lee and C.-J. Kim, Langmuir **25**, 12812 (2009).
[28]G. McHale, N. J. Shirtcliffe, and M. I. Newton, Langmuir **20**, 10146 (2004).
[29]C. W. Extrand, Langmuir **22**, 1711 (2006).
[30]T. Baldacchini, J. E. Carey, M. Zhou, and E. Mazur, Langmuir **22**, 4917 (2006).
[31]B. Bhushan, M. Nosonovsky, and Y. C. Jung, J. R. Soc., Interface **4**, 643 (2007).
[32]B. Bhushan, and Y. C. Jung, Prog. Mater. Sci. **56**, 1 (2011).

Downloaded 27 Apr 2011 to 128.172.52.138. Redistribution subject to AIP license or copyright; see http://rsi.aip.org/about/rights_and_permissions

APPENDIX IV: Influence of Flow on Longevity of Superhydrophobic Coatings

Following is a reprint of the paper "Influence of Flow on Longevity of Superhydrophobic Coatings," by Samaha, M.A., Tafreshi, H.V., and Gad-el-Hak, M., submitted to *Langmuir*, 2012.

Influence of Flow on Longevity of Superhydrophobic Coatings

Mohamed A. Samaha, Hooman Vahedi Tafreshi, and Mohamed Gad-el-Hak*

Department of Mechanical & Nuclear Engineering, Virginia Commonwealth University, Richmond, VA 23284-3015, USA

Abstract

Previous studies have demonstrated the capability of superhydrophobic surfaces to produce slip flow and drag reduction, which hold considerable promise for a broad range of applications. However, in order to implement such surfaces for practical utilizations, environmental factors such as water movement over the surface must be observed and understood. In this work, experiments were carried out to present a proof-of-concept study on the impact of flow on longevity of polystyrene fibrous coatings. The time-dependent hydrophobicity of a submerged coating in a pressure vessel was determined while exposing the coating to a rudimentary wall-jet flow. Rheological studies were also performed to determine the effect of the flow on drag reduction. The results show that the longevity of the surface deteriorates by increasing the flowrate. The flow appears to enhance the dissolution of air into water, which leads to a loss of drag-reduction.

Keywords

Superhydrophobic coatings; polystyrene fibers; longevity; drag reduction; mass transfer; convection; wall jet.

*Corresponding author (e-mail: gadelhak@vcu.edu; phone: +1 (804) 828-3576).

1 Introduction

Superhydrophobicity is a surface property that can be achieved by a combination of low surface energy and micro- or nanoscale surface roughness. The phenomenon is primarily manifested by water droplets beading on the solid surface with contact angles exceeding 150°. When submerged, these surfaces can entrap air between their micro- or nanostructures resulting in a surface with alternating air–water and solid–water interfaces. The presence of the air–water interface is responsible for the "slip effect" resulting in a reduction in the skin-friction drag exerted on a moving surface. The reader is referred to the review papers by Rothstein,[1] Shirtcliffe et al.,[2] and Samaha et al.,[3] and references therein. Superhydrophobic coatings provide a relatively simple, passive drag-reduction method, and may potentially become a viable alternative to the more complex and energy consuming active or reactive flow control techniques such as wall suction/blowing.[4] One of the challenges to overcome before field applications are feasible is slowing down the rate of loss of entrapped air to the environment when the coating is exposed to water flow. Longevity—the time until transition from dewetted (Cassie) to wetted (Wenzel) state—is the focus of this paper.

Superhydrophobic surfaces are often produced using the same microfabrication techniques developed for the electronic industry, and in many cases consist of a regular array of microposts or microridges.[5–7] Large-scale manufacturing of microfabricated superhydrophobic surfaces is prohibitively expensive. An alternative solution to circumvent the high cost is to produce surfaces made up of random deposition of hydrophobic particles[8–13] or electrospun fibers.[14,15] Electrospinning of superhydrophobic polymers is a simple, low-cost method that can be used to deposit micro- to nanofibrous coatings onto substrates of arbitrary geometry. The resulting

superhydrophobic surfaces could be applied in various ways, including self-cleaning, protection from corrosion, and reduction of skin-friction drag in underwater vessels such as submarines. Among several, three recent studies are related to the last application and the particular interest of the present paper. First, Shirtcliffe et al.[16] have developed a technique to cover the inside wall of a small copper tube (radius less than a millimeter) with a superhydrophobic surface and demonstrated drag reduction in laminar pipe flow. Second, McHale et al.[17] demonstrated that the drag reduction could be produced for a sphere coated with a superhydrophobic surface. Third, the same group[18] showed that the drag reduction diminishes as a superhydrophobic surface is subjected to higher flowrates.

The longevity of a submerged superhydrophobic surface depends primarily on the amount of time that air remains trapped within the surface microstructure. In other words, the degree of hydrophobicity and hence the beneficial effects are temporarily diminished by the reduction of the amount of air. Keeping and/or restoring the air layer between the surface and water were undertaken by few studies. For example, Stephani and Goldstein[19] utilized the electrolysis process to continuously generate air bubbles between a solid surface and water, which lead to producing drag reduction even if the surface is not hydrophobic. Lee and Kim[20] used a similar process to *rejuvenate* a dead microfabricated coatings, i.e., gas restoration for the wetted coatings to be converted back to be nonwetted.

Several approaches have been recently developed to estimate the longevity of superhydrophobic surfaces. Bobji et al.[21] used an optical technique to measure how long the surface could maintain its hydrophobicity under different hydrostatic pressures. This was accomplished by counting the number of shiny spots per unit area on the surface—an indication of the existence of an air–water interface. Similar studies were performed using a laser beam to investigate the effect of the

surface structure on the superhydrophobicity.[22] Poetes et al.[23] used a different optical technique to measure longevity of a superhydrophobic surface under pressure. Additionally, they mathematically interpreted the decay of longevity with pressure. Using optical measurements, Lei et al.[24] demonstrated that the wetting transition due to pressure could be either reversible (switching from nonwetted to wetted or vice versa) or irreversible (permanent wetting) depending on the value of the applied pressure. Rathgen and Mugele[25] developed an optical method to determine the contact angle and microscopic shape of the air–water interface under different hydrostatic pressure. Samaha et al.[26] developed an *in situ* noninvasive optical technique to accurately measure the longevity of submerged hydrophobic coatings using optical spectroscopy.

In this work, we study the effect of water movement on the degree of hydrophobicity and longevity of superhydrophobic polystyrene spun-fiber coatings as a step toward understanding the influence of environmental factors on the performance of superhydrophobic surfaces. No experimental study has yet been devoted to examine the impact of water flow on longevity. We developed superhydrophobic fibrous surfaces[15] using a recently developed DC biased AC-electrospinning process.[27] The fabrication of the fibrous coatings is explained in the next section. Section 3 describes our procedure for longevity measurements. This is followed by Section 4 in which an analysis is provided to determine the coating performance when subjected to a flow. The results of the study and related discussions are given in Section 5. Conclusions and recommendations for future studies are given in Section 6.

2 Fabrication

The hydrophobic polymer polystyrene (PS; Mn = 170,000) was purchased from Sigma-Aldrich Chemicals (St. Louis, Missouri). High-performance chromatography-grade toluene and N,N-Dimethylformamide (DMF) were obtained from the same supplier. Polymer fibers were fabricated using the solvents through the DC-biased AC-electrospinning process.[27] Fibers were electrospun from solutions with 18%, 25%, or 30% weight (wt) PS and deposited on a circular aluminum substrate 5 cm in diameter, but the data reported herein reflects only the first concentration. Full details of the experimental procedure to fabricate this coating are available in our previous work.[15] The surface morphology was determined using a field emission scanning electron microscope (FESEM) (S-70, Hitachi, Japan). As shown in Figure 1, the hydrophobic micro/nanofibers were produced as a layer over layer. The inset in the figure shows a water droplet on the coating with a static contact angle of 160 degrees, indicating superhydrophobicity. The contact angles were measured using a contact-angle ramé-hart goniometer (model number 100-25-A).[26] The deposited mat of hydrophobic fibers provides the surface roughness and porosity necessary to entrap air when the surface is immersed in water. As water flows over the surface, the interface between the entrapped air and water has very low skin friction resulting in slip flow and drag reduction.

To investigate other aspects of surface's hydrophobicity, both contact-angle hysteresis and threshold sliding angle are measured.[28–31] As the surface on which a water drop is placed is tilted, the downhill contact angle increases while the uphill contact angle decreases. As the tilt steepens, those two angles continue to increase and decrease respectively until the drop starts to move. Advancing and receding contact angles are defined as the downhill and uphill contact

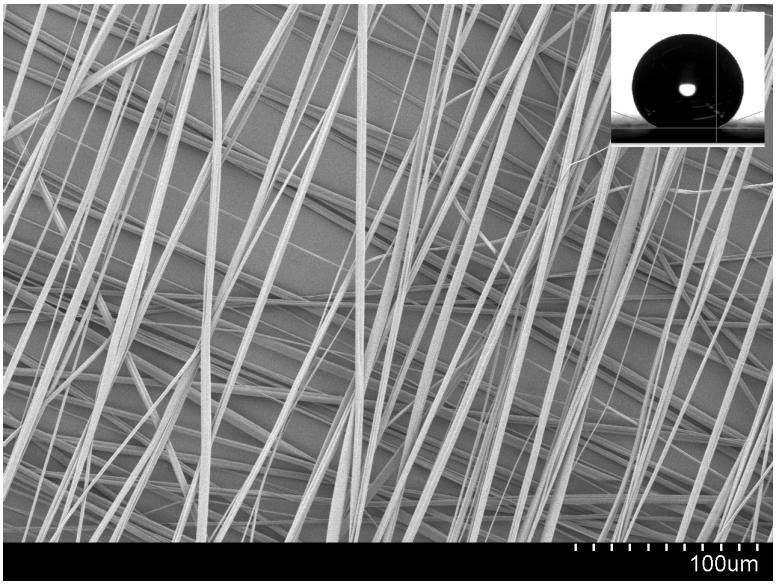

Figure 1: SEM image of 25% weight Polystyrene fibers with 1% weight glass beads. Upper right inset shows a water droplet on top of this particular coating with static contact angle of 160 degrees.

angles just before the drop starts to move. Hysteresis represents the difference between advancing and receding angles, while the threshold sliding angle is the tilting angle at incipient motion. Figure 2 is a plot of the difference between the downhill and uphill contact angles, $\Delta\alpha$, versus the tilting angle of a 9-mg deionized water droplet on the spun-fiber specimen. The figure shows that the contact-angle hysteresis is 11.5 degrees and the threshold sliding angle is 7.5 degrees. These angles are less that those of our previously reported surface,[26] demonstrating stronger superhydrophobicity. We reason that the coating used herein is thinner than that produced previously. Therefore, the terminal voltage difference is kept higher during the electrospinning process because with thinner coating the electrical resistance of the non-conductive polystyrene fibers is lower. This leads to producing fibers with smaller diameters, higher porosity, larger surface roughness, and higher degree of hydrophobicity.[14]

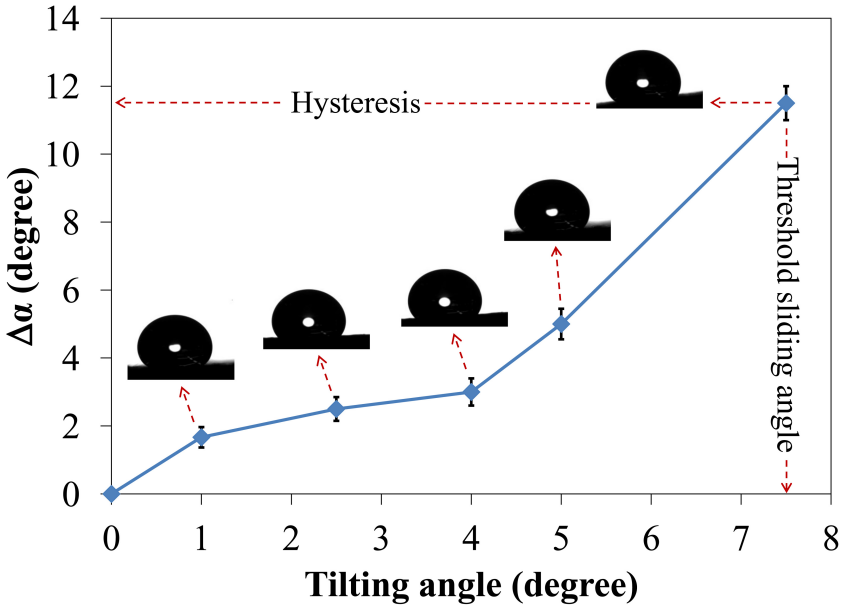

Figure 2: Contact-angle hystereses and threshold sliding angles for superhydrophobic fibrous coating.

3 Experiment

The present study investigates the effect of moving water on longevity of superhydrophobic surfaces to simulate a moving submersible object covered with a rough hydrophobic coating. As sketched in Figure 3, a three-dimensional wall-jet flow is produced using a LifeGard Aquatics Company's submersible pump, model number Quiet One 200, 0.50-m head, 3.34-lit/min flowrate. The piping system includes a stepper delivery valve to precisely control the flow. The 10-mm diameter tubes are flexible, transparent and smooth. The tested coating sample and the water-flow system are immersed underwater inside a pressure vessel.[26] The jet Reynolds number, $\mathrm{Re} \equiv U_o d/\nu$, is used to characterize the delivered flow, where U_o is the average water-jet velocity at nozzle exit that can be controlled using the flow control valve, d is the nozzle exit diameter (8.5 mm), and ν is the kinematic viscosity of water.

During the measurements, the coating with the substrate are completely and quickly im-

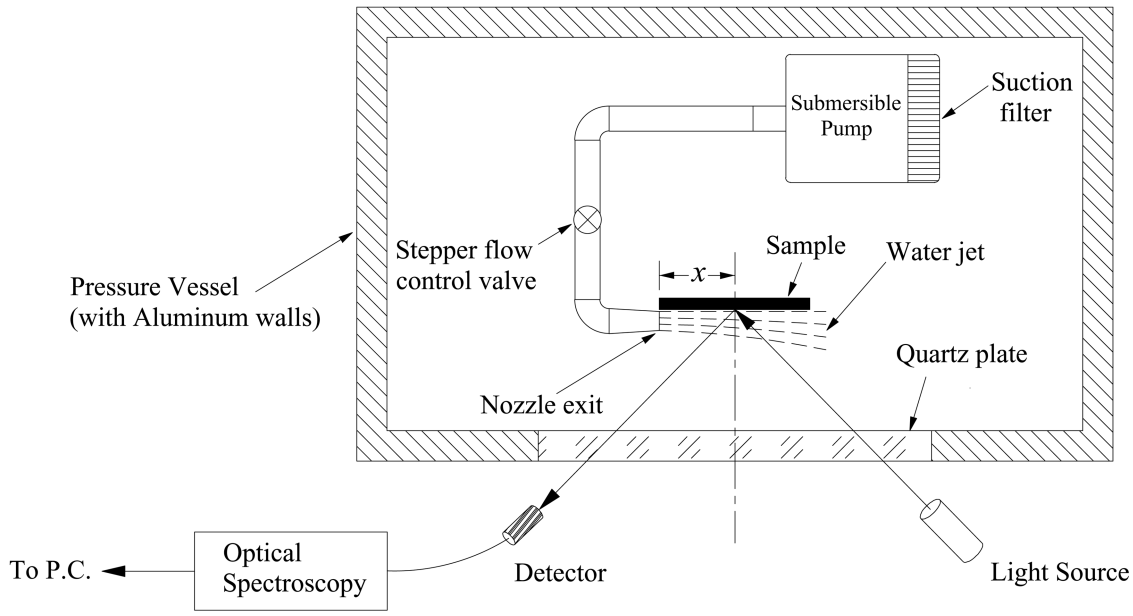

Figure 3: Schematic illustration of the setup used to investigate the effect of water movement on longevity of superhydrophobic fibrous coating.

mersed in water, hence the outer and lateral parts of the coating are exposed to water almost at the same time so that there is no way for the air to escape. The kinetics of air loss from the submerged superhydrophobic coating was measured using an optical spectroscopy system made by Photon Technology International, Inc. (model QuantaMaster^{TM} 30). The intensity of a broad-spectrum white light reflected from the submerged surface was measured as a function of time. As the reflectivity coefficient is greater for the air–water interface than for the solid–water interface, the intensity of the reflected light decreases as the amount of entrapped air is decreased (i.e., air is replaced by ambient water). The loss of trapped air will cause a transition from nonwetted (Cassie) state to wetted (Wenzel) state at which the light intensity signal becomes constant.[26]

In order to calibrate the flow delivered from the nozzle against the stepper-valve opening, the water-flow system was immersed in a water reservoir. The system delivers water to a graduated cylinder at zero static head. The flow resistance is only friction and eddy losses, which is the

same as the case of water flow inside the pressure vessel (Figure 3). Thus, at each valve opening, the flowrate can be determined by the volume of water collected in the graduated cylinder with time.

Skin-friction measurements were performed using a rheometer. The device is equipped with two parallel rotating discs separated by a small fluid-filled gap, and provides precise measurements of the stress–strain rate relation. The rotating disc is connected to a torque–speed measuring system used to calculate the shear stress developed by deionized water. The measured rotational speed is used to calculate the strain rate. The stress–strain rate relation was measured for both superhydrophobic samples as well as smooth control surfaces. More details about the setup and mathematical calculations to determine drag reduction were previously reported by Samaha et al.[26]

4 Analytical Considerations

In this section, we offer a rather simple argument on the well familiar concept of convective mass transfer. This will help placing the experimental results on a more firm foundation. Consider a superhydrophobic coating immersed in still water. In this case, the entrapped air dissolves in water by the well-known free-convection mass transfer[32,33] because of the difference in air concentration at the surface and above it. Air is weakly soluble in water and therefore Henry's Law is applicable. The air at the air–water interface can be considered saturated with water vapor. The water saturation pressure, P_{st}, and Henry's constant, H, corresponding to the water temperature ($22 \pm 0.1^{\circ}$C) could be determined. The temperature was measured using a Fisherbrand thermometer, 14-985E. Thus

$$P_v = P_{st} \tag{1}$$

where P_v is the partial pressure of water vapor in the gas side. The partial pressure of dry air in the gas side, P_d, is

$$P_d = P_a - P_v \tag{2}$$

where P_a is the atmospheric pressure. According to Henry's law, the mole fraction of air (Z_d) in the water at the surface becomes

$$Z_d = \frac{P_d}{H} \tag{3}$$

and the concentration of air in water at the surface, C_s will be

$$C_s = \rho \times \frac{M_a}{M_w} \times Z_d \tag{4}$$

where ρ is the aggregate density of air–water mixture, which is assumed to be the pure-water density at 22°C because the air concentration is small. M_a and M_w are the molecular weights of air and water, respectively. The Grashof number, Gr, could be calculated from the equation

$$\mathrm{Gr} = \frac{g(\rho_\infty - \rho_s)L_c^3}{\rho\nu^2} \tag{5}$$

where g is the gravitational acceleration, L_c is the characteristic length of the tested part of the sample (a spot with 3 mm diameter), ρ_∞ is the density of water away from the surface (the density of pure water), and ρ_s is the density of water at the surface. The difference $(\rho_\infty - \rho_s)$ is equal to the concentration of air in water at the surface (C_s) because the concentration of air away from the surface is zero (pure water). The calculations were performed based on the testing spot diameter and location. The Schmidt number, Sc, is determined from

$$\mathrm{Sc} = \frac{\nu}{D} \tag{6}$$

where D is the mass diffusivity of air in water at 22°C. Hence, the Rayleigh number, Ra, can be

found as

$$\mathrm{Ra} = \mathrm{Gr} \times \mathrm{Sc} \tag{7}$$

and the Sherwood number, Sh, could be calculated from the following correlation[32]

$$\mathrm{Sh} = 0.59(\mathrm{Ra})^{1/4}, \quad 10^5 < \mathrm{Ra} < 10^9 \tag{8}$$

The Sherwood number is the dimensionless mass-transfer convection coefficient

$$\mathrm{Sh} = \frac{h_m \times L_c}{D} \tag{9}$$

The rate of air mass transfer, $\dot{m}_a$, could be computed from

$$\dot{m}_a = \frac{m_a}{t} = h_m \times A_s \times (C_s - C_\infty) \tag{10}$$

where m_a is the total mass of air that transfered from the surface to water in time (t), A_s is the sample surface area, and $(C_s - C_\infty)$ is the difference in air concentration in water at and away from the surface respectively. Because all samples, which are tested under different flow conditions are identical, the surface area, A_s, is constant for all of them. Additionally, it is convenient to assume that m_a and $(C_s - C_\infty)$ are the same for all samples. Therefore, the water movement would only affect the mass-transfer convection coefficient (h_m) and hence, the longevity (t). From Equation 10, it is obvious that h_m is inversely proportional to t so that

$$\frac{h_{m1}}{h_{m2}} = \frac{t_2}{t_1} \tag{11}$$

By calculating the free convection coefficient, h_{m1}, for the still-water case using Equations (1)–(9) in addition to experimentally measuring the longevity for both still and moving water cases (t_1 and t_2, respectively), the forced mass-transfer convection coefficient, h_{m2}, due to the effect of water movement could be determined.

5 Results and Discussions

When a superhydrophobic surface is submerged in water, the spatial distribution of trapped air on the surface exhibits a mirror-like sheen at the air–water interface. Therefore, the kinetics of the trapped air's loss could be monitored by examining the intensity of reflected light from the surface over time to determine its longevity. We previously demonstrated the use of light scattering as an indirect means of characterizing the amount of air trapped within submerged superhydrophobic coatings against time.[26] In our technique, the reflected light spectrum could be measured as a function of jet Reynolds number, Re, and time. The spectrum is then integrated to obtain a wavelength-averaged reflection intensity. All measurements are carried out by projecting the light on a small portion of the sample for a light spot with a diameter of 3 mm on the sample. The distance x between the center of the spot and the nozzle exit is 9 mm (see Figure 3).

Figure 4 shows the normalized average reflected light intensity, I_n, versus time for four identical superhydrophobic fibrous coating samples subjected to different flow conditions, i.e., different Re. Each displayed point is an average of three different measurements. The normalized intensity is defined as

$$I_n = \frac{I - I_d}{I_f - I_d} \tag{12}$$

where I is the average integrated measured intensity across the range of wavelengths of visible light, I_d is the intensity for the completely hydrophilic sample (aged or dead sample), and I_f is the intensity for a superhydrophobic fresh sample at atmospheric pressure.

Figure 4 shows that the light intensity decreases with time for all samples, which indicates the loss of trapped air and a corresponding reduction in the degree of superhydrophobicity. This effect is believed to be due to the dissolution of air in water.[21,23] Figure 5 shows the period that

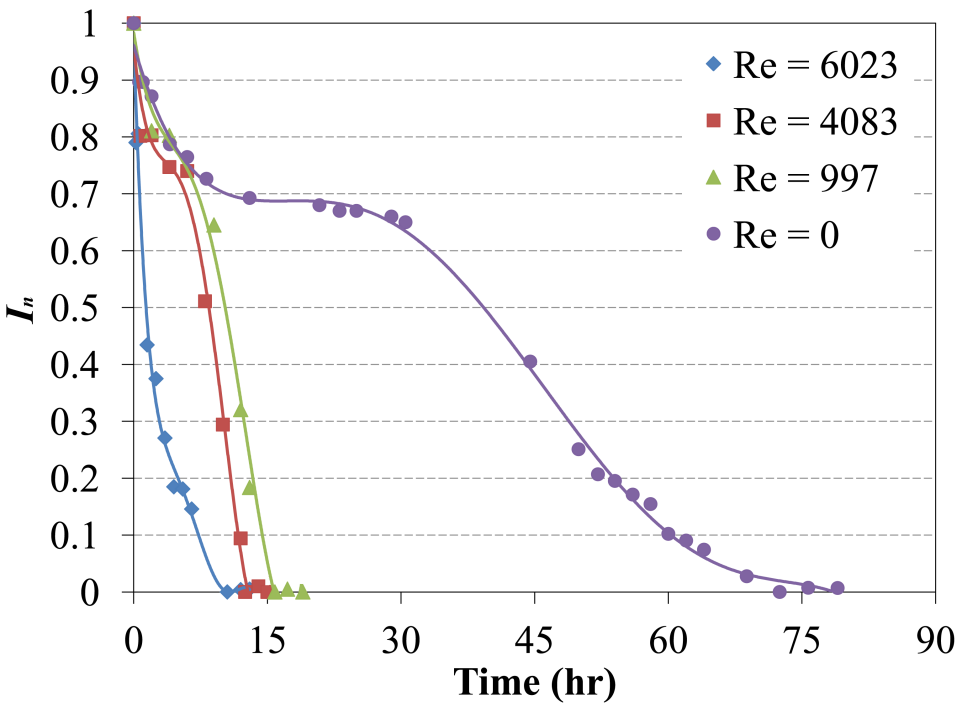

Figure 4: Effect of water movement on reflected light intensity from immersed coating samples. Solid lines are fifth-order polynomial fit of experimental data.

the samples take for wetting transition (longevity) against jet-Reynolds number (Re). Vertical and horizontal error bars are displayed but are too small to be visible. The figure demonstrates that as Re increases, longevity deteriorates. We reason that as water flows (even if with a relatively small Reynolds number), the flowrate strongly enhances the dissolution of the entrapped air in water where the mass-transfer free-convection regime turns into a forced convection one.

For further investigation, we repeated the previous measurements for identical samples with light spots located at different distances, x, but the nozzle-exit Reynolds number is kept constant (Re = 6023). Figure 6 shows the normalized average reflected light intensity, I_n, versus time and Figure 7 demonstrates the measured longevity at different distances, x. It is obvious that the longevity increases with increasing x. This is because of the reduction of the flow velocity in the flow direction (wall-jet flow characteristics) that reduces the rate of air dissolution in water.

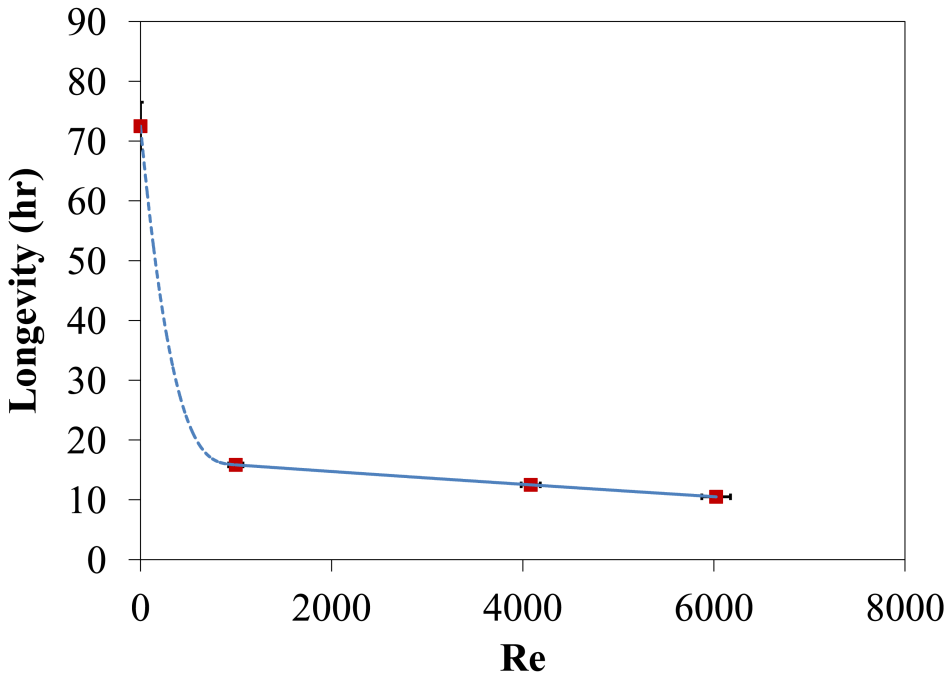

Figure 5: Effect of water movement on longevity of superhydrophobic fibrous coating. Solid and broken lines are best fit of experimental data in forced, free and mixed convection regimes.

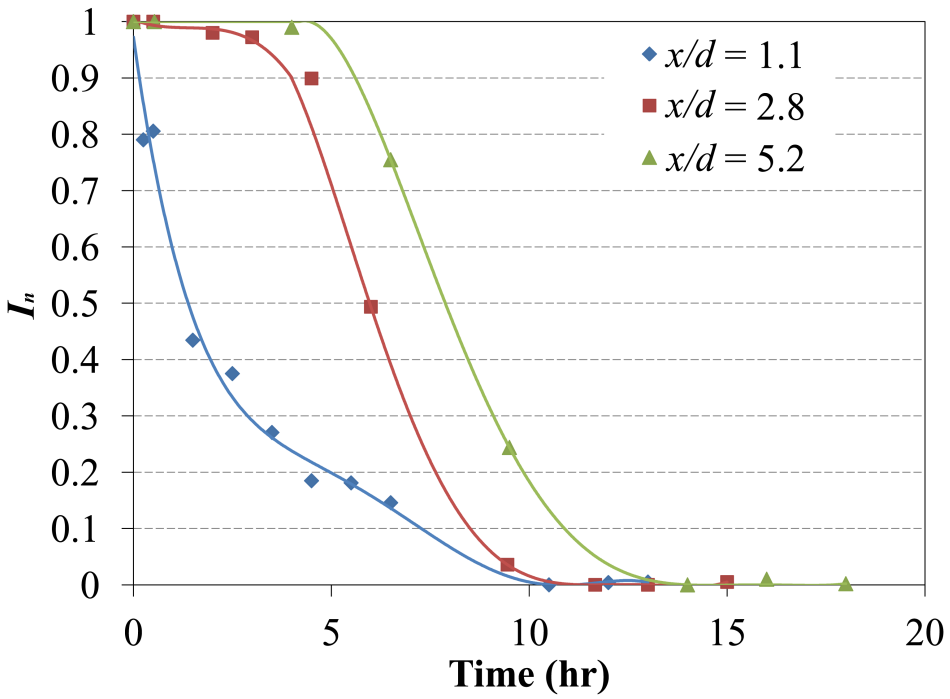

Figure 6: Time dependent reflected light intensity at several locations, x. Jet-Reynolds number is kept constant for all cases, Re = 6023. Solid lines are fifth-order polynomial fit of experimental data.

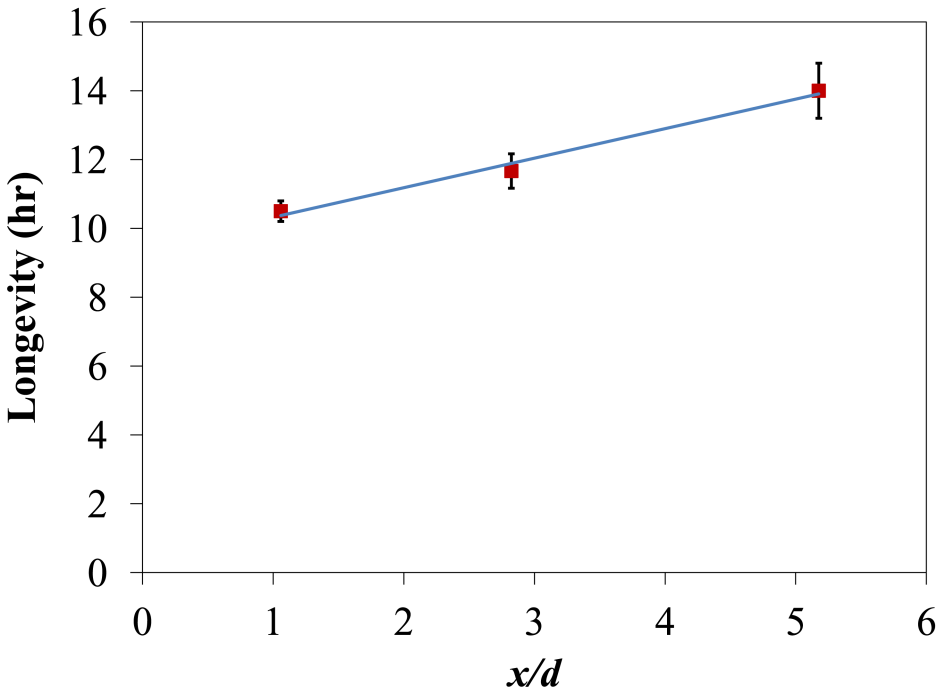

Figure 7: Longevity of the coating at several locations, x. Jet-Reynolds number is kept constant for all cases, Re = 6023. Solid line is best fit of experimental data.

As mentioned earlier, each point shown in Figures 5 and 7 is an average of three different measurements. The figures show that the standard deviations (demonstrated in the error bars) of the data are reasonable. Therefore, longevities of the identical samples are close to each other when the surfaces are subjected to the same flow conditions. This validates the implied assumption of Equation (11): the total mass of entrapped air, m_a, and concentration difference, $(C_s - C_\infty)$, are the same for identical samples.

In order to investigate the effect of wetting transition on the morphology of the coating, SEM images for typical samples before and after exposure to water were captured. For the latter case, the coating was immersed in water for three days to ensure that the wetting transition has occurred, then the sample was dried before taking the SEM photograph. It should be noted, however, that the scanning electron microscope we used does not allow the capturing of the

same spot from subsequent images. As shown in Figure 8, the hydrophobic microfibers for both cases have similar morphological characteristics. The range of fiber's diameter, porosity, and pores between fibers are similar in the two images. Therefore, air restoration for this kind of coating could be achieved as that accomplished for superhydrophobic surfaces with ordered microroughness.[20] This point will be pursed further in future work.

According to previous studies,[34–36] three-dimensional wall-bounded jets could be described as sketched in Figure 9. The velocity (u) is maximum at a location close to the wall. The maximum velocity (u_{max}) shifts up in the y-direction as x increases. The boundary-layer thickness increases and the value of the maximum velocity decreases in the flow direction (x). The velocity (u_{max}) also decays in the lateral direction (z). However, the velocity profiles are self-similar regardless of both the downstream distance x from the nozzle exit and lateral distance z from the plane of symmetry (x–y). The boundary layer at or near the nozzle exit is laminar then it transitions to turbulence at a certain downstream location. According to previously reported experiments,[37–39] the present low-Reynolds-number flow is laminar at the measurement locations. The laminar jet flow switches a free-convection mass-transfer case into a forced convection one with a concomitant higher mass-transfer coefficient.

We have calculated the convection coefficient for the still-water case (free convection) using Equations (1)–(9), and the coefficients for the water-movement cases using Equation (11). Figure 10 shows the dimensionless convection coefficient (Sherwood number) corresponding to the data shown in Figure 5, and demonstrates the expected increase of the convection coefficient (h_m) with increasing Reynolds number. The figure also demonstrates that h_m of the water-movement cases are much larger than that of the still-water one even for relatively low Reynolds number. Again, the flow enhances the dissolution of the entrapped air in water, which leads to much

(a)

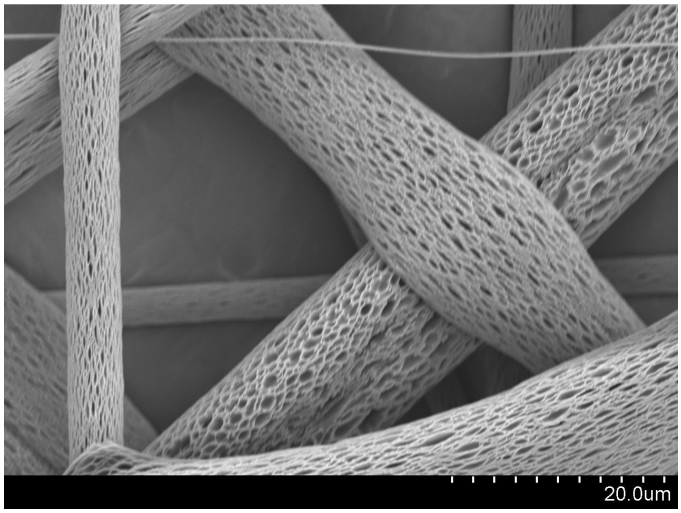

(b)

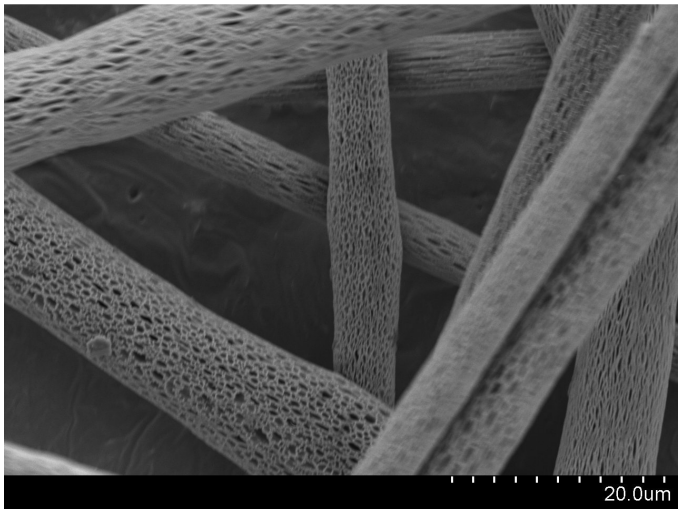

Figure 8: SEM images of superhydrophobic fibrous coating. (a) Before wetting transition; (b) after wetting transition. Images a and b are not for the same spot.

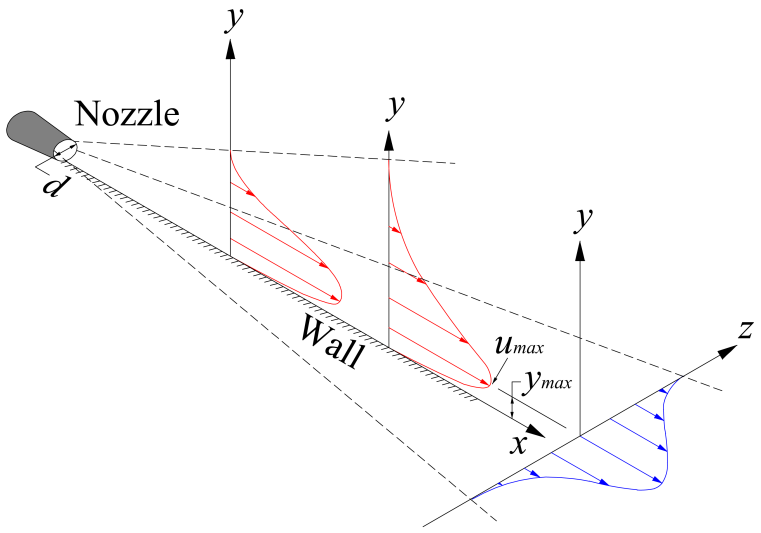

Figure 9: Schematic diagram for velocity profiles of three-dimensional wall jet.

higher convection coefficient. Similar conclusion could be drawn when changing the position x along the wall jet, as shown in Figure 11. The velocity decay in the flow direction results in decreasing the convection coefficient. Additionally, Figure 11 demonstrates that the convection coefficient decreases linearly within the specified range of distance x, which agrees well with prior studies.[40,41]

To further investigate the hydrophobicity of the coatings after exposure to different flow conditions, we measured the drag-reduction percentage (drag force of a coated surface compared to that of uncoated smooth one[26]) before and after exposing two identical samples to the longevity test for about 14 hours. The first sample was immersed in a stagnant water. The second one was subjected to a wall-jet flow with Re = 6023. As can be seen in Figure 12, before the two samples were subjected to the longevity test, the drag reduction of them is approximately the same, which verifies that the samples are identical. After the test is finished, the first sample loses only about 13.5% on average of its original drag-reduction but that of the second one was completely diminished. This validates the results shown in Figure 5 and confirms that the water-movement

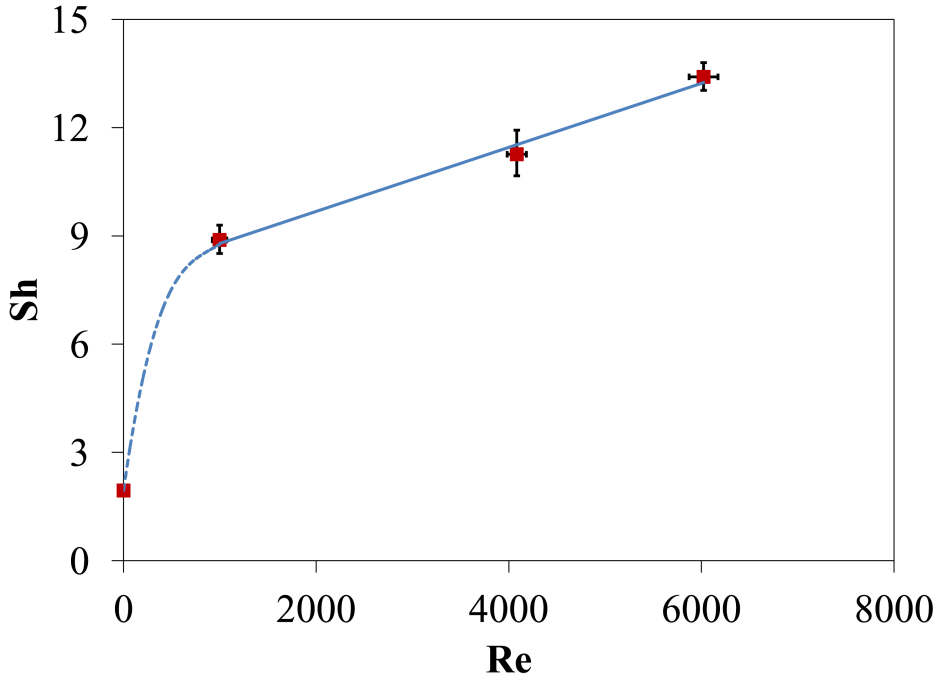

Figure 10: Dimensionless mass-transfer convection coefficient against jet-Reynolds number. Solid and broken lines are best fit of experimental data in forced, free and mixed convection regimes.

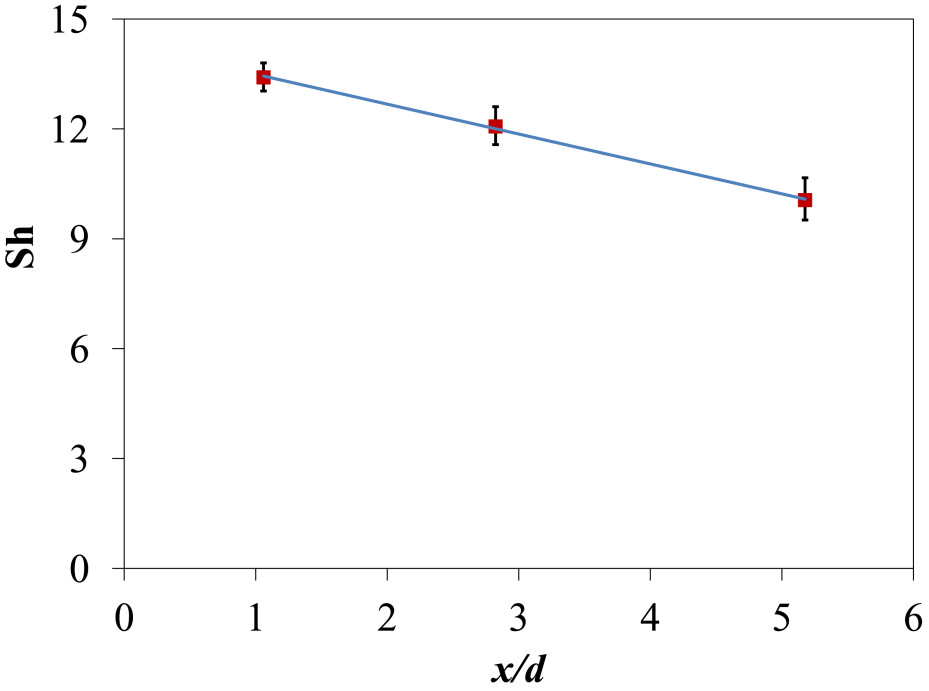

Figure 11: Dimensionless mass-transfer convection coefficient against location x. Jet-Reynolds number is kept constant for all cases, Re = 6023. Solid line is best fit of experimental data.

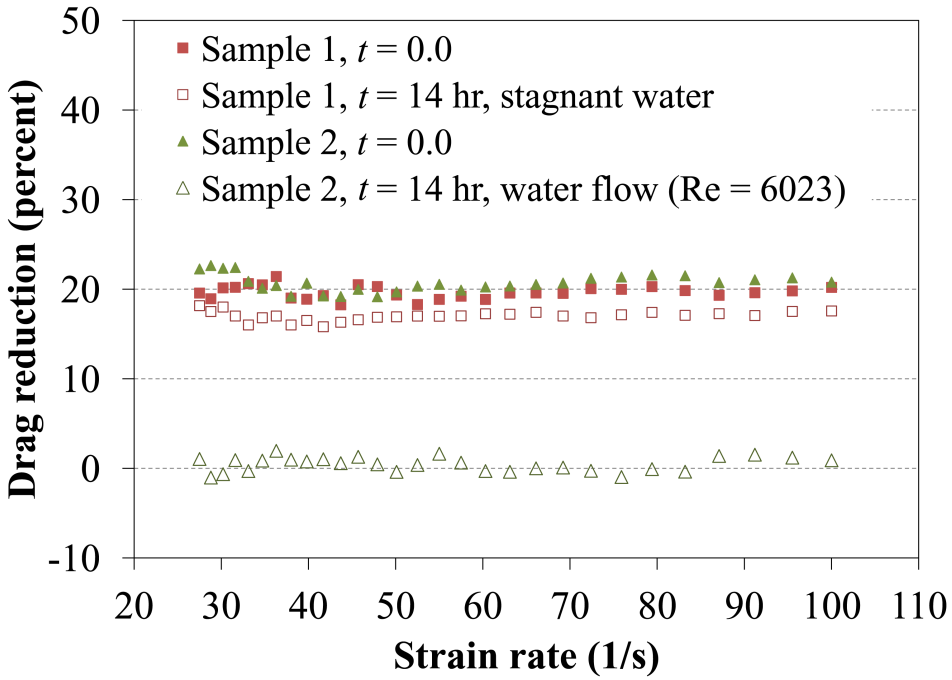

Figure 12: Drag reduction for two identical samples subjected to two different flow conditions.

over superhydrophobic coatings accelerates their wetting transition.

6 Conclusions

A light-scattering technique is utilized to measure the effect of water flow on how long a superhydrophobic surface can keep its favorable property (longevity). The hydrophobicity is diminished as the entrapped air layer between the surface and water is lost. This work presents experimental proof for the reduction of longevity with increasing flow velocity over electrospun fibrous superhydrophobic coatings. Increasing the flowrate increases the mass-transfer convection coefficient. For longevity, we reason that the stronger convection leads to enhancing the dissolution of entrapped air in water and thus to accelerating the transition to the wetted state. Our light-scattering data were compared to drag-reduction measurements for further verification, and good correlation was observed between the two techniques.

The results show that the water movement over superhydrophobic surfaces significantly affects their hydrophobicity, which opens a pathway for developing optimum coatings to be used for underwater applications. Such surfaces could survive longer under different flow conditions. Future research will consider air-restoration systems to enable the recovery (rejuvenation) of surface's hydrophobicity.

Acknowledgement

We thank Dr. Fredrick O. Ochanda for participating in capturing the three SEM images in this paper. This research is sponsored by the Defense Advanced Research Projects Agency (DARPA), contract number W91CRB-10-1-0003, technical sponsor Captain Christopher Warren, USN. The content of this paper does not necessarily reflect the position or the policy of the Government, and no official endorsement should be inferred.

References

1. Rothstein, J. P. Slip on superhydrophobic surfaces. *Annu. Rev. Fluid Mech.* **2010**, *42*, 89–109.

2. Shirtcliffe, N. J.; McHale, G.; Atherton, S.; Newton, M. I. An introduction to superhydrophobicity. *Adv. Colloid Interface Sci.* **2010**, *161*, 124–138.

3. Samaha, M. A.; Tafreshi, H. V.; Gad-el-Hak, M. Superhydrophobic surfaces: From the lotus leaf to the submarine. *C. R. Mec.* **2012**, *340*, 18.

4. Gad-el-Hak, M. *Flow Control: Passive, Active, and Reactive Flow Management*, Cambridge University Press, London, United Kingdom, 2000.

5. Shirtcliffe, N. J.; McHale, G.; Newton, M. I.; Chabrol, G.; Perry, C. C. Dual-scale roughness produces unusually water-repellent surfaces. *Adv. Mater.* **2004**, *16*, 1929–1932.

6. Davies, J.; Maynes, D.; Webb, B. W.; Woolford, B. Laminar flow in a microchannel with superhydrophobic walls exhibiting transverse ribs. *Phys. Fluids* **2006**, *18*, 087110.

7. Lee, C.; Choi, C-H.; Kim, C-J. Structured surfaces for giant liquid slip. *Phys. Rev. Lett.* **2008**, *101*, 064501.

8. Bhagat, S. D.; Kim, Y-H.; Suh, K-H.; Ahn, Y-S.; Yeo, J-G.; Han, J-H. Super hydrophobic silica aerogel powders with simultaneous surface modification, solvent exchange and sodium ion removal from hydrogels. *Microporous Mesoporous Mater.* **2008**, *112*, 504–509.

9. Yang, H.; Deng, Y. Preparation and physical properties of superhydrophobic papers. *J. Colloid Interface Sci.* **2008**, *325*, 588–593.

10. Lee, S.; Kim, D.; Hwang, W. Artificial lotus leaf structure made by blasting with sodium bicarbonate. *Curr. Appl Phys.* **2011**, *11*, 800–804.

11. Hwang, H. S.; Kim, N. H.; Lee, S. G.; Lee, D. Y.; Cho, K.; Park, I. Facile fabrication of transparent superhydrophobic surfaces by spray deposition. *ACS Appl. Mater. Interfaces* **2011**, *3*, 2179–2183.

12. Samaha, M. A.; Tafreshi, H. V.; Gad-el-Hak, M. Effects of hydrostatic pressure on the drag reduction of submerged aerogel-particle coatings. *Colloids Surf., A* **2012**, *399*, 62–70.

13. Emami, B.; Bucher, T. M.; Tafreshi, H. V.; Pestov, D.; Gad-el-Hak, M.; Tepper, G. C. Simulation of meniscus stability in superhydrophobic granular surfaces under hydrostatic pressures. *Colloids Surf., A* **2011**, *385*, 95–103.

14. Ma, M.; Mao, Y.; Gupta, M.; Gleason, K. K.; Rutledge, G. C. Superhydrophobic fabrics produced by electrospinning and chemical vapor deposition. *Macromolecules* **2005**, *38*, 9742–9748.

15. Ochanda, F. O.; Samaha, M. A.; Tafreshi, H. V.; Tepper, G. C.; Gad-el-Hak, M. Fabrication of superhydrophobic fiber coatings by DC-biased AC-electrospinning. *J. Appl. Polym. Sci.* **2012**, *123*, 1112–1119.

16. Shirtcliffe, N. J.; McHale, G.; Newton, M. I.; Zhang, Y. Superhydrophobic copper tubes with possible flow enhancement and drag reduction. *ACS Appl. Mater. Interfaces* **2009**, *1*, 1316–1323.

17. McHale, G.; Shirtcliffe, N. J.; Evans, C. R.; Newton, M. I. Terminal velocity and drag reduction measurements on superhydrophobic spheres. *Appl. Phys. Lett.* **2009**, *94*, 064104.

18. McHale, G.; Newton, M. I.; Shirtcliffe, N. J. Immersed superhydrophobic surfaces: gas exchange, slip and drag reduction properties. *Soft Matter* **2010**, *6*, 714–719.

19. Stephani, K. A.; Goldstein, D. B. An Examination of trapped bubbles for viscous drag reduction on submerged surfaces. *J. Fluid. Eng.—T. ASME* **2010**, *132*, 041303.

20. Lee, C.; Kim, C-J. Underwater restoration and retention of gases on superhydrophobic surfaces for drag reduction. *Phys. Rev. Lett.* **2011**, *106*, 014502.

21. Bobji, M. S.; Kumar, S. V.; Asthana, A.; Govardhan, R. N. Underwater sustainability of the "Cassie" state of wetting. *Langmuir* **2009**, *25*, 12120–12126.

22. Sakai, M.; Yanagisawa, T.; Nakajima, A.; Kameshima, Y.; Okada, K. Effect of surface structure on the sustainability of an air Layer on superhydrophobic coatings in a water–ethanol mixture. *Langmuir* **2009**, *25*, 13–16.

23. Poetes, R.; Holtzmann, K.; Franze, K.; Steiner, U. Metastable underwater superhydrophobicity. *Phys. Rev. Lett.* **2010**, *105*, 166104.

24. Lei, L.; Li, H.; Shi, J.; Chen, Y. Diffraction patterns of a water-submerged superhydrophobic grating under pressure. *Langmuir* **2010**, *26*, 3666–3669.

25. Rathgen, H.; Mugele, F. Microscopic shape and contact angle measurement at a superhydrophobic surface. *Faraday Discuss.* **2010**, *146*, 49–56.

26. Samaha, M. A.; Ochanda, F. O.; Tafreshi, H. V.; Tepper, G. C.; Gad-el-Hak, M. *In Situ*, non-invasive characterization of superhydrophobic coatings. *Rev. Sci. Instrum.* **2011**, *82*, 045109.

27. Sarkar, S.; Deevi, S.; Tepper, G. Biased AC electrospinning of aligned polymer nanofibers. *Macromol. Rapid Commun.* **2007**, *28*, 1034–1039.

28. Feng, L.; Li, S.; Li, Y., Li, H.; Zhang, L.; Zhai, J.; Song, Y.; Liu, B.; Jiang, L.; Zhu, D. Super-Hydrophobic Surfaces: From Natural to Artificial. *Adv. Mater.* **2002**, *14*, 1857–1860.

29. Quéré, D. Surface chemistry: Fakir droplets. *Nat. Mater.* **2002**, *1*, 14–15.

30. Extrand, C. W. Designing for optimum liquid repellency. *Langmuir* **2006**, *22*, 1711–1714.

31. McHale, G.; Shirtcliffe, N. J.; Newton, M. I. Contact-angle hysteresis on super-hydrophobic surfaces. *Langmuir* **2004**, *20*, 10146–10149.

32. Cengel, Y. A. *Heat Transfer: A Practical Approach*, McGraw-Hill, Boston, USA, 2003.

33. Bejan, A. *Convection Heat Transfer*, John Wiley & Sons, Hoboken, New Jersey, USA, 2004.

34. Swamy, N. V. C.; Gowda, B. h. L. Characteristics of three-dimensional wall jets. *Z. Flugwiss.* **1974**, *22*, 314–323.

35. Swamy, N. V. C.; Bandyopadhyay, P. Mean and turbulence characteristics of three-dimensional wall jets. *J. Fluid Mech.* **1975**, *71*, 541–562.

36. Schlichting, H. *Boundary-Layer Theory*, McGraw-Hill, New York, USA, 1979.

37. Eriksson, J. G.; Karlsson, M. R.; Persson, J. An experimental study of a two-dimensional plane turbulent wall jet. *Exp. Fluids* **1998**, *25*, 50–60.

38. Bajura, R. A.; Catalano, R. I. Transition in a two-dimensional plane wall jet. *J. Fluid Mech.* **1975**, *70*, 773–799.

39. Hsiao, F-B.; Sheu, S-S. Experimental studies on flow transition of a plane wall jet. *Aeronaut. J.* **1996**, *100*, 373–380.

40. Mabuchi, I.; Kumada, M. Studies on heat transfer to turbulent Jets with adjacent boundaries: 1st report, flow development and mass transfer in plane turbulent wall jet. *B. JSME* **1972**, *15*, 1236–1245.

41. Kanna, P. R.; Das, M. K. Conjugate forced convection heat transfer from a flat plate by laminar plane wall jet flow. *Int. J. Heat Mass Transfer* **2005**, *48*, 2896–2910.

APPENDIX V: Sustainability of Superhydrophobicity Under Pressure

Following is a reprint of the paper "Sustainability of Superhydrophobicity Under Pressure," by Samaha, M.A., Tafreshi, H.V., and Gad-el-Hak, M., submitted to *Physics of Fluids*, 2012.

Sustainability of superhydrophobicity under pressure

Mohamed A. Samaha,[1, a)] Hooman Vahedi Tafreshi,[1, b)] and Mohamed Gad-el-Hak[1, c)]

Department of Mechanical & Nuclear Engineering, Virginia Commonwealth University, Richmond, Virginia 23284-3015, USA

(Dated: 25 April 2012)

Prior studies have demonstrated that superhydrophobicity of submerged surfaces is influenced by hydrostatic pressure and other environmental effects. Sustainability of a superhydrophobic surface could be characterized by both how long it maintains the trapped air in its surface pores, so-called "longevity", and the pressure beyond which it undergoes a global wetting transition, so-called "terminal pressure". In this work, we investigate the effects of pressure on the performance of electrospun polystyrene fibrous coatings. The time-dependent hydrophobicity of the submerged coating in a pressure vessel is optically measured under elevated pressures. Rheological studies are also performed to determine the effects of pressure on drag reduction and slip length. The measurements indicate that surface longevity exponentially decays with increasing pressure in perfect agreement with the studies reported in the literature at lower pressures. It is found, however, that fibrous coatings could resist hydrostatic pressures significantly higher than those of previously reported surfaces. Our observations indicate that superhydrophobic fibrous coatings could potentially be used for underwater applications.

PACS numbers: (47), (68)

[a)]samahama@vcu.edu

[b)]htafreshi@vcu.edu; http://www.people.vcu.edu/~htafreshi/

[c)]gadelhak@vcu.edu; http://www.people.vcu.edu/~gadelhak/

I. INTRODUCTION

Exposing a rough hydrophobic surface to water could result in an effect known as superhydrophobicity, which characterized by water droplets beading on the surface at contact angles exceeding 150 degrees. According to Lafuma and Quéré,[1] superhydrophobicity could be explained using the models independently developed by Wenzel[2] and Cassie.[3] Microscopically rough hydrophobic surfaces could entrap air in their pores resulting in a surface with both air–water and solid–water interfaces. The presence of the air–water interface is responsible for the slip effect, characterized by an effective "slip length".[4] This in turn results in a significant reduction in the skin-friction drag exerted on a moving, submerged surface.[5,6] As long as air pockets are entrapped in the surface pores, the surface remains superhydrophobic. In other words, the degree of hydrophobicity depends on the amount of air entrapped on the surface. The longevity of a superhydrophobic surface—how long the surface could maintain the entrapped air—is critical, especially in underwater applications. Several approaches have been recently developed to estimate the longevity of superhydrophobic surfaces under hydrostatic pressure.[7–10] This area is the focus of the present research.

The first manmade superhydrophobic surfaces were produced using the same microfabrication techniques developed for the computer industry. The coatings typically consist of a regular array of microposts, shallow microcavities or microridges, etc.[11–14] The orientation of microroughness, flow characteristics, and shape of air–water interface (meniscus) could all significantly affect the slip condition and hence the drag reduction. For example, Woolford et al.[14] demonstrated that in a turbulent flow regime, streamwise ridges (i.e., flow direction parallel to the microridges) could lead to drag reduction, while spanwise ridges (i.e., flow direction perpendicular to the microridges) could lead to drag increase. Additionally, Steinberger et al.[15] demonstrated that the meniscus shape influences the boundary condition, which could increase the friction. Large-scale manufacturing of microfabricated superhydrophobic surfaces is prohibitively expensive. An alternative solution to circumvent the high cost is to produce surfaces made up of random deposition of hydrophobic particles[16–18] or electrospun fibers.[19,20] Electrospinning of superhydrophobic polymers is a simple, low-cost method that could be used to deposit micro- to nanofibrous coatings onto substrates of arbitrary geometry. The resulting superhydrophobic surfaces could be applied for various purposes, including self-cleaning, protection from corrosion, and, most significantly, reducing

skin-friction drag for underwater vessels such as torpedoes and submarines.

In 2006, Liu and Lange[21] provided a theoretical model to predict the so-called "critical pressure" at which a superhydrophobic surface starts departing from the Cassie state. Since then many other numerical and analytical studies have been performed to predict the critical pressure. Some of these studies predicted the meniscus stability for surfaces comprised of ordered[22,23] and/or random roughness.[18,24–26] Other studies have been performed to determine the meniscus shape at different pressures up to the critical pressure.[27–29] Samaha et al.[17] experimentally determined the so-called "terminal pressure" beyond which the surface undergoes a global transition from the Cassie state to the Wenzel state, and therefore can no longer generate drag reduction. Note that the *terminal pressure* differs from the *critical pressure*. The latter is the pressure above which the surface starts transitioning from the Cassie state but not necessarily globally reaching the Wenzel state. In other words, the critical pressure is lower than the terminal one.

In this work, we study the effects of elevated pressure on hydrophobicity and longevity of submerged superhydrophobic polystyrene fibrous coatings. As an example of such cost-effective fibrous surfaces, we produced an electrospun polystyrene mat and studied its time-dependent hydrophobicity under elevated pressures. The fibrous surfaces were produced[20] using a recently developed DC-biased AC-electrospinning process.[30] Fabrication and longevity are discussed in the next section. Results and discussions are given in Section III, followed by concluding remarks in Section IV.

II. SURFACE FABRICATION AND TESTING METHOD

Polystyrene (PS; Mn = 170,000), N,N-Dimethylformamide (DMF) and high-performance chromatography-grade toluene were purchased from Sigma-Aldrich Chemicals (St. Louis, Missouri). Fibrous surfaces were fabricated using the DC-biased AC-electrospinning technique.[30] The fibers were electrospun from solutions with 18% weight (wt) PS and deposited on circular aluminum substrate (5 cm diameter). Full details of the experimental procedure to fabricate the superhydrophobic coating are available in a previous paper.[20]

Figure 1 shows an example of the fibrous coatings. A mat of such hydrophobic fibers provides the surface roughness necessary to entrap air when immersed in water. Superhydrophobicity is exhibited in the figure inset, which shows a small water drop with a static

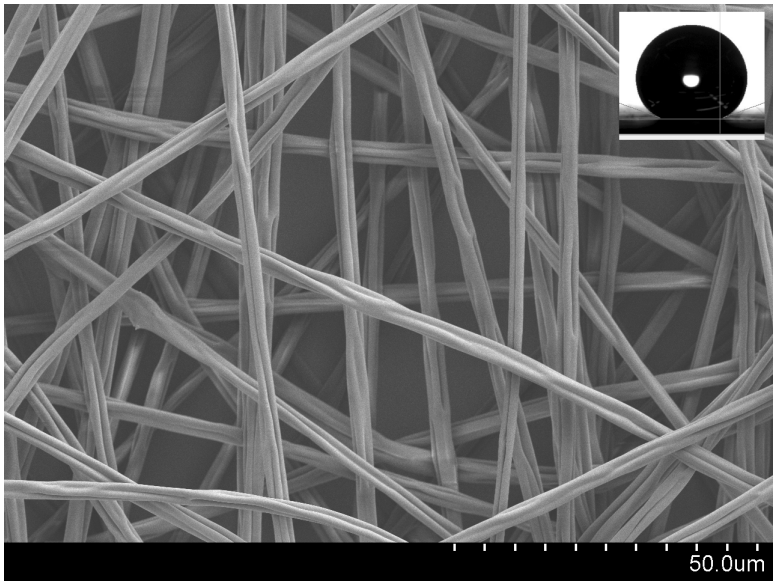

FIG. 1. SEM image of 18% weight Polystyrene fibers. Upper right inset shows a water droplet on top of this particular coating with static contact angle of 157 degrees.

contact angle of 157 degrees. The angles were measured using a contact-angle ramé-hart goniometer (model number 100-25-A).

When a superhydrophobic surface is submerged in water, the entrapped air exhibits a mirror-like sheen at the air–water interface. Therefore, the longevity of the trapped air could be monitored by examining the intensity of reflected light from the surface over time. Bobji et al.[7] used an optical technique to measure how long the surface could maintain its hydrophobicity under different hydrostatic pressures. Similar studies were performed using a laser beam to investigate the effect of the surface structure on superhydrophobicity.[8] Poetes et al.[9] also used an optical technique to test the longevity of a superhydrophobic surface under pressure and developed a mathematical relationship for the decay of longevity with pressure. Using optical measurements, Lei et al.[31] demonstrated that the wetting transition due to pressure could be either reversible (switching between nonwetted and wetted states) or permanently wetting depending on the pressure. Rathgen and Mugele[32] developed a laser-based method to determine the slope of the air–water interface on microscales under different hydrostatic pressures.

In the present research, the kinetics of air loss from the submerged superhydrophobic coatings is measured using an optical spectroscopy system made by Photon Technology International, Inc. (model QuantaMaster^{TM} 30). The intensity of a broad-spectrum white

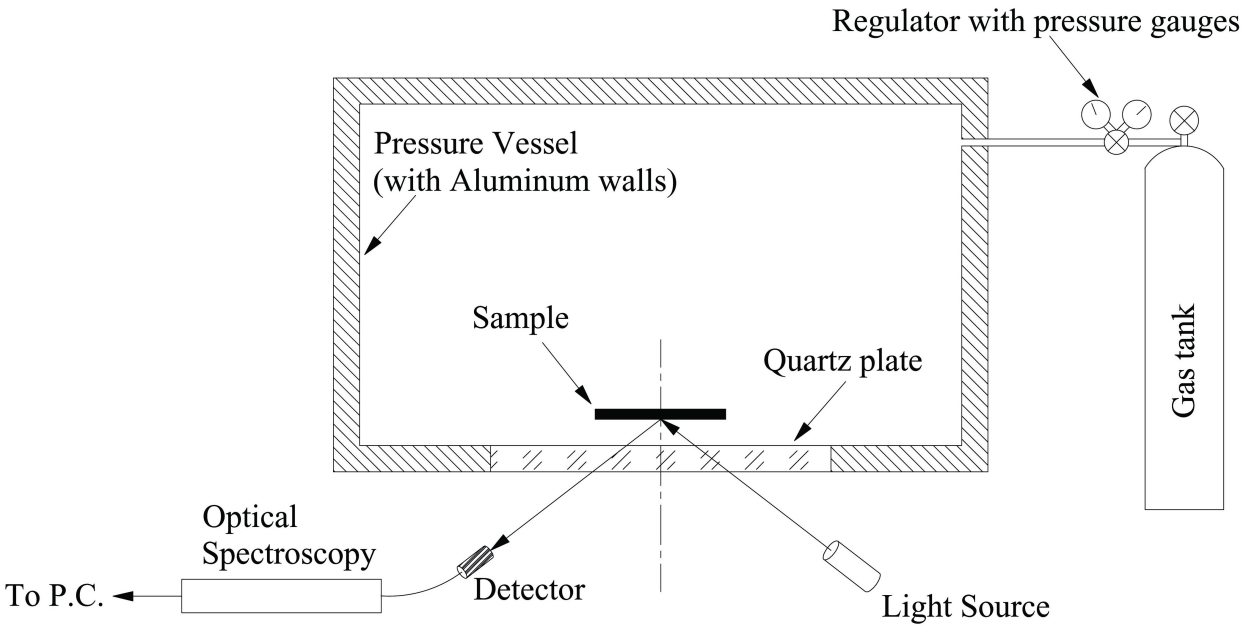

FIG. 2. Schematic illustration of setup used to investigate effect of elevated pressure on longevity of superhydrophobic fibrous coating. Figure reprinted with permission from Samaha et al.[17]

light reflected from the submerged surface under pressure is measured as a function of time using the setup schematically depicted in Figure 2. The pressure is produced using a nitrogen gas tank connected to the pressure vessel in which the sample was submerged. As the reflectivity coefficient is greater for the air–water interface than for the solid–water interface, the intensity of the reflected light decreases as the amount of the entrapped air decreases (i.e., air is replaced by ambient water). The loss of trapped air will cause a transition from nonwetted (Cassie) state to wetted (Wenzel) state at which the light intensity signal becomes constant.[10]

Skin-friction measurements were performed using an Anton Paar rheometer (model Physica MCR 301). The device is equipped with two parallel rotating discs separated by a small fluid-filled gap, and provides precise measurements of the stress–strain rate relation. The rotating disc is connected to a torque–speed measuring system used to calculate the shear stress developed by deionized water. The measured rotational speed is used to calculate the strain rate. The stress–strain rate relation was measured for both superhydrophobic samples as well as smooth control surfaces. More details about the setup and mathematical calculations to determine both drag reduction and slip length were previously reported by Samaha et al.[10]

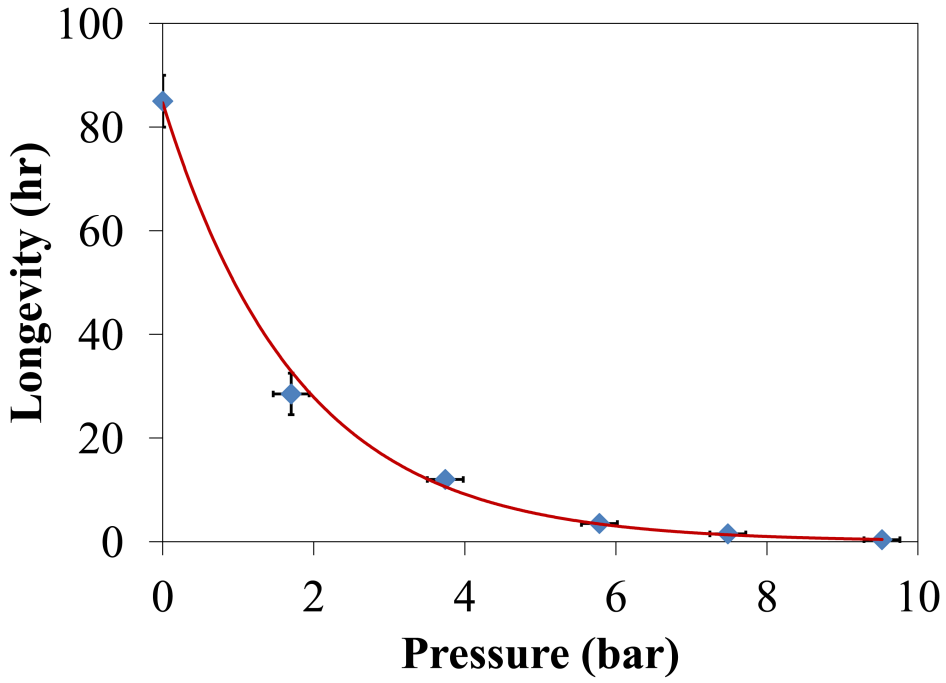

FIG. 3. Effect of elevated pressure on longevity of superhydrophobic fibrous coating. Solid line is exponential fit of experimental data.

III. RESULTS AND DISCUSSIONS

We previously demonstrated the use of light scattering as an in-situ, non-invasive probe for characterizing the time-dependent superhydrophobicity of a submerged surface.[10] The method relies on integrating the spectrum of reflected light to obtain a wavelength-averaged reflection intensity. All measurements are carried out by projecting the light on a small portion (3 mm in diameter) of a larger sample.

The experiments have shown that the light intensity decreases with time for all samples. This indicates a reduction of entrapped air and its associated superhydrophobicity over time, due perhaps to the dissolution of air in water.[7,9] Figure 3 shows an example of the longevity measurements versus pressure conducted for the aforementioned fibrous coatings. Each data point is the mean value of three measurements. The figure demonstrates that as pressure increases, longevity exponentially decreases in good agreement with a previously published theory.[9]

According to Poetes et al.,[9] the gases in the trapped air (N_2, O_2, etc.) could be considered

ideal gases whose fugacities f satisfy the following differential relation

$$\left(\frac{\partial \ln f}{\partial P}\right)_{T,c} = \frac{\overline{v}}{RT} \tag{1}$$

where P is the hydrostatic pressure, $\overline{v}$ is the molar volume, R is the gas constant, c is the dissolved gas concentration, and T is the temperature. By integrating both sides between a hydrostatic pressure, P, and atmospheric pressure, P_0, and substituting the equilibrium partial pressure P' for the fugacities, we get

$$\ln\left(\frac{P'}{P'_0}\right) = \frac{\overline{v}}{RT}[P - P_0] \tag{2}$$

or

$$P' = P'_0 \exp\left(\frac{\overline{v}}{RT}[P - P_0]\right) \tag{3}$$

Equation 3 indicates an exponential increase of the partial vapor pressures of the gases in the trapped air with hydrostatic pressure, which leads to an exponential increase of air solubility in water and hence exponential decay of coating's longevity (see Figure 3). Additionally, the figure indicates that the terminal pressure[17] for this particular coating could go up to 9.5 bars, which is two orders of magnitudes higher than those observed in previous studies.[7,9] We reason that the scale of microroughness (the distances between the fibers) is about five microns at some locations and approaches nanoscale at others (see Figure 1), while that of the previous studies[7,9] is of order a hundred microns. The significantly low microroughness scale of the present fibrous coating increases the sustainability of the air–water interface against pressure, indicating that such coatings could potentially be used for deep underwater applications.

To further investigate the superhydrophobicity of the coatings after exposure to elevated pressure, we measured the slip length as a quantity to characterize the slip produced by such a coating. According to Navier's model,[4] the magnitude of the slip velocity is proportional to the magnitude of the strain rate with the slip length being the proportionality constant so that

$$\delta = \frac{(U_{slip})_{wall}}{\frac{\partial u}{\partial y}|_{wall}} \tag{4}$$

where δ is the slip length, $(U_{slip})_{wall}$ is the slip velocity at the superhydrophobic wall, u is the streamwise velocity, and y is the normal direction. The slip length has been obtained before and after exposing two statistically identical samples to two different pressures for about 1.5

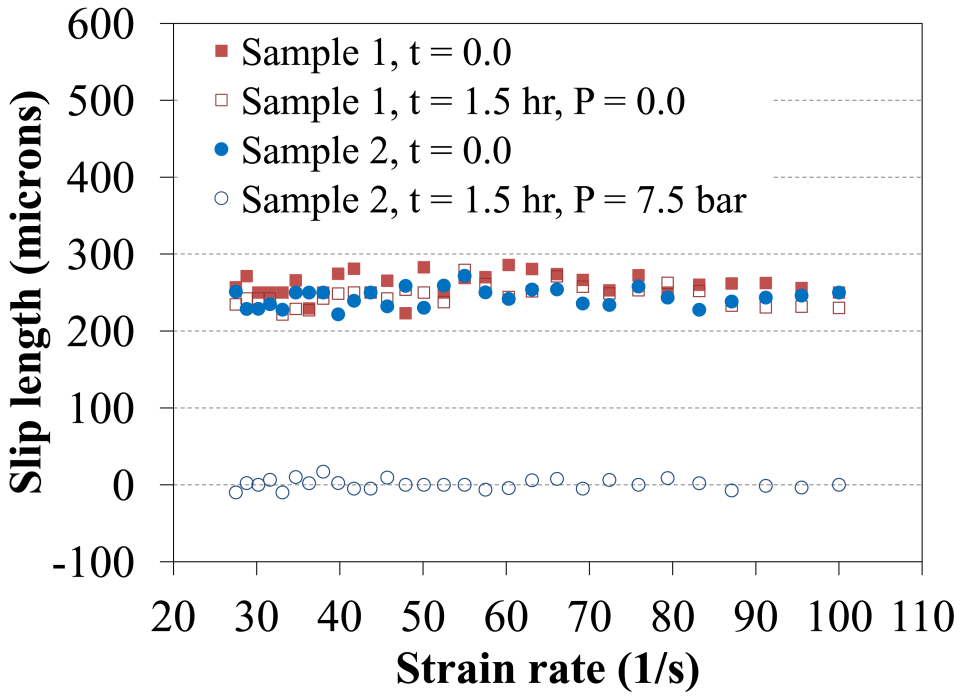

FIG. 4. Slip length for two identical samples subjected to two different elevated pressures during longevity test.

hour. The first sample was immersed in water at atmospheric pressure while the second one was subjected to 7.5 bars. As can be seen in Figure 4, the slip lengths are almost identical before the samples were exposed to elevated pressures. After the test, superhydrophobicity of the first sample remained almost unchanged (less than 5% decrease in slip length) while that of the second sample was completely diminished. This validates the results shown in Figure 3.

We also measured the drag-reduction percentage (drag force of a coated surface compared to that of uncoated smooth one[10]) for the above mentioned two samples. As can be seen in Figure 5, again, before the two samples were subjected to the longevity test, the drag reduction is approximately the same for both. At the end of the test, the first sample loses only about 4% on average of its original drag-reduction, but the second one completely loses its superhydrophobicity. This agrees well with the optical measurements and confirms that the elevated pressure over superhydrophobic coatings accelerates their wetting transition.

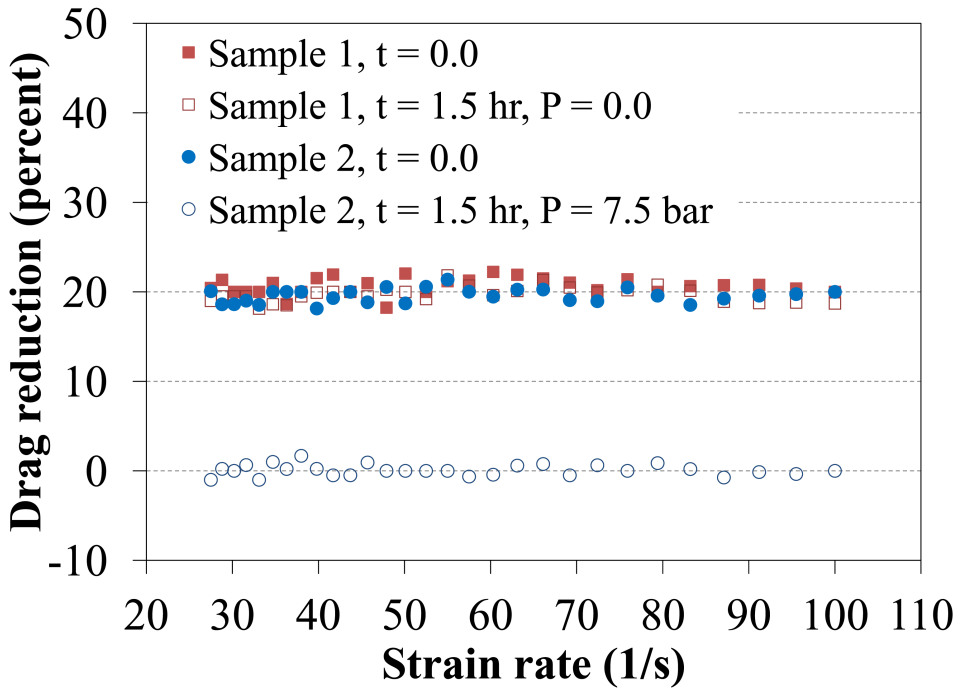

FIG. 5. Drag reduction for two identical samples subjected to two different elevated pressures during longevity test.

IV. CONCLUSIONS

In this work, we studied the time-dependent superhydrophobicity of electrospun polystyrene fibrous coatings for underwater applications. This has been accomplished by producing samples of DC-biased AC-spun fibrous mats and exposing them to elevated pressures while monitoring the decay of scattered light from the surface over time. These experiments are complimented with rheological tests to determine the effects of elevated pressures on the slip length and the skin-friction reduction achieved by the coating. The measurements indicated that surface longevity exponentially decays with increasing pressure in agreement with the study reported by Poetes et al.[9] However, it was found that fibrous coatings could sustain large hydrostatic pressure (up to 9.5 bars, at least for the coating used herein), which is significantly higher than those of previously reported microfabricated surfaces (e.g. 0.1 bar). In addition, the coating produces drag reduction up to 20% and slip length around 250 microns, which are both comparable to those obtained using micro- and nanofabricated surfaces.[13] Our observations indicate that superhydrophobic fibrous coatings could be a good candidate for deep underwater applications as a relatively simple passive (non-energy

consuming) drag-reduction method.

ACKNOWLEDGMENTS

This research is sponsored by the Defense Advanced Research Projects Agency (DARPA), contract number W91CRB-10-1-0003, technical sponsor Captain Christopher Warren, USN. The content of this paper does not necessarily reflect the position or the policy of the Government, and no official endorsement should be inferred.

REFERENCES

1. A. Lafuma and D. Quéré, "Superhydrophobic states," Nat. Mater. **2**, 457 (2003).

2. R.N. Wenzel, "Resistance of solid surfaces to wetting by water," Ind. Eng. Chem. **28**, 988 (1936).

3. A.B.D. Cassie and S. Baxter, "Wettability of porous surfaces," Trans. Faraday Soc. **40**, 546 (1944).

4. C.L.M.H. Navier, "Memoire sur les lois du mouvement des fluides," Mem. Acad. Sci. Inst. Fr. **6**, 389 (1823).

5. J.P. Rothstein, "Slip on superhydrophobic surfaces," Annu. Rev. Fluid Mech. **42**, 89 (2010).

6. M.A. Samaha, H.V. Tafreshi, and M. Gad-el-Hak, "Superhydrophobic surfaces: from the lotus leaf to the submarine," C. R. Mec. **340**, 18 (2012).

7. M. Bobji, S.V. Kumar, A. Asthana, and R.N. Govardhan, "Underwater sustainability of the "Cassie" state of wetting," Langmuir **25**, 12120 (2009).

8. M. Sakai, T. Yanagisawa, A. Nakajima, Y. Kameshima, and K. Okada, "Effect of surface structure on the sustainability of an air Layer on superhydrophobic coatings in a water–ethanol mixture," Langmuir **25**, 13 (2009).

9. R. Poetes, K. Holtzmann, K. Franze, and U. Steiner, "Metastable underwater superhydrophobicity," Phys. Rev. Lett. **105**, 166104 (2010).

10. M.A. Samaha, F.O. Ochanda, H.V. Tafreshi, G.C. Tepper, and M. Gad-el-Hak, "In Situ, non-invasive characterization of superhydrophobic coatings," Rev. Sci. Instrum. **82**, 045109 (2011).

11. J. Bico, C. Marzolin, and D. Quéré, "Pearl drops," Europhys. Lett. **47**, 220 (1999).

12. D. Maynes, K. Jeffs, B. Woolford, and B.W. Webb, "Laminar flow in a microchannel with hydrophobic surface patterned microribs oriented parallel to the flow direction," Phys. Fluids **19**, 093603 (2007).

13. C. Lee and C-J. Kim, "Maximizing the giant slip on superhydrophobic microstructures by nanostructuring their sidewalls," Langmuir **25**, 12812 (2009).

14. B. Woolford, J. Prince, D. Maynes, and B.W. Webb, "Particle image velocimetry characterization of turbulent channel flow with rib patterned superhydrophobic walls," Phys. Fluids **21**, 085106 (2009).

15. A. Steinberger, C. Conttin-Bizonne, P. Kleimann, and E. Charlaix, "High friction on a bubble mattress," Nat. Mater. **6**, 665 (2007).

16. S.D. Bhagat, Y-H. Kim, K-H. Suh, Y-S. Ahn, J-G. Yeo, and J-H. Han, "Super hydrophobic silica aerogel powders with simultaneous surface modification, solvent exchange and sodium ion removal from hydrogels," Microporous Mesoporous Mater. **112**, 504 (2008).

17. M.A. Samaha, H.V. Tafreshi, and M. Gad-el-Hak, "Effects of hydrostatic pressure on the drag reduction of submerged aerogel-particle coatings," Colloids Surf., A, DOI: 10.1016/ j.colsurfa.2012.02.025 (2012).

18. B. Emami, T.M. Bucher, H.V. Tafreshi, D. Pestov, M. Gad-el-Hak, and G.C. Tepper, "Simulation of meniscus stability in superhydrophobic granular surfaces under hydrostatic pressures," Colloids Surf., A **385**, 95 (2011).

19. M. Ma, Y. Mao, M. Gupta, K.K. Gleason, and G.C. Rutledge, "Superhydrophobic fabrics produced by electrospinning and chemical vapor deposition," Macromolecules **38**, 9742 (2005).

20. F.O. Ochanda, M.A. Samaha, H.V. Tafreshi, G.C. Tepper, and M. Gad-el-Hak, "Fabrication of superhydrophobic fiber coatings by DC-biased AC-electrospinning ," J. Appl. Polym. Sci. **123**, 1112 (2012).

21. B. Liu and F.F. Lange, "Pressure induced transition between superhydrophobic states: Configuration diagrams and effect of surface feature size," J. Colloid Interface Sci. **298**, 899 (2006).

22. N.A. Patankar, "Transition between superhydrophobic states on rough surfaces," Langmuir **20**, 7097 (2004) .

23. C.W. Extrand, "Designing for optimum liquid repellency," Langmuir **22**, 1711–1714 (2006).

24. M. Sbragaglia and A. Prosperetti, "Effective velocity boundary condition at a mixed slip surface," J. Fluid Mech. **578**, 435 (2007).

25. M.A. Samaha, H.V. Tafreshi, and M. Gad-el-Hak, "Modeling drag reduction and meniscus stability of superhydrophobic surfaces comprised of random roughness," Phys. Fluids **23**, 012001 (2011).

26. T.M. Bucher, B. Emami, H.V. Tafreshi, M. Gad-el-Hak, and G.C. Tepper , "Modeling resistance of nanofibrous superhydrophobic coatings to hydrostatic pressures: The role of microstructure," Phys. Fluids **24**, 022109 (2012).

27. B. Emami, H.V. Tafreshi, M. Gad-el-Hak, and G.C. Tepper, "Predicting shape and stability of air–water interface on superhydrophobic surfaces with randomly distributed, dissimilar posts," Appl. Phys. Lett. **98**, 203106 (2011).

28. B. Emami, H.V. Tafreshi, M. Gad-el-Hak, and G.C. Tepper, "Predicting shape and stability of air–water interface on superhydrophobic surfaces comprised of pores with arbitrary shapes and depths," Appl. Phys. Lett. **100**, 013104 (2012).

29. B. Emami, H.V. Tafreshi, M. Gad-el-Hak, and G.C. Tepper, "Effect of fiber orientation on shape and stability of air–water interface on submerged superhydrophobic electrospun thin coatings," J. Appl. Phys. **111**, 064325 (2012).

30. S. Sarkar, S. Deevi, and G. Tepper, "Biased AC electrospinning of aligned polymer nanofibers," Macromol. Rapid Commun. **28**, 1034 (2007).

31. L. Lei, H. Li, J. Shi, and Y. Chen, "Diffraction Patterns of a Water-Submerged Superhydrophobic Grating under Pressure," Langmuir **26**, 3666 (2010).

32. H. Rathgen and F. Mugele, "Microscopic shape and contact angle measurement at a superhydrophobic surface," Faraday Discuss. **146**, 49 (2010).

APPENDIX VI: Salinity Effects on Hydrophobicity and Longevity

Following is a reprint of the paper "Salinity Effects on the Degree of Hydrophobicity and Longevity for Superhydrophobic Fibrous Coatings," by Ochanda, F.O., Samaha, M.A., Tafreshi, H.V., Tepper, G.C., and Gad-el-Hak, M., *Journal of Applied Polymer Science*, vol. 124, pp. 5021–5026, 2012.

Salinity Effects on the Degree of Hydrophobicity and Longevity for Superhydrophobic Fibrous Coatings

Fredrick O. Ochanda, Mohamed A. Samaha, Hooman Vahedi Tafreshi, Gary C. Tepper, Mohamed Gad-el-Hak

Department of Mechanical & Nuclear Engineering, Virginia Commonwealth University, Richmond, Virginia 23284-3015

Received 13 July 2011; accepted 9 September 2011
DOI 10.1002/app.35615
Published online 11 December 2011 in Wiley Online Library (wileyonlinelibrary.com).

ABSTRACT: Previous studies on submerged superhydrophobic surfaces focused on performance variables such as drag reduction and longevity. However, to use such surfaces for practical applications, environmental factors such as water salinity must be investigated and understood. In this work, experiments were carried out to investigate the impact of salt (sodium chloride, NaCl) concentrations in aqueous solutions on the hydrophobicity and longevity of polystyrene (PS) fibrous coatings. Rheological studies using salt water as a test fluid were performed to determine the effect of salt concentration on drag reduction. Contact-angle measurements were used to validate the results from the rheometer. *In situ* noninvasive optical reflection was used to measure the longevity of the coating—time-dependent loss of entrapped air within the coating—as a function of salinity. The superhydrophobic coating used herein consisted of PS fibers that were deposited using DC-biased AC-electrospinning. Electrospinning is scalable and far less expensive than conventional methods (e.g., microfabrication), bringing the technology closer to large-scale submerged bodies such as submarines and ships. © 2011 Wiley Periodicals, Inc. J Appl Polym Sci 124: 5021–5026, 2012

Key words: biomimetic; superhydrophobic coatings; fibers; interfaces; polystyrene; drag reduction

INTRODUCTION

Surfaces with static contact angle (CA) greater than 150° are typically classified as superhydrophobic. Superhydrophobicity is exhibited in materials with a combination of low surface free energy and micro and/or nanoscale surface roughness. Natural superhydrophobic surfaces are exemplified by lotus leaves, which allow rain drops to roll off of them, carrying dirt away and creating a self-cleaning effect (lotus effect). When fully submersed in water, such a surface can entrap air between the micro/nanostructures resulting in a surface with both air–water and solid–water interfaces. The presence of the air–water interface is responsible for the slip effect, which results in a reduction in the skin-friction drag exerted on the surface.[1]

Synthetic superhydrophobic surfaces have been produced using the same microfabrication techniques developed for the computer industry and typically consist of a regular array of microposts or microridges etc.[2–7] The orientation (with respect to the flow), spacing, and aspect ratio of the microposts or microridges can be adjusted to optimize the generated drag reduction and the stability of the air–water interface (meniscus) against transition from dewetted (Cassie) to wetted (Wenzel) state.[7–9] Many synthetic strategies and materials have been reported for obtaining superhydrophobicity, including sol–gel processing[10] and solution casting,[11] chemical vapor deposition,[12] laser/plasma/chemical etching,[13] lithography,[14] electrical/chemical reaction and deposition,[15] layer-by-layer and self-assembly,[16] and electrospinning.[17] Except for the electrospinning, all of these methods are complicated and require special equipment, high temperature or vacuum conditions, or low-surface-energy material modification involving multiple steps, which makes it difficult for practical applications in large-scale coatings. Electrospinning is a simple, low-cost method that can be used to deposit micro- to nanotextured coatings of a hydrophobic polymer onto substrates of arbitrary geometry. The resulting superhydrophobic surfaces can be applied in diverse applications, including self-cleaning glasses and clothes, protection against corrosion of metallic parts (in bridges, under water constructions etc.), anti-snow sticking, and reducing skin-friction drag in underwater vessels such as submarines. Superhydrophobic coatings can be utilized as a passive method of flow control and may potentially become a viable

Correspondence to: M. Gad-el-Hak (gadelhak@vcu.edu).
Contract grant sponsor: Defense Advanced Research Projects Agency (DARPA); contract grant number: W91CRB-10-1-0003.

© 2011 Wiley Periodicals, Inc.

alternative to the more complex and energy consuming active or reactive flow control techniques such as wall suction/blowing.[18]

The longevity of a submerged superhydrophobic surface depends primarily on the amount of time that air remains trapped within the surface microstructure. In other words, the degree of hydrophobicity and hence the beneficial effects are diminished by the reduction of the amount of air. Recently, several approaches were developed to estimate the longevity of superhydrophobic surface, i.e., the time until transition from dewetted (Cassie) to wetted (Wenzel) state. Bobji et al.[19] used an optical technique to measure how long the surface can entrap air underwater at different pressures by measuring the number of shiny spots that indicates the interface between air and water. Similar studies were performed using a laser beam to investigate the effect of the surface structure on the longevity.[20] Moreover, Poetes et al.[21] used a similar technique for the same test but for different superhydrophobic coatings. Samaha et al.[22] provided a novel optical technique to more accurately measure the longevity of submerged hydrophobic coatings using optical spectroscopy and a pressure vessel. By using their technique, one can measure the longevity of coatings under different environments such as high/low pressure.

In this work, we assess the effect of salt (NaCl) concentration in water on the degree of hydrophobicity and longevity of superhydrophobic polystyrene (PS) spun-fiber coatings as a part of understanding the influence of environmental factors on the performance these simple, low-cost coatings. We developed superhydrophobic fibrous surfaces[17] using recently developed DC biased AC-electrospinning.[23] The degree of hydrophobicity of the coating was estimated via drag-reduction and contact-angle measurements, which used, respectively, a rheometer and a goniometer. The longevity is measured using the aforementioned optical technique.[22]

EXPERIMENTAL APPROACH

Hydrophobic polymer, PS (M_n = 170,000), was purchased from Sigma–Aldrich Chemicals (St. Louis, MI) and used as received. N,N-Dimethylformamide (DMF) and toluene at high-performance liquid chromatography grade were also obtained from Sigma–Aldrich and were used without further purification. Polymer fibers were fabricated using the DC-biased AC-electrospinning technique. Fibers were electrospun from solutions with 18%, 25%, and 30% weight (wt) PS, but the data reported herein concerns only the last concentration. The polymer was first dissolved in a solvent mixture of DMF and toluene with a 1 : 1 weight ratio. Full details of the experimental procedure to fabricate our superhydrophobic coating are available in our previous work.[17] The electrospun fibers were collected on an aluminum substrate, which was first coated with multipurpose glue to promote adhesion. The surface morphology was determined using a field emission scanning electron microscope (S-70, Hitachi, Japan). Rheological experiments were performed using a rheometer made by Anton Paar Corporation (model Physica MCR 301), equipped with two parallel rotating discs separated by a small fluid-filled gap to measure the stress–strain rate relation. One disc is stationary and attached to a water-cooling system for temperature control.

The second disc rotates at a prescribed speed and is connected to an air bearing to minimize friction. Compressed air at about 6 atm supports the bearing. The rotating disc is connected to a torque-speed measuring system used to calculate the shear stress developed by the fluid and hence drag reduction, and the measured rotational speed is used to calculate the strain rate. The stress–strain rate relation was measured for both superhydrophobic samples as well as smooth control surfaces. The test samples were attached to the stationary disc (bottom plate) and had the same diameter as the rotating disc (top plate) with temperature set at 20 ± 0.1°C. The test fluids were deionized (D.I.) water and sodium chloride solutions of different concentrations ranging from typical salt concentration in oceans (3.5 wt % NaCl) to 100% salt saturation in water (31 wt % NaCl). The test fluids were dispensed between the top plate and the test substrate attached to bottom plate by pipetting 2.0 mL to fill the gap between them. More details about the setup and mathematical calculations were previously reported by Samaha et al.[22]

The static CAs were measured using a contact-angle ramé-hart goniometer (model number 100-25-A) by placing droplets of deionized water (control) and sodium chloride solutions onto the electrospun surfaces. The salt concentration solutions were the same as in the rheological experiments. Droplets of about 3 μL in volume (diameter of about 1.8 mm) were gently deposited on the substrate using a microsyringe. All measurements were made at five different points for each sample at 20 ± 1°C. An image of the droplet was taken by an F1 Series Digital Camera and transferred to a PC for contact-angle determination.

The kinetics of air loss from submerged superhydrophobic coatings was measured using an optical spectroscopy system made by Photon Technology International (model Quanta Master™ 30). The intensity of a broad-spectrum white light reflected from the submerged surface was measured as a function of time. As the reflectivity coefficient is greater for the air–water interface than for the solid–water interface, the intensity of the reflected light

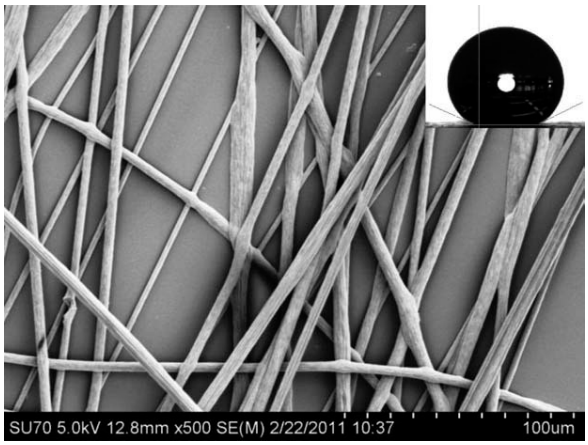

Figure 1 SEM image of hydrophobic polystyrene (PS) fibers made from 30% polymer solution. Upper right inset shows a water droplet on top of the coating with contact angle of 160°.

decreases as the amount of trapped air decreases. The loss of trapped air will cause a transition from nonwetted (Cassie) state to wetted (Wenzel) state. A detailed description of this apparatus is provided in a previous publication by Samaha et al.[22]

RESULTS AND DISCUSSION

Morphology

Making a coating that sturdily sticks to a substrate is essential for practical applications. Without strong adhesion, a coating would separate from its substrate, and hence its beneficial effects would disappear. Equally important is achieving strong adhesion between the different layers of the fibers. Spraying of a thin adhesive polymer film to the metal substrate before electrospinning resulted in a monolayer coating. After electrospinning, it was realized that initial layers of fibers adhered to the metal but subsequent layers did not. By careful control of pump rate and distance between spinneret and metal substrate, the fiber reached the collector when still wet, thus ensuring better adhesion between the different fiber layers. The coating was able to withstand immersion in water for several days during the longevity tests indicating that strong adhesion was achieved.

Figure 1 shows an SEM image of a typical PS micro/nanofiber coating. The inset in the figure shows a water droplet on the coating with a static CA of 160 ±1°, demonstrating the superhydrophobicity of the surface. The diameter of a single PS fiber is a few micrometers and the deposited mat of hydrophobic polymer fibers provides the surface roughness and porosity necessary to entrap air when the surface is immersed in water. As water flows over this surface, the interface between the entrapped air and the water causes very low skin friction, resulting in slip flow and drag reduction. The grid-like arrangement of fibers prevents liquid from penetrating the space (pitch) between fibers, similar to the microposts made by an ordered-microstructure fabrication method. Therefore, the fiber spacing must be close enough (typically micrometers as shown in the figure) to counteract gravitational and other pressures that might cause wetting into the space between the posts. However, if superhydrophobicity is to be achieved, the fraction of the water droplet surface that contacts the low surface energy posts should be much less than the fractional area of the water droplet contacting the air. According to the Cassie–Baxter relation,[24–26] the CA on a composite surface (θ_r) can be expressed as

$$\cos\theta_r = f_1 \cos\theta - f_2 \quad (1)$$

where f_1 and f_2 represent, respectively, the fractions of solid surface and air in a composite surface (i.e., $f_1 + f_2 = 1$), while θ is the equilibrium CA on a flat solid surface, which is 96.8° for a smooth PS film. From the equation, the fraction of the PS fibers to the whole apparent surface area is only 0.07, hence the contribution of trapped air is maximized.

Effect of salinity on hydrophobicity

Sodium chloride solutions of concentration ranging from 3.5 to 31 weight percent in D.I. water were prepared to investigate their effect on the hydrophobicity of the PS fiber coatings. Figure 2 shows the measured drag reduction (using equations demonstrated by Samaha et al.[22]) against strain rate for various water salinity levels. A drag reduction larger than 20% was observed at all NaCl concentrations.

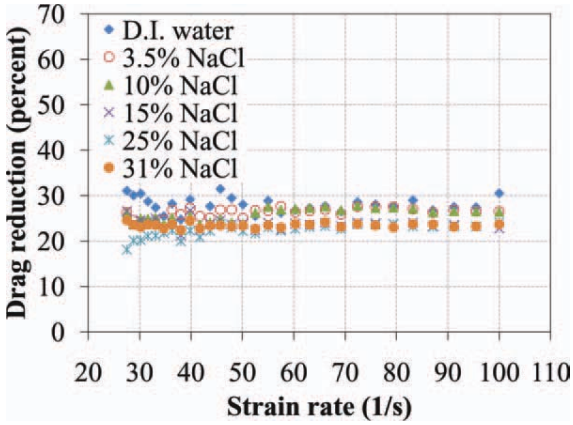

Figure 2 Rheometer test to estimate drag reduction of PS fibrous coating made from 30% polymer solution with D.I. water and NaCl solutions as test fluids. [Color figure can be viewed in the online issue, which is available at wileyonlinelibrary.com.]

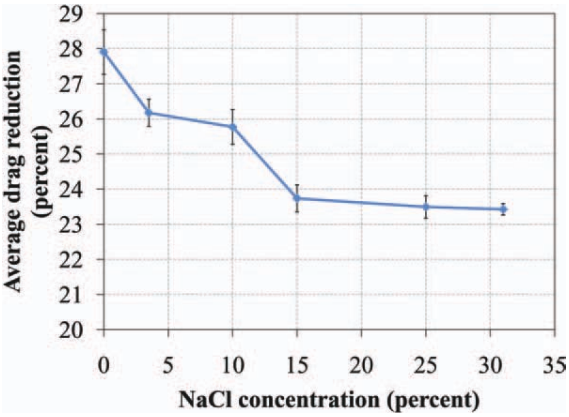

Figure 3 Effect of salt concentration on average drag reduction of PS fibrous coating. [Color figure can be viewed in the online issue, which is available at wileyonlinelibrary.com.]

Figure 3 is a plot of the drag reduction averaged over the full range of strain rate versus the NaCl concentration and shows a modest decrease in drag reduction with increasing salinity. It should be noted that the estimation of drag reduction depends on the ratio of the wall-shear stress (t) in case of slip to that of no slip.[22] We have repeated the measurements five times for each parameter and it was found that the percentage error in the measured shear stress ($\Delta t/t$) is <1% and this results in not >5% error in drag reduction. Therefore, the experimental uncertainty is far less when compared with the amplitude of the drag reduction reported in this work. We interpret the developed drag reduction to be a result of entrapped air between hydrophobic fibers.

Dynamic viscosities of solutions with different NaCl concentrations have been measured using the rheometer with no-slip moving and stationary discs as shown in Figure 4. It is obvious that the viscosity

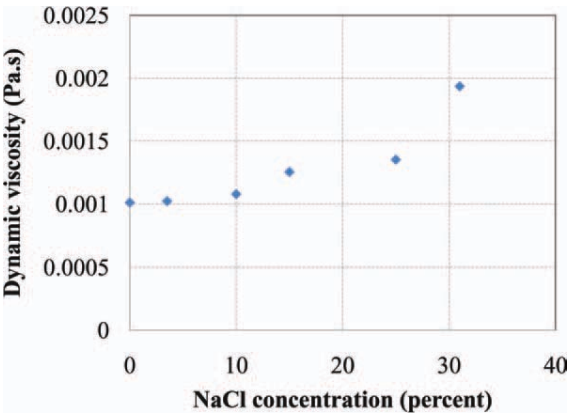

Figure 4 Variation of dynamic viscosity of NaCl solution as a function of salt concentration. [Color figure can be viewed in the online issue, which is available at wileyonlinelibrary.com.]

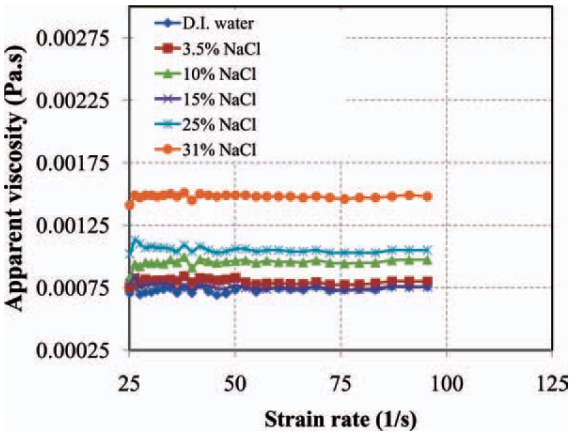

Figure 5 Apparent viscosity of NaCl solution at different concentrations as a function of strain rate measured for PS fibrous coating. [Color figure can be viewed in the online issue, which is available at wileyonlinelibrary.com.]

of NaCl solution increases with increasing salt concentration until the percentage difference in viscosity relative to that of deionized water reaches 91% at the saturation point. The increase in viscosity on adding ions to liquid water can indeed be explained from the rigid nature of the solvation structure formed by the ion and its first hydration shell.

It is well known[27,28] that when sodium chloride (NaCl) is dissolved in water, it dissociates into positively charged sodium (Na^+) and negatively charged chloride (Cl^-) ions. The partial positive charge of the hydrogen ends of the water molecules surround the negatively charged chloride ions, and the partial negative charge of the oxygen ends of the water molecules surround the positively charged sodium ions. This effect is thought to result primarily from water molecules directly bonded to the anion and is related to the OH...X bond polarity (where X is a halide, chloride in this case).[29] The amount of hydrogen bonds can be used to characterize the stability of the microstructure of water molecules.[30,31] In general, a larger amount of hydrogen bonds implies stronger intermolecular interactions among the water molecules, which would result in an increase in the viscosity. On the other hand, there is a bulk electrostatic modulation of molecular interactions that originates from the polarization and reorientation of water molecules in the bulk phase. Both electrostatics and solvent-induced forces are modified by the presence of salts,[32] which leads to an increase in the attractive force between the fluid and the surface, i.e., reduces hydrophobicity.

The apparent viscosity—combination of dynamic viscosity and slip effect—increases with increasing NaCl concentration due to an increase in fluid dynamic viscosity and a decrease in generated drag reduction (i.e., surface's hydrophobicity; see Figure 5). For example, if the NaCl concentration increases from

TABLE I
Variation of Specific Gravity as a Function of NaCl Concentration (Percent)

NaCl concentration (%)	Specific gravity at 20°C
0.0	1.000
3.5	1.026
10	1.074
15	1.112
25	1.193
31	1.247

0% to 31%, the apparent viscosity will increase by 103% owing to a percentage increase in dynamic viscosity by 91%, and a relative decrease in drag reduction of 16%. A similar trend has been observed in the specific gravity of the NaCl solution measured at a temperature of 20°C. Table I shows the expected gradual increase in specific gravity of the NaCl solution with increase in concentration, indicating that there is an increase in solution density with concentration when compared with that of pure water.

Contact-angle measurements of droplets with different NaCl concentrations were performed to verify the effect of salinity on hydrophobicity of the fibrous coatings used in the rheometer test. The CA decreased with increasing NaCl concentration in all cases, see Figure 6. The CA data are consistent with the drag-reduction results presented in Figure 3. However, the CA measurements were more sensitive to water salinity and ranged from 160° for pure water to about 143° at 100% salt saturation (31 wt % NaCl). Thus, with increasing concentration of electrolyte, the surface possesses a smaller CA, and less drag reduction, i.e., less hydrophobicity.

Theoretically, NaCl is adsorbed on PS fibers, which can be treated as an interaction of forces including van der waals attractive and electrostatic forces with the former favoring adsorption of Na^+ and Cl^- ions on PS surface. In general, the hydrophobicity of a surface and, hence, its hydrophobic force is controlled by changes in surface composition. We reason that the decrease in hydrophobic force in the presence of electrolytes (anion and cation) is due to the adsorption of the ions on the surface.[33,34] This is supported by Gouy–Chapman theory, which predicts that added salt systematically promotes solute adsorption because salt can alter the free energy of forming a charged monolayer with increasing ionic strength.[35]

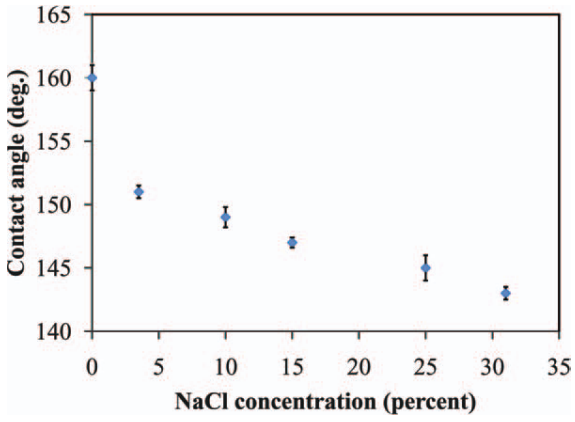

Figure 6 Effect of NaCl concentration on contact angle of PS fibrous coating. [Color figure can be viewed in the online issue, which is available at wileyonlinelibrary.com.]

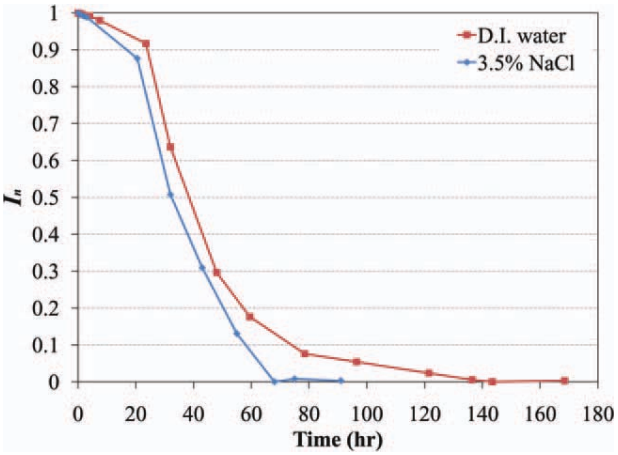

Figure 7 Effect of salinity on longevity of PS fibrous coating. [Color figure can be viewed in the online issue, which is available at wileyonlinelibrary.com.]

Longevity studies: salt effects

When a superhydrophobic surface is submerged in water, the spatial distribution of trapped air on its surface exhibits a mirror-like sheen at the air–water interface. Therefore, examining the intensity of reflected light from the surface over time to determine its longevity can monitor the kinetics of loss of the trapped air. We have used light scattering [22] as an indirect, time-dependent measurement of the amount of air trapped within a submerged superhydrophobic fiber surface. The reflected light spectrum was obtained as a function of time and was integrated to obtain wavelength-averaged reflection intensity. Figure 7 shows the normalized average reflected light intensity versus time for two typical samples of the superhydrophobic fibrous coating. One of them was immersed in D.I. water. The other one was immersed in 3.5 wt % NaCl solution (typical salinity of ocean water). The normalized average reflected light intensity, I_n, is defined as

$$I_n = \frac{I - I_d}{I_f - I_d} \tag{2}$$

where I is the average integrated measured intensity across the range of wavelengths of visible light, I_d is

the intensity for the completely hydrophilic sample (aged or dead sample), and I_f is the intensity for a new superhydrophobic sample (fresh sample).

It can be seen from Figure 7 that the light intensity decreases with time for both test fluids, which indicates the loss of trapped air and a corresponding reduction in the degree of superhydrophobicity. This effect is believed to be due to the dissolution of air in water.[19,21] Furthermore, it can be seen from the figure that the immersed sample in D.I. water becomes completely hydrophilic after 136 h, whereas the sample submerged in salt water takes only 68 h to become hydrophilic. Therefore, this observation indicates that the onset of wetting or transition from the Cassie state to the Wenzel state starts earlier for samples in salt solution than those in D.I. water. This can be explained by analyzing the parameters that affect the longevity of the surface. First parameter is the rate of air dissolution in water, which decreases with increasing salt concentration.[36] Second, air–water interface is supported by surface tension, which increases by increasing the concentration of NaCl.[37] Finally, as explained in "Effect of salinity on hydrophobicity" section, Na^+ and Cl^- ions are adsorbed on the PS surface and the accumulation of positive and negative charges with time leads to decrease in the hydrophobic force and hence reduces surface's longevity. Our results show that although the first and second parameters contribute to increase surface's longevity with adding salt, the effect of the accumulation of charges on the surface dominates and accelerates the transition to the wetted (Wenzel) state. It is worth mentioning that the results of longevity attained using the low-cost fabrication approach used herein are much longer than those reported for ordered-microstructure fabricated surfaces tested in pure water.[19]

CONCLUSIONS

We performed several experiments to determine how salt (NaCl) concentration in water influenced the hydrophobicity and longevity of PS fibrous coatings. Rheometer tests were provided to determine the effect of salinity on drag-reduction and contact-angle measurements were performed to validate the results obtained from the rheological study. The results show that both drag reduction and static CA (indicating the degree of hydrophobicity) decrease with increasing salt concentration. Moreover, *in situ*, noninvasive optical spectroscopy was performed and showed that the coating longevity was lower for salt water in comparison with D.I. water.

This work demonstrates the effect of water salinity on a superhydrophobic coating. This study opens a pathway for studying more environmental conditions that could affect the performance of superhydrophobic coatings used in practical applications.

References

1. Rothstein, J. P. Annu Rev Fluid Mech 2010, 42, 89.
2. Ou, J.; Perot, B.; Rothstein, J. P. Phys Fluids 2004, 16, 4635.
3. Ou, J.; Rothstein, J. P. Phys Fluids 2005, 17, 103606.
4. Davies, J.; Maynes, D.; Webb, B. W.; Woolford, B. Phys Fluids 2006, 18, 087110.
5. Maynes, D.; Jeffs, K.; Woolford, B.; Webb, B. W. Phys Fluids 2007, 19, 093603.
6. Daniello, R. J.; Waterhouse, N. E.; Rothstein, J. P. Phys Fluids 2009, 21, 085103.
7. Lee, C.; Choi, C.-H.; Kim, C.-J. Phys Rev Lett 2008, 101, 064501.
8. Lee, C.; Kim, C.-J. Langmuir 2009, 25, 12812.
9. Samaha, M. A.; Tafreshi, H. V.; Gad-el-Hak, M. Phys Fluids 2011, 23, 012001.
10. Shirtcliffe, N. J.; Hale, G.; Newton, H. I.; Perry, C. C. Langmuir 2003, 19, 5626.
11. Erbil, H. Y.; Demirel, A. L.; Avci, Y.; Mert, O. Science 2003, 299, 1377, 15.
12. Love, J. C.; Gates, B. D.; Wolfe, D. B.; Paul, K. E.; Whitesides, G. M. Nano Lett 2002, 2, 891.
13. Fresnais, J.; Chapel, J. P.; Poncin-Epaillard, F. Surf Coat Technol 2006, 200, 5296.
14. Pozzato, A.; Zilio, S. D.; Fois, G.; Vendramin, D.; Mistura, G.; Belotti, M.; Chen, Y.; Natali, M. Microelectron Eng 2006, 83, 884.
15. Shi, F.; Wang, Z. Q.; Zhang, X. Adv Mater 2005, 17, 1005.
16. Zhao, N.; Shi, F.; Wang, Z. Q.; Zhang, X. Langmuir 2005, 21, 4713.
17. Ochanda, F. O.; Samaha, M. A.; Tafreshi, H. V.; Tepper, G. C.; Gad-el-Hak, M. J Appl Polym Sci 2012, 123, 1112.
18. Gad-el-Hak, M. Flow Control: Passive, Active, and Reactive Flow Management; Cambridge University Press: London, United Kingdom, 2000.
19. Bobji, M. S.; Kumar, S. V.; Asthana, A.; Govardhan, R. N. Langmuir 2009, 25, 12120.
20. Sakai, M.; Yanagisawa, T.; Nakajima, A.; Kameshima, Y.; Okada, K. Langmuir 2009, 25, 13.
21. Poetes, R.; Holtzmann, K.; Franze, K.; Steiner, U. Phys Rev Lett 2010, 105, 166104.
22. Samaha, M. A.; Ochanda, F. O.; Tafreshi, H. V.; Tepper, G. C.; Gad-el-Hak, M. Rev Sci Instrum 2011, 82, 045109.
23. Sarkar, S.; Deevi, S.; Tepper, G. Macromol Rapid Commun 2007, 28, 1034.
24. Cassie, A. B. D.; Baxter, S. Trans Faraday Soc 1944, 40, 546, 16
25. Hoefnagels, H. F.; Wu, D.; de With, G.; Ming, W. Langmuir 2007, 23, 13158.
26. Chao-Hua, X.; Shun-Tian, J.; Jing, Z.; Li-Qiang, T.; Hong-Zheng, C.; Mang, W. Sci Technol Adv Mater 2008, 9, 035008.
27. Dillon, S. R.; Dougherty, R. C. J Phys Chem A 2002, 106, 7647.
28. Dougherty, R. C. J Phys Chem B 2001, 105, 4514.
29. Schultz, J. W.; Hornig, D. F. J Phys Chem 1961, 65, 2131.
30. Alenka, L.; David, C. Nature 1996, 379, 55.
31. Hummer, G.; Rasaiah, J. C.; Noworyta, J. P. Nature 2001, 414, 188.
32. Song, J. D.; Ryoo, R.; Jhon, M. S. Macromolecules 1991, 24, 1727.
33. Angarska, J. K.; Dimitrova, B. S.; Danov, K. D.; Kralchevsky, P. A.Ananthapadmanabhan, K. P.; Lips, A. Langmuir 2004, 20, 1799.
34. Christenson, H. K.; Claesson, P. M.; Berg, J.; Herder, P. C. J Phys Chem. 1989, 93, 1472.
35. Persson, C.; Jonsson, A.; Bergstrom, M.; Eriksson, J. C. J Colloid Interface Sci 2003, 267, 151.
36. Millero, F. J.; Huang, F.; Laferiere, A. L. Mater Chem 2002, 78, 217.
37. Jungwirth, P.; Tobias, D. J. J Phys Chem B 2001, 105, 10468.

APPENDIX VII: Experiments on Superhydrophobic Surfaces Comprised of Random Roughness

Following is a reprint of the paper "Effects of Hydrostatic Pressure on the Drag Reduction of Submerged Aerogel-Particle Coatings," by Samaha, M.A., Tafreshi, H.V., and Gad-el-Hak, M., *Colloids and Surfaces A: Physicochemical and Engineering Aspects*, vol. 399, pp. 62–70, 2012.

Colloids and Surfaces A: Physicochem. Eng. Aspects 399 (2012) 62–70

Contents lists available at SciVerse ScienceDirect

Colloids and Surfaces A: Physicochemical and Engineering Aspects

journal homepage: www.elsevier.com/locate/colsurfa

Effects of hydrostatic pressure on the drag reduction of submerged aerogel-particle coatings

Mohamed A. Samaha, Hooman Vahedi Tafreshi, Mohamed Gad-el-Hak*

Department of Mechanical & Nuclear Engineering, Virginia Commonwealth University, Richmond, VA 23284-3015, USA

ARTICLE INFO

Article history:
Received 1 December 2011
Received in revised form 16 January 2012
Accepted 17 February 2012
Available online 3 March 2012

Keywords:
Superhydrophobic aerogel
Critical pressure
Terminal pressure
Drag reduction
Random particles
Thresholding image

ABSTRACT

There are several techniques to fabricate superhydrophobic surfaces. The one used in this paper is closer to natural surfaces found, for example, on lotus leaves. Herein, hydrophobic aerogel particles with different average diameters are randomly deposited onto metallic substrates with a thin adhesive coating to achieve a combination of hydrophobicity and surface roughness. The resulting surfaces show different degrees of superhydrophobicity and are used to study the effects of elevated pressure on the drag reduction and the degree of hydrophobicity (survivability) of such surfaces when used for underwater applications. Several previous studies presented numerical and/or analytical models to evaluate the influence of pressure on the superhydrophobicity. Experimental studies, however, are lacking. In this work, we measure the impact of pressure on the stability of the meniscus (air–water interface). The experiments utilize three instruments: (i) a previously developed optical technique to characterize the time-dependent hydrophobicity in conjunction with a pressure vessel in which the submerged coating is exposed to elevated pressures; (ii) a parallel-plate rheometer where the coating's slip length and drag reduction are measured; and (iii) a goniometer to measure the static contact angle as well as contact-angle hysteresis. We also developed an image-thresholding technique to estimate the gas area fraction of the coating. The results indicate that there exists a new parameter, the terminal pressure, beyond which the surface undergoes a global transition from the Cassie state to the Wenzel state, and therefore can no longer generate drag reduction. This *terminal pressure* differs from the previously identified *critical pressure*. The latter is the pressure above which the surface starts the transition process at some location, but not necessarily at other spots due to the heterogeneity of the surface. For the particle coatings used herein, the terminal pressures are measured to range from 100 to 600 kPa, indicating that such coatings could potentially be used for deep underwater applications.

© 2012 Elsevier B.V. All rights reserved.

1. Introduction

Surfaces with static contact angles (CA) greater than 150° and significantly low contact-angle hysteresis are typically classified as superhydrophobic. Superhydrophobicity is exhibited in materials with a combination of low surface free-energy and micro- and/or nanoscale surface roughness. Amongst many others, examples of such surfaces in nature are the self-cleaning lotus leaves [1] and water striders [2]. When submerged, these surfaces can entrap air between their micro- or nanostructures resulting in a surface with both air–water and solid–water interfaces. The presence of the air–water interface is responsible for the slip effect, which could be characterized by the so called "slip length" [3]. This in turn results in a reduction in the skin-friction drag exerted on a moving surface [4,5]. Drag is the force produced by a fluid to resist the relative motion of a submerged solid. That force is the sum of the pressure drag, which mostly results from flow separation, and the skin-friction drag, which results from the no-slip condition. The latter component is reduced when partial flow slip takes place. Superhydrophobic coatings provide a relatively simple, passive drag-reduction method, and may potentially become a viable alternative to the more complex and energy consuming active or reactive flow control techniques such as wall suction/blowing [6]. There are at least three challenges to overcome before field applications are feasible: (1) scaling up the application of superhydrophobic coatings to large submersibles; (2) achieving low-cost fabrication; and (3) preventing the entrapped air from escaping under pressure for reasonably long time, or at least periodically *rejuvenating* the surface.

Superhydrophobic surfaces have often been produced using the same microfabrication techniques developed for the electronic industry, and in many cases consist of a regular array of microposts or microridges [7,8]. Orientation with respect to the flow, spacing, and aspect ratio of the microstructure could be adjusted

* Corresponding author. Tel.: +1 804 828 3576.
E-mail address: gadelhak@vcu.edu (M. Gad-el-Hak).

0927-7757/$ – see front matter © 2012 Elsevier B.V. All rights reserved.
doi:10.1016/j.colsurfa.2012.02.025

to optimize the performance of those surfaces. The orientation of microroughness, flow characteristics, and shape of air–water interface (meniscus) could all significantly affect the slip condition and hence the drag reduction. For example, Woolford et al. [9] demonstrated that in a turbulent flow regime, streamwise ridges (i.e., flow direction parallel to the microridges) could lead to drag reduction, while spanwise ridges (i.e., flow direction perpendicular to the microridges) could lead to drag increase. Woolford et al. reason that the transverse configuration results in higher turbulence intensity, higher total and turbulence shear stress, and higher production of turbulence, and vice versa for the longitudinal configuration. Additionally, Steinberger et al. [10] demonstrated that the meniscus shape influences the boundary condition, which could increase the friction. When the capillary number is significantly low (less than 10^{-4}), the capillary force dominates and the meniscus shape could be considered as a spherical cap that is stress independent. If the protrusion angle of the meniscus exceeds a specific limit, an immobile liquid layer with significant thickness is trapped close to the solid wall, which results in increasing the drag force higher than that of a hydrophilic smooth surface.

Clearly, large-scale manufacturing of microfabricated superhydrophobic surfaces is prohibitively expensive. An alternative solution to circumvent the cost is to produce surfaces made up of random deposition of hydrophobic particles or fibers [11,12]. Bhagat et al. [13] developed an inexpensive method for the rapid synthesis of hydrophobic silica aerogel powder. Yang and Deng [14] demonstrated a simple technique to produce superhydrophobic papers by using a multi-layer deposition of polymers and silica particles. Lee et al. [15] fabricated a granular superhydrophobic coating by blasting the surface with sodium bicarbonate. Hwang et al. [16] produced surfaces using spray-deposition to reach contact angles up to 178°. Meanwhile, Bobji et al. [17] used an optical technique to measure how long the surface can maintain its hydrophobicity under different hydrostatic pressures. This was accomplished by counting the number of shiny spots per unit area on the surface—an indication of the existence of an air–water interface.

Similar studies were performed using a laser beam to investigate the effect of the surface structure on the longevity [18]. Poetes et al. [19] used a similar technique for the same test but for different superhydrophobic coatings. Additionally, they mathematically interpreted the decay of the longevity with pressure. In 2006, Liu and Lange [20] provided a theoretical model to predict the so-called critical transition pressure beyond which superhydrophobic surfaces transitioned from the Cassie state to the Wenzel state. Since then, many other numerical and analytical studies have been performed to predict the critical pressure. Some of those studies predicted the meniscus stability for surfaces comprised of ordered [21–25] or random roughness [26]. Emami et al. [27] determined the wetting transition pressure for surfaces made of ordered and random spheres and posts. Other studies have been performed to determine the meniscus shape at different pressures up to the critical pressure [28]. Furthermore, Extrand [29] developed a mathematical model to determine the critical pressure for a surface comprised of microstructure roughness, which is superimposed with nanostructure one. Such a surface resembles the features of a lotus leaf. Extrand's model demonstrates that the nanostructure roughness enhances the hydrophobicity of the surface. In a related experimental study, Sheng and Zhang [30] demonstrated the effects of elevated pressures on the superhydrophobicity of lotus leaves by measuring the contact angle of a droplet on a leaf before and after the experiment.

According to Lafuma and Quéré [31], superhydrophobicity could be explained using the models independently developed by Wenzel [32] and Cassie [33]. The former is more applicable to slightly hydrophobic materials (contact angles just above 90° for a smooth surface). Both models have a linear relation between the apparent contact angle on a rough surface and the corresponding contact angle on a smooth surface. The Wenzel and Cassie models intersect at a contact angle that Lafuma and Quéré called 'critical angle' below which the metastability of the Cassie state may be observed. Therefore, in order to avoid the metastability, the material of the surface should have a smooth-surface contact angle greater than that above critical angle.

This work is a proof-of-concept study on the effects of elevated pressures on survivability of superhydrophobic surfaces consisting of randomly deposited polydisperse particles for underwater applications. As an example of such cost-effective granular superhydrophobic surfaces, we evaluate the drag-reduction performance and measure the slip length for coating made up of randomly deposited aerogel particles. We investigate the effects of the coating's morphological parameters, such as particle size and porosity, on both the wetting-transition pressure resistance and the drag-reduction advantage. A few analytical and numerical approaches were previously reported on relating the critical pressure to the morphological parameters of superhydrophobic coatings comprised of random roughness. However, no experimental study has yet been devoted to examining the influence of morphological parameters of coatings manufactured by random deposition of polydisperse particles. In particular, the present study evaluates the stability of the meniscus by measuring the pressure needed for wetting transition using our previously developed optical technique and a custom-built pressure vessel [34]. The degree of hydrophobicity of the coatings is characterized via goniometer measurements of the static contact-angle as well as contact-angle hysteresis. Additionally, the coatings' drag-reduction efficacy and slip length are measured via a parallel-plates rheometer. These parameters were measured before and after the surfaces were exposed to elevated pressures. The fabrication of our aerogel coatings is explained in the next section. Section 3 describes our procedure for meniscus-stability and skin-friction measurements. This is followed by Section 4, where our image-based technique for estimating the coating's gas area fraction is discussed. The results of the study and related discussions are given in Section 5. Conclusions and recommendations for future studies are given in Section 6.

2. Preparation of aerogel coatings

Hydrophobic aerogel beads made of amorphous silicon dioxide having almost 99.8% porosity were acquired from United Nuclear Scientific (Laingsburg, MI). The beads were ground and filtered through four stages of sieves purchased from McMaster.CARR (Chicago, IL) with mesh sizes of 43, 104, 150, and 210 μm. Starting with the smallest mesh size, the aerogel particles were sieved to separate the finest particles. The remaining particles in the first sieve were then filtered in the next one, and the procedure was repeated until four categories of aerogel particles were obtained. From each category, aerogel particles were deposited onto a metallic substrate coated with a thin polymer film for adhesion. The surface morphology was studied using a field-emission scanning electron microscope (FESEM) (S-70, Hitachi, Japan). Fig. 1 shows SEM images of the four aerogel coatings with different particle-size ranges. The inset in the figure shows a water droplet on each coating with a static contact angle of 155° or higher, and an average contact-angle hysteresis of about 3°, demonstrating each coating's superhydrophobicity. As can be seen in parts b–d of the same figure, few particles exist with sizes smaller than the prescribed range determined from the mesh size of a particular sieve. We reason that the electrostatic charge of the particles is responsible for attracting few particles to each other, and therefore giving the particle conglomerate a larger virtual size. The deposited particles provide the

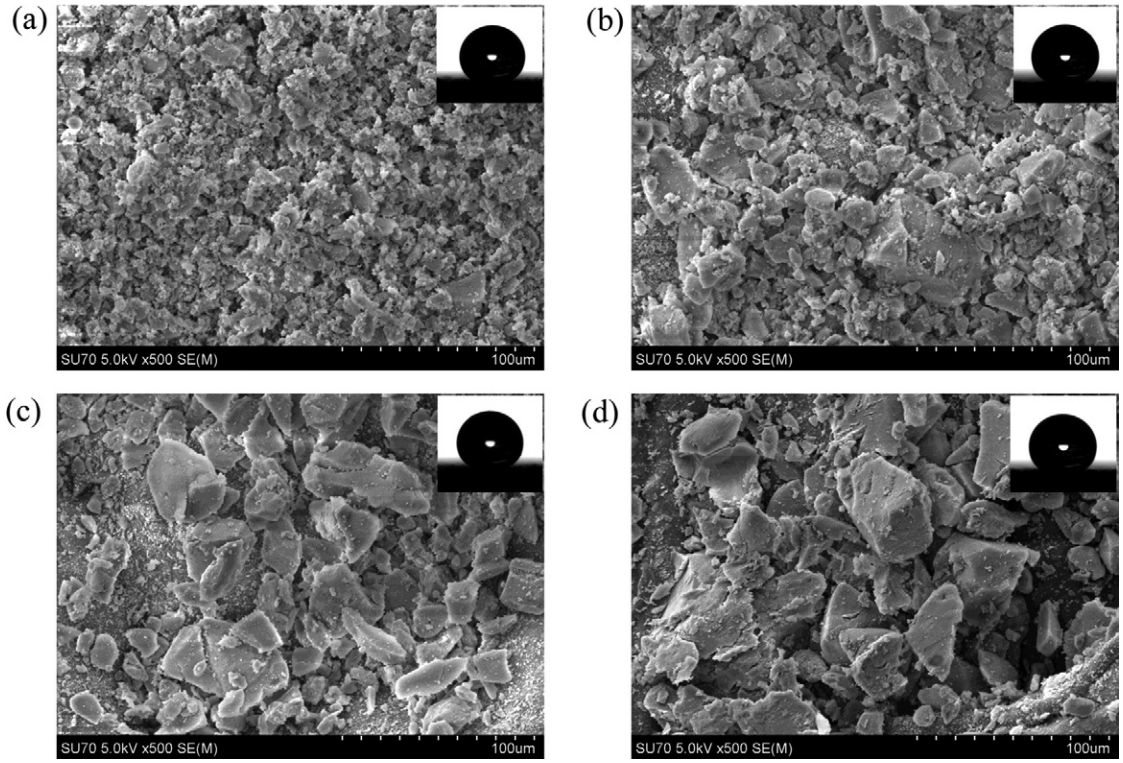

Fig. 1. SEM images of superhydrophobic aerogel coatings with different particle-size ranges. (a) 0–43 μm; (b) 43–104 μm; (c) 104–150 μm; (d) 150–210 μm. Upper right inset in each figure shows a water droplet on top of the particular coating.

surface roughness and porosity necessary to entrap air when the surface is submerged in water. As water flows over the coating, the interface between the entrapped air and the water has very low skin friction, resulting in slip flow and drag reduction.

3. Meniscus-stability and skin-friction experiments

The air–water interface over a superhydrophobic surface is stable if the exerted hydrostatic pressure is balanced by the capillary forces and the compression forces generated by the entrapped air in the pores. The balance of those opposing forces is highly dependent on both the pore size and gas area fraction of the coating. If the hydrostatic pressure is increased beyond the critical pressure, the air–water interface starts to break up, allowing water to intrude into the pores of the coating and the surface to transition to the Wenzel (wetted) state. The critical pressure can be obtained by raising the hydrostatic pressure in the pressure vessel while monitoring the air content of the coating. The pressure was produced using a nitrogen gas tank connected to a pressure vessel in which the sample was submerged (see Fig. 2).

The kinetics of air loss from submerged superhydrophobic coatings was measured using an optical spectroscopy system made by Photon Technology International, Inc. (model QuantaMaster^{TM} 30). The intensity of a broad-spectrum white light reflected from the submerged surface was measured as a function of pressure. As the reflectivity coefficient is greater for the air–water interface than for the solid–water interface, the intensity of the reflected light decreases as the amount of entrapped air is decreased (i.e., air is replaced by ambient water). The loss of trapped air will cause a transition from nonwetted (Cassie) state to wetted (Wenzel) state at which the whole air layer is completely lost and the light intensity signal becomes constant. A detailed description of this apparatus was provided by Samaha et al. [34].

Skin-friction measurements were performed using a rheometer made by Anton Paar Corporation (model Physica MCR 301). The device is equipped with two parallel rotating discs separated by a small fluid-filled gap, and provides precise measurements of the stress–strain rate relation. One disc is stationary and attached to a water cooling system for temperature control. The second disc rotates at a prescribed speed and is connected to an air bearing to minimize friction. Compressed air at about 6 atm supports the bearing. The rotating disc is connected to a torque–speed measuring system used to calculate the shear stress developed by a fluid of a known viscosity, and therefore measure the skin-friction drag. The measured rotational speed is used to calculate the strain rate. The stress–strain rate relation was measured for both superhydrophobic samples as well as smooth control surfaces. The test samples were attached to the stationary disc (bottom plate) and had the same diameter as the rotating disc (top plate) with temperature set at $20 \pm 0.1\,^{\circ}C$. The test fluid, deionized (D.I.) water, was dispensed between the top plate and the test substrate attached to bottom plate by pipetting 2.0 ml to fill the gap between them. More details about the setup and mathematical calculations to determine both slip length and drag reduction were previously reported by Samaha et al. [34].

Static contact angles and contact-angle hysteresis were measured using a contact-angle ramé-hart goniometer (model number 100-25-A) by placing droplets of deionized water onto the coating. Droplets of about 3 μl in volume (diameter of about 1.8 mm) were gently deposited on the substrate using a microsyringe. All measurements were made at five different points for each sample, maintained at a temperature of $20 \pm 0.1\,^{\circ}C$. An image of the droplet was taken by an F1 Series Digital Camera and transferred to a PC for contact-angle determination [34].

4. Gas area fraction

Gas area fraction significantly influences both the critical pressure and the drag-reduction advantage of a superhydrophobic surface [21–28]. Higher gas area fraction increases the percentage

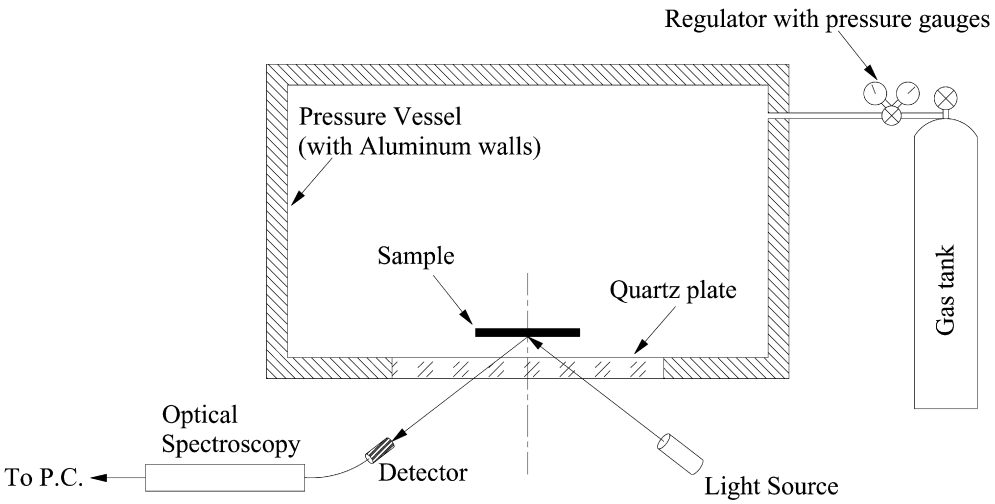

Fig. 2. Schematic illustration of the setup used for determining the wetting-transition pressure of aerogel coatings.

drag reduction, but lowers the critical pressure. To our knowledge, there is no direct method for predicting or measuring the gas area fraction on a superhydrophobic surface with random microstructure, because the gas area fraction, being directly proportional the 3-D shape of the air–water interface, varies with pressure as well. The problem becomes even more complex when the surface is made up of particles of irregular shapes and different sizes. In order to provide an estimate for the gas area fraction of our aerogel coatings, we have developed and validated an image processing technique in which we start by thresholding (segmenting) the SEM images to distinguish the upper surfaces of the particles from the background using Mathematica software. Through this process, the gray levels are split into two classes in an attempt to separate the objects of interest from the background, and to prepare the images for analysis [35]. Fig. 3 shows the thresholded images of those shown in Fig. 1. The white regions represent the upper areas of the particles that could be in contact with water when the surface is submerged. This could be estimated by calculating the total area covered with white pixels. Meanwhile, the black regions represent the voided locations in which air is entrapped. The ratio of the black area to the total one represents the gas area fraction (GAF). The segmentation process is performed using Ostu's algorithm [36] in which the gray levels of the original image are split into two classes at the optimum thresholding value at which the intra-class variance of both classes is minimal. Fig. 4 shows the generated histograms of both the original SEM images shown in Fig. 1 and their thresholded

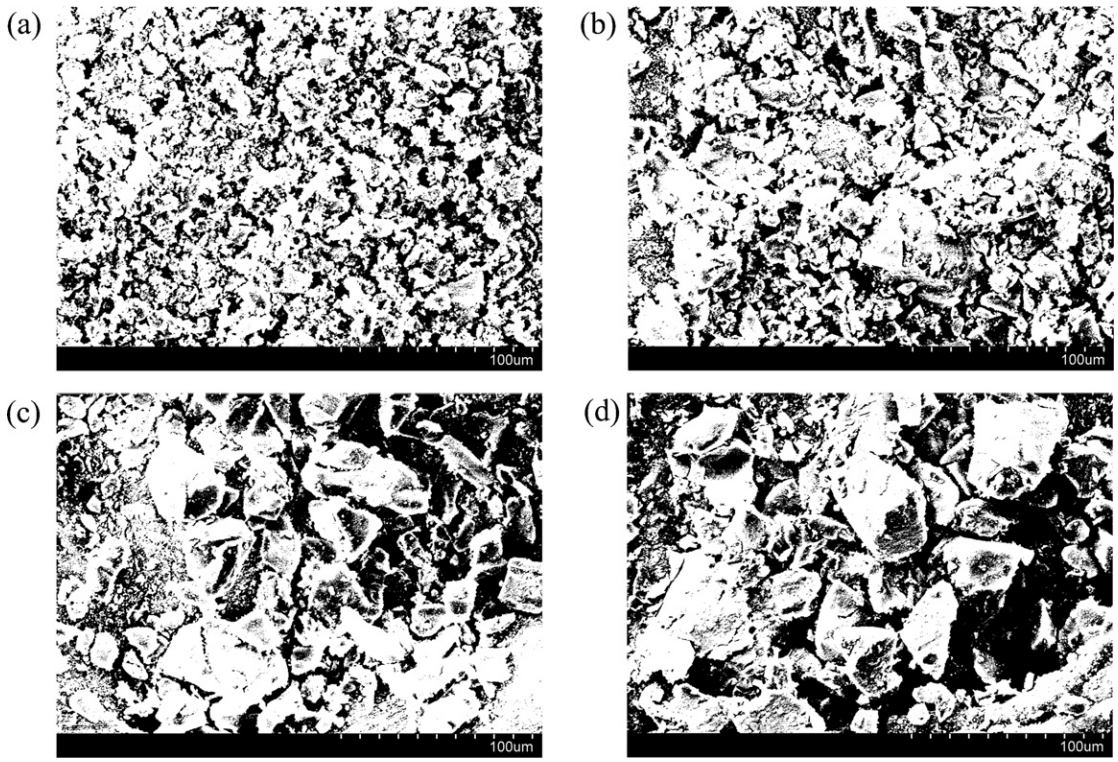

Fig. 3. Thresholded SEM images of superhydrophobic aerogel coatings with different particle-size ranges. (a) 0–43 μm; (b) 43–104 μm; (c) 104–150 μm; (d) 150–210 μm.

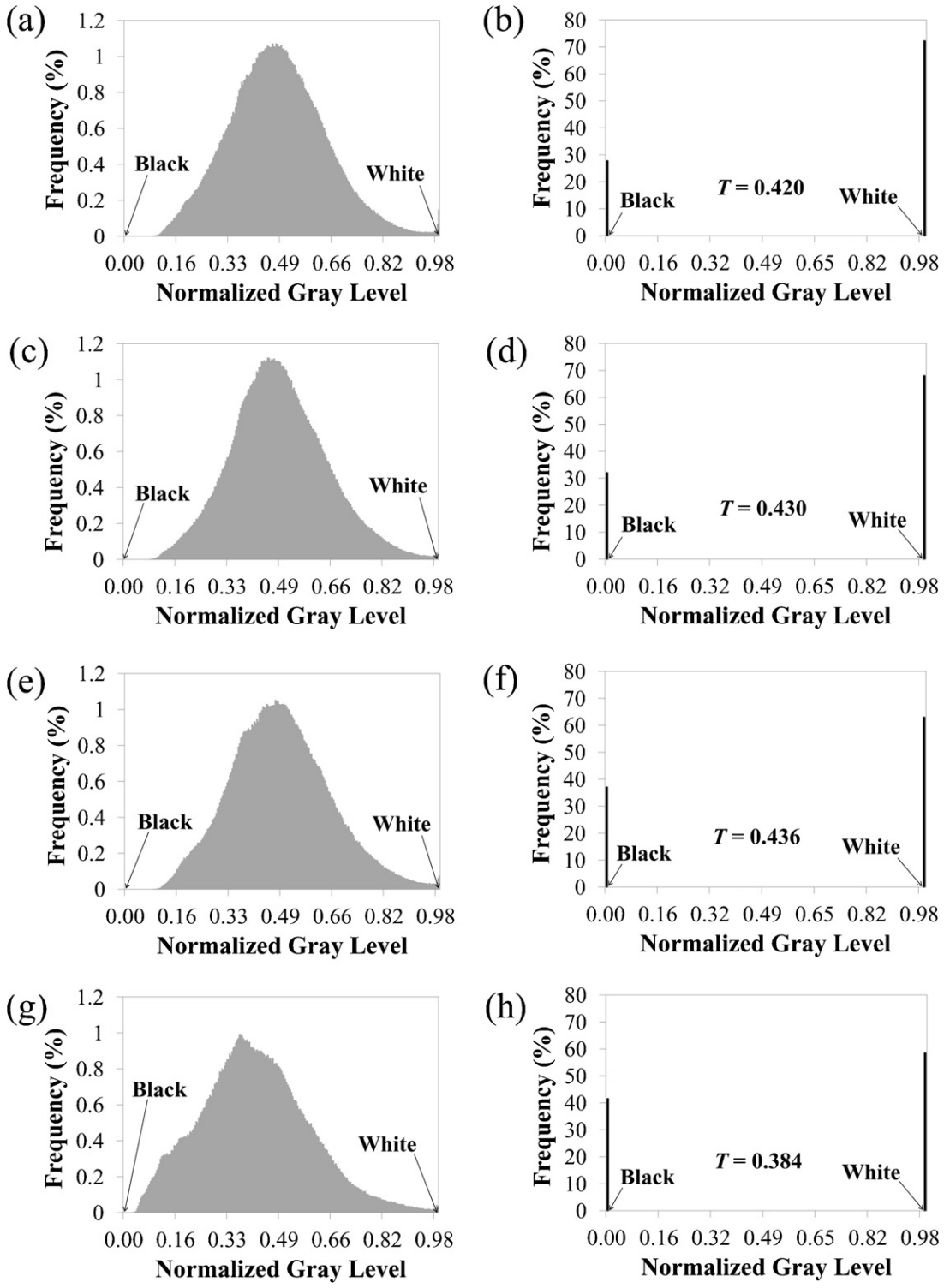

Fig. 4. Histogram of original and thresholded SEM images of superhydrophobic aerogel coatings with different particle-size ranges. (a) 0–43 μm; (b) thresholding of (a); (c) 43–104 μm; (d) thresholding of (c); (e) 104–150 μm; (f) thresholding of (e); (g) 150–210 μm; (h) thresholding of (g). Thresholding value *T* is indicated for each thresholding image.

ones shown in Fig. 3. The normalized thresholding value, *T*, of each image is indicated in Fig. 4.

Fig. 5 shows the calculated gas area fraction (GAF) for different samples, using the described image-thresholding technique, versus the maximum particle size (sieve-mesh size). The time-intensive calculations are repeated at about six different spots of each coating. The error bar shows the range of the standard divination of the results. The figure shows that as particle size increases, the gas fraction increases, which agrees with previous studies [37].

In order to show how the results could be affected by changing the thresholding value, a sensitivity analysis was performed for segmenting the coating shown in Fig. 1a. We changed the normalized thresholding value relative to the optimum one and calculated the corresponding changes in the gas area fraction (see

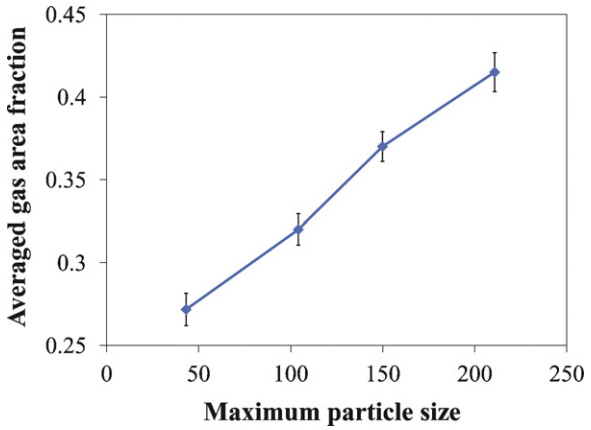

Fig. 5. Calculated gas area fraction using image-thresholding technique for different maximum particle size.

Fig. 6). The results reveal that the changes in the gas area fraction are almost linearly proportional to those of the normalized thresholding value indicating the importance of choosing a correct thresholding method.

To validate our image-thresholding process, we have applied this technique to SEM images obtained for a mesh grid with known dimensions (i.e., opening size). The SEM images are at three different magnifications and have the same brightness and contrast as those used for the aerogel images. Using the software Mathematica, we determined the gray-level histogram of both original and thresholded images. The latter images were used to determine the opening areas of the mesh grid. These values were then compared with the information provided by the manufacturer in terms of wire/filament diameter and opening of the mesh grid (wire diameter = 100 μm, GAF = 0.3). For the mesh at different magnification scales, Fig. 7 shows histograms of both the SEM images (a, c and e) and the corresponding thresholding ones (b, d and f). The normalized thresholding values are shown in each figure. The highest magnified image (Fig. 7e) has the same scale as that of the aerogel coatings. The results show that the percentage errors of the calculated gas area fraction (using the described segmentation technique) relative to the exact one are 1.8% for the lowest magnified image (Fig. 7b), 3.7% for the moderately magnified one (Fig. 7d), and 3.4% at the highest magnification scale (Fig. 7f). This good agreement demonstrates that the calculated gas fractions shown in Fig. 5 are trustworthy.

It is worth mentioning that, for an aerogel coating, there is no straightforward relationship between gas area fraction and gas volume fraction (i.e., porosity). However, it could be expected that for a coating produced with a similar technique, the gas area fraction increases with increasing the gas volume fraction. The latter was roughly estimated for the coatings of the present study to vary between 15% for the finest particles to about 45% for the largest particles. These values were obtained by estimating the total volume of the particles before depositing them on a substrate. In addition, the dimensions of the coating were measured after the particles were attached to the substrate. The coating's thickness was measured using a thickness gage (J-40-T) made by Electromatic Equipment Company. During estimating the initial volume of the particles stored in a vial, we considered the particles to pack together with a porosity of about 50%. This is an educated guess based on previous studies [38–41] for particles with irregular shapes and poly-disperse size distributions.

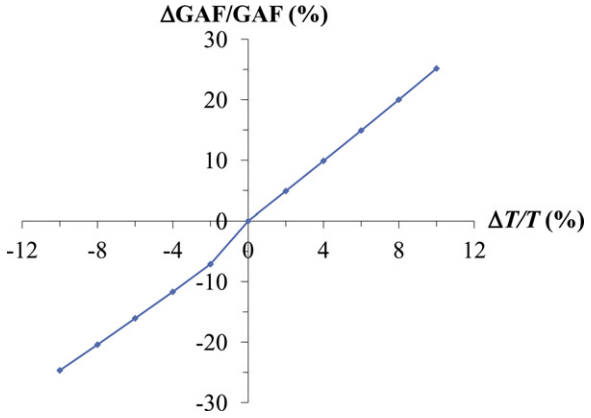

Fig. 6. Percentage change of gas area fraction versus that of normalized thresholding value.

5. Results and discussion

When a superhydrophobic surface is submerged in water, the spatial distribution of trapped air on the surface exhibits a mirror-like sheen at the air–water interface. Therefore, the kinetics of the trapped air's loss could be monitored by examining the intensity of reflected light from the surface with increasing pressure up to the critical one. We previously demonstrated the use of light scattering as an indirect means of characterizing the amount of air trapped within submerged superhydrophobic coatings against time, i.e., longevity [34]. In our technique, the reflected light spectrum can be measured as a function of pressure and integrated to obtain a wavelength-averaged reflection intensity. Fig. 8 shows the normalized average reflected light intensity, I_n, versus ambient pressure for the four aerogel samples with different average gas area fractions. The normalized average reflected light intensity is defined as

$$I_n = \frac{I - I_d}{I_f - I_d} \quad (1)$$

where I is the average integrated measured intensity across the range of wavelengths of visible light, I_d is the intensity for the completely hydrophilic sample (subjected to wetting-transition pressure), and I_f is the intensity for a superhydrophobic fresh sample at atmospheric pressure.

Fig. 8 shows that the light intensity decreases with increasing pressure for all coatings, indicating the loss of trapped air due to the breakup of the air–water interface. As mentioned earlier, this effect could be interpreted in terms of the balance between the liquid pressure from one side and the capillary forces and the air pressure inside entrapped the pores from the other side [21–28]. If the hydrostatic pressure overcomes the other two forces, the meniscus fails leading to the surface transitioning from the Cassie state to the Wenzel state. From the figure, it is obvious that the reduction in the light intensity with increasing pressure did not occur abruptly. This is due the heterogeneity of the coatings. Therefore, the failure happens locally wherever the local gas area fraction across the sample is larger than the critical value corresponding to the given hydrostatic pressure. As the light-beam covers the whole sample, the measurements are the integration of all wetted and non-wetted spots across the area of investigation. Thus, the pressure at which the entire surface is transitioned to the Wenzel state is henceforth referred to as the terminal pressure. The terminal pressure is to be contrasted to the critical pressure at which transition to wetted state only commences. Fig. 9 shows that the terminal pressure is reduced as the gas area fraction is increased, as expected [21–28]. Furthermore, the figure demonstrates a higher terminal pressure for the sample with 0.27 average gas fraction because this sample was made of the finest aerogel particles.

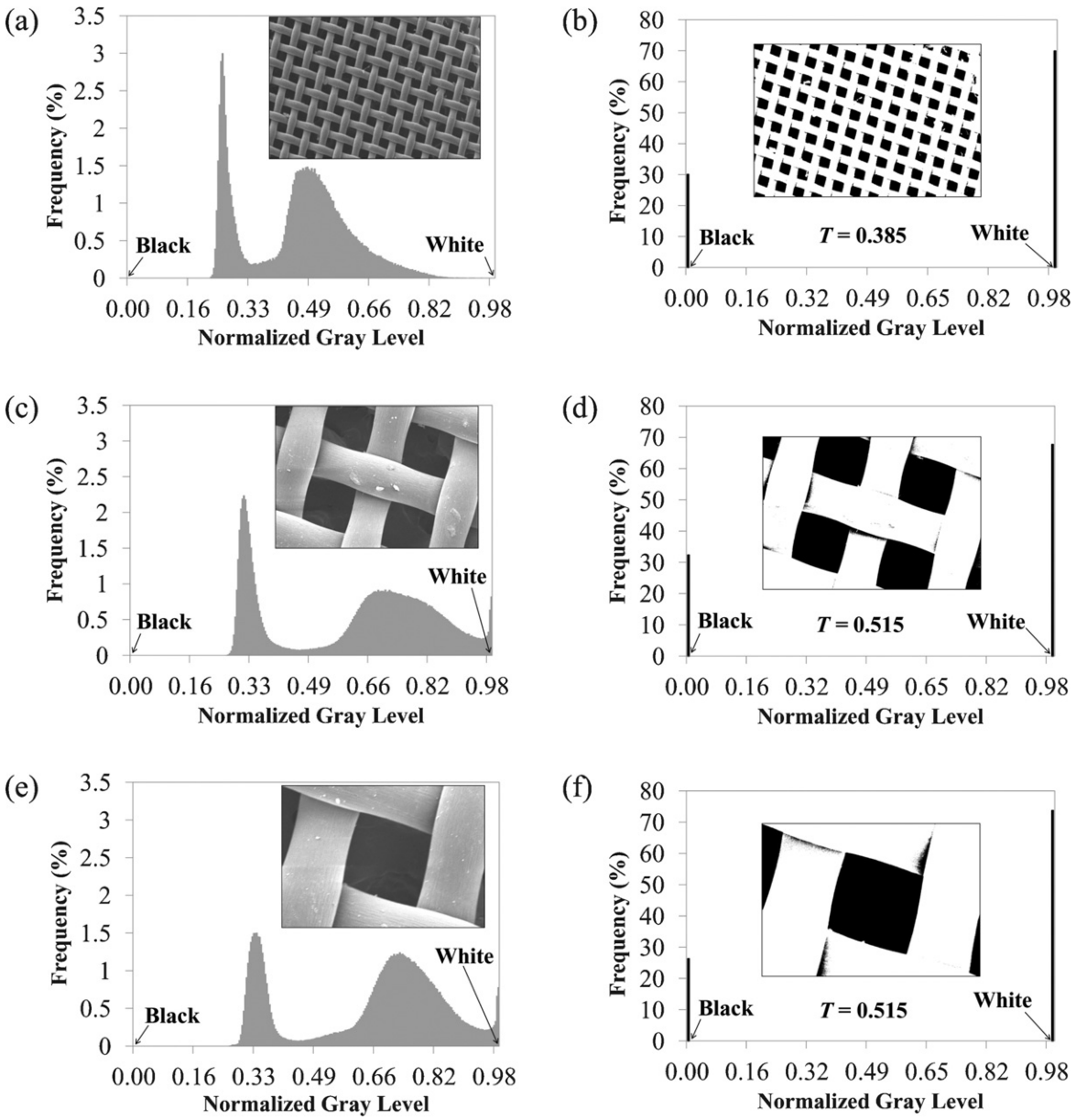

Fig. 7. Histogram of original and thresholded SEM images of a mesh grid with known dimensions. (a) Low-magnification SEM image; (b) thresholding of (a); (c) moderately magnified SEM image; (d) thresholding of (c); (e) highly magnified SEM image; (f) thresholding of (e). Thresholding value T is indicated for each thresholding image.

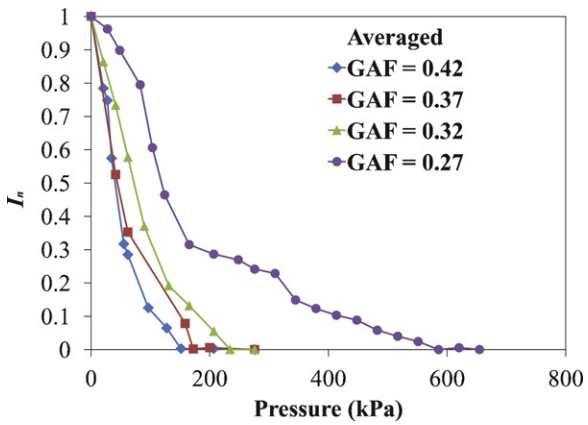

Fig. 8. Effect of pressure on reflected light intensity from immersed coating samples.

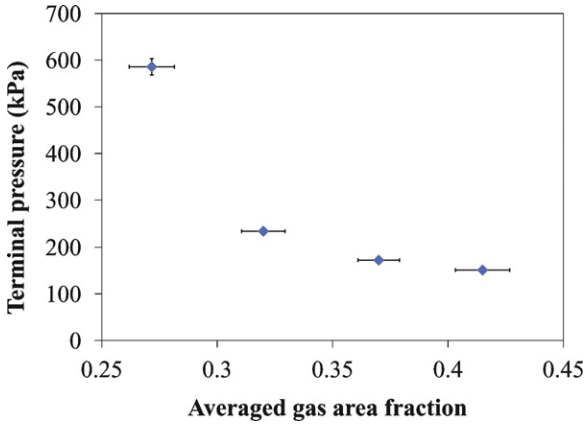

Fig. 9. Effect of gas area fraction on terminal pressure.

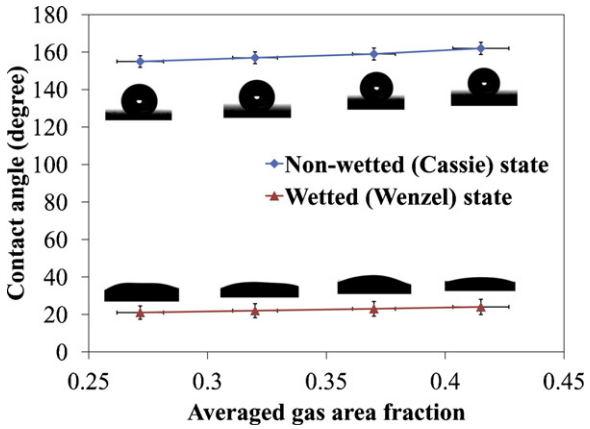

Fig. 10. Effect of gas area fraction on static contact angle for both wetted and non-wetted states.

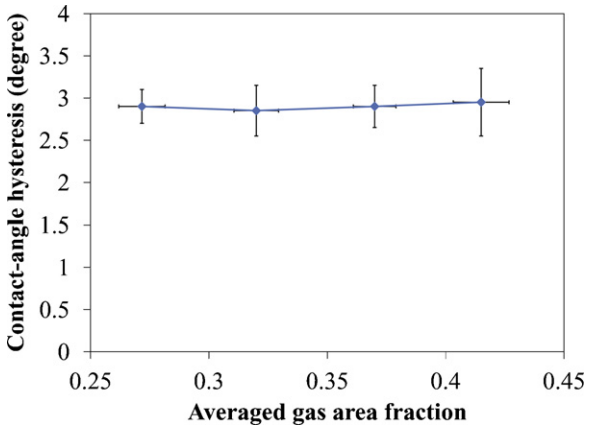

Fig. 11. Contact-angle hysteresis of fresh samples against averaged gas area fraction.

To further investigate the hydrophobicity of the coatings after exposure to pressures beyond their terminal pressures, we measured the static contact angle of water droplets on each coating using a goniometer [34] before and after the experiment. As can be seen in Fig. 10, the contact angles on all coatings decreased from about 155° to about 25°, indicating the total loss of superhydrophobicity. Fig. 11 shows the measured contact-angle hysteresis of the fresh samples (before applying any pressure). The figure demonstrates that the hysteresis for all samples is around 3°, which confirms the hydrophobicity of the fresh samples.

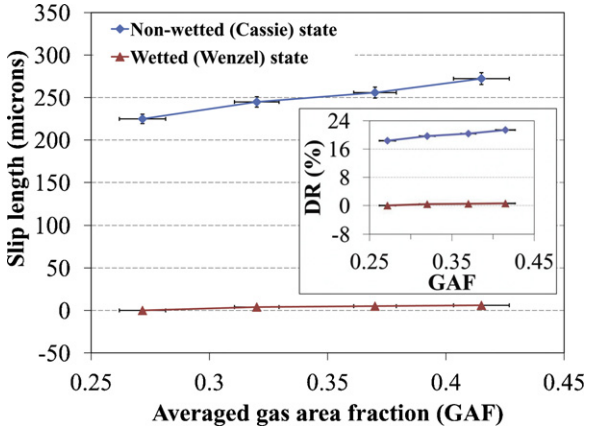

Fig. 12. Effect of gas area fraction on slip length for both wetted and non-wetted states. Inset shows corresponding drag reduction.

We also measured the slip length and drag-reduction percentage DR% (drag force of a coated surface compared to that of uncoated smooth one [34]) before and after exposing the different coatings to pressures beyond their terminal pressure. It is evident from Fig. 12 that after exposure to the elevated pressure, the slip length and the degree of drag reduction were diminished.

6. Conclusions

We used our in situ, noninvasive light-scattering technique to measure the terminal pressure of submerged superhydrophobic coatings made up of randomly deposited polydisperse aerogel particles. Four surfaces with different aerogel-particle mean sizes were tested. To estimate the coating's gas area fraction, an image-thresholding technique was applied to several SEM images of the four coatings. The image-processing technique was validated by testing a grid-mesh sample with known gas area fraction. The study reported here presents experimental proof for the increase of terminal pressure with decreasing gas area fraction over man-made granular superhydrophobic coatings because the samples with lower gas fraction are made of finer aerogel particles that can sustain higher pressures without transition to wetted state (by keeping the entrapped air layer). Our light-scattering data were compared to contact-angle, drag reduction, and slip-length measurements for mutual verification, and good agreements were observed among all measurements.

The measurements reported here show that terminal pressures as high as about 600 kPa (equivalent to an underwater depth of about 60 m) can be achieved with coatings made up aerogel particles. The present study opens a pathway for cost-effective fabricating superhydrophobic coatings for underwater applications.

Acknowledgment

This research is sponsored by the Defense Advanced Research Projects Agency (DARPA), Contract Number W91CRB-10-1-0003, technical sponsor Captain Christopher Warren, USN. The content of this paper does not necessarily reflect the position or the policy of the Government, and no official endorsement should be inferred.

References

[1] C. Neinhuis, W. Barthlott, Characterization and distribution of water-repellent, self-cleaning plant surfaces, Ann. Bot. 79 (1997) 667–677.
[2] X. Gao, L. Jiang, Water-repellent legs of water striders, Nature 432 (2004) 36.
[3] C.L.M.H. Navier, Mémoire sur les lois du mouvement des fluides, Mem. Acad. R. Sci. Inst. France 6 (1823) 389–440.
[4] J.P. Rothstein, Slip on superhydrophobic surfaces, Annu. Rev. Fluid Mech. 42 (2010) 89–109.
[5] M.A. Samaha, H.V. Tafreshi, M. Gad-el-Hak, Superhydrophobic surfaces: from the lotus leaf to the submarine, C. R. Mech. 340 (2012) 18–34.
[6] M. Gad-el-Hak, Flow Control: Passive, Active, and Reactive Flow Management, Cambridge University Press, London, United Kingdom, 2000.
[7] J. Davies, D. Maynes, B.W. Webb, B. Woolford, Laminar flow in a microchannel with superhydrophobic walls exhibiting transverse ribs, Phys. Fluids 18 (2006) 087110.
[8] C. Lee, C.-H. Choi, C.-J. Kim, Structured surfaces for giant liquid slip, Phys. Rev. Lett. 101 (2008) 064501.
[9] B. Woolford, J. Prince, D. Maynes, B.W. Webb, Particle image velocimetry characterization of turbulent channel flow with rib patterned superhydrophobic walls, Phys. Fluids 21 (2009) 085106.
[10] A. Steinberger, C. Conttin-Bizonne, P. Kleimann, E. Charlaix, High friction on a bubble mattress, Nat. Mater. 6 (2007) 665–668.
[11] M. Ma, Y. Mao, M. Gupta, K.K. Gleason, G.C. Rutledge, Superhydrophobic fabrics produced by electrospinning and chemical vapor deposition, Macromolecules 38 (2005) 9742–9748.
[12] F.O. Ochanda, M.A. Samaha, H.V. Tafreshi, G.C. Tepper, M. Gad-el-Hak, Fabrication of superhydrophobic fiber coatings by DC-biased AC-electrospinning, J. Appl. Polym. Sci. 123 (2012) 1112–1119.
[13] S.D. Bhagat, Y.-H. Kim, K-H. Suh, Y.-S. Ahn, J.-G. Yeo, J.-H. Han, Super hydrophobic silica aerogel powders with simultaneous surface modification, solvent exchange and sodium ion removal from hydrogels, Micropor. Mesopor. Mater. 112 (2008) 504–509.

[14] H. Yang, Y. Deng, Preparation and physical properties of superhydrophobic papers, J. Colloid Interface Sci. 325 (2008) 588–593.
[15] S. Lee, D. Kim, W. Hwang, Artificial lotus leaf structure made by blasting with sodium bicarbonate, Curr. Appl. Phys. 11 (2011) 800–804.
[16] H.S. Hwang, N.H. Kim, S.G. Lee, D.Y. Lee, K. Cho, I. Park, Facile fabrication of transparent superhydrophobic surfaces by spray deposition, ACS Appl. Mater. Interfaces 3 (2011) 2179–2183.
[17] M. Bobji, S.V. Kumar, A. Asthana, R.N. Govardhan, Underwater sustainability of the "Cassie" state of wetting, Langmuir 25 (2009) 12120–12126.
[18] M. Sakai, T. Yanagisawa, A. Nakajima, Y. Kameshima, K. Okada, Effect of surface structure on the sustainability of an air Layer on superhydrophobic coatings in a water–ethanol mixture, Langmuir 25 (2009) 13–16.
[19] R. Poetes, K. Holtzmann, K. Franze, U. Steiner, Metastable underwater superhydrophobicity, Phys. Rev. Lett. 105 (2010) 166104.
[20] B. Liu, F.F. Lange, Pressure induced transition between superhydrophobic states: configuration diagrams and effect of surface feature size, J. Colloid Interface Sci. 298 (2006) 899–909.
[21] N.A. Patankar, Transition between superhydrophobic states on rough surfaces, Langmuir 20 (2004) 7097–7102.
[22] L. Barbieri, E. Wagner, P. Hoffmann, Water wetting transition parameters of perfluorinated substrates with periodically distributed flat-top microscale obstacles, Langmuir 23 (2007) 1723–1734.
[23] C.W. Extrand, Criteria for ultralyophobic surfaces, Langmuir 20 (2004) 5013–5018.
[24] C.W. Extrand, Designing for optimum liquid repellency, Langmuir 22 (2006) 1711–1714.
[25] Q.S. Zheng, Y. Yu, Z.H. Zhao, Effects of hydraulic pressure on the stability and transition of wetting modes of superhydrophobic surfaces, Langmuir 21 (2005) 12207–12212.
[26] M.A. Samaha, H.V. Tafreshi, M. Gad-el-Hak, Modeling drag reduction and meniscus stability of superhydrophobic surfaces comprised of random roughness, Phys. Fluids 23 (2011) 012001.
[27] B. Emami, T.M. Bucher, H.V. Tafreshi, D. Pestov, M. Gad-el-Hak, G.C. Tepper, Simulation of meniscus stability in superhydrophobic granular surfaces under hydrostatic pressures, Colloid Surf. A 385 (2011) 95–103.
[28] B. Emami, H.V. Tafreshi, M. Gad-el-Hak, G.C. Tepper, Predicting shape and stability of air–water interface on superhydrophobic surfaces with randomly distributed, dissimilar posts, Appl. Phys. Lett. 98 (2011) 203106.
[29] C.W. Extrand, Repellency of the lotus leaf: resistance to water intrusion under hydrostatic pressure, Langmuir 27 (2011) 6920–6925.
[30] X. Sheng, J. Zhang, Air layer on superhydrophobic surface underwater, Colloid Surf. A 377 (2011) 374–378.
[31] A. Lafuma, D. Quéré, Superhydrophobic states, Nat. Mater. 2 (2003) 457–460.
[32] R.N. Wenzel, Resistance of solid surfaces to wetting by water, Ind. Eng. Chem. 28 (1936) 988–994.
[33] A.B.D. Cassie, S. Baxter, Wettability of porous surfaces, Trans. Faraday Soc. 40 (1944) 546–551.
[34] M.A. Samaha, F.O. Ochanda, H.V. Tafreshi, G.C. Tepper, M. Gad-el-Hak, In situ, non-invasive characterization of superhydrophobic coatings, Rev. Sci. Instrum. 82 (2011) 045109.
[35] S. Jaganathan, H.V. Tafreshi, B. Pourdeyhimi, A realistic approach for modeling permeability of fibrous media: 3-D imaging coupled with CFD simulation, Chem. Eng. Sci. 63 (2008) 244–252.
[36] N. Otsu, A threshold selection method from gray-level histograms, IEEE Trans. Syst. Man Cybern. 9 (1979) 62–66.
[37] C.E. Chaffey, I. Wagstaff, Shear thinning and thickening rheology: II. Volume fraction and size of dispersed particles, J. Colloid Interface Sci. 59 (1977) 63–75.
[38] J.P. Latham, Y. Lu, A. Munjiza, A random method for simulating loose packs of angular particles using tetrahedra, Geotechnique 51 (2001) 871–879.
[39] D.S. Stafford, T.L. Jackson, Using level sets for creating virtual random packs of non-spherical convex shapes, J. Comput. Phys. 229 (2010) 3295–3315.
[40] J. Baker, A. Kudrolli, Maximum and minimum stable random packings of platonic solids, Phys. Rev. E 82 (2010) 061304.
[41] S. Torquato, F.H. Stillinger, Jammed hard-particle packings: from Kepler to Bernal and beyond, Rev. Mod. Phys. 82 (2010) 2633–2640.

APPENDIX VIII: Numerical Studies on Superhydrophobic Surfaces Comprised of Random Roughness

Following is a reprint of the paper "Modeling Drag Reduction and Meniscus Stability of Superhydrophobic Surfaces Comprised of Random Roughness," by Samaha, M.A., Tafreshi, H.V., and Gad-el-Hak, M., *Physics of Fluids*, vol. 23, pp. 012001.1–012001.8, 2011.

Modeling drag reduction and meniscus stability of superhydrophobic surfaces comprised of random roughness

Mohamed A. Samaha,[a] Hooman Vahedi Tafreshi,[b] and Mohamed Gad-el-Hak[c]
Department of Mechanical Engineering, Virginia Commonwealth University, Richmond, Virginia 23284-3015, USA

(Received 30 July 2010; accepted 6 December 2010; published online 11 January 2011)

Previous studies dedicated to modeling drag reduction and stability of the air-water interface on superhydrophobic surfaces were conducted for microfabricated coatings produced by placing hydrophobic microposts/microridges arranged on a flat surface in aligned or staggered configurations. In this paper, we model the performance of superhydrophobic surfaces comprised of randomly distributed roughness (e.g., particles or microposts) that resembles natural superhydrophobic surfaces, or those produced via random deposition of hydrophobic particles. Such fabrication method is far less expensive than microfabrication, making the technology more practical for large submerged bodies such as submarines and ships. The present numerical simulations are aimed at improving our understanding of the drag reduction effect and the stability of the air-water interface in terms of the microstructure parameters. For comparison and validation, we have also simulated the flow over superhydrophobic surfaces made up of aligned or staggered microposts for channel flows as well as streamwise or spanwise ridges configurations for pipe flows. The present results are compared with theoretical and experimental studies reported in the literature. In particular, our simulation results are compared with work of Sbragaglia and Prosperetti, and good agreement has been observed for gas fractions up to about 0.9. The numerical simulations indicate that the random distribution of surface roughness has a favorable effect on drag reduction, as long as the gas fraction is kept the same. This effect peaks at about 30% as the gas fraction increases to 0.98. The stability of the meniscus, however, is strongly influenced by the average spacing between the roughness peaks, which needs to be carefully examined before a surface can be recommended for fabrication. It was found that at a given maximum allowable pressure, surfaces with random post distribution produce less drag reduction than those made up of staggered posts. © *2011 American Institute of Physics*. [doi:10.1063/1.3537833]

I. INTRODUCTION

A combination of hydrophobicity and micro- or nanoscale surface roughness can result in an effect known as superhydrophobicity, characterized by water droplets beading on the solid surface at contact angles exceeding 150°. When fully submersed in water, such surface can cause the so-called "slip effect," resulting in significant reduction in the skin-friction drag exerted on the surface.[1] Superhydrophobic coatings can be utilized as a passive method of flow control and may potentially become a viable alternative to the more complex and energy consuming active or reactive flow control techniques such as wall suction/blowing.[2]

Most engineered superhydrophobic surfaces are made up of microposts or microridges manufactured via advanced microfabrication techniques. The microposts can be fabricated in form of aligned (i.e., flow direction parallel to a side of a square formed by four posts) or staggered (i.e., flow direction parallel to a diagonal of a square formed by four posts) arrangement. On the other hand, microridges can be in the form of streamwise or spanwise configuration. Microfabricated superhydrophobic surfaces have been extensively studied in the last few years both experimentally and numerically.[3–9] The superhydrophobic surface can entrap air cavities between microposts or microridges producing two different interfaces. One of them is between air and water, which significantly reduces the shear stress. The second interface is between water and solid (ridges or posts), at which the customary resistance to the flow is considered. Cheng *et al.*,[10] for example, numerically calculated the influence of the total shear-free area or the air-water interface area (area at which slip effect takes place) as well as its dependency on the slip length. Kunert and Harting[11] numerically simulated hydrophobic rough microchannel flows. Lauga and Stone[12] numerically studied effects of gas fraction and periodicity on the slip length for a transverse configuration. They validated their results with those analytically predicted by Philip[13] for streamwise configuration. Davis and Lauga[14] demonstrated an analytical solution for a thin mesh superhydrophobic surface. In an earlier paper, the same authors[15] provided a mathematical model of laminar flow over a curved bubble "mattress." Sbragaglia and Prosperetti[16] analyzed the velocity boundary condition on a surface composed of slip sites with random distribution, somewhat similar to those studied in the current paper. They also investigated the effect of the

[a]Electronic mail: samahama@vcu.edu.
[b]Electronic mail: htafreshi@vcu.edu. URL: http://www.people.vcu.edu/~htafreshi/.
[c]Author to whom correspondence should be addressed. Electronic mail: gadelhak@vcu.edu. URL: http://www.people.vcu.edu/~gadelhak/.

 © 2011 American Institute of Physics

Downloaded 11 Jan 2011 to 128.172.192.45. Redistribution subject to AIP license or copyright; see http://pof.aip.org/about/rights_and_permissions

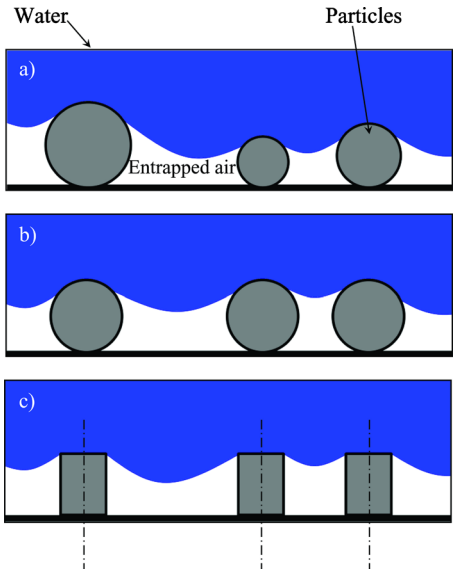

FIG. 1. (Color online) Schematic diagram showing the two major simplifications considered in our modeling of superhydrophobic roughened surfaces. (a) Actual surface. (b) Simplified system assuming that all peaks (particles) have an identical size. (c) Modeling the peaks with circular microposts.

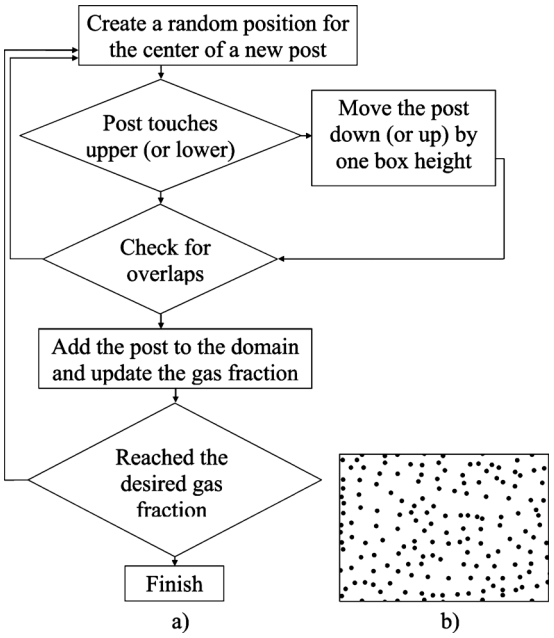

FIG. 2. (a) Post distribution algorithm. (b) Example of random surface used.

curvature of the air-water interface on the slip length for a streamwise configuration.[17]

The stability of the air-water interface (meniscus) for the staggered microposts is reported by Lee *et al.*[18] Similar studies, however, have not been reported for superhydrophobic surfaces with random roughness (e.g., lotus leaves) or surfaces made via random particle deposition, a far less expensive and simpler manufacturing technique.[19,20]

The objective of the present study is to simulate the performance of superhydrophobic surfaces having idealized random roughness or hydrophobic sites (posts or particles) and compare such surfaces to those manufactured via microfabrication. The comparison is based on the effect of the gas fraction (ratio of shear-free area to total area), which generally reduces the skin friction and increases the slip velocity.

In the next section, we present our algorithm for generating and characterizing randomly distributed circular objects representing the tip area of the surface roughness. Section III briefly describes our numerical simulation scheme along with a discussion on the choice of boundary conditions. In Sec. IV, we present a mesh-independence study and compare our numerical simulations with the experimental data of Lee *et al.*,[18] the theoretical results of Ybert *et al.*,[21] the analytical results of Philip,[13] and the numerical results of Lauga and Stone[12] in order to verify the accuracy of our numerical calculations. Results and discussions are given in Sec. V, followed by conclusions in Sec. VI.

II. VIRTUAL 2D SUPERHYDROPHOBIC SURFACES

Estimating the exact contact surface between water and randomly distributed peaks of natural or engineered rough surfaces is a major challenge. This is because the contact surface area may change depending on the height of the peaks, their diameter, and the hydrostatic pressure applied on the system (see Fig. 1). To simplify our case study, we assume the peaks of the hydrophobic particles to be identical in size. We also assume the contact area between water and each peak to be a flat surface, even though the actual surface is not. As shown in Fig. 1(c), therefore, the random particles are modeled as random microposts with equal heights.

To generate an idealized surface with randomly distributed cylindrical roughness, a FORTRAN program is developed to produce virtual superhydrophobic surfaces of different area fractions, defined as

$$\phi_g = \frac{A_0}{A_T} = 1 - \frac{A_s}{A_T}, \tag{1}$$

where ϕ_g is the gas fraction, A_0 is the shear-free area, A_s is the solid area (posts area), and A_T is the total area.

Our algorithm is explained in the flowchart shown in Fig. 2. The process starts by sequentially adding circular posts to a rectangular domain with a given size. The distance between a new post and existing ones is continuously monitored to avoid any overlaps. Moreover, to ensure that a high-quality mesh can be generated inside the domain, the posts were not allowed to touch one another. To do this, a minimum gap of $1.1d$ was enforced between the posts' center-to-center distance, where d is the post diameter. To generate periodic boundary conditions on the lateral sides of the domain, a distance equal to the size of the simulation box is added to or subtracted from the position of any post touching the lateral boundaries. This procedure continues until a desired area fraction is reached. At the end of the surface generation process, the geometry is exported to Gambit software (a preprocessor for FLUENT CFD code) via a script file for meshing. The mesh files were then exported to Fluent for finite-volume calculations.

Downloaded 11 Jan 2011 to 128.172.192.45. Redistribution subject to AIP license or copyright; see http://pof.aip.org/about/rights_and_permissions

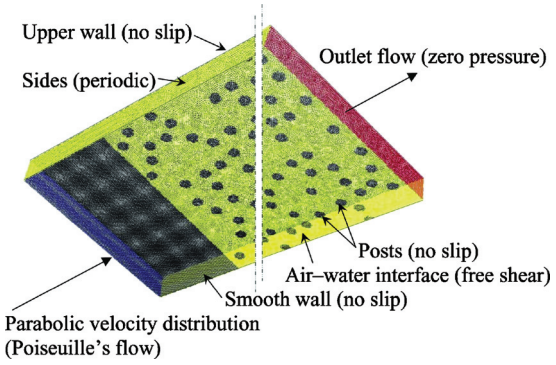

FIG. 3. (Color) Example of the simulation domain along with the boundary conditions.

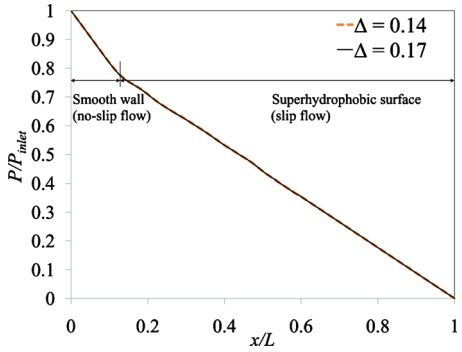

FIG. 4. (Color) Pressure distribution along a channel having a superhydrophobic bottom surface with gas fraction of 0.865, meshed with two different grid densities. Reynolds number is 11.85.

III. FLUID FLOW SIMULATIONS

The present study focuses on the steady, incompressible, laminar flow of water in a microchannel having a superhydrophobic bottom surface. The continuity and the momentum equations are numerically integrated using the CFD code from Fluent Inc.

$$\frac{\partial u_i}{\partial x_i} = 0, \tag{2}$$

$$\rho u_j \frac{\partial u_i}{\partial x_j} = -\frac{\partial P}{\partial x_i} + \mu \frac{\partial}{\partial x_j}\left(\frac{\partial u_i}{\partial x_j}\right), \tag{3}$$

where u_i is the velocity field, x_i is the Cartesian coordinates, ρ is the fluid density, P is the static pressure, and μ is the fluid viscosity. Figure 3 shows an example of the simulation domains along with the boundary conditions considered in the study. The domains were meshed using about 10^6 equal-sized unstructured tetrahedral cells. The shear-free regions (flow over the air cavities) were modeled with a zero velocity slope boundary condition

$$\left.\frac{\partial u_i}{\partial y}\right|_{y=0} \approx 0, \tag{4}$$

where y is the direction normal to the surface. When a liquid flows over a gas-filled cavity, the shear stress must match on both sides of the gas-liquid interface, and a coupled interface model should be used for the boundary. However, if the gas-liquid viscosity ratio is on the order of 10^{-2} or less, the results of the shear-free boundary condition agree well with those of coupled interface model.[10] We simulated the laminar flow of water at different Reynolds numbers, defined based on the average velocity at inlet and the channel's hydraulic diameter, $11.85 < \mathrm{Re} < 1778$, and for different gas fractions of $0.0 < \phi_g < 0.99$.

IV. VALIDATION AND MESH INDEPENDENCE

A. Mesh independence

To ensure that our results are independent of the choice of mesh size, we considered one of our superhydrophobic surfaces and meshed its solution domain using two different grid densities. Figure 4 compares the dimensionless pressure distribution obtained from these simulations. The pressure values shown in the figure are normalized using the channel pressure at inlet. x/L is the dimensionless distance measured from the inlet. The outlet pressure is set to be zero.

The results presented in Fig. 4 are obtained for dimensionless cell size Δ of 0.14 and 0.17 (normalized using post diameter). It can be seen that the two simulations are in perfect agreement with one another. Thus, cell size 0.17 is fair enough for our simulation. Note also that the slope of the pressure gradient for the smooth wall is higher than that for superhydrophobic surface. This is due to the presence of a shear-free area in the superhydrophobic surface, which lowers the wall's resistance to the flow.

B. Comparison with previous studies

For further validation, we simulated a series of superhydrophobic surfaces made up of microposts arranged in staggered configurations and compared their slip lengths with those reported in the literature. According to Navier's model,[22] the magnitude of the slip velocity is proportional to the magnitude of the strain rate. The slip length is the proportionality constant. Thus, the slip length δ is calculated from the following equation:

$$\delta = \frac{(U_{\mathrm{slip}})_{\mathrm{wall}}}{\left.\frac{\partial u}{\partial y}\right|_{\mathrm{wall}}}, \tag{5}$$

where $(U_{\mathrm{slip}})_{\mathrm{wall}}$ is the area-weighted average slip velocity at the superhydrophobic wall, u is the streamwise velocity, and y is the normal direction. The slope $(\partial u/\partial y|_{\mathrm{wall}})$ can be obtained by dividing the area-weighted average shear stress by water viscosity. It can be seen that slip velocity increases as the shear-free area increases. Figure 5 shows the calculated slip length (normalized by the pitch; the distance between two posts) versus gas fraction at a Reynolds number of 11.85 in comparison with those obtained theoretically by Ybert *et al.*[21] and experimentally by Lee *et al.*[18] A closer view at gas fractions below 0.6 and above 0.85 is given in the insets for better illustration. From the figure, it is obvious that when the gas fraction is less than 0.4, the slip length δ is proportional to ϕ_g^2. On the other hand, if the gas fraction is higher than 0.7, the slip length δ is proportional to $1/\sqrt{\phi_g}$. Within

Downloaded 11 Jan 2011 to 128.172.192.45. Redistribution subject to AIP license or copyright; see http://pof.aip.org/about/rights_and_permissions

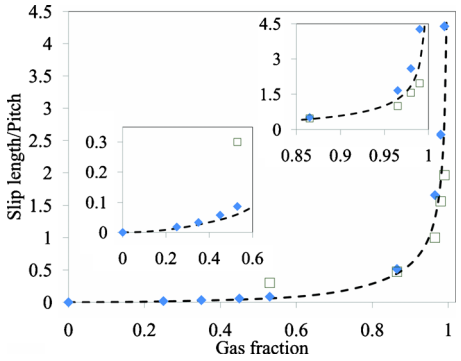

FIG. 5. (Color online) Comparison between slip length obtained from present simulations and those reported in the literature for channel flows. Present study (solid diamonds), experimental data of Lee *et al.* (Ref. 18) (open squares), and theory of Ybert *et al.* (Ref. 21) (dashed line).

the range $0.4<\phi_g<0.7$, interpolation is utilized. The above mathematical proportionalities are derived and validated by Ybert *et al.*[21]

It can be seen that the present numerical results are in close agreement with both the theory of Ybert *et al.*[21] and the experiment of Lee *et al.*[18] Note that both the present study and the theory of Ybert *et al.*[21] are derived for straight channels, while the experimental data of Lee *et al.*[18] were obtained using a rheometer (equivalent to a circular channel). The different geometries may explain the more pronounced deviation at the lowest gas fraction used.

More validation has been carried out.[23] Figure 6(a) shows our numerically calculated slip length for Stokes flow through a pipe that has streamwise configuration of free-

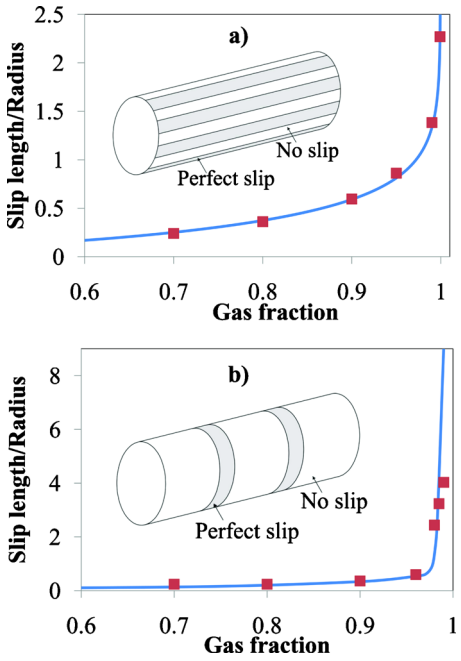

FIG. 6. (Color online) Comparison between slip length obtained from present simulations and those reported in the literature for pipe flows. (a) Streamwise configuration; present study (solid squares) and analytical results of Philip (Ref. 13) (solid line). (b) Spanwise configuration; present study (solid squares) and numerical results of Lauga and Stone (Ref. 12) (solid line).

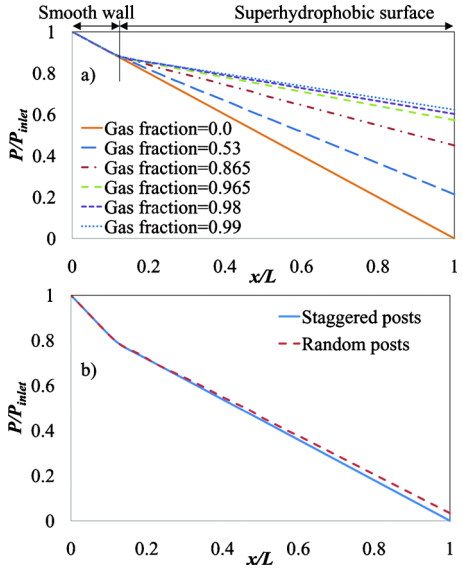

FIG. 7. (Color online) (a) Pressure distribution along the channel for different gas fraction (random posts, Re=11.85). (b) Pressure distribution for both random and staggered distribution posts (ϕ_g=0.865, Re=11.85).

shear patterns arranged periodically around the circumference at different gas fraction in comparison with the analytical results of Philip.[13] His equation reads

$$\frac{\delta}{R}=\frac{p}{\pi}\ln\left(\sec\frac{\pi\phi_g}{2}\right), \tag{6}$$

where δ is the slip length, R is the pipe radius, p is the periodicity (arc length of a unit cell that contains one slip and one no-slip pattern divided by the radius), and ϕ_g is the gas fraction. The periodicity in the figure is taken as $2\pi/6$ (i.e., 1.047), which means there were six strips of superhydrophobic coating around the circumference.

Perfect agreement between the numerical and analytical results is observed. Furthermore, Fig. 6(b) shows our results in comparison with the numerical data of Lauga and Stone[12] for a spanwise configuration. The periodicity (the axial length of a unit cell that contains one slip and one no-slip patterns divided by the radius) in the depicted case is 1. The figure indicates reasonable agreement between the two independent results. The problem solved in Fig. 6(b) is nonlinear and has no analytical solution, and that may explain the slight differences between our numerical results and those of Lauga and Stone.[12]

V. RESULTS AND DISCUSSION

A. Influence of gas fraction

The gas fraction has an important impact on the characteristics of a superhydrophobic surface, as it affects the slip length and therefore the pressure drop and the skin-friction coefficient. Figure 7(a) shows the pressure distribution along a channel having a superhydrophobic bottom surface consisting of random microposts. For all cases, the pressure at inlet is assumed to be the same as that of the case of zero gas fraction. The pressure values are normalized using the pressure at inlet. By increasing the gas fraction (i.e., reducing the

Downloaded 11 Jan 2011 to 128.172.192.45. Redistribution subject to AIP license or copyright; see http://pof.aip.org/about/rights_and_permissions

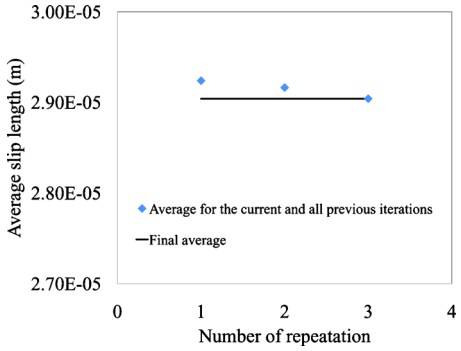

FIG. 8. (Color online) Average slip length for current and all previous repetitions vs number of repetitions, $\phi_g=0.865$.

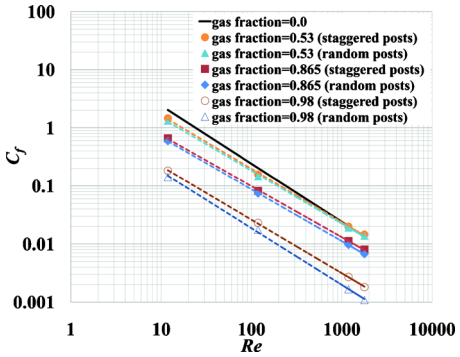

FIG. 9. (Color online) Skin-friction coefficient vs Reynolds number (Moody diagram) for different gas fractions.

posts diameter for a fixed total surface area), the slope of the pressure gradient is reduced, as is the case for aligned as well as staggered microposts. It is worth noting that for staggered circular posts, the gas fraction cannot be reduced below 0.1 due to the limit of maximum packing in 2D. For random posts, the limit is even greater. Figure 7(b) shows the pressure distribution along the channel for random posts in comparison with that obtained for staggered posts at a gas fraction of 0.865 and a Reynolds number of 11.85. We set the outlet pressure to be zero in case of the staggered posts. In addition, we assumed that the pressure at inlet is the same for both cases. It can be observed that the surface with random post distribution generates slightly less pressure drop than the one with staggered post configuration. The beneficial effect of random posts is improved as the gas fraction is increased, as discussed below.

Note that the gas fraction also influences the slip length. Referring to Fig. 5, it can be seen that by increasing the gas fraction, the slip length is increased because of the increasing average slip velocity leading to a decreasing average wall shear stress. To investigate whether or not the present simulations for surfaces with random post distributions are statistically representative, an ensemble of three surfaces with random post distributions is generated and the average slip length for each surface is computed. As can be seen from Fig. 8, the ensemble-averaged slip length is independent of the number of trials.

B. Effect of Reynolds number

In the canonical case of fully developed laminar flow between two parallel, smooth plates, the friction coefficient is a function of the Reynolds number ($C_f=24/\mathrm{Re}$), where $C_f=2\tau_{\mathrm{wall}}/\rho U^2$, τ_{wall} is area-weighted average shear stress, and U is average bulk fluid velocity. Our numerical results indicate that for superhydrophobic surfaces, similar functionality exists between the friction coefficient and Reynolds number, but with different constants depending on the gas fraction. As can be seen from Fig. 9, the friction coefficient decreases with increasing the gas fraction for surfaces with staggered posts and randomly distributed posts. We have also simulated aligned posts and found no difference between these and staggered ones as long as the gas fraction is kept constant.

As expected, higher gas fraction leads to lower skin friction. It is noticed from the figure that the random distribution of the posts results in lower skin- friction coefficient than that of staggered ones, but both have beneficial effects. In addition, the difference between the skin-friction coefficient of the random posts and that of the staggered posts increases by increasing the gas fraction. Figure 10 shows the normalized difference between the skin friction coefficients obtained for staggered and random posts, $\{[(C_f)_s-(C_f)_r]/(C_f)_s\}_{\mathrm{avg}}$. The differences are average values obtained for different Reynolds numbers in the range of $11.85<\mathrm{Re}<1778$. The figure shows that the reduction in the random posts' skin-friction coefficient relative to the staggered one is more significant at high gas fractions.

To explain these effects, we plotted in Fig. 11 the slip-velocity contours at the air-water interface for both staggered and random posts for a gas fraction of 0.865. Our results show that the area-weighted average slip velocity (normalized with the average velocity at the inlet) is 0.9645 and 0.9511 in the case of random and staggered posts, respectively. It can be seen that with the random post configuration, there is always a possibility that the flow will find larger passages (i.e., lower resistance) between the posts leading to a lower overall friction. In such areas, the slip velocity has reached a maximum value of about 0.179 m/s. Moreover, as the gas fraction increases, the number of such passages increases and hence the flow resistance continuously decreases, which leads to a larger difference between the staggered and random posts' skin-friction coefficients. It is worth mention-

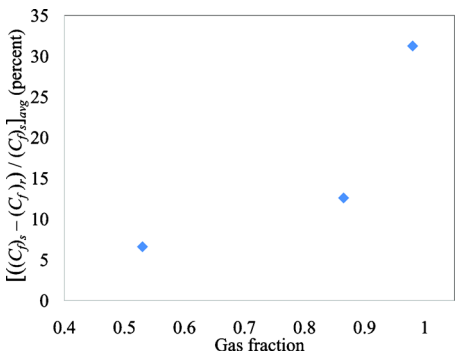

FIG. 10. (Color online) Average percentage difference between the skin-friction coefficients of the staggered and random posts vs gas fraction.

Downloaded 11 Jan 2011 to 128.172.192.45. Redistribution subject to AIP license or copyright; see http://pof.aip.org/about/rights_and_permissions

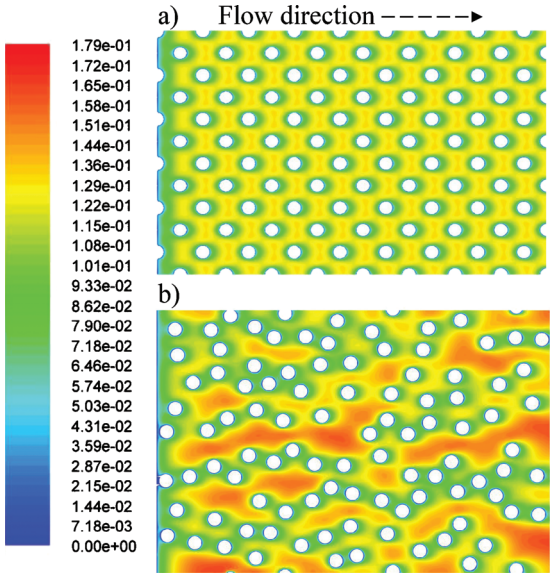

FIG. 11. (Color) Slip velocity contours at the air-water interface. Velocity scale is in m/s; ϕ_g=0.865. (a) Staggered posts and (b) random posts.

ing that similar effects have also been observed for fluid flow through random networks of fibers or particles. In a recent study, Tahir and Tafreshi[24] showed that the resistance caused by a staggered or even an in-line network of obstacles (i.e., fiber normal to the flow direction) is more than that obtained from its random counterpart having identical microstructural parameters (see also Hosseini and Tafreshi).[25] In addition, for flows through porous media, the difference between the friction factors of staggered and random configurations increases by increasing the gas fraction.

Figure 12 depicts for random posts the monotonic increase in slip length as the gas fraction ϕ_g increases. For comparison the analytical expression derived by Sbragaglia and Prosperetti,[16] $[\delta=(8/9\pi)(\phi_g/1-\phi_g)a]$, where a is the diameter of a post, is shown in the same figure. The agreement is reasonable up until a gas fraction of about 0.9, at which value the slip length predicted by our numerical results becomes significantly larger than that predicted by the theory of Sbragaglia and Prosperetti. These authors state that their theory is rigorous in the low-gas-fraction limit, but is extended heuristically to finite ϕ_g using data available at the time, which did not go beyond ϕ_g=0.9.

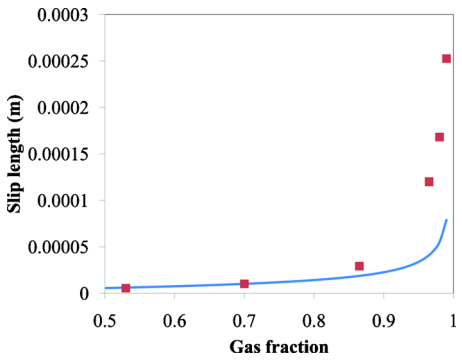

FIG. 12. (Color online) Slip length vs gas fraction. Present study (solid squares); Sbragaglia and Prosperetti (Ref. 16) (solid line).

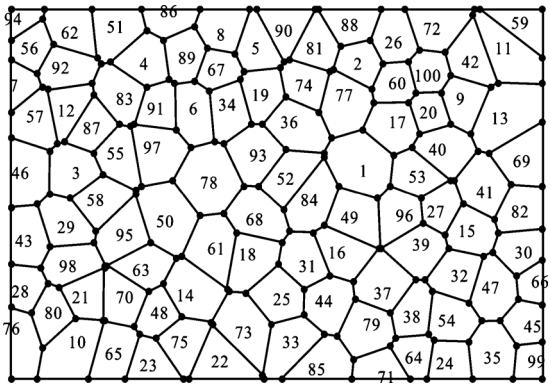

FIG. 13. Voronoi diagram obtained for randomly distributed posts. The numbers shown in this figure refer to the posts and their locations.

C. Stability of air-water interface

In this subsection, we study the condition at which the air-water interface (meniscus) may transition from the nonwetted state (Cassie state) to the wetted state (Wenzel state). This is important in practical applications for submersed bodies because once the thin gas layer is replaced by liquid, none of the beneficial effects remain. The aforementioned transition is interpreted by two approaches: one is based on minimizing the thermodynamic free energy[26,27] and the other is via balancing forces.[28–30] Lee and Kim[31] used the latter approach to develop an equation to determine the maximum allowable hydrostatic pressure in terms of the surface microstructure,

$$P_{\max}\phi_g \leq \frac{-2\gamma\sqrt{\pi(1-\phi_g)}\cos\theta}{L}, \tag{7}$$

where $P_{\max}$ is the maximum allowable pressure without transition, ϕ_g is the gas fraction, γ is the surface tension of the liquid (72×10^{-3} N/m in case of water), θ is the contact angle, and L is the pitch (distance between two posts).

It is noticed that if Eq. (7) is used with both staggered and aligned posts, the same result is obtained provided that the gas fraction, pitch, surface tension, and contact angle are kept the same for the two cases. To use Eq. (7) for a surface with random post distribution, one needs to obtain a characteristic length (spacing) for the open area between the posts. To do so, we divided our superhydrophobic surface into cells by generating the so-called Voronoi diagram.[32] In Fig. 13, each post has a Voronoi cell consisting of all points on the surface that are closer to this post than to any other post. The sides of a Voronoi cell are locations of the points on the surface that are equidistant from the two nearest posts. The Voronoi nodes are the points equidistant from three (or more) posts.

The Voronoi diagram is used here to determine the local gas fraction and the maximum pitch for each post. This information is used in Eq. (7) to determine the maximum allowable hydrostatic pressure, which corresponds to the post that has the maximum local gas fraction. For instance in Fig. 13, one obtains the maximum local gas fraction to be at post (cell) number 13. The maximum allowable pressure is then calculated at this cell. The other parameter that reduces

Downloaded 11 Jan 2011 to 128.172.192.45. Redistribution subject to AIP license or copyright; see http://pof.aip.org/about/rights_and_permissions

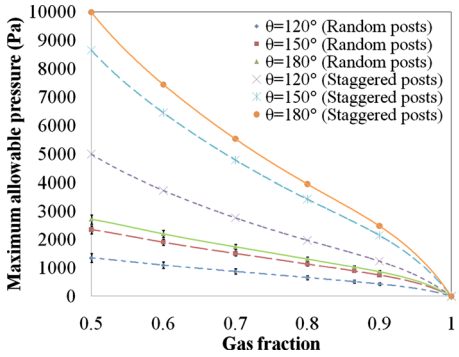

FIG. 14. (Color online) Maximum allowable pressure as a function of gas fraction and contact angle for both random and staggered posts.

the maximum allowable pressure is the pitch, which sometimes dramatically increases as a result of the posts being randomly distributed. In Fig. 13, the maximum pitch is found to be between post numbers 13 and 41.

We generated an ensemble of ten different random post distributions and calculated the maximum allowable pressure for each case as shown in Fig. 14. The simulations are also repeated for different contact angles from 120° to 180°. The results of staggered posts are also shown in this figure for comparison. It is obvious that the maximum allowable pressure is reduced dramatically in case of random posts. The results of this figure indicate that superhydrophobic surfaces with random roughness distributions are much more susceptible to failure under hydrostatic pressure, as the allowable maximum pressure is much less in the case of random posts. So, although random posts result in more drag reduction, the longevity of such coating is reduced.

In order to investigate the impact of the maximum allowable pressure on the drag reduction for both staggered and random posts, a comparison between the skin-friction coefficients of those two types of posts is shown in Fig. 15(a). The coefficients are average values obtained for different Reynolds numbers in the range of $11.85 < \mathrm{Re} < 1778$. It is obvious that the friction coefficient associated with the random posts is always higher than that of staggered posts. The reason is that, at the same maximum allowable pressure and contact angle, the permitted gas fraction for the random posts is always lower than that for the staggered posts (see Fig. 14). Plotting the same information from a different perspective, Fig. 15(b) shows the normalized difference between the skin friction coefficients obtained for staggered and random posts, $\{[(C_f)_s - (C_f)_r]/(C_f)_s\}_{\mathrm{avg}}$. The negative sign on the ordinate indicates that the friction coefficient of the random posts is higher than that of the staggered posts, but that trends is slowed down to a minimum at a pressure of around 1500 Pa.

Figure 16 shows the ensemble-averaged maximum allowable pressure, where the average is calculated for the current and all previous attempts. It is clear that the maximum allowable pressure is approximately the same for all attempts to rerandomize the posts. This indicates that the results presented herein are not affected by statistical errors.

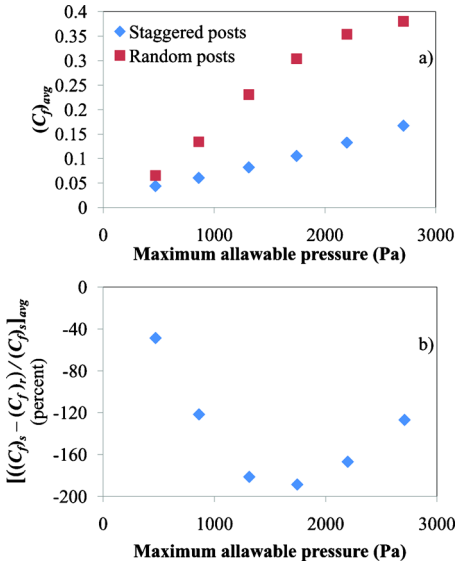

FIG. 15. (Color online) (a) Average skin friction coefficient against maximum allowable pressure. (b) Percentage difference between skin-friction coefficients of staggered and random posts.

VI. CONCLUSIONS

Drag reduction and air-water interface (meniscus) stability analysis for superhydrophobic surfaces having random roughness are conducted numerically and reported in this paper. Examples of such surfaces are those found in nature (e.g., lotus leaf) or produced by random deposition of hydrophobic particles. Such surfaces are far less expensive to make as compared to those made with microfabrication techniques.

Comparing the present results to previous theoretical and experimental studies using staggered microposts for channel flows and streamwise- and spanwise-ridge configurations for pipe flows validates the accuracy of our simulations. In particular, our results indicate that the skin-friction coefficient (i.e., pressure drop) decreases by increasing the surface gas fraction (i.e., shear-free area). The friction coefficient on a surface with random roughness is found to have a relationship with Reynolds number similar to that of the flow over a smooth surface, although with different constants being a function of the gas fraction.

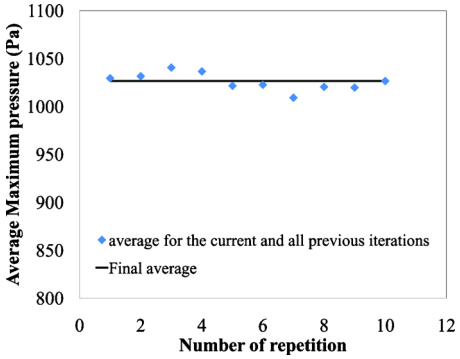

FIG. 16. (Color online) Average maximum allowable pressure vs the number of repetitions for different attempts to randomize the posts.

Downloaded 11 Jan 2011 to 128.172.192.45. Redistribution subject to AIP license or copyright; see http://pof.aip.org/about/rights_and_permissions

Comparing surfaces having random hydrophobic roughness (particles) with those having staggered microposts, we showed that the former causes less friction drag, especially at high gas fractions. The difference in the average skin- friction coefficients between these two configurations is increased by increasing the gas fraction. Our interface stability analysis using the Voronoi algorithm, however, has revealed that superhydrophobic surfaces made by randomly depositing microparticles or microposts are more susceptible to elevated hydrostatic pressures. It was shown that at a given maximum allowable pressure, surfaces with random post distribution produce less drag reduction than those made up of staggered post. Our simulation results are compared with work of Sbragaglia and Prosperetti, and good agreement has been observed for gas fractions up to about 0.9.

ACKNOWLEDGMENTS

This research is sponsored by the Defense Advanced Research Projects Agency (DARPA), Contract No. W91CRB-10-1-0003, technical sponsor Captain Christopher Warren, USN. The content of this paper does not necessarily reflect the position or the policy of the Government and no official endorsement should be inferred.

[1] J. P. Rothstein, "Slip on superhydrophobic surfaces," Annu. Rev. Fluid Mech. **42**, 89 (2010).
[2] M. Gad-el-Hak, *Flow Control: Passive, Active, and Reactive Flow Management* (Cambridge University Press, London, 2000).
[3] J. Ou, J. B. Perot, and J. P. Rothstein, "Laminar drag reduction in microchannels using ultrahydrophobic surfaces," Phys. Fluids **16**, 4635 (2004).
[4] J. Ou and J. P. Rothstein, "Direct velocity measurements of the flow past drag-reducing ultrahydrophobic surfaces," Phys. Fluids **17**, 103606 (2005).
[5] P. Joseph, C. Cottin-Bizonne, J.-M. Benoit, C. Ybert, C. Journet, P. Tabeling, and L. Bocquet, "Slippage of water past superhydrophobic carbon nanotube forests in microchannels," Phys. Rev. Lett. **97**, 156104 (2006).
[6] R. Truesdell, A. Mammoli, P. Vorobieff, P. van Swol, and C. J. Brinker, "Drag reduction on a patterned superhydrophobic surface," Phys. Rev. Lett. **97**, 044504 (2006).
[7] M. Martell, J. B. Perot, and J. P. Rothstein, "Direct numerical simulations of turbulent flows over superhydrophobic surfaces," J. Fluid Mech. **620**, 31 (2009).
[8] C. J. Teo and B. C. Khoo, "Analysis of stokes flow in microchannels with superhydrophobic surfaces containing a periodic array of micro-grooves," Microfluid. Nanofluid. **7**, 353 (2009).
[9] R. Daniello, N. E. Waterhouse, and J. P. Rothstein, "Turbulent drag reduction using superhydrophobic surfaces," Phys. Fluids **21**, 085103 (2009).
[10] Y. P. Cheng, C. J. Teo, and B. C. Khoo, "Microchannel flow with superhydrophobic surfaces: Effects of Reynolds number and pattern width to channel height ratio," Phys. Fluids **21**, 122004 (2009).
[11] C. Kunert and J. Harting, "Simulation of fluid flow in hydrophobic rough microchannels," Int. J. Comput. Fluid Dyn. **22**, 475 (2008).
[12] E. Lauga and H. A. Stone, "Effective slip in pressure-driven Stokes flow," J. Fluid Mech. **489**, 55 (2003).
[13] J. Philip, "Flow satisfying mixed no-slip and no-shear conditions," Z. Angew. Math. Phys. **23**, 353 (1972).
[14] A. M. J. Davis and E. Lauga, "The friction of a mesh-like superhydrophobic surface," Phys. Fluids **21**, 113101 (2009).
[15] A. M. J. Davis and E. Lauga, "Geometric transition in friction for flow over a bubble mattress," Phys. Fluids **21**, 011701 (2009).
[16] M. Sbragaglia and A. Prosperetti, "Effective velocity boundary condition at a mixed slip surface," J. Fluid Mech. **578**, 435 (2007).
[17] M. Sbragaglia and A. Prosperetti, "A note on the effective slip properties for microchannel flows with ultrahydrophobic surfaces," Phys. Fluids **19**, 043603 (2007).
[18] C. Lee, C.-H. Choi, and C.-J. Kim, "Structured surfaces for giant liquid slip," Phys. Rev. Lett. **101**, 064501 (2008).
[19] H. Yang and Y. Deng, "Preparation and physical properties of superhydrophobic papers," J. Colloid Interface Sci. **325**, 588 (2008).
[20] S. D. Bhagat, Y.-H. Kim, K.-H. Suh, Y.-S. Ahn, J.-G. Yeo, and J.-H. Han, "Superhydrophobic silica aerogel powders with simultaneous surface modification, solvent exchange and sodium ion removal from hydrogels," Microporous Mesoporous Mater. **112**, 504 (2008).
[21] C. Ybert, C. Barentin, C.-B. Cécile, P. Joseph, and L. Bocquet, "Achieving large slip with superhydrophobic surfaces: Scaling laws for generic geometries," Phys. Fluids **19**, 123601 (2007).
[22] C. L. M. H. Navier, "Memoire sur les lois du mouvement des fluides," Mem. Acad. Sci. Inst. Fr. **6**, 389 (1823).
[23] The additional validation was suggested by an anonymous reviewer.
[24] M. A. Tahir and H. V. Tafreshi, "Influence of fiber orientation on the transverse permeability of fibrous media," Phys. Fluids **21**, 083604 (2009).
[25] S. A. Hosseini and H. V. Tafreshi, "Modeling particle filtration in disordered 2-D domains: A comparison with cell models," Sep. Purif. Technol. **74**, 160 (2010).
[26] N. A. Patankar, "Transition between superhydrophobic states on rough surfaces," Langmuir **20**, 7097 (2004).
[27] L. Barbieri, E. Wagner, and P. Hoffmann, "Water wetting transition parameters of perfluorinated substrates with periodically distributed flat-top microscale obstacles," Langmuir **23**, 1723 (2007).
[28] C. W. Extrand, "Criteria for ultralyophobic surfaces," Langmuir **20**, 5013 (2004).
[29] C. W. Extrand, "Designing for optimum liquid repellency," Langmuir **22**, 1711 (2006).
[30] Q. S. Zheng, Y. Yu, and Z. H. Zhao, "Effects of hydraulic pressure on the stability and transition of wetting modes of superhydrophobic surfaces," Langmuir **21**, 12207 (2005).
[31] C. Lee and C.-J. Kim, "Maximizing the giant slip on superhydrophobic microstructures by nanostructuring their sidewalls," Langmuir **25**, 12812 (2009).
[32] A. Okabe, B. Boots, K. Sugihara, and S. N. Chiu, *Spatial Tessellations: Concepts and Applications of Voronoi Diagrams* (Wiley, Chichester, 2000).

Downloaded 11 Jan 2011 to 128.172.192.45. Redistribution subject to AIP license or copyright; see http://pof.aip.org/about/rights_and_permissions

Vita

Mohamed Samaha is a graduate student in the Virginia Commonwealth University, Department of Mechanical & Nuclear Engineering after completing his master of science in mechanical engineering from Faculty of engineering, Alexandria University, Egypt, 2007. He have been awarded ten academic honors & professional recognition that demonstrate excellence in education, research, publication, and teaching. The most recent one is outstanding graduate teaching assistant (GTA) award from the School of Engineering, Virginia Commonwealth University. Additionally, he won a national competition for a scholarship to participate in a tutorial school on "Fluid Dynamics: Topics in Turbulence", which was jointly hosted by the Johns Hopkins University and the University of Maryland, 24–28 May 2010. Moreover, he has obtained Essam A. Salem award for the best master of science in fluid mechanics, Alexandria University, Egypt, 2007.

From his masters and doctoral research, Mohamed has published eight journal papers and two more under review. Additional, he gave four presentations in the 64^{th} Annual Meeting of the American Physical Society's Division of Fluid Dynamics (DFD) held in Baltimore, Maryland, November 20^{th} to 22^{nd}, 2011. He has also five other proceeding papers. In addition to these, he is a reviewer in four prestigious journals.

In both Virginia Commonwealth University and Alexandria University, Mohamed has worked as a teaching assistant for different classes including fluid mechanics, thermodynamics, heat transfer, energy conversion systems, and hydraulics.